The Carbon Budget of the Mekong River Basin: A Spatial and Temporal Study of Chemical Weathering

Katy Elizabeth Relph

Department of Earth Sciences
University of Cambridge

This thesis is submitted for the degree of
Doctor of Philosophy

Queens' College
September 2019

Declaration

I hereby declare that except where specific reference is made to the work of others, the contents of this dissertation are original and have not been submitted in whole or in part for consideration for any other degree or qualification at the University of Cambridge, or any other University. This dissertation is my own work and contains nothing which is the outcome of work done in collaboration with others, except as specified in the text and Acknowledgements. This dissertation contains fewer 275 numbered pages of which not more than 225 pages are text, appendices, illustrations and bibliography, as stipulated by the Degree Committee of Earth Sciences.

Katy Elizabeth Relph
September 2019

The Carbon Budget of the Mekong River Basin: A Spatial and Temporal Study of Chemical Weathering

Katy Elizabeth Relph

The chemical weathering of silicate rocks with carbonic acid is thought to play an important role in the consumption of atmospheric carbon dioxide (CO_2), which regulates global climate over million–year timescales. However, the climatic implications of chemical weathering of carbonate rocks with sulfuric acid, a process that can release geologically stored carbon to the atmosphere, are not thoroughly understood. Depending on the reaction environment the lithologically–sourced carbon released from the sulfuric acid weathering of carbonates can either degas as CO_2 instantaneously to the atmosphere, or can be transferred as bicarbonate (HCO_3^-) to the oceans to be precipitated as carbonate, releasing CO_2 on million–year timescales. It is important to consider the timescale of CO_2 release to assess whether a river basin is a transient, or long–term source of carbon to the atmosphere. Few studies have highlighted the importance of this weathering reaction and less have quantified the impact of CO_2 release from sulfuric acid weathering of carbonates in large scale catchments.

Quantifying carbonate weathering with sulfuric acid requires the source of riverine sulfate (SO_4^{2-}) to be determined. This comes predominantly from two sources: sedimentary sulfate and sulfide. Sulfate released from the weathering of gypsum or anhydrite plays no role in the carbon cycle. Oxidative weathering of sedimentary sulfides, predominantly pyrite, produces sulfuric acid which can react with carbonates to release CO_2. Here, new coupled sulfur, $\delta^{34}S_{SO_4}$, and oxygen, $\delta^{18}O_{SO_4}$, isotope data on dissolved riverine sulfate and river water isotopes, $\delta^{18}O_{H_2O}$, from one of the world's largest rivers, the Mekong in Southeast Asia, are presented. A new two end member mixing model is used to partition sources of dissolved sulfate. Importantly, sulfate sources cannot be distinguished using $\delta^{34}S_{SO_4}$ alone, and hence $\delta^{18}O_{SO_4}$ must also be determined.

The Mekong is the world's 10th largest river in terms of discharge, yet is disproportionately understudied compared to many other large rivers where chemical weathering rates have been investigated. This study sampled 36 tributaries and 10 locations along the main channel to calculate the carbon budget of the Mekong River. Samples were collected over three field seasons, as well as a bi-monthly time–series from 2014-2017. HCO_3^- and SO_4^{2-} concentrations in the Mekong are up to 2709μmol/L and 720.3μmol/L respectively, and generally decrease downstream from the headwaters on the Tibetan Plateau. Samples display up to 20.7‰ difference in $\Delta^{18}O_{SO_4-H_2O}$, and $\delta^{34}S_{SO_4}$ ranges by ~13.5‰ over the basin. The proportion of sulfate derived from the oxidative weathering of pyrite, f_{pyr}, calculated by the two end member mixing model varies between 0.18 and 0.83 in Mekong tributaries with a mean of 0.60 in the main channel.

Sources of dissolved inorganic carbon (DIC) are partitioned using a forward model which incorporates the source of acidity in weathering reactions (carbonic or sulfuric) and the use of individual Ca/Na and Mg/K ratios in silicate end members of each tributary. Charge balance calculations with partitioned cations suggest the most likely reaction pathway of CO_2 release from sulfuric acid weathering of carbonates is instantaneous degassing. The weathering of carbonates by carbonic acid accounts for on average 81% of the total DIC flux for all tributaries, whilst carbonic acid weathering of silicates contributes on average 19% (ranging 7-60%) of the total DIC flux in tributaries. Using a framework to track partitioned Ca^{2+} ions, CO_2 consumption or release in the Mekong basin is shown graphically.

On timescales shorter than carbonate precipitation, all Mekong tributaries are a sink of atmospheric CO_2. Annually, the instantaneous release of CO_2 from oxidative pyrite–driven weathering of carbonates is ∼16 times smaller than the drawdown of atmospheric carbon by carbonic acid weathering of both silicate and carbonate minerals. On million–year timescales, the headwater regions in China and one karst dominated tributary in the Middle Mekong release CO_2. The carbon budget of the Mekong varies throughout the year: during the monsoonal months the Mekong consumes atmospheric CO_2 but CO_2 is released during the dry season. Carbonic acid weathering of carbonates is carbon–neutral on million–year timescales, whereas the release of CO_2 from sulfuric acid weathering of carbonates is large enough to marginally offset the long–term sequestration of atmospheric CO_2 by carbonic acid weathering of silicates. Time–series samples and discharge measurements at Chroy Changvar, close to the mouth, are used to determine that the Mekong River basin is an annual net source of $0.01 tC.km^{-2}.yr^{-1}$ to the atmosphere. This differs to previous estimates, which indicate atmospheric CO_2 consumption by the Mekong. This thesis highlights the importance of determining the origin of sulfate in the world's largest rivers for the global carbon cycle, particularly in catchments with a high proportion of carbonate lithology.

In memory of

Professor Don Eccleston, FRCPsych, PhD, DSc

without whom I may never have been on this adventure

> Believe me, my young friend, there is nothing - absolutely nothing - half so much worth doing as simply messing about in boats.
>
> *The Wind in the Willows, Kenneth Grahame*

Acknowledgements

This thesis is in memory of Don, whom I distinctly remember saying: 'Of course you should do a PhD, why on Earth wouldn't you?!' You were right, Don. The past four years have been some of the most intellectually rewarding, adventurous and enjoyable. I have been able to pursue research, learning from brilliant, inspiring scientists, surrounded by good friends, all of whom I wish to thank.

I would like to acknowledge Ruth Robinson, who set me on this journey in 2014 in St. Andrews. I am most thankful to my two supervisors, Ed Tipper and Mike Bickle, who throughout my PhD have provided me with incredible support and direction. I am grateful to Ed for always being generous with his time when our '10 minute' chats turned into thought–provoking, afternoon–long discussions. Through whirlpools and delirious heat, thank you Ed for agreeing to my military precision field trips to cram in that extra sample. The field trips carried out to sample the Mekong river, starting in 2014, have been adventures of a lifetime. I don't think I will ever forget going out to find food in Kratie, Cambodia, after a long day in the field and an even longer evening filtering only to be met with energy drinks, dragon fruit and 'special' eggs. I want to thank Mike for his kind, wise words. Discussions with Mike and feedback throughout my thesis write-up have greatly enriched both myself and this project.

I would like to thank the people that joined me on fieldwork: Tom Perkins, Rita Santos, Linshu Feng, Jotis Baronas, and Will McMahon, who were all vital in the success of the field trips and made the long filtering nights much more entertaining. I wish to thank Sally and Andy for putting me up and feeding me whilst I was playing with 'Mekong mud' and to Molly who greatly assisted in the daily time-series collection in Phnom Penh, even after the 5.30 am tuk–tuk run. Thanks also go to Dan Parsons and Chris Hackney at University of Hull and to Steve Darby at University of Southampton, for all your logistical help, MRC data, loan of aDcp instruments, and fun nights on the Mekong. Also thanks to Ben10 and Soun for showing me the *real* Mekong.

Within the Department I would like to thank Hazel Chapman who gave me my first introduction to clean laboratory geochemistry. Thank you for your patience Hazel, and for teaching me the intricacies of column chemistry and the Sector 54. I would like to thank Ruth Hindshaw for taking the time to teach me new column chemistry methods and for introducing me to the Neptune. Thank you to Hal Bradbury, without whom there would be no anion measurements. Thank you for your help running the Dionex and for your advice. Thanks also go to Mervyn Greaves for showing me the ropes on the Agilent, and to Jo Clegg and Jason Day for their assistance in all things lab and sample preparation related. I extend my thanks to Sasha Turchyn and Gilad Antler for allowing me into your lab to discuss and test all things sulfur, and also to James Rolfe for his patience when analysing said sulfur. I am grateful to Christina Larkin and Tom Williams who taught me everything about neodymium isotopes. I would like to particularly thank Christina for being an excellent sounding board for a myriad of ideas. And thank you to Sambuddha Misra for scones, inspiring conversations, Neptune help and encouragement to think differently, both in and out of the clean lab.

I want to especially thank my friend Madeleine Bohlin, whose passionate, thoughtful and meticulous approach to geochemistry is inspirational to me. I am a better geochemist for the conversations with Madeleine in her office across the mezzanine. Thanks also go to Emily Stevenson, whose enthusiasm for all things science and discussions on the intricacies of sulfur and strontium have been invaluable.

I am fortunate enough to have gathered many friends along the way in the Department, rowing and at Queens' College. Special thanks go to Kathy Gunn, Charlotte Jackson, Victoria Honour, Lil Read, Lexi Scammell, and Jenny Woods for their friendship, fun times and food; and to the 'Drum boys': Simon Stevenson, Conor O'Malley and Paddy Ball for providing the laughs and technical know-how which has been a thesis-saver. I would like to thank Lil Read for her support especially during thesis writing, Lil's proof-reading services were always available no-matter where in the world she was. Charlotte, thank you for your constant encouragement and contagious motivation, whether that be whilst I was working hard rowing with Queens' WI or through the last few days working on my thesis.

Finally, to my sister Laura, thank you for always making me laugh, for your loyal and honest opinions and for bringing me back to the 'real' world. To my Mum and Dad, you support and inspire me. The word thank you is not a big enough for the love and gratitude I have for you both.

Katy

Contents

5 Quantifying Sulfuric Acid Weathering 95

List of Figures

List of Tables

Nomenclature

Notation	**Definition**
^{87}Sr/^{86}Sr	Ratio of ^{87}Sr to ^{86}Sr
^{143}Nd/^{144}Nd	Ratio of ^{143}Nd to ^{144}Nd
ε_{Nd}	Deviation of ^{143}Nd/^{144}Nd from CHUR
δD	Deuterium isotopic signature of water; ratio of stable hydrogen isotopes ^{1}H to ^{2}H, relative to VSMOW in ‰
$\delta^{18}O_{H_2O}$	Ratio of stable oxygen isotopes ^{18}O to ^{16}O in water, relative to VSMOW in ‰
$\delta^{18}O_{SO_4}$	Isotopic signature of oxygen in SO_4^{2-} ions
$\Delta^{18}\mathrm{O}_{SO_4-H_2O}$	Difference in oxygen isotopic signature of SO_4^{2-} and H_2O
δ^{34}S	Ratio of stable sulfur isotopes ^{34}S/^{32}S relative to the standard VCDT, in ‰
$\delta^{34}S_{SO_4}$	Isotopic composition of sulfur in SO_4^{2-} ions
$\varepsilon_{SO_4-O_2}$	Kinetic oxygen isotope fractionation factor between molecular oxygen and SO_4^{2-}
$\varepsilon_{SO_4-H_2O}$	Kinetic oxygen isotope fractionation factor between water derived oxygen and SO_4^{2-}
$\varepsilon_{SO_4-FeS_2}$	Sulfur isotope fractionation between pyrite and SO_4^{2-}
f_{gyp}	The fraction of SO_4^{2-} delivered from sedimentary sulfates (primary sulfate)
f_{pyr}	The fraction of SO_4^{2-} delivered from oxidative weathering of sulfides (secondary sulfate)
X_{sil}	Cations delivered from weathering of silicate minerals as a fraction of cations delivered from silicate and carbonate minerals
F_{sulf}	Acidity sourced from H_2SO_4 as a fraction of H_2CO_3 and H_2SO_4 available to weather minerals
F_{carb}	Cations delivered from weathering of carbonate minerals as a fraction of cations delivered from silicate and carbonate minerals

Acronymns

aDcp	Acoustic Doppler current profile
BSR	Bacterial Sulfate Reduction
CHUR	CHondritic Uniform Reservoir
CO_2	Carbon Dioxide
DIC	Dissolved Inorganic Carbon
DOC	Dissolved Organic Carbon
EAM	East Asian Monsoon
IM	Indian Monsoon
m.a.s.l.	Metres above sea level
MRC	Mekong River Commission
VCDT	Vienna Canyon Diablo Troilite
VSMOW	Vienna Standard Mean Ocean Water
WNPM	Western North Pacific Monsoon

Chapter 1

Introduction

1.1 Chemical Weathering as a Climate Regulator

Climate change is one of the biggest issues facing our planet this century. Not only must we understand how the climate changes over time, but how these changes are regulated. The Earth's climate is intrinsically inter–linked to the long–term global carbon cycle, which takes into consideration the transfer of carbon dioxide (CO_2) between rocks and the surficial system, consisting of the atmosphere, hydrosphere and biosphere (Berner, 1999). Two key processes in the global carbon cycle are the chemical weathering of silicate rocks and carbonate precipitation in the oceans. These two processes balance CO_2 degassing from the solid Earth and maintain a habitable environment on our planet. Atmospherically derived carbonic acid reacts with silicate minerals, liberating cations and anions which are subsequently precipitated as carbonate in oceans. This process sequesters CO_2 from the atmosphere into the rock reservoir over long–term timescales ($>10^5$ years) (Berner *et al.*, 1983; Sundquist, 1991; Urey, 1952; Walker *et al.*, 1981).

The size of the surficial reservoir, specifically the levels of CO_2 in the atmosphere which is an important greenhouse gas, moderates the global climate (Kasting, 1987). However, the surficial reservoir stores orders of magnitude less carbon than the rock reservoir stores (3 x 10^{18} mol C and 5 x 10^{21} mol C, respectively) (Berner & Caldeira, 1997; Sundquist & Visser, 2003). Therefore the

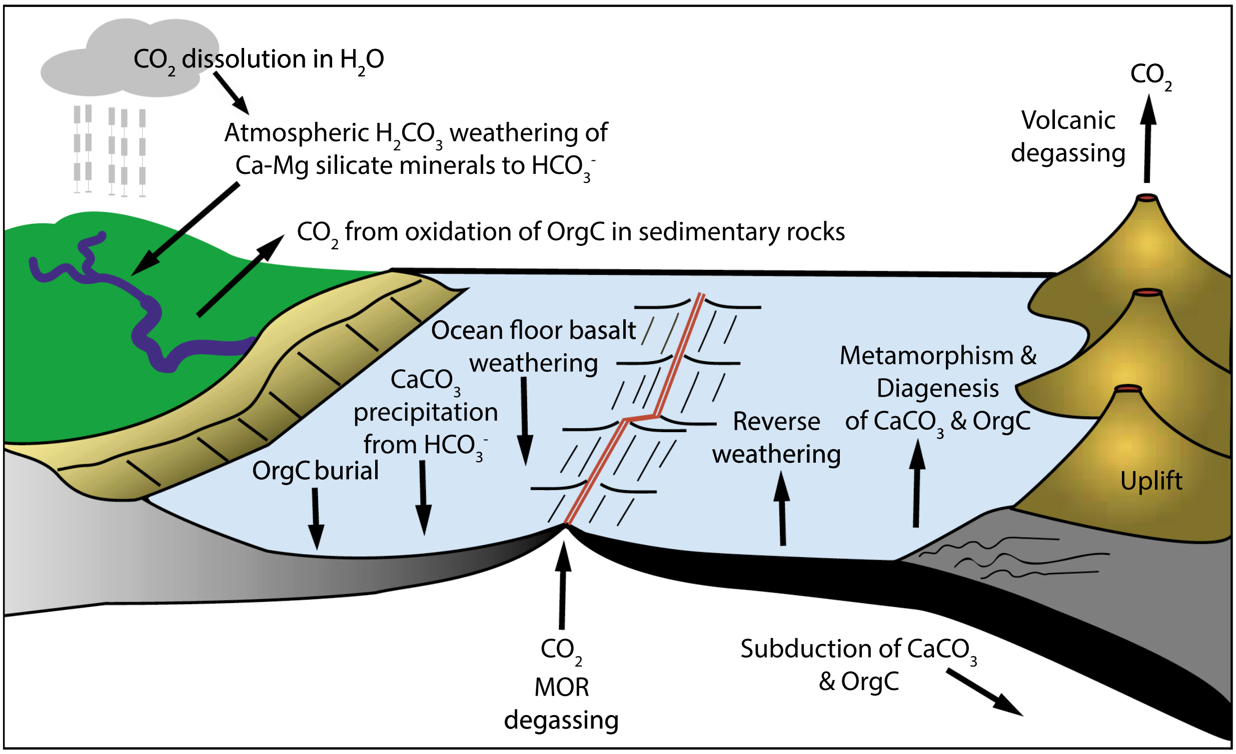

Figure 1.1: The long term global carbon cycle. Arrows represent carbon transfer between the rock reservoir and the surficial reservoir (atmosphere and ocean). Carbon is transferred as carbon dioxide gas (CO_2) unless stated as aqueous dissolved inorganic carbon (HCO_3^-) and stored in the rock reservoir as carbonate ($CaCO_3$) or organic carbon (OrgC, CH_2O). CO_2 is degassed into the atmosphere in a number of ways; volcanic emissions from mid-ocean ridge (MOR) spreading, continental volcanoes over subduction zones, metamorphic or diagenetic decarbonation of limestones, and oxidation of organic carbon. Reverse weathering on the seafloor is an unconstrained source of atmospheric CO_2. CO_2 is removed from the atmosphere by silicate weathering and sequestered into the rock reservoir by carbonate precipitation. Organic carbon burial also removes atmospheric CO_2 as does ocean floor basalt weathering to an unknown degree. Modified after Berner (1999), Gaillardet & Galy (2008), and Kump *et al.* (2000).

surface reservoir is critically sensitive to small changes in the relatively big fluxes of carbon in and out of the rock reservoir (8 x 10^{18} mol C per million years) (Berner & Caldeira, 1997; Sundquist & Visser, 2003). Degassing of the Earth's interior provides a source of CO_2 to the atmosphere, via volcanic emissions from ocean-floor spreading and subduction zones, and metamorphic and diagenetic decarbonation of limestones and organic matter (Berner, 2004; Berner & Caldeira, 1997) (Figure 1.1). CO_2 is removed via precipitation of carbonate in the ocean and burial of organic matter, with the carbonate precipitation flux around three times larger than the organic carbon burial flux (Gaillardet & Galy, 2008; Sundquist & Visser, 2003). The balance between inputs and outputs of atmospheric CO_2 from the sources mentioned above is governed by silicate weathering. The rate of CO_2 consumption by silicate weathering is dependent on changes in climate, controlled by the level of atmospheric CO_2, therefore silicate weathering provides a negative feedback process on climate change.

Controls on chemical weathering rates have been debated since the 1980's. Berner *et al.* (1983) proposed that ocean spreading rates control the degassing of CO_2 and therefore chemical weathering rates, which adjust rapidly to balance the degassing of CO_2. This idea was challenged by Raymo *et al.* (1988) who suggested that CO_2 removal by tectonism forces climate. Specifically Raymo *et al.* (1988) attributed the cooling of global climate at the start of the Cenozoic (Zachos *et al.*, 2001) to the Himalayan orogeny. The uplift of the Himalayas increases continental relief which subsequently generates orographically driven runoff and increases erosion. When combined, these factors increase silicate weathering which reduces atmospheric CO_2. Raymo *et al.* (1988) interpreted the marine $^{87}Sr/^{86}Sr$ isotope record through the Cenozoic (Hess *et al.*, 1986) as evidence that increased erosion was cooling the Earth. Principal sources of Sr to the ocean are from continental weathering and hydrothermal alteration of ocean basalts (Palmer & Edmond, 1989), both sources have distinctly different $^{87}Sr/^{86}Sr$ signatures. Continental silicate rocks have much higher $^{87}Sr/^{86}Sr$ than oceanic basalts, so the increase in radiogenic $^{87}Sr/^{86}Sr$ through the Cenozoic was ascribed to an increase in continental silicate rock weathering (Raymo, 1991). However, studies have shown that Himalayan carbonate minerals are extremely radiogenic (up to $^{87}Sr/^{86}Sr=0.86$) (Blum *et al.*, 1998; Galy *et al.*, 1999), thus the increase in $^{87}Sr/^{86}Sr$ points to the importance of the Himalayas, but how much of this is due to carbonate and silicate mineral weathering is still uncertain. Furthermore, an increase in erosion would not change the $^{87}Sr/^{86}Sr$ isotope record, but an increase in the weatherability of the Earth's crust would reduce global temperatures.

The processes controlling the rates of carbon transfer and the influence on the Earth's climate are still not yet completely understood (Bluth & Kump, 1994; Coogan & Gillis, 2013; Gaillardet & Galy, 2008; Willenbring & von Blanckenburg, 2010). There is more to learn on the interactions of temperature, runoff and erosion on chemical weathering, on reverse weathering, an additional, yet unquantified, source of CO_2 (Mackenzie & Garrels, 1966), and carbonic acid weathering of ocean floor basalt (Coogan & Gillis, 2013). These all require quantifying and implementing into global carbon models (Coogan *et al.*, 2019). It is vital to have a comprehensive understanding of these forcings in order to predict the response of the global carbon cycle to anthropogenic perturbations caused by land use change and fossil fuel combustion (Karl & Trenberth, 2003; Lenton & Britton, 2006; Zachos *et al.*, 2008).

It is, however, clear that silicate weathering is the principal sink for atmospheric CO_2 and provides a sensitive feedback mechanism stabilising Earth's climate (Anderson, 2005; Gislason *et al.*, 2009; Li *et al.*, 2016; Oliva *et al.*, 2003; White & Blum, 1995; White *et al.*, 1999a). Quantifying modern silicate weathering fluxes is a key step to further understanding controls on silicate weathering and its role in the global carbon cycle. Chemical weathering can be quantified by measuring the dissolved load of river water, the chemistry of which is an integration of processes occurring within the whole basin. Chemical weathering fluxes are a product of the concentration of the dissolved load and discharge.

In an effort to calculate chemical weathering fluxes, field studies have been conducted with two different but complimentary approaches. A first approach is using small scale monolithological catchments to study the controls of weathering, with a hope to constrain the effects of variables such as temperature, elevation, and runoff (Bluth & Kump, 1994; Dessert *et al.*, 2003; Drever & Zobrist, 1992; Gislason *et al.*, 1996; Louvat & Allègre, 1997, 1998; Oliva *et al.*, 1999, 2003; Probst *et al.*, 1992; West *et al.*, 2002; White & Blum, 1995). Detailed work on the progression of weathering fronts, mineral transfer and coupled processes between weathering and climate in the critical zone (the bio-geochemically and physically active section of the Earth's surface that concerns vegetation down to the lower limit of groundwater) has been possible by the establishment of Critical Zone Observatories in small catchments (Brantley *et al.*, 2007, 2013; Jin *et al.*, 2010; White *et al.*, 2015).

A second approach is looking at large scale catchments to provide continental-scale insights on chemical weathering. Chemical weathering and inorganic carbon fluxes of large rivers such as the Amazon, Congo, Mackenzie, and the Ganges-Brahmaputra have been particularly well studied (Bickle *et al.*, 2018; Dupré *et al.*, 1996; Edmond *et al.*, 1995, 1996; Gaillardet *et al.*, 1995, 1997, 1999; Galy & France-Lanord, 1999; Meybeck, 1987; Millot *et al.*, 2002; Moon *et al.*, 2014; Mortatti & Probst, 2003; Négrel *et al.*, 1993; Picouet *et al.*, 2002; Stallard & Edmond, 1983; Suchet *et al.*, 2003; Tipper *et al.*, 2006; Viers *et al.*, 2000; West *et al.*, 2005). However, a complete carbon budget, which consolidates the inorganic and organic carbon fluxes, has only been published on the Mackenzie River basin (Horan *et al.*, 2019). Weathering regimes can be studied in large river basins due to the differing effects of heterogeneous lithology and a range in climate and topography. In large rivers, geochemical signals from both weathering-limited and transport-limited regimes are integrated. In weathering-limited regimes, present in actively eroding mountainous regions, weathering may be incomplete due to the fast removal of material from the system. Conversely, in transport-limited regimes in floodplains weathering is complete and thick soils can build up due to the lack of material transported (Stallard & Edmond, 1983).

A difficulty encountered by large scale catchment studies is calculating the absolute contribution of different lithologies to the dissolved load. Although samples collected at the mouth of a river integrate signals from processes throughout the basin, a single sample is not necessarily characteristic of the spatial and temporal heterogeneity in a river basin. It is complex to identify the signal pertaining to the weathering of silicate minerals, needed to calculate atmospheric CO_2 consumption within a river basin, given the lithological diversity in large catchments. The dissolution of carbonates, for example, contributes about double the amount of dissolved solids to the global weathering flux compared to silicate minerals, 640 x 10^6 t/yr and 300 x 10^6 t/yr respectively, whilst evaporites dissolution contributes a further 144 x 10^6 t/yr of dissolved solids (Gaillardet *et al.*, 1999). Correctly identifying the flux of solutes from each lithology is vital, as the fate of solutes from chemical weathering reactions have significantly different consequences for the carbon cycle. The dissolution of evaporites, such as gypsum and halite, provides solutes to the weathering zone but the reaction does not form part of the carbon cycle. When carbonates react with atmospheric or soil-derived carbonic acid the reaction is a carbon neutral process over million–year timescales, as the carbonate is just re-deposited in the oceans, whilst the same acids reacting with silicate rocks cause deposition of carbonate in the oceans leading to a net drawdown of atmospheric CO_2 acting to stabilise global climate.

Recent work has highlighted the significance of sulfuric acid weathering of carbonates as a component of the long–term carbon cycle (Calmels *et al.*, 2007; Emberson *et al.*, 2018; Torres *et al.*, 2014, 2017; Zolkos *et al.*, 2018). Sulfide oxidation coupled to carbonate dissolution releases CO_2 to the atmosphere (Calmels *et al.*, 2007). Torres *et al.* (2014) suggest that the global flux of CO_2 released from carbonate rock via sulfuric acid weathering is the transient source needed to balance the CO_2 drawdown from enhanced silicate weathering during the Cenozoic.

Chemical weathering reactions with carbonic and sulfuric acid occur on different timescales and in different environments, each with a unique carbon cycle implication. It is necessary to understand these reactions and the products released into the weathering zone in order to apportion river geochemistry between chemical reactions, and subsequently infer the carbon budget of a river. In Chapter 2 the chemical weathering reactions considered by this thesis are described in detail.

This thesis will take the large basin approach to quantify the inorganic carbon budget of the Mekong river. The Mekong is an Asian mega river, rising on the Tibetan plateau flowing through the mountainous region of the Eastern Syntaxis of the Himalayas, an area of rapid erosion. Despite the fact that the Mekong river contributes the world's tenth largest discharge (Dai &

Trenberth, 2002) and tenth largest sediment load to the worlds oceans (Milliman & Meade, 1983), it is an understudied basin. The Mekong river basin provides a perfect natural laboratory to study the impact of sulfuric acid weathering. This climatically and geologically diverse catchment contains evaporites, granites, basalts, carbonates and metamorphosed units and is amongst the main contributors of global sulfate fluxes to the worlds oceans. The Mekong sulfate flux is 50% larger than that delivered by the Ganges, the largest Himalayan draining river (Burke *et al.*, 2018). In comparison to the largest river in the world (the Amazon), the Mekong contributes 7% of the discharge and a disproportionate 23% of the Amazon's sulfate flux (Burke *et al.*, 2018). Here I present the most comprehensive temporal and spatial sampling dataset conducted on the Mekong River to date.

1.2 The Mekong River Basin

Five of the 12 largest rivers on Earth drain the Himalayas and the Tibetan Plateau: the Yangtze, Brahmaputra, Mekong, Ganges and Irrawaddy rivers contribute 8.3% of the world's fresh-water discharge to the global oceans despite only covering 4.5% of the total drained land area (Milliman & Farnsworth, 2011). The collision between northwards moving India and the Eurasian plate during the Eocene uplifted the Himalayas and the Tibetan Plateau (Brookfield, 1998). Subsequent NE-SW shortening, then right–lateral shear of India past southern China caused a further 1000-2000km northward motion of India and the lithospheric deformation observed in the Eastern Himalayan Syntaxis today (Hallet & Molnar, 2001). The geomorphologic manifestation of the crustal strain and thickening of the Eastern Syntaxis of the Himalayas, at the southeastern margin of the Tibetan Plateau, is reflected in the sigmoidal shape and close proximity of three major rivers: the Salween, Mekong and Yangtze which run only tens of kilometres apart for ~300km. The Eastern Syntaxis of the Himalayas is an area of high relief and high elevation (the Tibetan Plateau is over 4500 m.a.s.l., Clark *et al.*, 2004; Harris, 2006) where rapid exhumation has been ongoing since ca. 5 million years ago (Lang *et al.*, 2016). Studies of the physical and chemical weathering of large Himalayan rivers have been used to investigate the potential link between mountain uplift, exhumation, erosion, and silicate weathering, and their combined impact on global climate (Raymo *et al.*, 1988; Raymo & Ruddiman, 1992; Goddéris & François, 1995). Whilst there have been many studies of dissolved solids in the Ganges-Brahmaputra Rivers draining the southern flank of the Himalayas (e.g. Bickle *et al.*, 2015; Galy & France-Lanord, 2001; Hren *et al.*, 2007; Karim & Veizer, 2000; Krishnaswami & Singh, 1998, 2005), there are substantially fewer studies on the three rivers draining the Eastern

Syntaxis of the Himalayas, most noticeably the Mekong River.

1.2.1 Modern Geomorphology of the Mekong River Basin

The Mekong River, also known as the Lancang Jiang in China, is 4880km long and flows through six countries, draining a pan–shaped basin area of 795,000km^2 (Kummu & Varis, 2007). The drainage pattern of the Mekong is complex, which has developed in an intrabasinal setting of a continental collision belt where heterogeneous geology and active tectonics have controlled the course of the Mekong river and its tributaries, and the landscape of the basin (Clark *et al.*, 2004; Tandon & Sinha, 2007). The river basin can be split into three sections by distinct changes in geomorphology, basin width, and channel type that demarcate the transitions between the Upper, Middle and Lower Mekong. The geology, climate and hydrology of the Mekong River and its tributaries will be discussed in terms of these three sections for simplification of this large and geologically complex basin (Figure 1.2).

The Mekong's sources are the Zaqu River and the Angqu River, both originating on the northern flank on the Tanggulashan Mountains on the Tibetan Plateau at an altitude of 4970 m.a.s.l. (Kummu & Varis, 2007; Wu *et al.*, 2008). The Upper Mekong, between the source and southern Yunnan province, China, is characterised by steep topography and narrow gorges where the main channel flows in a curvilinear fashion through the Eastern Syntaxis of the Himalayas (Carling, 2009). There is a distinct widening of the basin and elevation drops to ca. 600 m.a.s.l. where the Mekong exits southern China and the Middle Mekong begins.

As the river exits China, a deep bedrock canyon marks the border between Myanmar and Laos until it reaches the junction of these two countries with Thailand (20° N), where the Mekong changes direction sharply and flows towards the east marking the border of Laos to the north and Thailand to the south. The sharp change in channel alignment is caused by faulting, specifically the left–lateral strike–slip Mae Chan Fault (Fenton *et al.*, 2003, and Figure 1.2). The Mekong channel is deeply cut in rock in a narrow valley until the channel takes a further sharp turn at about 30km upstream from Luang Prabang, aligning along the Nan Suture (Carling, 2009). From Luang Prabang the river continues in a general southwest direction in steep straight channels, with high cross-channel rock ribs (tens of metres high) and rapids for ∼250km, before another sharp turn of the river towards the east to Vientiane (Gupta & Liew, 2007). Incised meanders ∼500-600m wide then straight channels up to 1400m wide are characteristic of the channel between the final

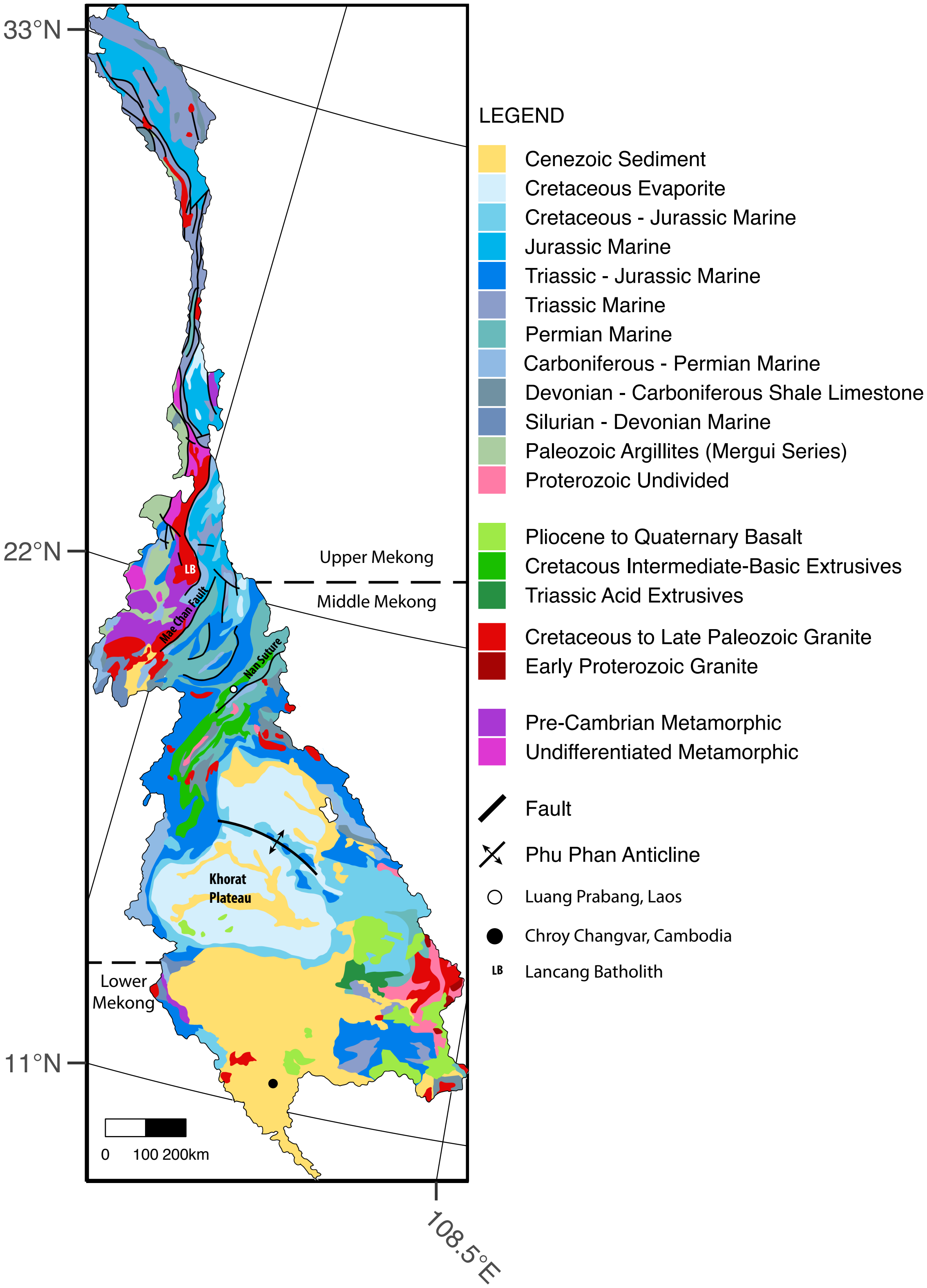

Figure 1.2: Geological map of the Mekong River basin. The basin is split into Upper, Middle and Lower Mekong. Main stem sampling sites Luang Prabang and Chroy Changvar are identified. Geology is modified after Chinese Academy of Geological Sciences (1975).

sharp turn in the Mekong and Vientiane. The channel becomes shallow (up to 13m deep in the wet season) and meanders past Vientiane widening out to 2km by Thakhek where the Mekong flows through alluvium (Gupta & Liew, 2007). The Mekong main channel becomes a bedrock river again south of Thakhek. Over the next 150km downstream, the channel has high steep alluvial banks and is up to 5km wide. South of Pakse, the river anastomoses forming the area known as the '4000 islands' where the whole river width is 15km (Carling, 2009). The anastomosing channels terminate at the 10.783km wide Khone Prapheng Falls; the widest waterfall in the world (World Waterfall Database, 2019). The waterfall demarcates the national border between Laos and Cambodia and the beginning of the Lower Mekong.

The Middle Mekong is characterised by the addition of many large tributaries which drain different geology and topography on the right and left banks of the main channel. On the left bank of the Mekong, tributaries drain the steep Annamite mountain range. The Annamite mountains mark the national border between Vietnam to the east, Laos to the northwest and west and Cambodia to the southwest. Where Thailand, Myanmar and Laos meet, the landscape remains mountainous. Much lower relief is found in central and southeast Thailand in the Khorat Plateau, which is on average 150m.a.s.l. (Carling, 2009). The Khorat Plateau is bound by the Loei–Petchuan Fold Belt on the west and the Annamite mountains in the east. Tributaries draining the Khorat Plateau flow on a gentle gradient (Gupta & Liew, 2007), the largest of which are the Mun and the Chi that meet the Mekong north of Pakse.

In the Lower Mekong, beyond the Khone Prapheng Falls, the channel is still bed-rock controlled due to the geology until Kratie where the free alluvial channel contains subaqueous dunes and overbank flooding is common during the wet season (Gupta & Liew, 2007). South of Phnom Penh, the Tonle Sap joins the Mekong which then starts to divide into the distributaries of the Mekong delta where the Mekong discharges into the South China Sea. For much of the monsoon, the Tonle Sap river flows backwards into the Tonle Sap lake which is fed by the Mekong river. The complex hydrodynamics of the Tonle Sap (Kabeya *et al.*, 2008; Kummu & Sarkkula, 2008) are not discussed further in this thesis.

1.2.2 Geology

The geology of the Mekong basin is poorly documented (Gupta & Liew, 2007). Global Lithological Models (GLiM) identify carbonates, mixed sedimentary and basic volcanic rocks in the Mekong basin (Hartmann & Moosdorf, 2012). Several geological maps exist for areas of the Mekong basin (e.g. Chinese Academy of Geological Sciences, 1975; Fromaget & Saurin, 1952), generally bound by national borders, but detailed lithological descriptions and trans-boundary mapped areas are rare.

1.2.2.1 Upper Mekong

The narrow Upper Mekong basin consists of mixed sedimentary and granitic rocks of Palaeozoic and Mesozoic age with outcrops of Pre-Cambrian metamorphic basement (Gupta & Liew, 2007; Noh *et al.*, 2009, and Figure 1.2). Specifically, the headwaters of the Mekong drain Palaeozoic–Triassic sedimentary rocks from the Qiangtang Block and clastic sedimentary rocks from the Mesozoic arc (Borges *et al.*, 2008; Liu *et al.*, 2011). Whilst evaporites, clastic, and metamorphic rocks (sandstone, shale, schist, chert and limestone) are present, carbonates dominant the lithology (Gupta & Liew, 2007; Liu *et al.*, 2011; Noh *et al.*, 2009; Wu *et al.*, 2008). The Mergui Series, of Carboniferous-Permian age, is made up of argillite, limestone, quartzite and volcanic detritus and is visible to the southeast of the Upper Mekong (Jiang *et al.*, 2017). The Lancang granite batholith, dated to the mid-Permian, outcrops at the southern Chinese border with Myanmar and Laos (Leloup *et al.*, 1995; Noh *et al.*, 2009).

1.2.2.2 Middle Mekong

The Middle Mekong has distinct geology either side of the main channel. The right bank is dominated by the Khorat Plateau and the left bank is predominantly Mesozoic marine sediments and karst topography. The Khorat Plateau is divided into two basins which are separated by the Phu Phan NW–SE trending anticline: the Sakon Nakon basin to the north and Khorat basin to the south (Tabakh *et al.*, 1998). The Khorat Plateau is a continental basin that underwent three major marine influx events during the Cretaceous, due to relative sea level rise. Evaporites that precipitated following sea level regression are within the Maha Sarakham Formation which is mined for it's high levels of potassium rich salt (Hansen *et al.*, 2016; Tabakh *et al.*, 1999). The geology of the Khorat Plateau is described in more detail in Section 5.5.

In northern and central Laos karst topography is well developed on Plateaus within the Annamite mountain range, and form sheer walls to some northeastern Laos tributaries, such as the Nam Ou (Kiernan, 2015). The Hinboun and Nam Kading tributaries drain Carboniferous–Lower Permian Khammoun Limestones and Cretaceous–Jurassic sandstones and conglomerates in central

Laos (Ponta & Aharon, 2014). Cretaceous intermediate–basic extrusive units trend NE–SW between Luang Prabang and Vientiane.

1.2.2.3 Lower Mekong

Upstream of the border between Laos and Cambodia, the Mekong flows over Mesozoic basalt forming the '4000 islands' (Gupta, 2007). The Kong tributary flows over Proterozoic units, and Neogene basalt units, and some small outcrops of Proterozoic granites (Gupta, 2009). South of Kratie the river flows over Quaternary alluvium overlaying Jurassic and Triassic red beds, additionally Pliocene–Pleistocene basalts outcrop between Kratie and Chroy Changvar (Carling, 2009).

1.2.3 Climate and Hydrology

The single peak flood pulse hydrograph of the Mekong main channel is typical of monsoonal rivers (Adamson *et al.*, 2009; Tipper *et al.*, 2006). The climate is dominated by a wet–season between June and November and dry–season between December to May. There is a 20-fold increase in discharge during peak monsoon, discharge varies from $\sim$2100 $m^3.sec^{-1}$ in the dry season to $\sim$41,000 $m^3.sec^{-1}$ at peak monsoon in August to September (Mekong River Commission, 2016, and Figure 1.3). The discharge contribution varies between areas of the Mekong: the Upper Mekong contributes 16%, the Middle Mekong, where the majority of tributaries are found, contributes 56% and three large tributaries in the Lower Mekong contribute the remaining 28% of the mean annual discharge (Adamson *et al.*, 2009). A disproportionately large volume of water arrives from tributaries draining the Annamite mountains in northwest Laos (e.g. Nam Ou, Nam Ngjium, Nam Kading) and in Cambodia (the Tonle Kong, Tonle San and Tonle Srepok tributaries) (Gupta & Liew, 2007).

The Mekong lies at the intersection of three monsoon systems: the Indian Monsoon (IM), the East Asian Monsoon (EAM), and the Western North Pacific Monsoon (WNPM) (Darby *et al.*, 2013; Delgado *et al.*, 2010; Xue *et al.*, 2011). Convective heat over the Bay of Bengal forces the IM precipitation, the monsoon arrives at the southwest side of the Mekong basin first before travelling across the basin in a northeast direction (Delgado *et al.*, 2012). Discharge in Middle Mekong is correlated most with the IM (Xue *et al.*, 2011). The EAM and WNPM air masses are driven by convective heat source over the South China Sea and the Southeast Asian Archipelagos. The EAM and WNPM travel northwest reaching the southeast Mekong basin first. At the Eastern Highlands

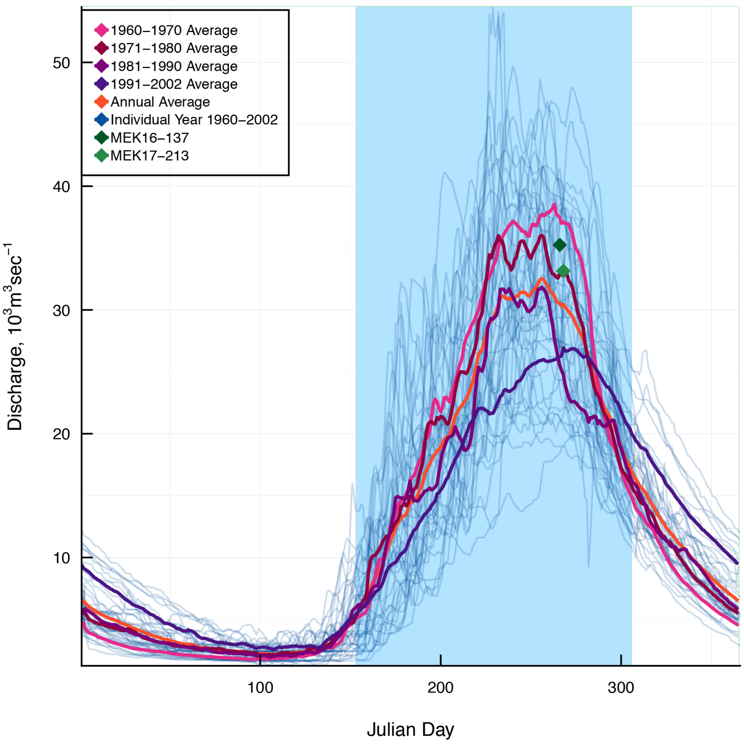

Figure 1.3: Monsoonal hydrograph of the Mekong River at Chroy Changvar, Cambodia. Hydrographs from 1960–2002 are shown with decadal averages to highlight regular timing, but annual variation, in magnitude of peak monsoon (Mekong River Commission, 2016). The blue area represents the wet season between June and November. Sample points locate time of sampling relative to an average monsoon discharge at Chroy Changvar. Samples are from Kratie, one station upstream of Chroy Changvar on the main channel, collected in 2016 and 2017. Discharge value is from aDcp measurements during sampling. There are no major tributaries that enter the main channel between Kratie and Chroy Changvar, therefore discharge comparison is reasonable.

of the Annamite mountains which form the border of Laos and Vietnam, orographic precipitation condenses (Darby *et al.*, 2013; Delgado *et al.*, 2012), hence the Lower Mekong discharge is correlated with the EAM (Xue *et al.*, 2011). The monsoons impact the discharge in the Mekong basin in a south to north direction, increasing discharge in the lower catchments before northern ones. The hydrographs of Middle and Lower Mekong are dominated by the monsoon where more than 80% of the total basin discharge originates, for this reason Lu & Siew (2006) argue that the effect of dam building is limited to the Upper Mekong. In addition to the Middle and Lower Mekong flow regimes being dominated by the three monsoon systems they are also sporadically affected by tropical cyclones, particularly in the east of the basin over the Annamite mountains rather than the Khorat Plateau (Darby *et al.*, 2016). The Upper Mekong is mainly fed by snow melting on the Tibetan Plateau in Spring and affected by the monsoon to a small degree (Delgado *et al.*, 2010). Although the Upper Mekong only contributes a small percentage of the mean annual discharge to the South China Sea (Kummu & Varis, 2007), it is the dominant source of discharge in the lower Mekong during the dry season (Cook *et al.*, 2012).

The coldest temperatures in the Mekong are found in Tibet, ranging between -4 to +13°C over the year on the Tibetan-Yunnan Province border. Further south in Yunnan, temperatures range between +8 to +26°C . As elevation decreases into the Middle Mekong temperatures rise to mean highs of +26°C in June. Between China and northern Thailand there is still a 10°C variation in temperatures throughout the year, with the lowest temperatures generally in January. Between Luang Prabang and the Delta, temperatures only vary by ∼4°C over the year. The highest temperatures measured in the river basin, up to +31°C in April, are in the Lower Mekong at Phnom Penh (Mekong River Commission, 2005).

The combination of elevation, hydrology and temperature affect the climate. According to the Köppen–Geiger classification (Peel *et al.*, 2007), the Upper Mekong basin close to the source has a temperate climate with dry winters and warm summers, further south in Yunnan province the summer months are hotter. Northern Laos receives dry winters but the remainder of the Middle and Lower Mekong has a tropical monsoon or tropical savannah climate where temperatures never drop below 10°C.

1.2.4 Research in the Mekong River Basin

The Mekong river basin supports a large population of ca. 73 million people (Eastham *et al.*, 2008), which places anthropogenic stress in terms of dam building, sand mining, farming, deforestation and irrigation on nutrient content in the water, discharge, fish migration pathways, fish stocks, agriculture and sediment supply (Ou & Winemiller, 2016; Stone, 2016; Ziv *et al.*, 2012). It has been suggested that Laos will become the battery of Southeast Asia as hydropower dams multiply (Fasman, 2016). Most studies, therefore, have focussed on the impacts of anthropogenic stress on the Mekong basin.

Many studies use historical data collected by the Mekong River Commission, dating from before 2005, to investigate changes in hydrograph regime (e.g. Lu & Siew, 2006; Tang *et al.*, 2014; Wild & Loucks, 2014) and sediment delivery due to damming (e.g. Bravard *et al.*, 2014; Fu *et al.*, 2008; Gupta *et al.*, 2002; Kondolf *et al.*, 2014; Kummu *et al.*, 2010; Lu & Siew, 2006; Shrestha *et al.*, 2013; Xue *et al.*, 2011; Zhao *et al.*, 2012, 2015), $p\mathrm{CO}_2$ and degassing of CO_2 from rivers (e.g. Alin *et al.*, 2011; Li *et al.*, 2013), soil erosion (e.g. Chaplot *et al.*, 2005), and variability in organic matter (e.g. Ellis *et al.*, 2012).

Another area of study is the erosion regime of the Tibetan Plateau and the Eastern Syntaxis of the Himalayas. Studies have measured detrital ^{10}Be to determine erosion rates of 0.7 mm.yr^{-1} in the Upper Mekong (Henck *et al.*, 2011). Thermochronometric dating in the steepest section of the Upper Mekong provide constraints on erosion history of the uppermost ∼6km of the crust and suggest that erosion rates decrease towards the north, from 28.5° N to 30° N (Yang *et al.*, 2016). An investigation into weathering using Li isotopes suggested the weathering intensity is lower in the Upper Mekong compared to other large global rivers, due to the arid cold climate (Liu *et al.*, 2011).

Geochemical studies aiming to quantify inorganic carbon fluxes and investigate weathering have either been based on historical time–series (Li *et al.*, 2014a) or based solely on samples collected from the Upper Mekong (Noh *et al.*, 2009; Zhang *et al.*, 2016). Li *et al.* (2014a) provide a first look at the weathering signal of the Mekong using the Mekong River Commission (2016) data available. However, they do not correct for sulfide input and they use Himalayan silicate mineral ratios for partitioning weathering sources, which are not applicable to the lithology in the Mekong catchment. Wu *et al.* (2008) measured major cations in river bed sediment samples collected the Upper Mekong, and estimated silicate molar ratios of 0.17 for Ca/Na and 0.5 for Mg/K. Water chemistry is dominated by Ca^{2+} and HCO_3^- where 40% of total cations are delivered from carbonate weathering (Zhang *et al.*, 2016). Using silicate molar ratios from Wu *et al.* (2008), the Upper Mekong is determined to be a sink of 0.84–1 tC.km^{-2}.yr^{-1} carbon on the short term (Wu *et al.*, 2008; Zhang *et al.*, 2016). Noh *et al.* (2009) suggest that the Upper Mekong consumes 1.2 tC.km^{-2}.yr^{-1} on the long–term, and that up to half of the variation in CO_2 consumption rates around the Tibetan plateau are controlled by runoff and relief. If the long–term budget is corrected for CO_2 release from the oxidative pyrite–driven weathering of carbonates (which Noh *et al.* (2009) calculate by assuming all SO_4^{2-} is derived from pyrite), then Upper Mekong CO_2 consumption is reduced to 0.86 tC.km^{-2}.yr^{-1}. However, CO_2 consumption estimates by both Wu *et al.* (2008) and Noh *et al.* (2009) are an overestimate of long–term carbon drawdown because they include Na and K in their calculation, which do not form carbonates and therefore cannot sequester atmospheric CO_2. Finally, where the Mekong River has been included in global summaries of inorganic carbon riverine flux such as Meybeck (1987) and Gaillardet *et al.* (1999), data is based on a one spot sample collected at the mouth of the river.

1.3 Thesis Overview

This thesis will calculate an inorganic carbon budget for the Mekong river basin. The concept of chemical weathering, links to climate and the use of dissolved load in river waters to quantify chemical weathering fluxes are introduced in this Chapter. The complex geology and monsoon dominated hydrograph of the continental scale Mekong river basin is also described in this Chapter. The continental scale, globally important solute fluxes and tectonically active setting of this Asian mega–river emphasise the need to understand the chemical weathering signatures of the Mekong River basin. Chemical weathering reactions can occur between carbonate and silicate minerals and carbonic and sulfuric acid. Five idealised dissolution reactions are set out in **Chapter 2** and the impact of their products on atmospheric CO_2 and global climate are discussed in terms of short–term and long–term timescales. Samples to investigate chemical weathering were collected over three field seasons; 2014, 2016, and 2017 during monsoon seasons. Additionally a time-series was collected throughout 2014–2017. The spatial and temporal sampling strategy and subsequent laboratory methodology for processing and analysing samples collected for this work are described in **Chapter 3**. A key methodological development in this thesis was sediment digestion of an order of magnitude less sample mass than XRF techniques, enabling efficient cation and multi-isotope analysis of 50mg samples. The geochemical characteristics of the dissolved load and bedload in the Mekong main channel and its tributaries are discussed in **Chapter 4**. The foundation of ideas and assumptions made for modelling acidity sources and correctly partitioning solutes to chemical weathering reactions is grounded in knowledge gathered from the analysis of major cations and anions, and $^{87}\mathrm{Sr}/^{86}\mathrm{Sr}$ and $\delta^{18}O$ in river water which is combined with $^{87}\mathrm{Sr}/^{86}\mathrm{Sr}$ and ε_{Nd} isotopes to further understand geological provenance. In **Chapter 5** sources of sulfate are partitioned with a two end member mixing model using sulfur and oxygen isotopes in dissolved sulfate. Values from this model are used to calculate the flux of oxidative pyrite weathering in the Mekong. In **Chapter 6** a forward model based on Galy & France-Lanord (1999) is developed and used to partition river solutes between the five generalised reactions described in Chapter 2. This forward model takes into account sulfuric acid sources, calculated in Chapter 5, addressing the shortcomings of solute partitioning in previous large river studies. The net inorganic carbon budget for the Mekong river is also calculated in Chapter 6, and the global implications of this result are discussed. **Chapter 7** summarises this thesis and considers the importance of quantifying sulfuric acid weathering as a source of CO_2 to the atmosphere.

Chapter 2

Chemical Weathering Reactions: Implications for Carbon Budgets on Short and Long Timescales

2.1 Introduction

There are many dissolution reactions which supply the products of weathering to the aqueous phase. The reactions depend on the weathering agent or source of acidity (predominantly carbonic or sulfuric acid) as well as the mineral reactants - carbonates, silicates, evaporates, and variable mineral components within these groups. Multiple chemical weathering reactions deliver dissolved inorganic carbon (DIC) to river water. Bicarbonate, HCO_3^-, is the dominant form of DIC measured in river waters because it is stable at pH between $6 - 8.2$. Carbonate species, CO_3^{2-}, are only present in significant quantities at pH greater than 8.5 (Drever, 1997). The source of DIC and relative amount of DIC released from weathering reactions have different implications for the carbon cycle. Some reactions are a source of atmospheric CO_2 and some are a sink.

When considering the impact of the carbon budget on climate it is necessary to clarify the different timescales over which reactions occur. The shortest timescales at which chemical weathering is likely to be important to climate include reactions occurring on the order of $<10^5$ years. Such instantaneous reactions include dissolution reactions which release solutes into the weathering environment. Long-term reactions occur on the order of $>10^5$ years. On this timescale carbonate precipitation occurs in the oceans, permanently sequestering some CO_2 whilst the remainder is released back into the atmosphere. For the purposes of this study, short and long term processes are distinguished by the presence or lack of carbonate precipitation in the oceans (Berner & Berner, 2012). In order to understand the potential impact on the climate, the reactions below are discussed under these two timescales.

Five idealised reactions are considered to describe the products of chemical weathering during dissolution. These reactions can be considered to occur on an instantaneous or short timescale, and therefore describe the processes occurring in the catchment or critical zone during mineral dissolution. They should correspond to the predicted water chemistry that is observed within a river. The products of interest are DIC species (mainly HCO_3^-), SO_4^{2-}, Ca^{2+}, Mg^{2+}, K^+ and Na^+ because the relative abundances of major anions and cations and their isotopic compositions can partition DIC to it's mineral and acidity source. The DIC released by each of these reactions will be calculated before the impact on atmospheric CO_2 is assessed. Over long timescales the products of dissolution undergo subsequent reactions (principally the formation of $CaCO_3$ in marine environments) with differing implications for the carbon cycle and the climate compared to the instantaneous timescale. The reactions and the fate of the dissolution products discussed below are illustrated in Figure 2.1.

2.2 Short Term Carbonic and Sulfuric Acid Weathering of Carbonates and Silicates

CO_2 gas present in either the atmosphere or in the soil (respired by plant roots) is readily dissolved in rain water or pore water respectively, forming carbonic acid (H_2CO_3) (Drever, 1997). A representative reaction of silicate minerals reacting with carbonic acid to form clays (Figure 2.1A) is described by the following equation:

$$\mathbf{2C}O_2 + 3H_2O + CaAl_2Si_2O_8 \Rightarrow \mathbf{2HCO_3^-} + Ca^{2+}_{aq} + Al_2Si_2O_5(OH)_4 \tag{2.1}$$

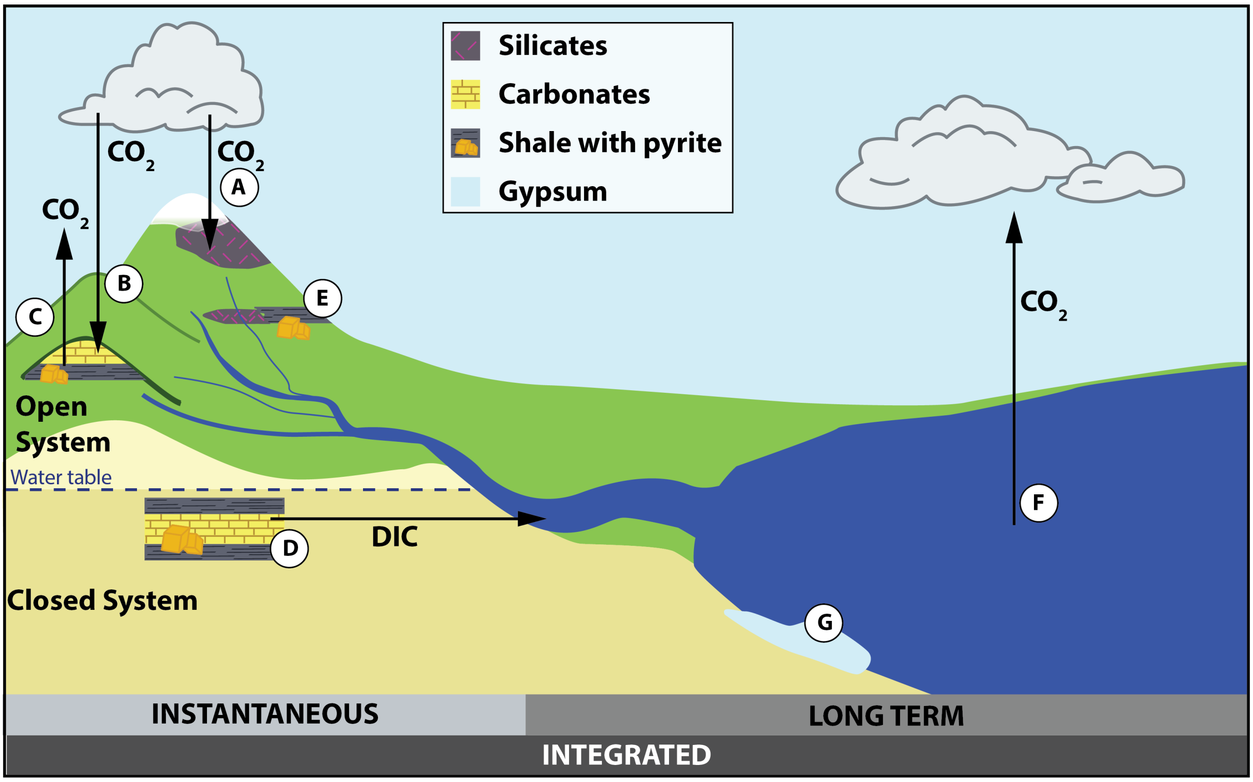

Figure 2.1: Timescales and environments of chemical weathering reactions. Inorganic carbon is globally cycled through the chemical weathering of rocks and subsequent precipitation reactions. Letters indicate a reaction occurring and arrows represent the transfer of carbon in the form of carbon dioxide (CO_2) or dissolved inorganic carbon, DIC (HCO_3^-). Chemical reactions occur in an open system where the reaction site is open to the atmosphere, for example on a hill slope or floodplain, or in confined environments where the reaction site is not directly connected to the atmosphere, for example below the water table. Carbonic acid (H_2CO_3) weathering of silicates (A) and carbonate rocks (B) draws down CO_2 from the atmosphere. Sulfuric acid (H_2SO_4) weathering of carbonates in an open environment releases carbon that degases instantaneously as CO_2 to the atmosphere (C). In a confined environment, the carbon released from sulfuric acid reacting with carbonate minerals is transferred as HCO_3^- from the reaction site to rivers and then on to the oceans (D). Sulfuric acid weathering of silicate minerals does not release carbon in any form (E). The HCO_3^- that is transported to the ocean precipitates as $CaCO_3$ and releases CO_2 back to the atmosphere (F). The source of HCO_3^- precipitated in carbonate has different climatic implications, discussed in the text. Ca^{2+} and SO_4^{2-} ions delivered from (C), (D), and (E) to the oceans can precipitate as gypsum under suitable conditions (G). Reactions are categorised into two timescales. Reactions that occur in the critical zone during mineral dissolution are instantaneous (short term) and reactions occurring on the long term happen over more than 10^5 years. The net carbon budget for a river catchment at any one time is calculated for reactions that are integrated over all timescales. Figure after Gaillardet & Galy (2008).

where atmospheric CO_2 dissolves in H_2O forming H_2CO_3 that weathers the Ca-silicate mineral anorthite ($CaAl_2Si_2O_8$), an end member plagioclase feldspar used here to represent all Ca- and Mg-silicates (Brantley, 2003). Bicarbonate (HCO_3^-) and Ca^{2+} ions are released into solution and $Al_2Si_2O_5(OH)_4$ is a kaolinite-clay by-product. This reaction draws down two moles of CO_2 from the atmosphere for each mole of Ca^{2+} released into solution (Berner *et al.*, 1983). Two moles of HCO_3^- are released when H_2CO_3 dissolves silicate minerals, where the C is entirely atmospheric derived.

The reaction of carbonic acid with carbonates (Figure 2.1B) can be described by:

$$H_2O + \mathbf{CO}_2 + Ca\mathbf{CO}_3 \Rightarrow \mathbf{2HCO_3^-} + Ca^{2+} \tag{2.2}$$

For each mole of CO_2 drawn down from the atmosphere and transferred to the HCO_3^- ion, one mole of Ca^{2+} is released into solution by carbonate dissolution (Berner *et al.*, 1983). Carbonate ($CaCO_3$) releases a further mole of C, and hence two moles of HCO_3^- are present in river water.

Silicate and carbonate minerals can also react with sulfuric acid (H_2SO_4), generated by the oxidative weathering of pyrite or anthropogenic emissions. The reaction of sulfuric acid with carbonate minerals releases carbon either as gaseous CO_2, or dissolved HCO_3^-, depending on the environment in which the reaction occurs. In an open system where the reaction site is connected to the atmosphere (Figure 2.1C), the reaction of sulfuric acid with carbonates can be described by:

$$H_2SO_4 + Ca\mathbf{CO}_3 \Rightarrow \mathbf{CO_{2(g)}} + Ca^{2+} + SO_4^{2-} + H_2O \tag{2.3}$$

where the CO_2 released by this reaction can degas instantaneously to the atmosphere. In this case, one mole of CO_2 is instantaneously degassed to the atmosphere with one mole each of sulfate (SO_4^{2-}) and Ca^{2+} released to the weathering zone (Equation 2.3) (Torres *et al.*, 2014).

In a reaction between sulfuric acid and carbonate minerals in a confined environment where the reaction site is not directly connected to the atmosphere (Equation 2.4), the carbon released from carbonates cannot degas as CO_2 to the atmosphere (Figure 2.1D) (Berner *et al.*, 1983; Spence & Telmer, 2005; Calmels *et al.*, 2007; Torres *et al.*, 2014).

$$H_2SO_4 + 2Ca\mathbf{CO}_3 \Rightarrow \mathbf{2HCO_3^-} + 2Ca^{2+} + SO_4^{2-} \tag{2.4}$$

Carbon released from $CaCO_3$ instead dissolves in water to form H_2CO_3, and a second mineral could be weathered by the generated H_2CO_3. For example H_2CO_3 could react with carbonate minerals present, equivalent to Equation 2.2, or silicate minerals, where the reaction would be equivalent to Equation 2.1. Equation 2.4 is effectively the sum of Equation 2.3, the sulfuric acid weathering of carbonates in an open environment, and Equation 2.2, the carbonic acid weathering of carbonates. The reaction of H_2SO_4 with carbonates in Equation 2.4 does not release any CO_2 on a short term timescale because the carbon is transferred to HCO_3^-. On this timescale, in a confined environment, the products of the reaction are two moles each of HCO_3^- and Ca^{2+} and one mole of SO_4^{2-} which are delivered to the oceans.

Although carbonates may have faster dissolution kinetics compared to silicates (White *et al.*, 1999b), it is possible for sulfuric acid to react with silicate minerals in the system (Berner *et al.*, 1983; Spence & Telmer, 2005), for example magmatic sulfides may oxidise and weather nearby silicates. Sulfuric acid weathers a representative silicate mineral anorthite to kaolinite-clay by:

$$H_2SO_4 + CaAl_2Si_2O_8 + H_2O \Rightarrow Ca^{2+} + SO_4^{2-} + Al_2Si_2O_5(OH)_4 \tag{2.5}$$

While this reaction does not participate in the carbon cycle, because neither the acid source nor the lithology contain carbon, it does produce SO_4^{2-} and Ca^{2+}. These ions are important to consider with cations and anions, to calculate DIC (Section 6.3.1).

River chemistry will be composed of the products of some combination of Equations 2.1, 2.2, 2.3 (or 2.4 depending on environment), and 2.5 that occur on short term timescales. It is convenient to express the reactants and products mathematically as a matrix, similar to the modal decomposition method for partitioning river chemistry (Garrels & Mackenzie, 1967; Price *et al.*, 2008). The following matrix (Equation 2.6) displays the solutes measured in the river as the matrix product of the molar products of Equations 2.1 to 2.5 and the amount of each of the reactions occurring. The columns of the first matrix are the five reactions (Equations 2.1 - 2.5) where the reactions are given an abbreviated name, for example $SilH_2CO_3$ is an abbreviation of the reaction between silicate minerals (Sil) and carbonic acid (H_2CO_3). The superscripts O and C, used for the reactions between carbonates and sulfuric acid, represent open and closed reaction environments, respectively. The rows are the solutes (Ca^{2+}, SO_4^{2-}, and HCO_3^-) produced by each of the five reactions. The values within the first matrix are the stoichiometric coefficients of the solutes produced by each reaction described by Equations 2.1 to 2.5. The variables in the second matrix are the relative amount, n, of each of the Reactions 2.1 ($n_{Sil}H_2CO_3$), 2.2 ($n_{Carb}H_2CO_3$), 2.3 ($n_{Carb}H_2SO_4^O$), 2.4 ($n_{Carb}H_2SO_4^C$) and 2.5 ($n_{Sil}H_2SO_4$) occurring. The product of these two matrices is the idealised river chemistry that would be predicted depending on the relative contributions from Reactions 2.1 to 2.5. This means that it is possible to predict the ions produced by each reaction. With the knowledge of which ions are sourced from each reaction, i.e. the second matrix which represents the amount of each reaction occurring, the carbon implications can be quantified.

$$\begin{array}{c|ccccc|} & SilH_2CO_3 & CarbH_2CO_3 & CarbH_2SO_4^O & CarbH_2SO_4^C & SilH_2SO_4 \\ Ca^{2+} & 1 & 1 & 1 & 2 & 1 \\ HCO_3^- & 2 & 2 & 0 & 2 & 0 \\ SO_4^{2-} & 0 & 0 & 1 & 1 & 1 \end{array} \cdot \begin{pmatrix} n_{Sil}H_2CO_3 \\ n_{Carb}H_2CO_3 \\ n_{Carb}H_2SO_4^O \\ n_{Carb}H_2SO_4^C \\ n_{Sil}H_2SO_4 \end{pmatrix} = \begin{array}{c} \mu mol/l \\ \begin{pmatrix} Ca_{Riv} \\ HCO^-_{3_{Riv}} \\ SO^{2-}_{4_{Riv}} \end{pmatrix} \end{array} \tag{2.6}$$

2.2.1 Short Term Dissolved Inorganic Carbon

To understand the short–term implications of terrestrial weathering on the climate, it is necessary to apportion the total dissolved inorganic carbon, ΣDIC, between the weathering reactions from which it is sourced. There are two reasons why the ΣDIC in river water cannot be partitioned using measured HCO_3^- directly. Firstly, not all reactions deliver HCO_3^- to the weathering zone; the sulfuric acid weathering of carbonates in an open environment (Equation 2.3) degases CO_2. Similarly, silicate mineral weathering involving sulfuric acid does not deliver DIC to the river (Equation 2.5). Secondly, reactions deliver HCO_3^- and cations in different proportions. Cations, however, are delivered from all weathering reactions and can be partitioned to rock and acidity sources using the stoichiometries determined in Equations 2.1-2.5. In Equations 2.7-2.11 cations are used to partition the amount of DIC delivered from individual weathering reactions before the implication of this DIC on the carbon cycle is assessed in Section 2.2.2. Cations, X, are labelled with their lithological source (carbonate, $_{carb}$ or silicate, $_{sil}$) and acid reactant (carbonic, ^{carbonic} or sulfuric, ^{sulfuric}), i.e. $X^{acid}_{lithology}$. The partitioning of elements is discussed in detail in Section 6.3. This section and the next, Section 2.2.2, build a framework by which to understand the implications of the carbon cycle in the Mekong river. These equations will be used in Chapter 6 to calculate the inorganic carbon budget of the Mekong river on the long and short term.

DIC from Carbonic Acid Weathering of Silicate Minerals

The dissolution of silicate minerals neutralises carbonic acid (Equation 2.1) and releases two moles of HCO_3^-, both of which are from H_2CO_3 which is ultimately derived from the atmosphere. For each mole of HCO_3^- released one mole each of Ca^{2+}, Mg^{2+}, Na^+ and K^+ are also released into solution from silicate minerals. When the cation charge is considered the charge equivalent ratio of HCO_3^-:cation is 2 for Ca^{2+} and Mg^{2+} and 1 for K^+ and Na^+, therefore the DIC produced by carbonic acid weathering of silicates on the short term (${}^{carbonic}_{sil}$DIC) is calculated using cations by the following equation:

$$ {}^{carbonic}_{sil}DIC = 2*(Ca^{carbonic}_{sil} + Mg^{carbonic}_{sil}) + Na^{carbonic}_{sil} + K^{carbonic}_{sil} \tag{2.7} $$

DIC from Carbonic Acid Weathering of Carbonate Minerals

The molar amount of HCO_3^- released from the reaction of carbonic acid with carbonates (${}^{carbonic}_{carb}$DIC) is twice as much as Ca^{2+} or Mg^{2+} released into solution (negligible Na^+ or K^+ are delivered by this reaction). Half of the molar amount of carbon in ${}^{carbonic}_{carb}$DIC is from H_2CO_3, derived from atmospheric CO_2, the remaining half is from the carbonate mineral. DIC delivered from the carbonic weathering of carbonate minerals (Equation 2.2) is therefore calculated in Equation 2.8.

$$ {}^{carbonic}_{carb}DIC = 2*(Ca^{carbonic}_{carb} + Mg^{carbonic}_{carb}) \tag{2.8} $$

DIC from Sulfuric Acid Weathering of Carbonate and Silicate Minerals

When carbonates are weathered by sulfuric acid in an open system the carbon released may fully degas as CO_2 (Equation 2.3), and hence there is no DIC present in the river (Equation 2.9).

$$ {}^{sulfuric\ O}_{carb}DIC = 0 \tag{2.9} $$

Conversely, in confined environments, the CO_2 released by sulfuric acid weathering of carbonates cannot degas and instead dissolves in water, producing two moles of HCO_3^- (Equation 2.4). Both moles of carbon are derived from carbonate minerals which also release an equal amount of Ca^{2+} into solution, thus HCO_3^-:Ca^{2+} is 1. ${}^{sulfuric\ C}_{carb}DIC$ is written in equivalent units, whereby two moles of HCO_3^- is equal to one mole each of Ca^{2+} and Mg^{2+} and the coefficients cancel resulting in:

$$ {}^{sulfuric\ C}_{carb}DIC = Ca^{sulfuric}_{carb} + Mg^{sulfuric}_{carb} \tag{2.10} $$

When silicate minerals are weathered by sulfuric acid there is no source of carbon (Equation 2.5) and hence no DIC is released (Equation 2.11).

$$ {}^{sulfuric}_{sil}DIC = 0 \tag{2.11} $$

Short Term Total DIC

The total dissolved inorganic carbon (ΣDIC) delivered to the weathering zone and subsequently transported to the river on the short term can be calculated by summing the DIC delivered by each reaction (Equations 2.7, 2.8, 2.10). If the stoichiometries used in Equations 2.7-2.11 are correct, the total calculated DIC equals the measured HCO_3^- in the river. However, the way in which ΣDIC is calculated will vary depending on whether the reaction environment is assumed to be open (ΣDIC^O) or confined (ΣDIC^C). The following equation describes total DIC delivered from reactions occurring in an open environment:

$$ \Sigma DIC^O = {}^{carbonic}_{sil}DIC + {}^{carbonic}_{carb}DIC \tag{2.12} $$

Total DIC delivered from reactions occuring in a confined environment is calculated as the following:

$$ \Sigma DIC^C = {}^{carbonic}_{sil}DIC + {}^{carbonic}_{carb}DIC + {}^{sulfuric\ C}_{carb}DIC \tag{2.13} $$

To validate the method used to calculate DIC delivered from each reaction, ΣDIC can be checked against measured HCO_3^-. River water is electrostatically neutral (Drever, 1997), therefore the measured HCO_3^- anion must balance the DIC calculated using charge equivalent cations. The relative accuracy of calculated DIC via Equation 2.12 or 2.13 compared to measured HCO_3^- could indicate the most probable reaction environment for sulfuric acid weathering of carbonates: open or confined (discussed in Chapter 6). The dominant reaction pathway of sulfuric acid weathering of carbonates will impact the timescale of CO_2 release on the atmosphere.

2.2.2 Short Term CO_2 Consumption

Measured DIC in the river can be lithospheric or atmospheric in origin which has different consequences for the carbon cycle. Therefore the total CO_2 consumed (ΣCO_{2Short}) is not equal to total dissolved inorganic carbon, ΣDIC, in the river. Only carbon species that are sourced from the atmosphere (as H_2CO_3) or returned to the atmosphere (as CO_2) are considered for calculating the effect of chemical weathering on atmospheric CO_2 consumption, ΣCO_{2Short}. The matrix solution 2.6 describing the river chemistry on the short term becomes modified to Equation 2.14 and 2.15, which describes the molar amount of CO_2 consumed or released by each reaction occurring in an open or confined environment, respectively.

The two matrix solutions in Equations 2.14- 2.15 display the net atmospheric CO_2 in an open and closed environment, respectively, as the matrix product of the molar amount of CO_2 consumed or released by Equations 2.1 to 2.5 and the amount of each of the reactions occurring. The columns of the first matrix are the reactions that occur in an open environment, where carbon can be degassed as CO_2 through sulfuric acid weathering of carbonates (Equation 2.14) or a confined environment where carbon is released from carbonate minerals and transferred as HCO_3^- to the oceans (Equation 2.15). The values within the first matrix are the stoichiometric coefficients of CO_2 consumed (positive integers) or released (negative integers) or where there is no net difference in atmospheric CO_2 (zero value). The variables in the second matrix are the relative amount of each of the reactions 2.1 to 2.5 occurring. The product of these two matrices is the net atmospheric CO_2 budget that would be predicted for a river catchment depending on the relative contributions from reactions 2.1 to 2.5 in an open (Equation 2.14) or closed (Equation 2.15) environment.

$$\begin{array}{cc} OPEN & \begin{array}{cccc} SilH_2CO_3 & CarbH_2CO_3 & CarbH_2SO_4^O & SilH_2SO_4 \end{array} \\ CO_2 & \left(\begin{array}{cccc} 2 & 1 & -1 & 0 \end{array}\right) \end{array} \cdot \begin{pmatrix} n_{Sil}H_2CO_3 \\ n_{Carb}H_2CO_3 \\ n_{Carb}H_2SO_4^O \\ n_{Sil}H_2SO_4 \end{pmatrix} = \begin{pmatrix} Short\ Term \\ Net \\ Atmospheric \\ CO_2 \end{pmatrix} \tag{2.14}$$

$$\begin{array}{ccccc} CLOSED & SilH_2CO_3 & CarbH_2CO_3 & CarbH_2SO_4^C & SilH_2SO_4 \\ CO_2 & \left(2 \right. & 1 & 0 & \left. 0 \right) \end{array} \cdot \begin{pmatrix} n_{Sil}H_2CO_3 \\ n_{Carb}H_2CO_3 \\ n_{Carb}H_2SO_4^C \\ n_{Sil}H_2SO_4 \end{pmatrix} = \begin{pmatrix} Short\ Term \\ Net \\ Atmospheric \\ CO_2 \end{pmatrix} \qquad (2.15)$$

In the same way that measured HCO_3^- cannot be used to partitioned DIC between weathering reactions, neither can it be used to calculate the short term CO_2 budget of a river catchment. The CO_2 budget is calculated using the stoichiometries of carbon and Ca^{2+} in Equations 2.1 to 2.5 and summarised in matrix solution 2.6. As DIC has also been calculated using cation stoichiometries, the relationship between DIC and CO_2 budget is discussed in terms of CO_2:Ca^{2+} stoichiometry. Reactions involving H_2CO_3 draw down atmospheric carbon on the short term. DIC associated with all silicate mineral dissolution (Ca^{2+}, Mg^{2+}, Na^+ and K^+) by carbonic acid is entirely atmospheric in origin thus ${}^{carbonic}_{sil}$DIC is equivalent to CO_2. The dissolution of Ca^{2+} and Mg^{2+} silicates are charge balanced by two moles of HCO_3^-, ie. CO_2:$Ca_{sil}^{carbonic}$ or $Mg_{sil}^{carbonic}$ is 2 (the same value displayed in matrix 2.14 and matrix 2.15). Each mole of Na^+ or K^+ released from silicate minerals is charge balanced by one mole of atmospheric derived HCO_3^-, therefore CO_2:$Na_{sil}^{carbonic}$ or $K_{sil}^{carbonic}$ is 1. Carbonic acid weathering of carbonates produces two moles of HCO_3^- where one mole is atmospheric derived carbon and one mole is from the mineral thus CO_2 consumption on the short term is half of ${}^{carbonic}_{carb}$DIC. The release of Ca^{2+} or Mg^{2+} from carbonates is charge balanced by both moles of HCO_3^-, but only one mole of carbon is removed from the atmosphere therefore CO_2:$Ca_{carb}^{carbonic}$ or CO_2:$Mg_{carb}^{carbonic}$ is 1. All carbon participating in the reaction of sulfuric acid with carbonates is lithologically derived but the timescale of geologically stored carbon being released as CO_2 differs depending on environment. In an open environment (Equation 2.3) one mole of carbon per mole of H_2SO_4, or mole of Ca^{2+}, is degassed back into the atmosphere as CO_2 instantaneously so CO_2:$Ca_{carb}^{sulfuric}$ or $Mg_{carb}^{sulfuric}$ is -1 (the same value in matrix 2.14). In a confined environment (Equation 2.4) the carbon remains in solution as H_2CO_3 which is able to weather a further silicate or carbonate mineral, producing a total of two moles of DIC per mole of H_2SO_4, or mole of Ca^{2+}. This DIC is transported to the ocean and thus no carbon is consumed or released on the short term (hence the value in matrix 2.15 is 0). Carbon is however released on the timescale of carbonate precipitation and is dealt with in Section 2.3. In the case of sulfuric acid weathering of silicates because the reaction does not involve carbon, the value in matrices 2.14 and 2.15 is 0. Thus the total CO$_2$ consumption over short timescales, ΣCO_{2Short}, can be calculated using partitioned river solutes for open (Equation 2.16) and confined (Equation 2.17) environments.

$$\begin{aligned}\Sigma CO_{2\ Short}^{O} =& 2*(Ca_{sil}^{carbonic}+Mg_{sil}^{carbonic})+Na_{sil}^{carbonic}+K_{sil}^{carbonic}\\ &+Ca_{carb}^{carbonic}+Mg_{carb}^{carbonic}-Ca_{carb}^{sulfuric}-Mg_{carb}^{sulfuric}\end{aligned} \tag{2.16}$$

$$\begin{aligned}\Sigma CO_{2\ Short}^{C} =& 2*(Ca_{sil}^{carbonic}+Mg_{sil}^{carbonic})+Na_{sil}^{carbonic}+K_{sil}^{carbonic}\\ &+Ca_{carb}^{carbonic}+Mg_{carb}^{carbonic}\end{aligned} \tag{2.17}$$

2.3 Long Term Carbonic and Sulfuric Acid Weathering of Carbonates and Silicates

Chemical weathering on the continents delivers solutes to the oceans. In the ocean solutes Ca^{2+} and HCO$_3^-$ can precipitate as carbonate (CaCO$_3$) releasing CO$_2$ to the atmosphere on the order of 10^5-10^6 years (Berner *et al.*, 1983, and Figure 2.1F). The effect of chemical weathering to atmospheric CO$_2$ on long term timescales can be calculated assuming that the products of short reactions (Equations 2.3-2.5) are all delivered to the oceans. The following Reactions 2.21 to 2.22 describe the fate of weathering products on the long term.

Carbonic acid weathering of silicate minerals delivers two moles of C to the oceans per mole of Ca^{2+}. However all C is atmospheric derived, so when CaCO$_3$ precipitation occurs, one mole of CO$_2$ is degassed per mole of Ca^{2+} and one mole of C per mole of Ca^{2+} is sequestered into geological storage (Equation 2.18). This reaction completes the climate stabilising cycle of silicate weathering drawdown, sequestering atmospheric CO$_2$ into the rock record, described by Urey (1952) (Equation 2.19). Although the weathering of Na and K silicate minerals draws down CO$_2$ they do not form abundant carbonate minerals in the ocean so cannot lock up carbon (Berner, 1992). Instead, Na$^+$ and K$^+$ may participate in reverse weathering reactions and cation exchange reactions in estuarine and ocean crust environments, which releases CO$_2$ and offsets the CO$_2$ drawdown from continental silicate weathering (Berner *et al.*, 1983; Mackenzie & Garrels, 1966; Mackenzie & Kump, 1995; Michalopoulos & Aller, 1995).

$$H_2O+\mathbf{2CO_2}+CaAl_2Si_2O_8\Rightarrow Ca\mathbf{C}O_3+\mathbf{CO_2}+H_2O+Al_2Si_2O_5(OH)_4 \tag{2.18}$$

$$\mathbf{CO_2} + CaSiO_3 \Rightarrow \mathbf{CaCO_3} + SiO_2 \tag{2.19}$$

The solutes delivered to the oceans by carbonic acid weathering of carbonates (Equation 2.2) precipitate one mole of carbonate per mole of Ca^{2+} and degas one mole of CO_2 to the atmosphere on the long term (Equation 2.20). Therefore carbonic acid weathering of carbonates is carbon neutral on long term timescales, releasing 1 mole of CO_2 back to the atmosphere per mole of Ca^{2+} that was originally released into solution, and sequestering one mole of C back into carbonate minerals.

$$H_2\mathbf{C}O_3 + Ca\mathbf{C}O_3 \Rightarrow Ca\mathbf{C}O_3 + \mathbf{CO_2} + H_2O \tag{2.20}$$

Sulfuric acid weathering of carbonates in an open environment (Equation 2.3) delivers no DIC to the oceans because the carbon released from carbonate minerals instantaneously degasses as CO_2 and the carbon implications are therefore only considered on the short term. The reaction does deliver SO_4^{2-} and Ca^{2+} which are important to consider on the long term because carbon is tracked using the Ca^{2+} ion.

$$H_2SO_4 + Ca\mathbf{C}O_3 \Rightarrow Ca^{2+} + SO_4^{2-} + H_2O \;\; (+\, CO_2) \tag{2.21}$$

The two moles of DIC from the reaction of sulfuric acid and carbonate minerals in a confined environment are transported to the oceans (Equation 2.4) and precipitate as carbonate, releasing one mole of lithologically sourced carbon back to the atmosphere (Equation 2.22, Calmels *et al.*, 2007). This reaction becomes a CO_2 source on long timescales.

$$H_2SO_4 + \mathbf{2}Ca\mathbf{C}O_3 \Rightarrow Ca\mathbf{C}O_3 + \mathbf{CO_2} + Ca^{2+} + SO_4^{2-} \tag{2.22}$$

Sulfuric acid weathering of silicates plays no direct part in the carbon cycle but releases SO_4^{2-} and Ca^{2+} to the weathering zone and to the ocean. However, we track carbon by the Ca^{2+} ion, so this equation is as important to take into account as Equation 2.21.

$$H_2SO_4 + CaAl_2Si_2O_8 + H_2O \Rightarrow Ca^{2+} + SO_4^{2-} + Al_2Si_2O_5(OH)_4 \tag{2.23}$$

There are multiple fates of the SO_4^{2-} and Ca^{2+} products of sulfuric acid weathering of silicates and carbonates (Equations 2.21, 2.22 and 2.23). Other than carbonate precipitation, Ca^{2+} could combine with SO_4^{2-} to precipitate gypsum or anyhydrite (Equation 2.24) if the conditions were suitable (Figure 2.1G) . A confined basin and arid environment is required to promote evaporation and precipitation of evaporites (Berner, 2004).

$$Ca^{2+} + SO_4^{2-} \Rightarrow CaSO_4 \tag{2.24}$$

SO_4^{2-} is also removed from seawater via oxidation of organic carbon in marine sediments by bacterial sulfate reduction, reducing SO_4^{2-} to H_2S (Equation 2.25, Berner, 1985; Calmels *et al.*, 2007). Sulfide could then be oxidised back to sulfate or react with iron oxides to form pyrite, FeS_2 (Berner, 2004). The oxidised product of organic carbon is HCO_3^- which could go on to react with Ca^{2+} in the oceans and precipitate carbonate eventually sequestering one mole of carbon into geological storage (Bradbury & Turchyn, 2018).

$$SO_4^{2-} + 2CH_2O \Rightarrow H_2S + 2HCO_3^- \tag{2.25}$$

The residence time of SO_4^{2-} in seawater is several orders of magnitude greater than that of DIC ($>10^7$ years vs 10^5 years, Broecker, 2003; Claypool *et al.*, 1980), and hence HCO_3^- is removed from the oceans at a faster rate than SO_4^{2-}. The consequence of this is a decoupling of instantaneous CO_2 release by sulfuric acid weathering of carbonates in an open environment and the long term CO_2 sequestration from SO_4^{2-} reduction in the oceans (Calmels *et al.*, 2007; Berner & Berner, 2012; Torres *et al.*, 2014). A detailed consideration of the role of SO_4^{2-} and Ca^{2+} in ocean cycles is beyond the scope of this study, which focusses on catchment processes.

2.3.1 Long Term CO_2 Consumption

Total CO_2 consumption on long timescales, is the amount of CO_2 consumed by silicate weathering coupled to carbonate precipitation, offset by CO_2 released by sulfuric acid weathering of carbonates. The matrix solutions 2.14 and 2.15 describing the net atmospheric CO_2 budget on the short term become modified to matrices 2.26 and 2.27 respectively, which describe the net atmospheric CO_2 budget of the river catchment on the long term. Matrices 2.26 and 2.27 are set up in the same way as matrices 2.14 and 2.15; the matrix solutions are a product of the molar amount of CO_2 consumed or released by long term Equations 2.18 to 2.23 and the amount of each of the reactions occurring.

Carbonic acid weathering of silicates is a net sink of CO_2 sequestering one mole of CO_2 per mole of Ca^{2+} released from a silicate mineral, hence coefficients in matrices 2.26 and 2.27 are 1. Carbonic acid weathering of carbonates is C neutral on the long term after returning C to it's original source, therefore coefficients in matrices 2.26 and 2.27 are 0. Sulfuric acid reacting with carbonate minerals in an open environment releases CO_2 instantaneously with no DIC transported to the ocean. This reaction is carbon neutral on long term timescales hence the coefficient in matrix 2.26 is also 0. However, in a confined environment, sulfuric acid weathering of carbonates delivers DIC to the oceans, which releases one mole of CO_2 when DIC is precipitated as carbonate, hence the coefficient in matrix 2.27 is -1. There is no DIC delivered to the weathering zone or to the ocean by sulfuric acid reacting with silicate minerals hence the coefficient in matrices 2.26 and 2.27 is 0.

$$\begin{array}{lc} OPEN & \begin{array}{cccc} SilH_2CO_3 & CarbH_2CO_3 & CarbH_2SO_4^O & SilH_2SO_4 \end{array} \\ CO_2 & \begin{pmatrix} 1 & \quad 0 & \quad 0 & \quad 0 \end{pmatrix} \end{array} \cdot \overset{\mu mol/l}{\begin{pmatrix} n_{Sil}H_2CO_3 \\ n_{Carb}H_2CO_3 \\ n_{Carb}H_2SO_4^O \\ n_{Sil}H_2SO_4 \end{pmatrix}} = \begin{pmatrix} Long\ Term \\ Net \\ Atmospheric \\ CO_2 \end{pmatrix} \tag{2.26}$$

$$\begin{array}{lc} CLOSED & \begin{array}{cccc} SilH_2CO_3 & CarbH_2CO_3 & CarbH_2SO_4^C & SilH_2SO_4 \end{array} \\ CO_2 & \begin{pmatrix} 1 & \quad 0 & \quad -1 & \quad 0 \end{pmatrix} \end{array} \cdot \overset{\mu mol/l}{\begin{pmatrix} n_{Sil}H_2CO_3 \\ n_{Carb}H_2CO_3 \\ n_{Carb}H_2SO_4^C \\ n_{Sil}H_2SO_4 \end{pmatrix}} = \begin{pmatrix} Long\ Term \\ Net \\ Atmospheric \\ CO_2 \end{pmatrix} \tag{2.27}$$

The total CO_2 consumed and released on timescales longer than 10^5 years (ΣCO_{2Long}) can be calculated using Equation 2.28.

$$\Sigma CO_2\ _{long} = Ca_{sil}^{carb} + Mg_{sil}^{carb} - Ca_{carb}^{sulfC} - Mg_{carb}^{sulfC} \tag{2.28}$$

The net CO_2 budget on the long term (ΣCO_{2Long}) is effectively the moles of CO_2 sequestered into carbonate minerals after removal from the atmosphere by carbonic acid weathering of silicate minerals, offset by the long–term CO_2 release when carbonate derived from lithological carbon is precipitated in the oceans. Although all silicate mineral dissolution (Ca^{2+}, Mg^{2+}, Na^+ and K^+) draws down atmospheric CO_2, only Ca^{2+} and Mg^{2+} participate in sequestering the CO_2 into carbonates. Two mole of CO_2 for each mole of Ca^{2+} and Mg^{2+} are removed from the atmosphere but only one mole of CO_2 is sequestered, hence the stoichiometric ratio of CO_2:$Ca_{sil}^{carbonic}$ or $Mg_{sil}^{carbonic}$ is 1. For each mole of Ca^{2+} or Mg^{2+} released during the sulfuric acid weathering of carbonates in a confined environment, one mole of CO_2 is also released, so the stoichiometric ratio of CO_2:$Ca_{carb}^{sulfuric\ C}$ or $Mg_{carb}^{sulfuric\ C}$ is -1.

The net C budget of a river catchment at any one time is when reactions are integrated over all timescales ($\Sigma CO_{2Integrated}$). The integrated carbon budget is the CO_2 sequestered into carbonate minerals after removal from the atmosphere by carbonic acid weathering of silicate minerals (Equation 2.18), offset by the CO_2 released by sulfuric acid weathering of carbonates instantaneously as CO_2 (Equation 2.3) and on the long term after DIC has been transported to the oceans and is released as CO_2 when lithological carbon is precipitated as carbonate (Equation 2.22). The overall integrated CO_2 budget for a river catchment, independent of timescale of CO_2 release, $\Sigma CO_{2Integrated}$, can be calculated by Equation 2.29.

$$\Sigma CO_{2\ integrated} = Ca_{sil}^{carb} + Mg_{sil}^{carb} - Ca_{carb}^{sulfO} - Mg_{carb}^{sulfO} - Ca_{carb}^{sulfC} - Mg_{carb}^{sulfC} \tag{2.29}$$

2.4 Conclusions

The impact of chemical weathering reactions on level of atmospheric CO_2 and therefore climate, differs depending on timescale. Short–term chemical weathering reactions where carbonic acid is the reagent draw down atmospheric CO_2, but in the long–term only part of this atmospheric CO_2 is sequestered into the rock record. Reactions that release lithologically sourced carbon to the atmosphere involve sulfuric acid as the acidity source. The impact of CO_2 release could be measured on short–term timescales, if the reaction of sulfuric acid with carbonates occurred in an open environment where CO_2 was able to instantaneously degas. A short–term ($<10^5$ years) imbalance could occur if the flux of CO_2 release is larger than the CO_2 drawdown from carbonic acid weathering of silicate and carbonate minerals. Or the impact of CO_2 release could be measured on the long–term, if carbonate dissolution by sulfuric acid in a confined reaction site releases carbon as HCO_3^-. HCO_3^- is transported to the oceans and precipitated as carbonate, subsequently releasing the lithologically sourced carbon to the atmosphere on timescales longer than 10^5 years. When considering the carbon budget of a river basin at any point in time, i.e. an integrated timescale, only the CO_2 consumption from long term carbonic acid weathering of silicates and the release of CO_2 from sulfuric acid weathering of carbonates is accounted for.

This chapter has outlined the different products released by five idealised equations between carbonate and silicate minerals and carbonic and sulfuric acid, and the long–term fate of the reaction products have been discussed in terms of carbon implications. The framework described in this Chapter to calculate dissolved inorganic carbon will be used to quantify the inorganic carbon budget for the Mekong River on different timescales in Chapter 6.

Chapter 3

Methodology

3.1 Field Sampling Procedure

The suite of samples collected from the Mekong River and it's tributaries by this study is the most comprehensive in both type of sample and spatial coverage of the basin. A total of 394 water, rain, suspended sediment, and bank samples with a further 115 time-series water samples have been collected between 2014-2017.

Samples of the Mekong River and it's tributaries were collected by two methods. For the main channel and larger tributaries, when a boat could be acquired, samples were collected from the river where there was the largest variation in water velocity in the water column. A rig was mounted to the boat from which a depth sampler was lowered into the river and closed at chosen depths allowing 8L samples of water and suspended sediment to be collected over a depth profile (Figure 3.1). Dissolved elements are assumed to be equilibrated throughout the water column, chemistry should not change with depth, hence water samples were collected from the surface sample in a depth profile. For smaller tributaries samples were collected by lowering a 3-times-washed bucket from a bridge into the fastest flow of the river (Figure 3.1). Temperature and pH were measured using a Hannah instrument (HI-991300) probe either directly in the river water or in a bucket if sampling from a bridge. The instrument was calibrated every few days using buffer solutions of known pH (pH 4.01 and 7.01). Bank sediment samples were collected to represent bed load which was not possible to collect. Bank sediment was collected into plastic zip-lock bags from below the water line where possible and away from human or animal disturbance, using a scoop washed in the river water downstream of the sample being taken.


8L sampling unit rigged to boat

Sampling from a bridge using a bucket

Filter units to separate water from sediment

2016 field team

Figure 3.1: Sample collection by boat and bridge. Clockwise: Rig used to mount 8L depth sampler to collect depth profiles. When boats were not available, or for sampling smaller tributaries, a bucket was suspended over a bridge, samples were collected from the fastest flowing part of the stream. The sediment laden waters of a Cambodian tributary with the 2016 field team. Samples were transported back to our field laboratory and filtered through 142mm 0.2μm PES filters, using 2.5L pressurised units, within 12hours of collection.

River waters were filtered within 6 hours of collection through 142mm 0.2μm PES filters. 2.5 litres of filtered water was discarded before collection of samples. Bottles for collecting water samples were rinsed three times with the filtered sample before filling the bottle to a meniscus with the sample. Water samples for the analysis of cations were collected in acid washed HDPE bottles and acidified to $pH < 2$ using distilled HNO_3. A separate aliquot was collected for anions and measurements of $\delta^{18}O_{H_2O}$ and δD using 18.2MΩ H_2O washed amber HDPE bottles. Amber bottles are used to prevent light affecting unacidified water and sediment samples, discouraging bacterial growth. Total alkalinity was measured by Gran titration with 0.05M HCl (Drever, 1997). Repeat titrations in the field were reproducible to 3.4% (2σ). Due to low SO_4^{2-} concentrations measured in the 2014 field season, a pre-concentration step was conducted in the field in 2016 and 2017. Two litres of filtered river water were loaded onto columns filled with 5mL Dowex 1X8-200, 100-200 mesh, anion exchange resin (Hindshaw *et al.*, 2016). The SO_4^{2-} was stored on the resin and kept in a fridge until the time of sample preparation (sulfate pre-concentration methodology is described in more detail in Chapter 5). Bank and suspended sediment samples were dried upon return to University of Cambridge in an oven at ~40°C. Water samples were stored in a cold room (~5°C) until needed. Other samples collected from the Mekong were dissolved organic carbon (DOC), dissolved inorganic carbon (DIC), ^{14}C and CO_2 degassing measurements (Table 3.1) which were not analysed for this thesis.

3.1.1 Spatial Sampling Strategy

Water samples were collected in consecutive peak monsoon periods 2014, 2016 and 2017. A total of 50 sites were sampled in the Mekong river basin, spanning ~ 70% of it's length from source to sea. The Mekong main channel was sampled at 10 locations and all accessible tributaries were sampled (n=36), close to their confluence with the Mekong (Figure 3.2). 70% of the Mekong's discharge is delivered during the monsoon months so sampling during peak monsoon captures the largest weathering signal.

3.1.2 Temporal Sampling Strategy

Samples were collected bi-monthly at Chroy Changvar by the Mekong River Commission (MRC) from 2014-2017 (with a small hiatus in early 2015). The sample site is upstream of the city of Phnom Penh, upstream of the confluence with the Tonle Sap (Figure 3.3). Clean bottles, filters

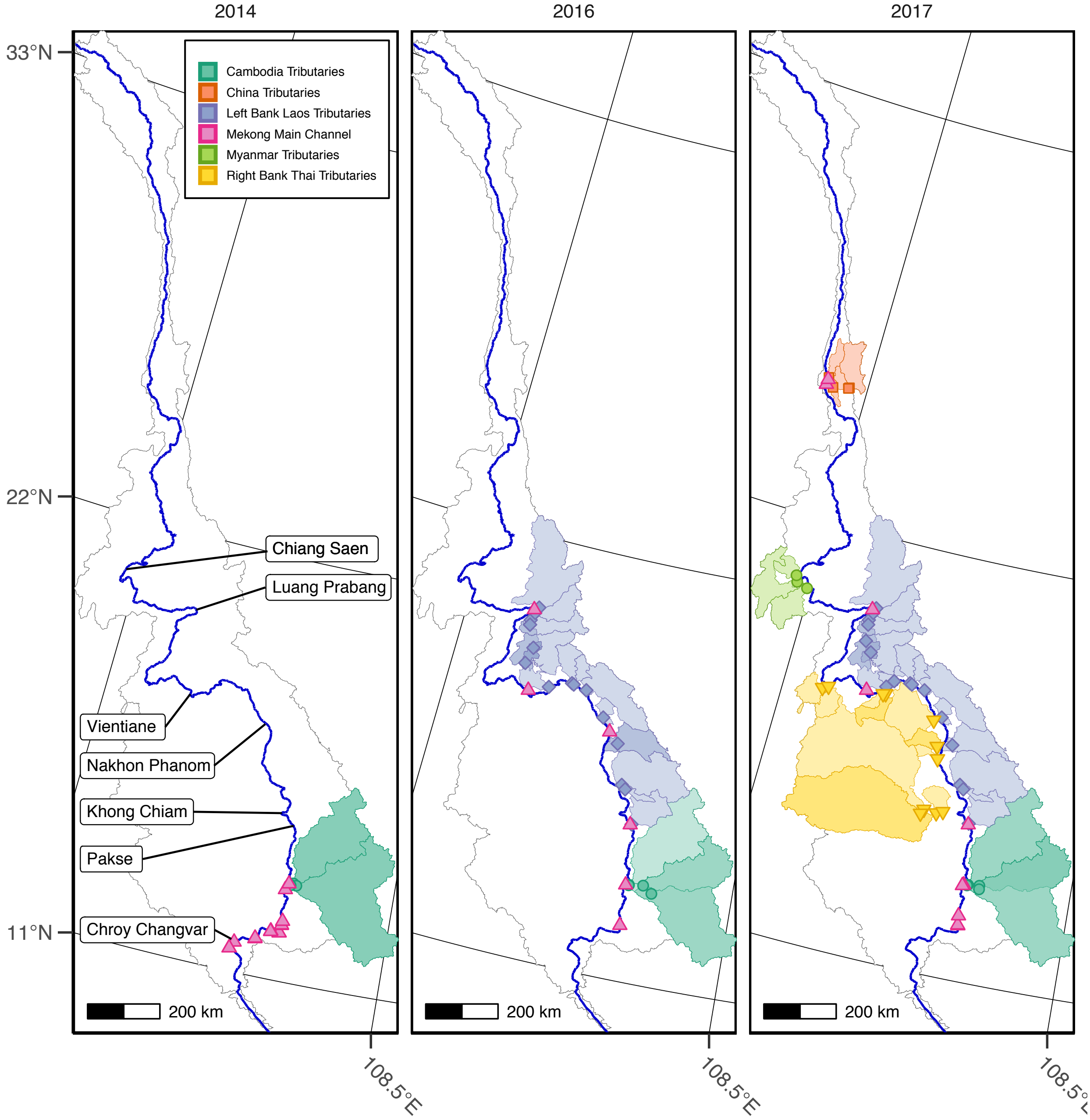

Figure 3.2: Sampling locations on the main stem and tributaries of the Mekong River. Samples in this thesis were collected over three field seasons, 2014, 2016, and 2017. In 2014 tributaries and the main stem only in Cambodia were sampled, in 2016 tributaries in both Laos on the the left bank of the Mekong and Cambodia were sampled, and in 2017 the main stem (pink triangles) was sampled from China downstream to Cambodia with tributaries draining the Upper Mekong in China (orange squares), the right bank in Thailand (yellow inverted triangles), Myanmar (light green circles) (accessed at the border of Cambodia and Myanmar), and Cambodian tributaries (blue green circles) were sampled. Labels indicate the main stem sample sites in the MRC dataset and used in Chapter 4.3.2.3.

and syringes were sent to the MRC to facilitate sample collection, then samples were sent back to University of Cambridge for analysis.

Daily samples were collected over three weeks in July 2014 at the same location as the time-series collected by the MRC to observe high resolution variation in water chemistry and to check the sampling quality of the MRC.

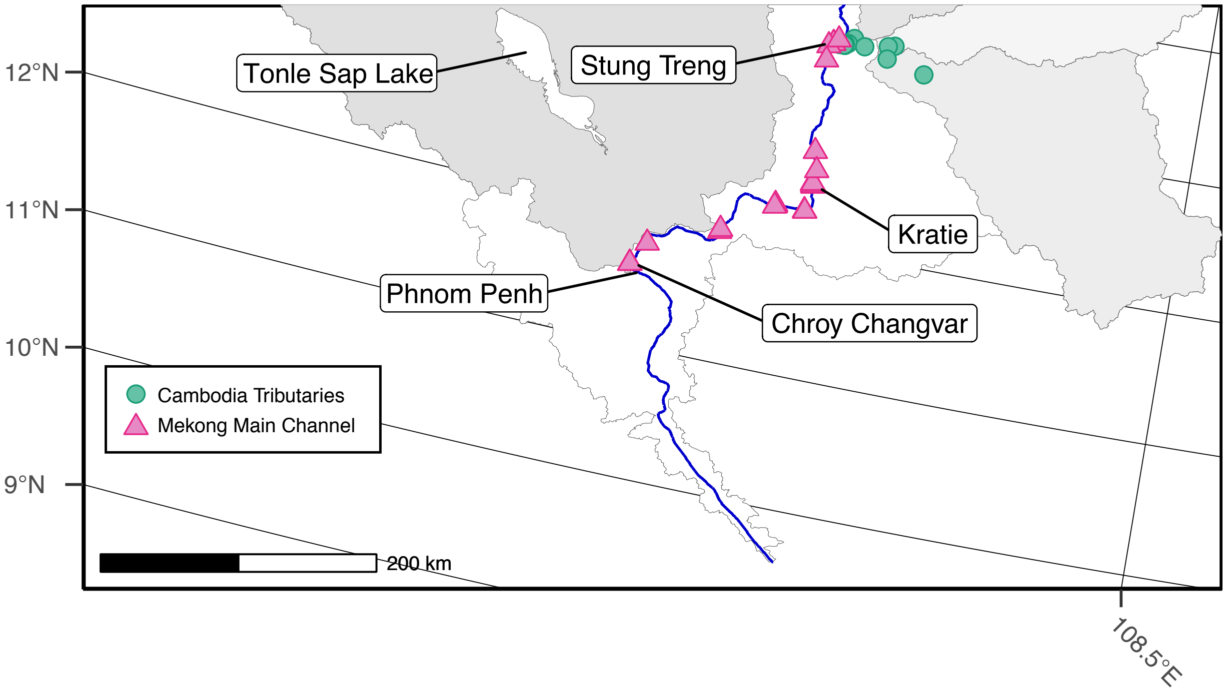

Figure 3.3: Time-series sample site: Chroy Changvar, Cambodia. The map is orientated over the mouth of the Mekong river basin. Time-series samples collected for the study are from Chroy Changvar, upstream of Phnom Penh. At Phnom Penh, the Tonle Sap joins the main Mekong, the samples collected at Chroy Changvar are far enough upstream not to be affected by any back flow from the confluence. Other main stem sites sampled for this study, visible in this map, are Kratie and Stung Treng.

3.1.3 Measurement of Discharge

At main stem sites samples were typically attained by lowering the 8L depth sampler into the water from a boat. At these locations discharge measurements could be made with acoustic Doppler current profiling (aDcp) surveys. A RDI Teledyne RioGrande 600kHz instrument loaned from Prof. Dan Parsons at University of Hull, was mounted to the boat. Then the boat traversed the river perpendicular to the river bank, creating a cross-section of the river channel. Post-processing of cross-sections were made using the Velocity Mapping Toolbox (Parsons *et al.*, 2013). The location of the depth profile within the channel was determined by the results of the aDcp survey. The location in the channel with the largest velocity gradient was chosen to collect samples with a representative distribution in suspended sediment grain size.

Table 3.1: Sample collection

Sample	Storage	Storage Preparation	Volume Collected	Additions To Sample
Anion	High density poly-ethylene (HDPE) bottles, PP lids	Cleaned in 10% HNO_3 for 24hrs, cleaned in 18.2MQ for 24hrs	60mL	
Cation			60mL	Distilled 15M HNO_3
Archive			500mL/1L	
Sulfate	20ml Solid Phase Extraction tube with 5mL DOWEX 1X8-200 Anion Exchange Resin	Resin washed in 60mL 3M HCl, 60mL 18.2MQ H_2O	2L loaded onto column	
DIC	Amber glass bottle	Washed in 18.2MQ for 24hrs then 2hrs at 550°C	30mL	H_3PO_4
DOC				
14C	FlexFoil Plus bag		1L	
Suspended sediment	Amber glass bottle		125mL	
Bank sediment	Plastic zip-lock bag			

3.1.4 Other Data

The MRC has a collection of historical data from 1985 to 2000 that is open access (http://portal.mrcmekong.org/search/search). This dataset contains monthly measurements of discharge ($m^3.sec^{-1}$) and chemical analyses (cation and anion in meq/L units) for multiple main stem and some tributary stations in the Mekong river basin. The data was filtered for quality control first, by changing meq/L units to μmol/L, secondly, by calculating the charge balance (CB) of the river water (Equation 3.1). Data was discarded if the charge of total cations did not balance with the charge of total anions within 6%. The MRC data was used for applying discharge to flux calculations where aDcp measurements were not available and for analysing downstream trends in the main stem (Chapter 4).

$$CB = \frac{(2*Ca^{2+} + 2*Mg^{2+} + Na^{+} + K^{+}) - (2*SO_4^{2-} + Cl^{-} + HCO_3^{-})}{(2*Ca^{2+} + 2*Mg^{2+} + Na^{+} + K^{+}) + (2*SO_4^{2-} + Cl^{-} + HCO_3^{-})} * 100\% \tag{3.1}$$

Discharge data at Chroy Changvar, the same location as the time-series sample site, measured by the MRC is available from 1960-2002 (C Hackney 2016, personal communication, 11 February). Discharge data for Cambodian and some Laos tributaries are sourced from Someth *et al.* (2013) and Nippon Koei (2001), respectively.

3.2 Sediment Sample Preparation for Chemical Analyses

Acids used in sample dissolution and column chemistry were distilled in Quartz or Teflon stills to ensure minimal blank contamination. Preparation of sediments for chemical analysis was performed using the fused-bead method. All post-sample collection chemical analyses were made in a clean laboratory suite in the Department of Earth Sciences, University of Cambridge.

3.2.1 Sequential Extractions from Bank Sediment

Carbonate and silicate source rock compositions were targeted using a four–step modified standard sequential extraction procedure (Tessier *et al.*, 1979), on bedload samples collected from 30 tributaries of the Mekong. Samples were collected from below the water line of sand banks where possible, otherwise from fresh deposits on river terraces. Samples ranging from course sand to fine clays were oven dried at 40°C or freeze dried, then 400mg of sample was added to a pre-cleaned 50mL centrifuge tube. The following reagents were sequentially added to and removed from the sample (detailed in Table 3.2) in class 1000 clean laboratories at room temperature using teflon distilled acids. First, a weak 1M ammonium chloride (NH_4Cl) leaches cations in the exchangeable pool, cations that are weakly bound to the surface or interlayers of clays. Then an acid-reductive leach is used to target weakly bound amorphous Fe-oxyhydroxides, Mn-oxyhydroxides and low-Mg carbonates. This leach is a mix of: 5mM Hydroxylamine-Hydrochloride (HH), to reduce the Mn-oxyhydroxides, 1.5% acetic acid which attacks Fe-oxyhydroxides and forms a ferric acetate salt and Na-EDTA complexing agent to prevent reprecipitation of trace metal cations, which is buffered with NaOH to keep pH stable as in Blaser *et al.* (2016). This leach should have minimal silicate contamination and be a pure carbonate end member. Next a 1.7M acetic acid leach targets low Mg-carbonates and remaining crystalline Fe-oxyhydroxides. Finally 1M HCl leaches high Mg-carbonates. The acetic and HCl acid reagents may leach into the detrital fraction but immobile elements such as Al and Fe will give an indication of any leaching of the silicate fraction into this phase. The remaining residue should reflect the silicate rock source. Leachates and dissolved residue sediment were analysed for major cations and Sr concentrations on an Agilent ICP-OES. $^{87}Sr/^{86}Sr$ was measured on dissolved residue sediment in fused micro-beads as outlined below and on a selection of high Ca-Sr leachates using a MC-ICP-MS. ϵNd was measured on the residue sediment on a MC-ICP-MS.

Table 3.2: Leaching procedure

Step	**Sample**	**Ultra-sonicator**	**Reaction period**	**Centrifuge**	**Remove supernatent**
1M NH_4Cl	Add 16mL NH_4Cl to sample, cap and shake vigorously	20 minutes	0hr	15 minutes at 5000rpm	Pipette off NH_4Cl into new centrifuge tube
5mM HH	Add 10mL HH to residue sample, cap and shake vigorously	0 minutes	1hr on the shaker table	15 minutes at 5000rpm	Pipette off HH into new centrifuge tube
Water wash	Add 30mL water to residue, shake vigorously	0 minutes	0hr	15 minutes at 5000rpm	Pipette off water and discard, repeat addition through to removal of water 3 times
1.7M AcOH	Add 16mL AcOH to residue sample, cap and shake vigorously, removing any gas as required	20 minutes	3hr on the shaker table	15 minutes at 5000rpm	Pipette off AcOH into new centrifuge tube
1M HCl	Add 16mL HCl to residue sample, cap and shake vigorously, removing any gas as required	0 minutes	>8hrs (overnight) on the shaker table	15 minutes at 5000rpm	Pipette off HCl into new centrifuge tube
Residue	Residue sample dried in oven at 80°C for 24hours then weighed.				
Residue dissolution	Dry residue is heated at 950°C for 8hours to ignite organics. Ignited powder is dissolved in a lithium tetraborate, lithium metaborate flux forming a glass micro-bead. This glass bead is dissolved in 50mL 2.5% HNO_3.				

3.2.2 Fused Micro-Bead Digestion

To measure the composition of sediments, the sample must first be dissolved. Moreover, for cation and multiple isotope analyses to be performed on sediment samples it is beneficial to use one digestion method that is suitable for all analyses, not least because the small size of some samples allows only one digestion of the sediment. Sediment can be digested by placing the sample and hydrofluoric acid, HF, into a teflon beaker and adding heat and pressure. This method releases silicon tetrafluoride, SiF_4, as a volatile gas, consequently Si concentrations cannot be measured in the sample. A common way to dissolve sediment is by alkaline fused bead digestion and analysis by X-Ray Fluorescence (XRF) spectrometry (Gazulla *et al.*, 2008). However, analysis by XRF requires 0.5g of sediment which precludes analysis of extremely small samples. Therefore a fused bead method was developed to digest sediment samples which requires only 50mg of sample, an order of magnitude smaller than XRF analysis, and which is suitable to then perform multiple analyses.

Sediment is dried in an oven at 100°C for 2 hours then the sample is weighed into ceramic crucibles. Lidded crucibles are placed into a furnace at 950°C for 420 minutes to oxidise, de-water and decarbonate the sample. 50mg of ignited sample, 200mg super pure lithium metaborate flux ($LiBO_2$) and 50mg super pure lithium tetraborate flux ($Li_2B_4O_2$) was weighed into a platinum crucible and heated atop a Meeker burner (1200°C) until homogenised. The molten mixture was poured into a mould to cool then 100mg of the glass bead was weighed into a 50mL centrifuge tube. The centrifuge tube was pre-cleaned by soaking for 24hours in 10% HNO_3 followed by 24 hours in 18.2MQ water then left in a clean drying cabinet until dry. To dissolve the glass bead, 50mL 2.5% HNO_3 and a teflon coated magnetic stirrer was added to the centrifuge tube before placing the centrifuge tube on a magnetic hotplate for 12 hours. Constant agitation of the dissolving glass bead is needed, in the form of the teflon coated magnetic stirrers, to prevent settling and re-precipitation of silicates on the surface of the glass bead. Platinum crucibles are used as they are non-reactive with the constituents. To decrease weighing errors, the smallest constituent weighed is 50mg however the total bead is too concentrated to analyse if all 300mg are dissolved in 50mLs. Therefore only a third of the glass bead is dissolved, which also keeps acid volume to a minimum. Moreover, because the HNO_3 acid concentration is only 2.5%, no further dilution is needed before running the dissolved sample on the Agilent for cation concentrations.

3.2.3 Verification of Fused Micro-Bead Digestion Method

The digestion of sediment by glass bead fusion is used for analysis $^{87}Sr/^{86}Sr$ and ε_{Nd} isotopes in bulk bank samples, bulk suspended sediment samples and sediment residue from leaching. A series of checks were made to ensure there was no loss or isotope fractionation of elements through sediment digestion in a fused bead or subsequent dissolution in 2.5% HNO_3. USGS Sediment standards were digested in three ways; first by placing sediment in a teflon beaker with HF on a hotplate, second making a bead using the HF digest (to ensure no homogeneity due to standard sediment aliquots), third by making a bead using the standard method. Then the samples were dried down, refluxed in concentrated HNO_3, dried down again and taken up in a reagent suitable for column chemistry. An aliquot of the dissolved standards were separated for $^{87}Sr/^{86}Sr$ chemistry and measured. An aliquot of the dissolved standards were also separated for $^{143}Nd/^{144}Nd$. Sr can be collected during the Nd separation procedure and this Nd column cut is also analysed for $^{87}Sr/^{86}Sr$ to compare to $^{87}Sr/^{86}Sr$ analysed directly from the digestion methods. The results in Table 3.3 show that this developed fused micro-bead method to dissolve sediment does not fractionate $^{87}Sr/^{86}Sr$ or ε_{Nd} isotopes. Moreover, the 50mLs of digested sample generated by this digestion method could also be used for the analysis of Ca and Mg isotopes.

3.3 Cation Analysis

Major cation (and Sr, and S) concentrations were measured by Inductively Coupled Plasma Optical Emission Spectroscopy (ICP-OES) on an Agilent 5100. Optimal set up of radial and axial detectors for particular wavelengths of an element was determined by external standard measurements before analysing samples.

3.3.1 Water Sample Cation Analysis

Samples were measured against synthetic multi-elemental calibration lines made from mono-elemental standards. The calibration line was made to match the matrix of river waters typical to Southeast Asian rivers. External standards and acid blanks were run between every 10 samples to check for drift. No samples were corrected for drift. Measured external standards SPS-SW2, SLRS-5 and SLRS-6 were accurate to within ±5% of certified values (within ±7.3% for Fe) and precise to within ±5% 2σ for Al, K, Mg, Mn, Na, S, Si, Sr and within ±5.8% 2σ for Ca and Fe, n=137. Elements Al, Fe and Mn were measured in river water samples as a check on for particle contamination during the field collection process.

Table 3.3: Fused micro-bead method verification. ^{87}Sr/^{86}Sr and ε_{Nd} isotope ratios measured in digested USGS standard sediment. Sediment was dissolved with HF on a hotplate (HF Hotplate Digest), the dissolved sediment from HF digestion was made into a bead (Bead of HF Hotplate Digest) and sediment was digested using the standard fused bead procedure (Bead Digest). Aliquots of the dissolved sediment were put through columns to separate ^{87}Sr/^{86}Sr and ^{143}Nd/^{144}Nd. A cut containing Sr was taken from the dissolved sediment aliquots put through Nd separation columns and analysed for ^{87}Sr/^{86}Sr (Nd Col. Cut). Isotopic values are compared against certified standard values (Difference from Standard) and standard error (2SE) of all digestion methods is calculated. Standard values are from 1: Jochum *et al.* (2005), 2: average of values from Cheong *et al.* (2013); Raczek *et al.* (2003); Weis *et al.* (2006), 3: Raczek *et al.* (2003), and 4: average of values from Cheong *et al.* (2013); Raczek *et al.* (2003); Saji *et al.* (2016).

Digestion Method	HF Hotplate Digest		Bead of HF Hotplate Digest	Bead Digest		HF Hotplate Digest Nd Col. Cut	Bead Digest Nd Col. Cut	Standard Value	2SE	Difference from Standard
$^{87}Sr/^{86}Sr$ Isotopes										
USGS Standard	^{87}Sr/^{86}Sr		^{87}Sr/^{86}Sr	^{87}Sr/^{86}Sr		^{87}Sr/^{86}Sr	^{87}Sr/^{86}Sr	^{87}Sr/^{86}Sr	ppm	ppm
GSP-1	0.768502		0.768491						19	
SDC-1				0.734728		0.734667	0.734706		83	
G-2	0.709752		0.709744	0.709788		0.709749	0.709766	0.709771 [1]	50	-11
BHVO-2	0.703494			0.703502				0.703478 [1]	17	20
ε_{Nd} Isotopes										
USGS Standard	ε_{Nd}	2σ		ε_{Nd}	2σ			ε_{Nd}	ε_{Nd}	ε_{Nd}
BHVO-2	6.74	0.22		6.86	0.19			6.428 [2]	0.16	0.37
GSP-1	-24.70	0.14		-24.71	0.19			-24.676 [3]	0.01	-0.03
BCR-2	-0.25	0.11		-0.08	0.17			-0.052 [4]	0.25	-0.11
G-2	-8.09	0.16		-8.10	0.19			-7.873 [1]	0.02	-0.22
SDC-1	-11.05	0.14		-11.28	0.14				0.32	
SCO-1	-10.68	0.18						-10.163 [1]		-0.52

3.3.2 Sediment Sample Cation Analysis

Sediment digested via the fused bead method and subsequently dissolved in 2.5% HNO_3 is run directly on the Agilent ICP-OES. Although 50mg of sediment is digested, only ca. one third is dissolved in 50mLs 2.5% HNO_3 so the concentration of elements in the solution is dilute enough to run directly on the instrument without saturating the detectors. A calibration line was made to match the lithium-borate matrix of the dissolved sediment samples using external sediment standards dissolved in the same method. In order to span the correct magnitude for each element, 15mg each of USGS standard Hawaiian Basalt BHVO-2 and Mica Schist SDC-1 were added to 50mg Lithium borate flux then made into a fused bead. One third of the bead was dissolved in 2.5% HNO_3 and then diluted to the correct concentrations with a dissolved fused bead containing only lithium-borate flux. Using a 'blank' lithium-borate bead instead of water or acid to dilute the calibration line ensures the ratio of sediment to sample in the matrix remained the same throughout the calibration line. Certified reference sediment standards USGS Granite G-2, Hawaiian Basalt BHVO-2, Columbia River Basalt BCR-2, Mica Schist SDC-1, and Cody Shale SCo-1 were measured between 10 samples on the Agilent. Repeated analyses of external standards were accurate to within ±5% for Al, Ca, Mg, Si, Sr, Ti, within ±7% for Ba, K, V, Zn and within ±9% for Fe, Mn, Na of certified values, n=173.

Each sequential extraction was measured against a unique calibration line suitable for the matrix of the respective leachate. Leachate calibration lines were made from mono-elemental standards, then the approximate matrix (NH_4Cl, HH, AcOH, HCl) was added. External standards were run between sets of 5 samples to ensure measurement accuracy, SPS-SW2 water and Columbia River Basalt BCR-2 were chosen because no standards with the same matrix as the leachates are available. The 50% calibration standard was also run as a bracketing standard between sets of 5 samples to check instrument drift.

3.4 Anion Analysis

Anions Cl^- and SO_4^{2-} were measured on a Thermo Scientific Dionex ICS-5000+ High Performance Ion Chromatographer (HPIC) using a 4 x 250mm Ionpac AS18 column with 24-31mM potassium hydroxide eluent. An in-house calibration line was made using mono-anion standards based on concentrations measured in other Asian rivers, to reduce matrix effects. Repeated analyses of external standard LGC6025 River water (from Menethorpe Beck, Yorkshire, UK) were accurate to within ±3.7% of certified values for Cl^- and SO_4^{2-}, n=85.

3.5 Elemental Separation and Isotope Analysis

Analysis of sulfur and oxygen isotopes in dissolved sulfate, $\delta^{34}S_{SO_4}$ and $\delta^{18}O_{SO_4}$ respectively, are discussed in Chapter 5.

3.5.1 Strontium Separation and ^{87}Sr/^{86}Sr Isotope Analysis

Strontium was separated and measured in two ways. For samples collected before 2016, Sr was separated using Dowex 50Wx8 cation exchange resin with 200-400 mesh particle size then ^{87}Sr/^{86}Sr ratios were measured on a VG Sector 54 solid source mass-spectrometer using triple-collector dynamic algorithm (Bickle *et al.*, 2003). In samples collected after 2016, 500ng strontium was separated using Biorad Micro Bio-Spin columns with Eichrom SrSpec resin then ^{87}Sr/^{86}Sr ratios were measured on a Thermo Neptune MC-ICP-MS (Hindshaw *et al.*, 2018) with each measurement comprising 30 cycles with 8 second integration. The Neptune method was setup to correct for rubidium interferences on ^{87}Sr by monitoring ^{85}Rb, and ^{84}Kr and ^{86}Kr interferences were corrected by measuring ^{83}Kr. Repeated measurements of NBS 987 gave a ^{87}Sr/^{86}Sr value of 0.710285 ±36ppm (2σ, n=63) and the seawater value was 0.709200 ± 33ppm (2σ, n=17), which is within error of the accepted value of 0.709179.

3.5.2 Neodymium Separation and ε_{Nd} Isotope Analysis

Neodymium is a rare earth element, with five stable and two radiogenic isotopes, that is concentrated in silicate minerals. Variations in the ratio of radiogenic ^{143}Nd to stable ^{144}Nd are used to provenance lithologies of different ages (e.g. Singh & France-Lanord, 2002). Neodymium isotope ratios (^{143}Nd/^{144}Nd) are used in conjunction with strontium isotope ratios (^{87}Sr/^{86}Sr) because processes by which both isotope ratios are set, during formation of volcanic rocks through partial melting of the mantle, are independent yet complimentary (Faure & Mensing, 2005). During partial melting, Rb and Nd are concentrated in the melt phase whilst Sm and Sr remain in the residual solids, setting the Sm/Nd and Rb/Sr ratios in rocks and minerals (Peucker-Ehrenbrink *et al.*, 2010). ^{143}Nd/^{144}Nd and ^{87}Sr/^{86}Sr ratios vary due to the subsequent radioactive decay of ^{87}Rb to ^{87}Sr and

^{147}Sm to ^{143}Nd (Blum & Erel, 2003; Allègre, 2008). Hence, ^{87}Sr/^{86}Sr and ^{143}Nd/^{144}Nd isotope ratios in a rock or mineral vary as a function of age and lithology (Goldstein & Jacobsen, 1987; Asahara *et al.*, 2012).

To analyse ^{143}Nd/^{144}Nd, rare earth elements (REE) were isolated using Eichron TRUspec^{TM} resin (100-150μm mesh) in 100μL Teflon columns. Nd was then extracted using Eichron LNspec^{TM} resin (50-100μm mesh) in volumetrically calibrated Teflon columns (following Piotrowski *et al.*, 2009). ^{143}Nd/^{144}Nd isotopic composition was measured on a Neptune multi-collector plasma mass spectrometer (MC-ICPMS) with an Elemental Scientific Inc. APEX IR desolvating nebuliser introduction system. Samarium interferences were monitored by measuring mass 149. No interferences were detected and oxide production was monitored during the run. Bracketing standard JNDi-1 was measured every three samples to correct for offset and drift. Repeated measurements of JNDI-1 gave a value of -10.08 ±0.29 1σ (n=56) compared to the standard value of -10.202 (Tanaka *et al.*, 2000). External standards USGS Cody Scale SCo-1 was measured at -10.29 ±0.12 1σ within 0.12 ε_{Nd} of published values (Jochum *et al.*, 2005). The error quoted on samples is the larger value from external error or internal error (internal being the instrument standard deviation of multiple measurements). ^{143}Nd/^{144}Nd ratios are expressed as ε_{Nd}, i.e. deviation x10,000, relative to present-day chondritic uniform reservoir (CHUR) value (^{143}Nd/^{144}Nd=0.512636) of Jacobsen & Wasserburg (1980).

$$\epsilon Nd_{(0)} = \left[\frac{(^{143}Nd/^{144}Nd)_{measured}}{(^{143}Nd/^{144}Nd)^{0}_{CHUR}} - 1 \right] * \ 10^{4} \tag{3.2}$$

3.5.3 $\delta^{18}O_{H_2O}$ and δD Measurement

$\delta^{18}O_{H_2O}$ and δD of the river water were measured simultaneously by cavity ring down mass spectrometry using a Picarro L1102-i interfaced with a A0211 high-precision vaporizer. Samples were calibrated against JRW, SPIT and BOTTY standards. $\delta^{18}O_{H_2O}$ and δD results are expressed relative to Vienna Standard Mean Ocean Water (VSMOW) in parts per thousand (‰). Repeat measurements of the standards had a precision of $\delta^{18}O_{H_2O}$ = 0.1‰, δD = 0.6‰, 2σ (n=28).

Chapter 4

Chemistry and Isotopic Composition of the Dissolved Load and Bedload of the Mekong River and it's Tributaries

4.1 Introduction

Chemical weathering and physical erosion of rocks are key geochemical processes that affect the carbon cycle. Specifically, the weathering of silicate minerals draws down CO_2 from the atmosphere converting it to bicarbonate, eventually leading to carbonate precipitation in the oceans. Pioneering work by Walker *et al.* (1981) and Berner *et al.* (1983) has shown it is the role of silicate weathering that acts to regulate long-term climate.

Large rivers export the majority of weathering products from land to oceans, hence river water chemistry provides critical information on the chemical weathering fluxes and their controlling processes. Furthermore, a better understanding of the natural geochemical signature of river waters, and the terrestrial processes causing those signatures, is crucial to provide a baseline from which deviations caused by anthropogenic activities can be assessed.

Quantifying the flux of solutes from the world's largest rivers to the ocean is important for understanding bio-geochemical cycling, but the signal at the mouth of large rivers does not provide a representative account of the potentially variable processes occurring throughout large river catchments. The Mekong river in South East Asia is particularly well suited to investigating spatial and temporal geochemical processes because the river's headwaters drain an area of high erosion on the Eastern Syntaxis of the Himalayas and the nature of the basin is large in size with complex geology and a range in climate and topography. This chapter will discuss the chemistry of the dissolved load and bank sediment in the Mekong river. A forward model is applied to elements in the dissolved load to partition them to their lithological sources and infer the key weathering reactions occurring. Finally a silicate and carbonate weathering budget for the Mekong river basin is estimated.

4.2 Division of Mekong River Basin

It is convenient to split the Mekong river basin into sections in order to clearly describe the spatial location of chemical data (Figure 4.1). Obvious geological units (Figure 1.2), topographic features (Figure 4.6A) and main stem sampling locations have been used to divide the basin. The first section is the Upper Mekong: the basin area between the source of the Mekong and southern China. Samples collected in China are collected at the highest altitude, the altitude drops significantly between Yunnan and Luang Prabang (Figure 4.6A). The Middle Mekong extends from southern China to Pakse and is split into three sections. First, tributaries draining Myanmar and northern Thailand are grouped, joining the Mekong where northeast Myanmar borders northern Thailand and southwest China. Secondly, tributaries draining the left bank of the Mekong in Laos are grouped. These tributaries drain the Annamite mountain range which has higher topography and receives more rainfall than the final group of tributaries in the Middle Mekong. Tributaries grouped into the third section of the Middle Mekong drain the Khorat Plateau, a distinct geological feature of the right bank of the Mekong in Thailand (Figure 1.2). The Middle and Lower Mekong are separated by the Khone Phapheng Falls and the border between Laos, Thailand, and Cambodia. Large flood plains and a noticeably wider river channel dominate in Cambodia with three tributaries draining the southern Annamite mountains in northwestern Cambodia contributing 28% of the Mekong river basin discharge (Adamson *et al.*, 2009). Time-series samples were collected at Chroy Changvar (Phnom Penh), Cambodia, close to the mouth of the Mekong before the channel divides into distributaries.

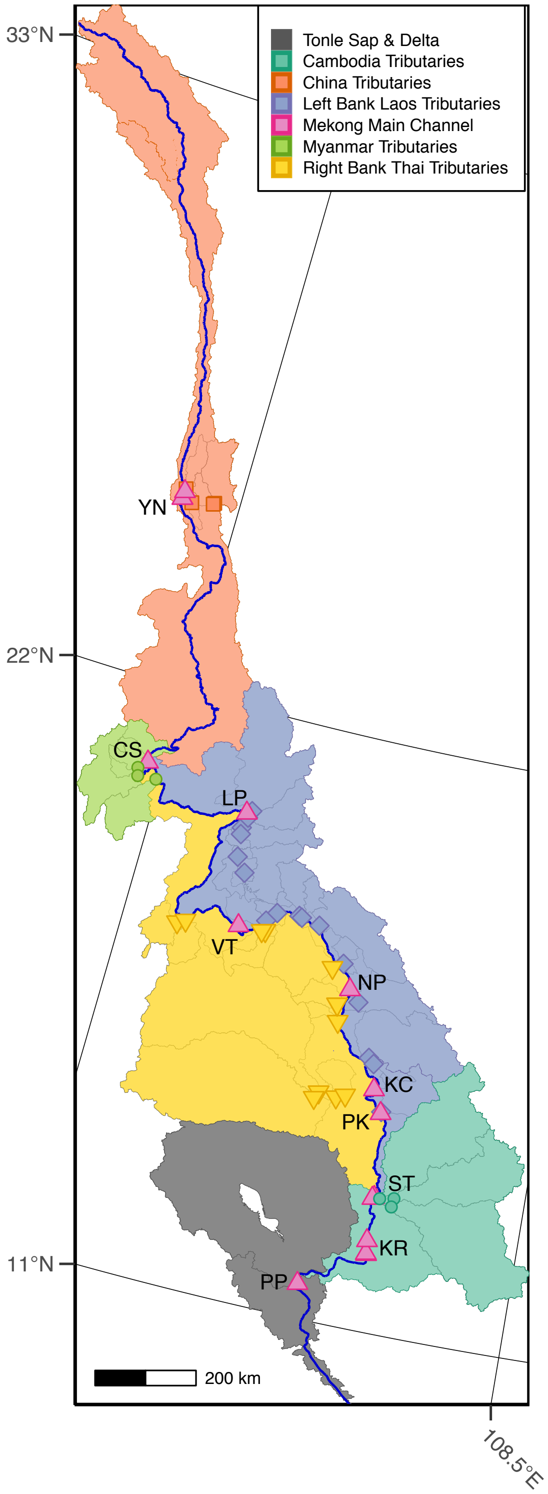

Figure 4.1: Division of Mekong river basin. Main stem sample sites (pink triangles) collected in 2014, 2016 and 2017 field seasons are Yunnan (YN), Luang Prabang (LP), Vientiane (VT), Pakse (PK), Stung Treng (ST), Kratie (KR) and Phnom Penh (Chroy Changvar) (PP), other main stem sites Chiang Saen (CS), Nakhon Phanom (NP), and Khong Chiam (KC) are MRC historical time series sample sites. Tributaries have been split into five main sections with locations of sampling denoted by a shape; China (orange squares), Myanmar and Northern Thailand (yellow green circles), Laos (purple diamonds), Thailand (yellow inverted triangle), Cambodia (blue green circles) (see text for how tributaries are sectioned). No data is presented from the Tonle Sap lake or distributaries in the Delta region (grey).

4.3 Results

4.3.1 River Sediment Chemistry

Sediment collected from the river bank or the river bed is an integration of the weathered products of each lithological unit within a river basin. Five main chemical components contribute to the chemistry of bulk bank sediment: silicate minerals, carbonate minerals (calcite and dolomite), iron-oxyhydroxides, and an exchangeable fraction. There is also a major fraction of organic carbon, which is not the focus of the present study. Characterising the silicate and carbonate fractions, and therefore the lithology in the basin, is particularly important when quantifying how much each lithological type contributes to the weathering flux.

To investigate the chemistry of the individual components bank sediment was sequentially leached, aiming to remove a targeted component of the bulk sediment with each step. Bank sediments are leached instead of suspended sediment from the river water column because chemical gradients are observed in sediments collected at different depths, and for the very simple logistical reason that suspended sediment samples are small and there is more bank material to work with. The chemical gradients in suspended sediments are caused by hydrodynamic sorting of minerals, from fine grained Al-rich clay at the river channel surface to increasingly coarse Si-rich quartz mineral enrichment at the river bed (Bouchez *et al.*, 2011a,b; Lupker *et al.*, 2011). It is assumed that bank sediment is a representative homogenisation of the rocks in the river basin being weathered, however is it possible that incongruent weathering leads to mineral bias in the bulk sediment.

Clays present in sediment have negatively charged surfaces and so adsorb cations by electrostatic forces (Drever, 1997). Adsorbed cations can easily exchange with the surrounding environment (Lupker *et al.*, 2016). The first leaching step uses ammonium chloride (NH_4Cl) to target adsorbed cations, known as the exchangeable fraction. Next, hydroxylamine-hydrochloride (HH) solution is added to extract oxyhydroxides from the sediment. Acetic acid (AcOH) is then added to leach low Mg-carbonates (calcite) from the sediment and finally hydrochloric acid (HCl) is added to target high Mg-carbonates (dolomite). The detrital silicate component remains after these four components are removed. The methodology of sequential leaching, after Tessier *et al.* (1979), is detailed further in Chapter 3.2.1. Bank sediment from every accessible catchment has been leached. Major cation concentration data was analysed for each leachate and remaining detrital sediment and $^{87}Sr/^{86}Sr$ and ε_{Nd} has been analysed on the detrital fraction for all tributaries following alkaline fusion by ICP-OES (Table 4.1). Data for all elemental separation and isotopic analysis is described

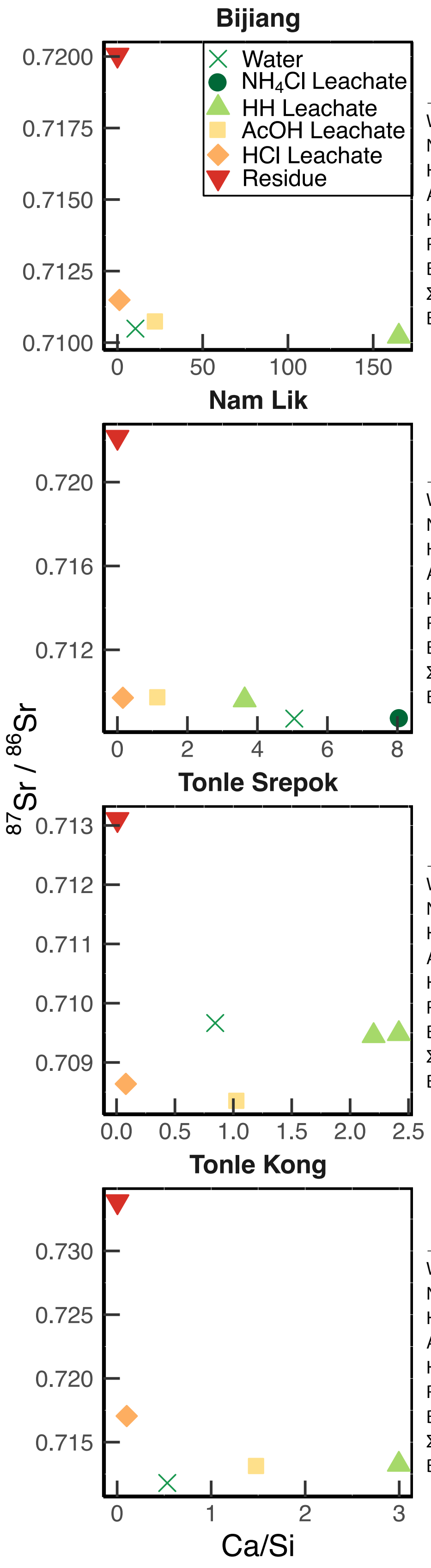

	Al ppm	Al %	Ca ppm	Ca %	Fe ppm	Fe %	Si ppm	Si %	Sr ppm	Sr %	$^{87}Sr/^{86}Sr$
Water	0		39		0		4		0.40		0.710488
NH_4Cl	1	0.0	5038	20.3		0.0	7	0.0	21	15.6	
HH	123	0.2	12968	52.4	788	2.7	79	0.0	20	14.7	0.710217
AcOH	136	0.2	2309	9.3	295	1.0	105	0.0	4	3.3	0.710740
HCl	924	1.5	756	3.1	1476	5.0	640	0.2	5	3.8	0.711490
Residue	65185	106.5	405	1.6	29167	99.6	333027	106.1	85	63.5	0.720054
Bank	61233		24766		29295		313758		134		
Σ(L, R)	66369		21477		31726		333858		136		
B-Σ(L, R)%	-8		13		-8		-6		-1		

	Al ppm	Al %	Ca ppm	Ca %	Fe ppm	Fe %	Si ppm	Si %	Sr ppm	Sr %	$^{87}Sr/^{86}Sr$
Water	0		40		0		8		0.15		0.708720
NH_4Cl	2	0.0	1002	39.3	3	0.0	125	0.0	7	8.3	0.708739
HH	97	0.1	352	13.8	283	0.6	97	0.0	2	2.2	0.709603
AcOH	92	0.1	486	19.1	124	0.3	426	0.1	1	1.8	0.709738
HCl	949	1.2	294	11.5	2258	5.0	1884	0.6	2	2.5	0.709713
Residue	75652	97.0	415	16.3	43312	96.2	330442	99.1	70	88.1	0.722146
Bank	77956		2548		45034		333300		80		
Σ(L, R)	76793		2549		45980		332974		82		
B-Σ(L, R)%	1		0		-2		0		-3		

	Al ppm	Al %	Ca ppm	Ca %	Fe ppm	Fe %	Si ppm	Si %	Sr ppm	Sr %	$^{87}Sr/^{86}Sr$
Water	0		4		0		5		0.03		0.709665
NH_4Cl	1	0.0	2125	39.3	0	0.0	22	0.0	19	21.9	
HH	213	0.3	250	4.6	1011	1.8	113	0.0	2	2.2	0.709449
AcOH	63	0.1	161	3.0	298	0.5	157	0.1	2	1.9	0.708353
HCl	2072	2.9	122	2.3	6427	11.7	1536	0.6	2	1.9	0.708638
Residue	68399	95.8	2377	44.0	44136	80.4	303575	112.4	69	80.1	0.713103
Bank	71433		5407		54873		270196		86		
Σ(L, R)	70748		5036		51872		305403		93		
B-Σ(L, R)%	1		7		5		-13		-8		

	Al ppm	Al %	Ca ppm	Ca %	Fe ppm	Fe %	Si ppm	Si %	Sr ppm	Sr %	$^{87}Sr/^{86}Sr$
Water	0		3		0		6		0.02		0.711798
NH_4Cl	5	0.0	801	33.3	2	0.0	8	0.0	6	6.3	
HH	178	0.2	119	4.9	1375	2.6	40	0.0	1	0.8	0.713247
AcOH	108	0.1	111	4.6	551	1.0	75	0.0	0	0.5	0.713133
HCl	1181	1.1	67	2.8	3595	6.8	654	0.2	0	0.5	0.717049
Residue	101363	97.6	888	37.0	45803	87.2	284824	94.7	82	90.7	0.733875
Bank	103885		2402		52503		300695		90		
Σ(L, R)	102834		1985		51325		285601		89		
B-Σ(L, R)%	1		17		2		5		1		

Figure 4.2 *(Caption over page)*

in Chapter 3. The leachates for four tributaries have also been analysed for ^{87}Sr/^{86}Sr. The four tributaries are from the Upper, Middle, and Lower Mekong, spanning the length of the sampling sites.

Ensuring that the leaching reagents target the correct source of cations is crucial to characterising each component of the bulk sediment. To check the validity of the leaching process, the presence of immobile elements such as Al and Fe in the AcOH or HCl leachate is measured. Their presence would indicate contamination from the silicate fraction, or Fe oxides, or amorphous silica and aluminium phases. Concentrations and percentage contribution of each component to total bulk sediment is presented for several elements (Figure 4.2). The mass balance of the leachates and residue have been verified against the bulk bank sediment. There is 0% - 17% difference (mean=0.25%) between the sum of the leachates and residue and the bulk bank sample, confirming the process from sediment leaching through to analysis is recovering the complete chemistry of the bank sample. The residue is most concentrated in Al and Fe whereas the leachates contain less than 2.9% Al and less than 11.7% Fe, confirming that the leaching reagents are not being contaminated by the silicate fraction. There is one order of magnitude difference in the concentrations of elements of presented samples. The contribution to total Ca and Sr from components varies for each sample, highlighting the heterogeneity of lithologies in the basin.

Ca/Si values decrease from the first fraction leached by NH_4Cl to the detrital residue, whilst ^{87}Sr/^{86}Sr isotope values become generally more radiogenic. Ca/Si values are similar for the residue and HCl leach, but the ^{87}Sr/^{86}Sr values vary significantly. Ca/Si values of the HH leachate is around double the value of the AcOH leachates. ^{87}Sr/^{86}Sr values in the HH leachate range between 0.708976–0.714444 (for 13 bank samples). ^{87}Sr/^{86}Sr values in the silicate residue range between

Figure 4.2 *(previous page)*: Characterisation of bank sediment components by sequential leaching. Elemental ratio Ca/Si and ^{87}Sr/^{86}Sr isotope characterisation of bank sediment sequential leaches compared to water from the same location. Bank sediment is sequentially leached in the following order: ammonium chloride (NH_4Cl), hydroxylamine-hydrochloride (HH), acetic acid (AcOH), hydrochloric acid (HCl) to leave detrital sediment. Major cation and Sr concentrations (ppm) and ^{87}Sr/^{86}Sr isotopes of leachates, residue and bulk sediment are listed in the adjacent tables, with percentage contribution of the leachates and residue to the total concentration in the bulk sediment. The sum of all leachates and residue, $\sum(L, R)$, is reported. The difference, as a percentage, between the measured bulk bank sample and sum of all leachates and residue, $B - \sum(L, R)\%$ is also reported. Bank samples leached for Bijiang, Nam Lik, Tonle Srepok and Tonle Kong are: MEK17-116, MEK17-147, MEK16-124, and MEK16-114, respectively with corresponding waters: MEK17-115, MEK17-146, MEK16-125, and MEK16-119, respectively.

0.707753–0.745808 (for 33 bank samples).

The distinct chemistry of lithologies that comprise the bulk bank sediment is illustrated by the spread of the leached components. The detrital sediment is most radiogenic and has the lowest Ca/Si ratio, characteristic of silicate minerals. The HH and AcOH leaches have similarly low ^{87}Sr/^{86}Sr values for all samples, with the exception of the Tonle Srepok. These leaches likely target the low-Mg carbonate fraction. ^{87}Sr/^{86}Sr in the Tonle Kong water does not lie between the other leachate values, it is 1335ppm less radiogenic than the value for the HH leachate. There maybe several reasons for this; firstly, the AcOH leachate may be contaminated by the silicate fraction, increasing the ^{87}Sr/^{86}Sr isotope value; or the water chemistry could be affected by the exchange pool, for which ^{87}Sr/^{86}Sr isotopes have not yet been analysed. ^{87}Sr/^{86}Sr analysed on the exchangeable fraction for the Nam Lik is less radiogenic than the carbonate fraction. In the Nam Lik the water chemistry is closer to the chemistry of the exchangeable fraction than the silicate fraction. The water chemistry of the Tonle Srepok is more heavily influenced by the silicate fraction than the other samples; the water is more radiogenic than the low- and high-Mg carbonate fractions, but is similar to the ^{87}Sr/^{86}Sr value for the HH leachate.

4.3.1.1 Detrital Sediment Composition

The silicate minerals in bank sediment are characterised by analysis of the detrital residue remaining after bank sediments are leached. Major element concentrations, and ^{87}Sr/^{86}Sr and ε_{Nd} isotope data of the leached bank sediments are given in Table 4.1. There is large variation in elemental ratios of the silicate fraction from river bank sediment of Mekong tributaries (Figure 4.3). The mean Ca/Na ratio for silicates in the Mekong is 0.21, which is lower than the value for average crustal continental rocks (0.6, Rudnick & Gao (2003)). There is an asymmetrical distribution towards high Ca/Na ratios in Mekong tributaries, similar to the distribution of Ca/Na ratios from rivers that cover a significant climate difference in North America and Europe (White & Blum, 1995). Gaillardet *et al.* (1999) suggest this is indicative of weathering-limited regimes, where Ca has already been weathered and transported away. However, Mekong Ca/Na values fall mostly in the same range of values for wet tropical rivers which are transport-limited (Gaillardet *et al.*, 1999). Ca/Na ratios on bank samples collected in the Upper Mekong in previous studies are 0.17 (Wu *et al.*, 2008); higher than values analysed in the upper Mekong for this study (0.12 at Baoshan) but within the range of Ca/Na ratios of all samples. Mg/Na values range from 0.35-6.16, with a similar distribution in values to Ca/Na. There is a much smaller range in Mg/K values (0.18-1.03) than for Mg/Na and Ca/Na. Mg/K values are symmetrically distributed about a mean of 0.53. Mg/K ratios on bank samples collected in the Upper Mekong in previous studies are 0.5 (Wu *et al.*, 2008); lower than values analysed in the upper Mekong for this study (0.67 at Baoshan) but also within the range of Mg/K ratios of all samples.

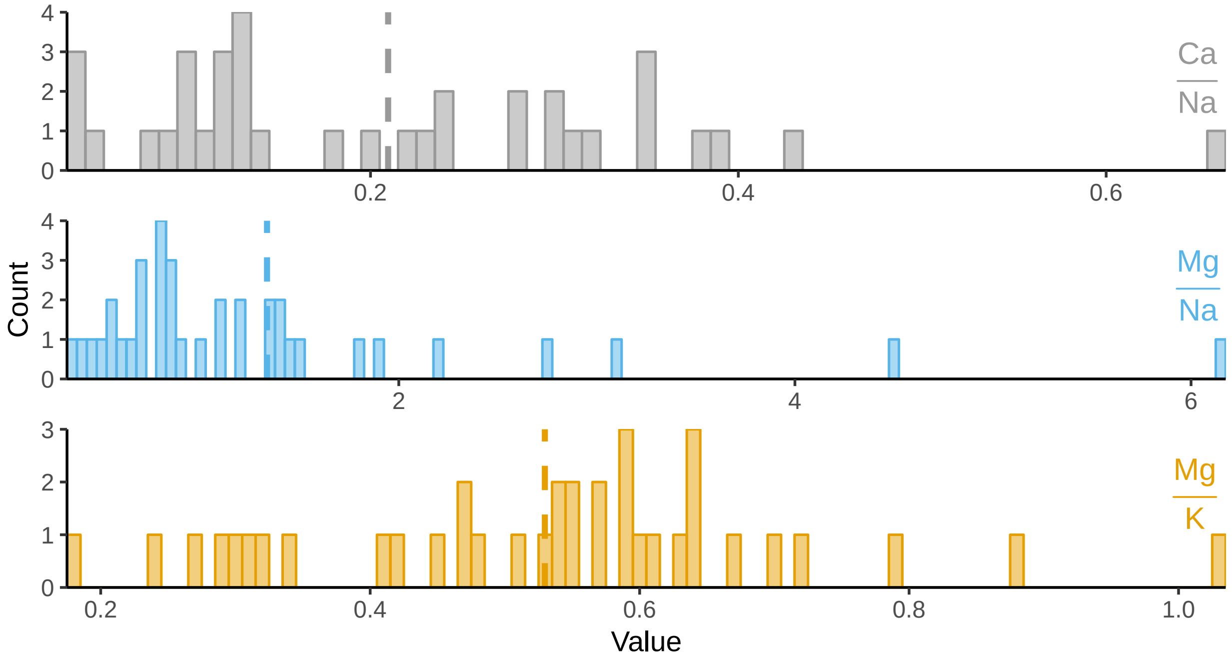

Figure 4.3: Range of Ca/Na, Mg/Na and Mg/K ratios measured in silicate fraction of river bank sediments. River bank sediment collected from each accessible tributary in the Mekong basin was leached until the silicate fraction remained. The various ratios analysed in these sediments are displayed as histograms, with mean value highlighted by the dashed line. Mean values and 1σ errors are 0.21 ± 0.14, 1.33 ± 1.17, and 0.53 ± 0.18 for Ca/Na, Mg/Na, and Mg/K, respectively.

Radiogenic isotope systems rubidium-strontium (Rb-Sr) and samarium-neodymium (Sm-Nd) are useful tracers of sediment provenance when analysed in the silicate fraction of bulk sediment. Elements, particularly Sm-Nd, do not become depleted from the source lithology by chemical weathering, transport, or diagenesis processes (Faure, 1977). Therefore, Sm/Nd ratio records crustal formation (i.e. initial source) rather than the weathering history of the sediment (Gaillardet *et al.*, 2003, and explained further in Section 3.5.2). Thus, $^{87}Sr/^{86}Sr$ and $^{143}Nd/^{144}Nd$ isotopes have been used as tracers for the provenance of river sediment (e.g. Cameron & Hattori, 1997; Goldstein & Jacobsen, 1987, 1988; Négrel *et al.*, 2000; Padoan *et al.*, 2011; Weldeab *et al.*, 2002). ε_{Nd} values of the silicate fraction of Mekong tributary bank sediment span a large range from -15.02 to -0.34

Table 4.1: Major cation concentrations and $^{87}Sr/^{86}Sr$ and ε_{Nd} isotope data in the silicate fraction of river bank sediment. Data of dissolved residue remaining after leaching away the exchangeable fraction, iron oxides, calcite and dolomite from bank sediment samples. Methodology is explained in Chapter 3.

Sample	Date	Location	Latitude	Longitude	Distance from source	Al	Ca	Fe	K	Mg	Na	Si(OH)$_4$	Sr	$^{87}Sr/^{86}Sr$	SD	ε_{Nd}	Error
					km				mmol/kg				μmol/kg		ppm		ε_{Nd}
Silicate fraction of river bank sediment																	
MEK17-251	2017-10-05	Bang Sai	16.64201	104.70013	3665	1044	7	168	137	95	21	14816	181	0.732429	4	-14.3821	0.19
MEK17-116	2017-09-14	Bijiang	25.61971	99.35675	1344	2416	10	522	521	374	272	11858	973	0.720054	2	-12.3362	0.22
MEK17-121	2017-09-15	Heihui	25.51380	99.99306	1375	2446	10	513	480	290	207	12592	557	0.719232	30	-11.4741	0.19
MEK17-238	2017-10-04	Hueang	17.73097	101.48609	3028	731	12	155	119	65	94	14952	324	0.719237	34	-11.2252	0.21
MEK17-241	2017-10-04	Loei	17.80364	101.62602	3037	1636	27	314	205	120	268	13327	680	0.71408	13	-9.15913	0.18
MEK17-234	2017-10-03	Mae Ing	20.13722	100.42036	2413	2539	70	497	437	131	250	12249	1030	0.717	40	-9.59012	0.15
MEK17-231	2017-10-02	Mae Kok	20.22702	100.12872	2349	2107	56	292	785	144	235	12755	759	0.743042		-14.0231	0.35
MEK17-228	2017-10-02	Mae Ruak	20.38762	100.06233	2332	4376	34	761	585	315	114	9581	584	0.733992	14	-12.4841	0.19
MEK17-106	2017-09-12	Mekong Baoshan	25.42888	99.34305	1441	3074	46	669	644	434	389	12159	1211				
MEK17-214	2017-09-25	Mekong Kratie	12.46088	106.01347	4299	3078	27	651	494	265	318	12097	948				
MEK17-136	2017-09-17	Mekong Luang Prabang	20.05912	102.20328	2684	1328	53	227	383	117	301	13695	788				
MEK17-188	2017-09-22	Mekong Pakse			3944	4462	29	906	580	345	229	10049	733				
CAMB140725-162	2014-07-25	Mekong Phnom Penh	11.77886	105.01689	4512	2542	47	576	441	280	344	12816	958				
MEK17-255	2017-10-06	Mun D/S	15.24218	104.95591	3787	1331	7	269	204	160	26	14361	330	0.717963	7	-7.75998	0.21
MEK16-054	2016-09-15	Nam Hinboun	17.72652	104.56755	3543	1633	25	336	283	168	308	14430	702	0.724346	11	-15.0225	0.36
MEK17-168	2017-09-20	Nam Kading	18.32294	103.99822	3430	1459	32	279	349	101	91	13150	405	0.731126	47	-11.082	0.35
MEK17-140	2017-09-18	Nam Khan	19.76572	102.18217	2710	1369	66	307	325	104	296	14074	902	0.714639	15	-6.42154	0.24
MEK17-147	2017-09-18	Nam Lik	19.21585	102.24453	3115	2804	10	776	396	347	285	11766	802	0.722146	6	-7.21303	0.35
MEK17-161	2017-09-20	Nam Mang	18.36961	103.19951	3333	1765	14	339	332	175	56	8479	244	0.745808	29	-13.713	0.16
MEK17-142	2017-09-18	Nam Ming	19.64305	102.19626	2662	2333	7	577	303	143	167	12312	785	0.718153	15	-7.35772	0.19
MEK17-163	2017-09-20	Nam Ngiap	18.41801	103.60166	3377	3024	74	644	503	225	190	10580	561	0.72899	26	-10.4585	0.41
MEK17-159	2017-09-20	Nam Ngjum	18.13910	103.05362	3291	1790	44	384	264	169	189	13085	547	0.716165	39	-7.77315	0.19
MEK17-126	2017-09-17	Nam Ou	20.11513	102.29173	2684	1177	25	310	169	103	127	14382	499	0.716533	23	-10.6748	0.38
MEK16-016	2016-09-12	Nam Xeng	19.97917	102.24716	2696	2167	24	508	361	204	239	12054	727	0.718772	29	-8.71653	0.41
MEK17-148	2017-09-18	Nam Xong	18.95441	102.43916	3074	2194	210	782	265	273	491	11783	1282	0.707753	38	-0.34237	0.41
MEK17-243	2017-10-05	Pak Suai	17.97503	103.00108	3264	3596	25	769	519	284	209	9975	965	0.717681	42	-9.04892	0.23
MEK17-246	2017-10-05	Songkhram	17.61142	104.39639	3525	355	6	52	85	34	18	15676	113	0.732096	28	-10.4188	0.36
MEK16-114	2016-09-20	Tonle Kong	13.56067	106.03835	4152	3757	22	820	610	254	172	10141	935	0.733875	35	-11.1027	0.36
MEK17-206	2017-09-24	Tonle Kong	13.56070	106.03941	4152	1595	55	400	398	134	185	13561	810	0.726174	39	-11.7735	0.18
MEK16-127	2016-09-21	Tonle San	13.61719	106.37907	4121	2501	66	453	586	139	173	12178	1043	0.731497	33	-14.5004	0.38
MEK16-113	2016-09-20	Tonle Srepok D/S	13.55287	106.03150	4152	2683	61	492	515	140	175	11389	884	0.734068	7	-13.3486	0.35
MEK16-124	2016-09-21	Tonle Srepok U/S	13.44487	106.60462	4122	2535	59	790	280	136	190	10809	790	0.713103	18	-5.70916	0.20
MEK17-174	2017-09-21	Xe Bangfai	17.07775	104.98663	3627	875	16	164	154	78	124	14524	387	0.726506	18	-14.2941	0.23
MEK17-177	2017-09-21	Xe Banghiang	16.09737	105.37608	3761	1797	20	333	356	168	168	12891	466	0.732117	25	-12.6306	0.23
MEK16-079	2016-09-17	Xe Bangnouan	16.00396	105.47945	3784	1972	17	377	373	237	171	8109	427	0.730894	3	-13.3137	0.23
MEK16-088	2016-09-18	Xe Don	15.13205	105.80823	3944	2863	10	793	298	192	88	11674	318	0.732124	213	-10.4024	0.17
MEK17-118	2017-09-15	Yinjiang	25.40018	99.54830	1441	1014	49	248	229	131	73	13125	1222	0.712102	36	-8.7283	0.22

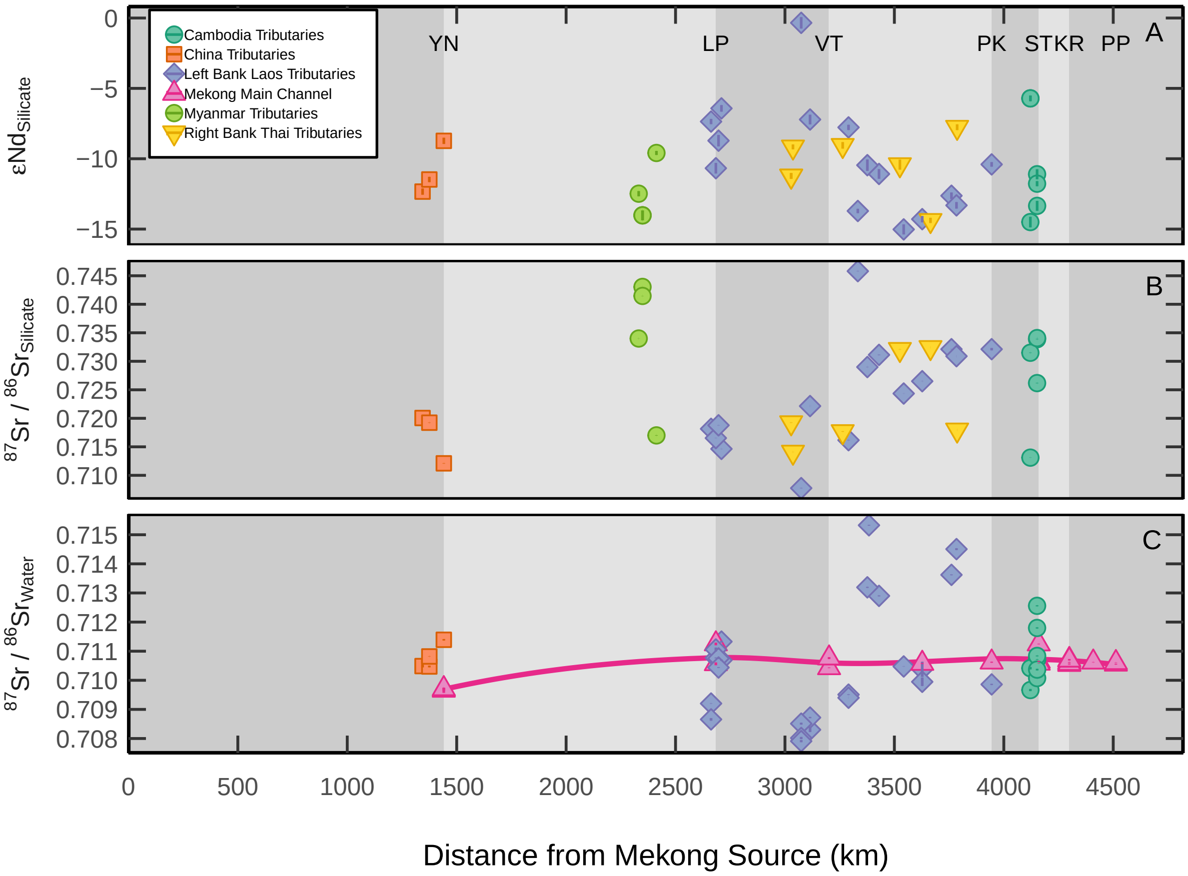

Figure 4.4: ε_{Nd} (A) and ^{87}Sr/^{86}Sr (B) isotope values in the silicate fraction of river bank sediment and ^{87}Sr/^{86}Sr (C) values of dissolved load. The dissolved ^{87}Sr/^{86}Sr data will be discussed in Section 4.3.2. 1σ errors are smaller than symbols. No isotope data is presented for the main stem silicate fraction. Tributaries are divided into groups as detailed in section 4.2, and the main stem samples are joined by a pink line.

(Figure 4.4a). There is no distinct grouping of samples collected from similar geographic sections of the Mekong, demonstrating the complex and mixed geology in the whole Mekong basin. ^{87}Sr/^{86}Sr values in the same silicate fractions of Mekong tributaries vary from 0.707753 to 0.745808 (Table 4.1). The low ^{87}Sr/^{86}Sr and ε_{Nd} values indicate a presence of basalt which has a signature of ^{87}Sr/^{86}Sr 0.702 to 0.707 and ε_{Nd} 3–12 (Allègre, 2008; Lacan *et al.*, 2012). There is a general increase in ^{87}Sr/^{86}Sr ratios downstream with some high anomolies (Figure 4.4b). The highest, or most radiogenic ^{87}Sr/^{86}Sr values are found in one Laotian tributary, the Nam Mang (0.745808), which drains Late Palaeozoic granites and also in the Myanmar tributaries (0.717000–0.743043) which drain the Lancang Batholith (Noh *et al.*, 2009, and Figure 1.2). The two lowest ^{87}Sr/^{86}Sr ratios measured in Mekong tributaries are in Cambodia; the Tonle Srepok (0.713103) which drains mostly Pliocene to Quaternary basalts and Triassic-Jurassic Marine units, and northern Laos, the Nam Xong (0.707753) drains Cretaceous Intermediate-Basic extrusive units (Figure 1.2).

^{87}Sr/^{86}Sr and ^{143}Nd/^{144}Nd isotopes correlate in detrital fractions of tributary sediments (Figure 4.5). The range in ^{87}Sr/^{86}Sr and ε_{Nd} values suggest multiple silicate lithologies and the large range in ε_{Nd} values indicate a range of ages in the silicate minerals (e.g. Cameron & Hattori, 1997). The geology of the Mekong river basin is complex (Figure 1.2) and each tributary drains multiple lithologies. Data from mono-lithological catchments would cluster into distinct groups, however the Mekong tributary data is on a mixing line suggesting a mixture between many different rock types. This is especially important for Sr because it means that identifying one single Sr isotope end-member for silicate rocks is impossible at the scale of the basin.

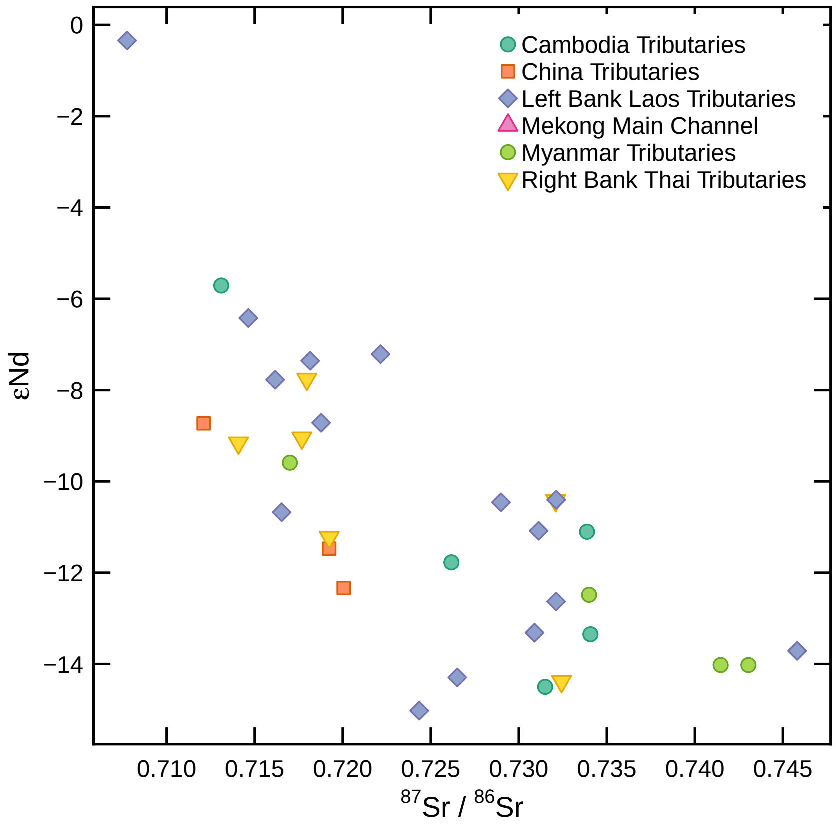

Figure 4.5: ^{87}Sr/^{86}Sr and ε_{Nd} in Mekong tributary detrital sediment. There is a large spread in isotopic values highlighting the range in silicate lithologies of varying ages in the Mekong river basin. Errors are smaller than symbols.

4.3.2 Chemistry of the Mekong River Dissolved Load

The data for major elements, Sr and radiogenic strontium isotopes in the river waters are given in Table 4.2 for the main stem and Table 4.3 for the tributaries.

River water pH decreases downstream (8.77 to 7.03) from mildly alkaline in the Upper

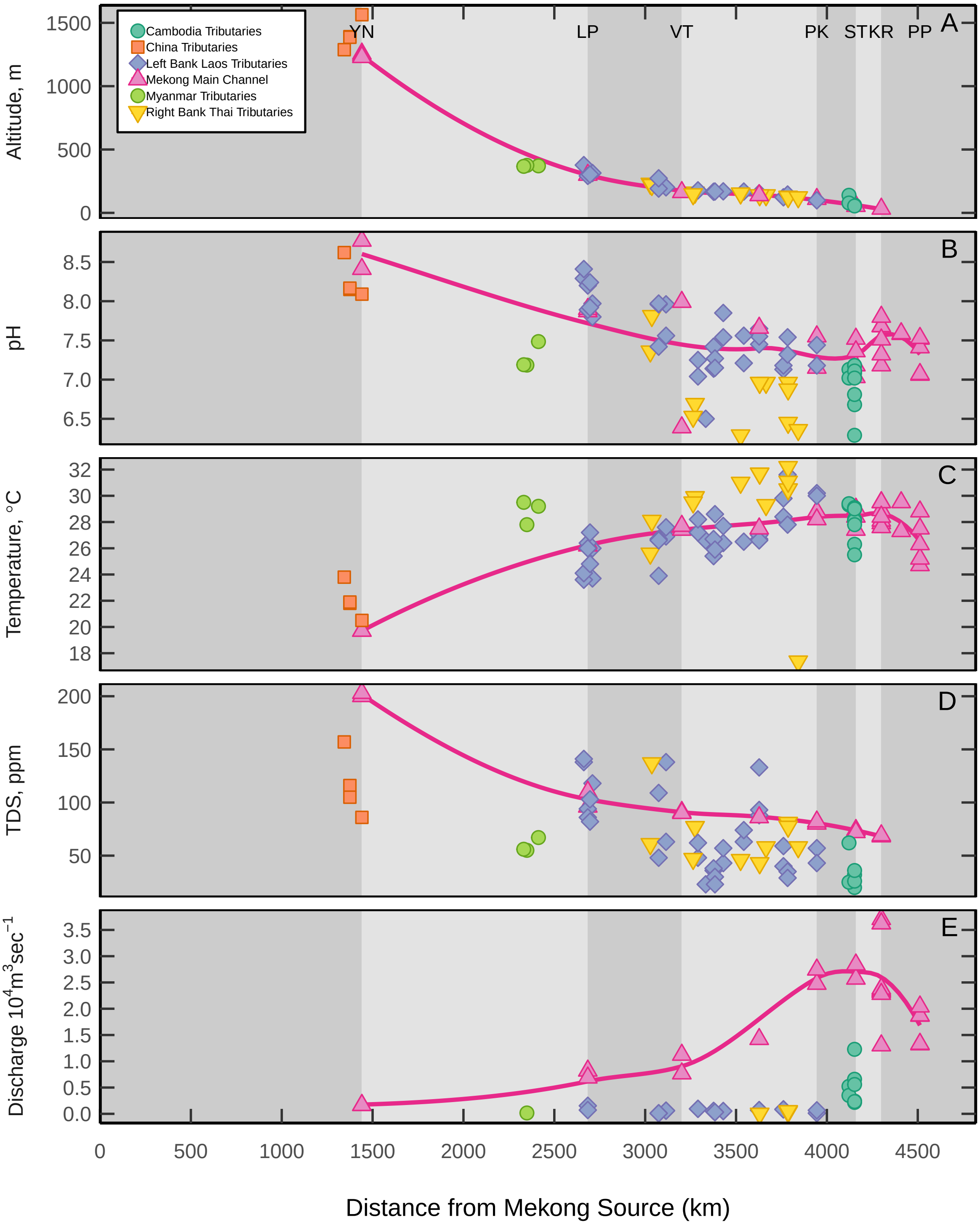

Figure 4.6: Basic characteristics in the Mekong river and it's tributaries downstream. A: Altitude drops rapidly between the source and 2500m downstream. B: Downstream pH becomes circumneutral from slightly alkaline in the Upper Mekong. C: Temperature increases downstream due to the climate changing from cold in the Upper Mekong to monsoonal in the Lower Mekong (Peel *et al.*, 2007). D: Total Dissolved Solids (TDS) decreases downstream due to continual dilution from increasing discharge downstream. E: Discharge data is from aDcp measurements, Mekong River Commission (2016), Someth *et al.* (2013) and Nippon Koei (2001), and is not available for all samples. Tributaries are divided into groups between Yunnan (YN), Luang Prabang (LP), Vientiane (V), Pakse (PK), Stung Treng (ST), Kratie (KR) and Phnom Penh (PP), as detailed in Section 4.2 and the main stem samples are joined by a pink line.

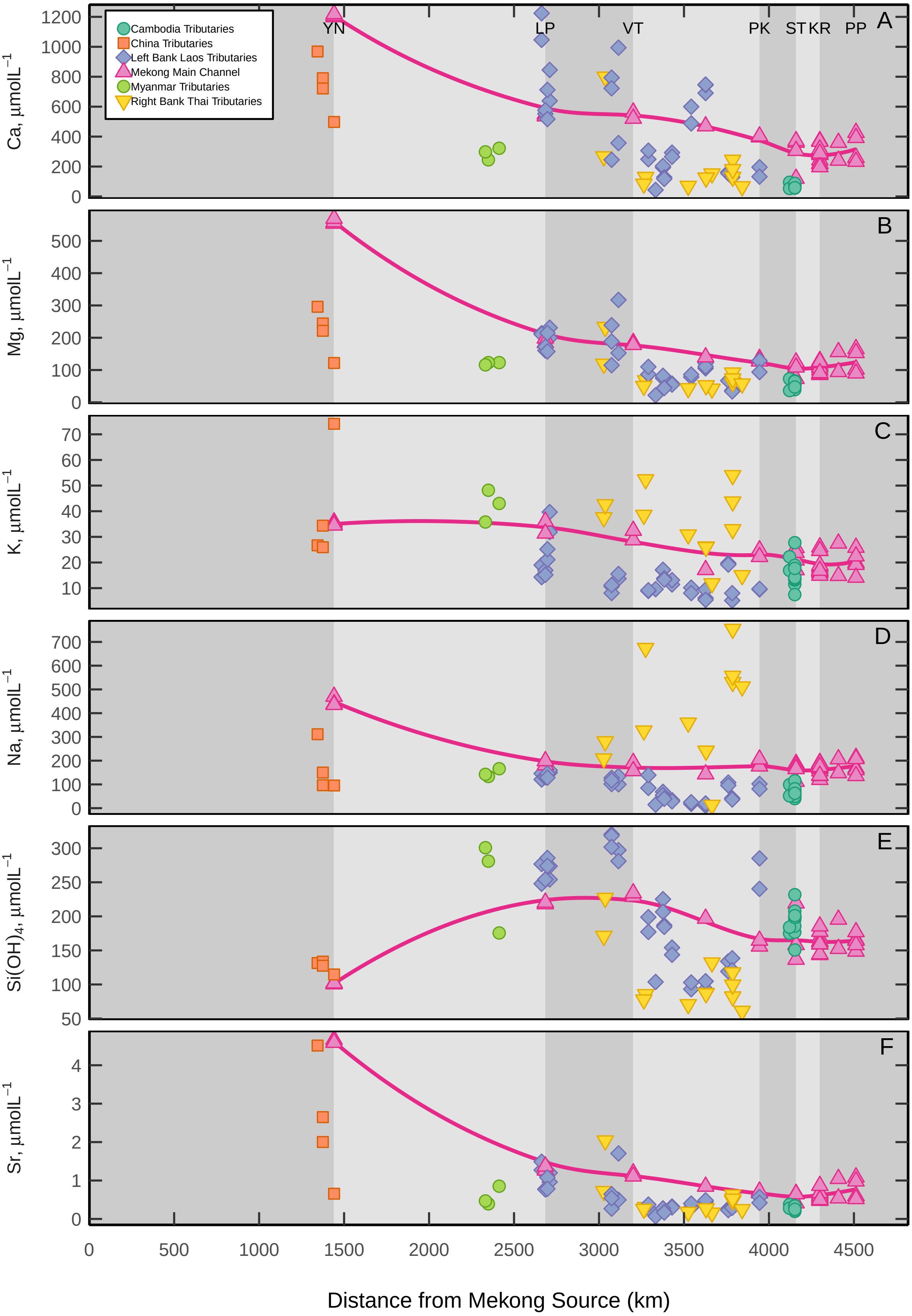

Figure 4.7 *(Caption over page)*

Mekong to circum-neutral in the Lower Mekong. There are some tributaries that are mildly acidic, down to pH 6.29, from the Middle Mekong draining the Thai right bank and also Cambodian tributaries in the Lower Mekong. Water temperatures vary from 17.4 °C to 32.2 °C and correlate with altitude of the basin. Altitude decreases from river source to mouth concurrently with the climate changing along the vast length of the Mekong, from cold in the source region through temperate with warm summers to hot summers in southern China to tropical savannah in the middle Mekong to tropical monsoon in the Middle to Lower Mekong (Peel *et al.*, 2007), these climatic changes are reflected in the river water temperature which increases downstream.

Total dissolved solids (TDS) range from 68mg/L to 203mg/L in the main stem, decreasing downstream due to dilution from increasing discharge. TDS in the Upper Mekong at Baoshan (203mg/L) is similar to previously published values by (Noh *et al.*, 2009). The Mekong TDS decreases by half to 110mg/L between the river exiting China to Luang Prabang, 1243km downstream. Tributary TDS vary from 20mg/L to 157mg/L. The tributaries with the highest TDS mostly drain the left bank, entering the Mekong main channel between Luang Prabang and Pakse. The tributaries with the most dilute TDS drain the left bank in Laos and Cambodia and enter the main stem between Vientiane and Phnom Penh.

Major element concentrations are spatially heterogeneous. The downstream chemical profile of the Mekong river and it's tributaries varies for each element (Figure 4.7 and Figure 4.8). Concentrations of major cations Ca^{2+}, Mg^{2+}, Na^{+}, K^{+} vary by 2 orders of magnitude. Ca^{2+} and Mg^{2+} follow the same trend; the highest concentrations are sampled in the Upper Mekong then concentrations decrease downstream. Ca^{2+} concentrations in the Upper Mekong are 1223μmol/L which decrease to 182μmol/L at the mouth of the Mekong. Similarly Mg^{2+} decreases from 570 to 72μmol/L downstream. However the tributary characteristics vary between Ca^{2+} and Mg^{2+}, more left bank tributaries have a higher Ca^{2+} concentration than the main stem whereas most tributaries are more dilute in Mg^{2+} than the main stem. Tributaries in Cambodia that enter the Mekong close to the mouth both show lower concentrations in Ca^{2+} and Mg^{2+} compared to the main stem at

Figure 4.7 *(previous page)*: Downstream cation concentrations in the Mekong river and it's tributaries. Concentrations of major cations Ca^{2+} (A), Mg^{2+} (B), K^{+} (C), Na^{+} (D) and $Si(OH)_4$ (E) and Sr (F) in the Mekong main stem evolve downstream due to input from spatially heterogenous tributaries and a dilution effect. These values are rain corrected. Tributaries are divided into groups between Yunnan (YN), Luang Prabang (LP), Vientiane (V), Pakse (PK), Stung Treng (ST), Kratie (KR) and Phnom Penh (PP), as detailed in section 4.2 and the main stem samples are joined by a pink line.

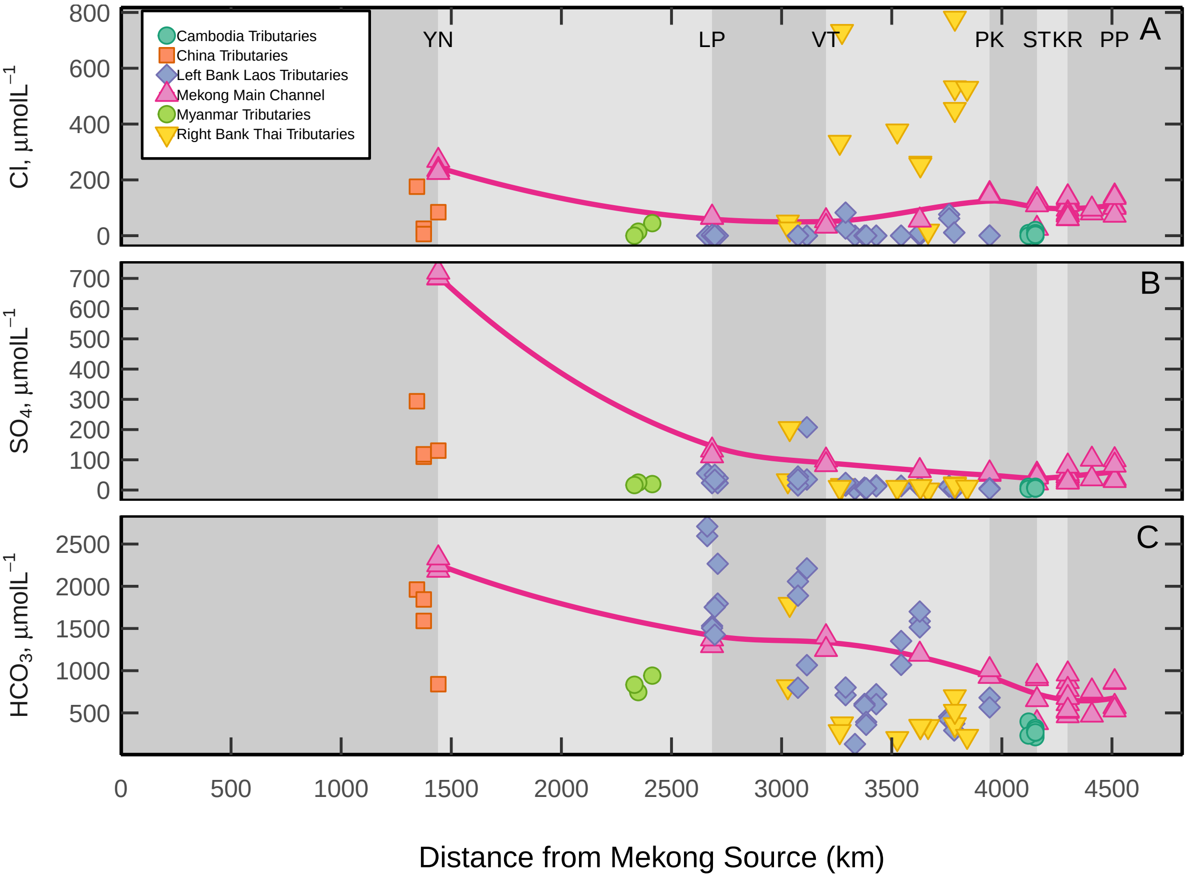

Figure 4.8: Downstream anion concentrations in the Mekong river and it's tributaries. Concentrations of anions Cl^- (A), SO_4^{2-} (B) and HCO_3^- (C) in the Mekong main stem evolve downstream due to input from spatially heterogenous tributaries and a dilution effect. HCO_3^- is calculated via Gran Titration in the field for most samples and all values are rain corrected. Tributaries are divided into groups between Yunnan (YN), Luang Prabang (LP), Vientiane (V), Pakse (PK), Stung Treng (ST), Kratie (KR) and Phnom Penh (PP), as detailed in section 4.2 and the main stem samples are joined by a pink line.

Stung Treng. In the main stem, Ca^{2+} and Mg^{2+} concentrations decrease by half between Yunnan and Luang Prabang, then there is a slower decline in concentration throughout the Middle and Lower Mekong with a mean value of 342μmol/L and 126μmol/L for Ca^{2+} and Mg^{2+}, respectively. K^+ and Na^+ show much smaller decrease in concentration downstream however there is a large variation in concentrations of the tributaries. K^+ has a significantly lower concentration than all other major elements with a range of 12-37μmol/L in the main stem and 3-75μmol/L in the tributaries. Tributaries draining the right bank of the Middle Mekong, on the Khorat Plateau along with tributaries in Yunnan, eastern Myanmar and Cambodia have the highest K^+ concentrations. The tributaries sampled on the right bank of the Mekong in Thailand also have very high Na^+ concentrations, the highest in the Mekong basin. Na^+ concentrations range 100-487μmol/L in the main stem and the tributaries vary between 9-771μmol/L. The tributaries in the Middle Mekong draining the right bank have a distinct character with high K^+ and Na^+ values and low Ca^{2+}, Mg^{2+} and $Si(OH)_4$ concentrations.

Dissolved $^{87}Sr/^{86}Sr$ values have a smaller range than the $^{87}Sr/^{86}Sr$ values in the solid silicate fraction (Figure 4.4c). There is very little variation in the main stem river water, which becomes slightly more radiogenic downstream, $^{87}Sr/^{86}Sr$ increases from 0.709654 to 0.711248. More variation is found in the tributary $^{87}Sr/^{86}Sr$ values which range from 0.707909 to 0.715325 and the tributaries that are more radiogenic than the main stem are found in the Upper Mekong, Middle Mekong between Vientiane and Pakse on the left bank and in the Cambodia tributaries in the Lower Mekong.

4.3.2.1 Rain Correction

The atmosphere provides a source of solutes to river water (Drever, 1997) which could be significant in the monsoon dominated Mekong basin in particular, because some of the river waters are dilute. Therefore the solute contribution from rainfall must be calculated and river water chemical composition corrected, before quantifying chemical fluxes derived from rock weathering. Five rain samples were collected in the Mekong Basin from the Upper Mekong in China, the Middle Mekong in Laos and Thailand and two samples from the Lower Mekong in Cambodia (Table 4.4). Due to the high Ca and Si concentrations in MEK17-144, the purity of this rain sample is questioned. The sampling location for this sample was close to a road and so dust may be causing the higher concentrations. For this reason, this sample is not used in the rain correction. Two samples were collected at Stung Treng at the beginning and end of a rain episode. There is between 15% to 30% difference in concentrations so the samples are averaged before being applied in the rain correction.

River water chemistry is corrected for rain inputs using chloride concentrations, Cl^- and cation, X, to Cl^- ratios in rainwater samples, following Galy & France-Lanord (1999). All major cations are corrected using the following two equations where X^* is the corrected concentration, X_{river} is the measured element in the river, Cl_{river} is the measured Cl^- in the river and X_{rain} is the concentration of any element in the rain.

Cl^- in the river is assumed to be a conservative tracer of rain, however the presence of evaporites in the Mekong basin increases river water Cl^- concentration. Cl^- in the rain is therefore used to calculate a corrected Cl^-, Cl^*_{river} Equation 4.2. Five rain samples were collected in the Mekong Basin where Cl_{rain} concentration ranges from $4.2\mu mol/L$ to $36\mu mol/L$. In cases where

Table 4.2: Dissolved major cations and anions and $^{87}Sr/^{86}Sr$ isotope data for Mekong main channel rivers, sampled repeatedly in 2014, 2016 and 2017. CB = Charge Balance, SE= Standard External Error. Asterisk denotes rain corrected data.

Sample	Date	Location	Latitude	Longitude	T	pH	Distance from source	Discharge	Ca^*	K^*	Mg^*	Na^*	$Si(OH)_4$	Sr	Cl^{-*}	SO_4^{2-*}	HCO_3^{-*}	CB	$^{87}Sr/^{86}Sr$	SE
							m^3	m^3sec^{-1}	μmol/L									%		ppm
Main Channel																				
CAMB140620-01	2014-06-20	Stung Treng	13.41142	105.93682	28.4	7.36	4159.5	0	116	21	73	100	219	0.41	14	22	393	8	0.711246	10
CAMB140621-10	2014-06-21	Kratie	12.57906	106.02214	29.5	7.32	4299.3	13004	284	22	125	163	177	0.86	62	78	679	7		0
CAMB140622-13	2014-06-22	Kampong Cham	11.99766	105.47427	29.5	7.59	4408.8	0	356	25	156	195	195	1.04	83	100	753	10		0
CAMB140627-22	2014-06-27	Phnom Penh	11.60189	104.93286	28.8	7.06	4512.1	13196	423	23	165	201	158	1.08	130	99	851	10		0
CAMB140718-66	2014-07-18	Phnom Penh	11.60189	104.93286	25.2	7.41	4512.1	18699	256	17	102	149	164	0.60	89	37	578	10	0.710551	14
CAMB140719-69	2014-07-19	Kratie	12.25240	105.79440	28.4	7.51	4299.3	22805	193	14	91	126	185	0.49	50	25	534	8		0
CAMB140720-87	2014-07-20	Kratie	12.26716	105.79840	28.1	7.68	4299.3	23194	312	17	122	177	145	0.67	126	53	534	17	0.710575	9
CAMB140720-88	2014-07-20	Kratie	12.25799	105.79892	28.1	7.68	4299.3	23194	239	14	99	144	162	0.55	83	37			0.710622	7
CAMB140721-100	2014-07-21	Kratie	12.26081	105.99789	27.9	7.68	4299.3	23466	214	14	89	126	163	0.51	64	31	472	13	0.710607	7
CAMB140721-101	2014-07-21	Kratie	12.26469	105.99548	27.9	7.68	4299.3	23466	287	15	113	155	143	0.62	108	47			0.710541	9
CAMB140722-108	2014-07-22	Kratie	12.47990	106.01453	27.6	7.8	4299.3	23811	213	12	88	125	159	0.50	69	31	522	8	0.710688	7
CAMB140722-114	2014-07-22	Kratie	12.46490	106.01490	27.6	7.8	4299.3	23811	274	14	108	158	144	0.59	99	45	610	9		0
CAMB140723-140	2014-07-23	Stung Treng	13.57912	105.99351	27.4	7.03	4159.5	0	302	15	108	154	136	0.65	98	42	655	10	0.710583	8
CAMB140725-161	2014-07-25	Phnom Penh	11.77886	105.01689	26.3	7.53	4512.1	20404	229	12	90	124	148	0.52	61	30	538	10	0.710605	7
MEK16-007	2016-09-11	Vientiane	17.96318	102.57250	27.4	6.39	3201.6	7666	566	29	185	208	229	1.20	77	101	1414	2	0.710428	7
MEK16-033	2016-09-13	Luang Prabang	20.05657	102.20424	26.4	7.9	2684.2	6881	540	32	185	216	221	1.37	90	115	1388	0	0.710565	8
MEK16-073	2016-09-16	Thakhek	17.39547	104.80124	27.5	7.66	3627.4	14213	466	15	140	132	197	0.84	43	63	1219	0	0.710578	8
MEK16-096	2016-09-18	Pakse	15.11918	105.77769	28.2	7.55	3944.4	27430	399	20	127	194	164	0.71	132	55	1037	1	0.710621	18
MEK16-106	2016-09-19	Stung Treng	13.54414	105.96294	29	7.52	4159.5	25704	356	18	114	176	158	0.65	117	47	930	1	0.710651	20
MEK16-137	2016-09-22	Kratie	12.46879	106.02033	29.5	7.68	4299.3	37049	216	16	85	108	163	0.47	48	25	635	2	0.710709	7
MEK17-002	2017-02-03	Kratie	12.71852	105.98771			4299.3	3010	551	25	238	249	167	1.36	203	143			0.710733	8
MEK17-003	2017-02-04	Stung Treng	13.52036	105.93351			4159.5	0	604	32	265	284	175	1.49	262	150			0.710606	7
MEK17-107	2017-09-12	Baoshan	25.43179	99.34164	19.7	8.41	1441	1656	1203	36	555	487	101	4.67	294	703	2201	2	0.709654	86
MEK17-112	2017-09-14	Yunnan	25.56539	99.35099			1441	0	1223	35	570	452	102	4.59	250	722	2348	1	0.709707	21
MEK17-114	2017-09-14	Baoshan	25.42880	99.34175	19.7	8.77	1441	1656	1212	35	559	455	103	4.60	261	704	2267	1	0.709695	54
MEK17-135	2017-09-17	Luang Prabang	20.05551	102.20493	26.2	7.87	2684.2	8204	553	37	199	198	218	1.27	89	134	1309	3	0.711248	46
MEK17-157	2017-09-19	Vientiane	17.96290	102.57471	27.7	7.99	3201.6	11216	524	33	179	174	234	1.11	58	85	1263	4	0.710762	34
MEK17-189	2017-09-22	Pakse	15.11795	105.77606	28.8	7.15	3944.4	24722	392	22	135	165	156	0.67	138	50	958	3		
MEK17-195	2017-09-23	Stung Treng	13.54414	105.96165	29	7.18	4159.5	28395	367	23	124	165	158	0.66	114	51	959	1		
MEK17-213	2017-09-25	Kratie	12.45853	106.01926	28.9	7.18	4299.3	36218	368	24	128	180	168	0.68	121	45	896	5		
MEK17-225	2017-09-25	Kratie	12.47850	106.01113	28.9	7.18	4299.3	36218	362	22	125	174	159	0.67	126	46				

Table 4.3 *(continues on next page)*: Dissolved major cations and anions and ^{87}Sr/^{86}Sr isotope data for Mekong tributary rivers, sampled repeatedly in 2014, 2016 and 2017. D/S = Downstream, U/S= Upstream, CB = Charge Balance, SE= Standard Error, Asterisk denotes rain corrected data.

Sample	Date	Location	Latitude	Longitude	T	pH	Distance from source	Discharge	Ca*	K*	Mg*	Na*	Si(OH)$_4$	Sr	Cl^{-*}	SO$_4^{2-*}$	HCO$_3^{-*}$	CB	^{87}Sr/^{86}Sr	SE
							km	m^{3}sec^{-1}	μmol/L									%		ppm
Tributaries																				
MEK17-250	2017-10-05	Bang Sai	16.64196	104.70036	29.3	6.96	3665	-	156	12	42	30	132	0.16	41	2	354	6		
MEK17-115	2017-09-14	Bijiang	25.61971	99.35675	23.8	8.62	1344.1	-	972	27	297	328	132	4.52	200	296	1975	3	0.710488	46
MEK17-256	2017-10-06	Chi	15.2655	104.6444	32.2	6.96	3786.5	340	248	55	93	547	118	0.64	477	23	706	3		
MEK17-123	2017-09-15	Heihui	25.5138	99.99306	21.8	8.15	1375	-	793	27	245	167	134	2.65	49	112	1857	3	0.710474	30
MEK17-236	2017-10-04	Hueang	17.73047	101.48663	25.6	7.36	3028.3	-	270	38	120	225	171	0.72	74	33	825	5		
MEK17-247	2017-10-05	Kam	16.95821	104.62198	31.7	6.96	3630	37	129	27	53	258	88	0.28	284	14				
MEK17-248	2017-10-05	Kam	16.95821	104.62198	31.7	6.96	3630	37	128	27	53	258	87	0.28	279	14				
MEK17-240	2017-10-04	Loei	17.80348	101.62645	28.1	7.8125	3036.6	-	802	43	234	298	227	2.04	49	206	1801	4		
MEK17-252	2017-10-05	Luang	17.99485	103.06357	29.9	6.69	3274.3	-	133	53	68	691	86	0.31	757	18	385	-1		
MEK17-233	2017-10-03	Mae Ing	20.13746	100.42019	29.2	7.485	2412.7	-	325	44	124	183	176	0.86	69	22	955	3		
MEK17-230	2017-10-02	Mae Kok	20.22765	100.1288	27.8	7.185	2349.1	161	248	49	124	150	281	0.40	39	27	760	6		
MEK17-226	2017-10-02	Mae Ruak	20.38762	100.06233	29.5	7.19	2331.7	-	297	32	116	147	301	0.47	7	16	841	7		
MEK17-254	2017-10-06	Mun D/S	15.24337	104.95473	31.08	6.875	3786.7	531	185	44	74	574	100	0.53	555	20	533	1		
MEK17-257	2017-10-06	Mun U/S	15.14259	104.58293	30.5	6.45	3786.7	531	133	34	63	771	83	0.48	804	19	376	0		
MEK16-053	2016-09-15	Nam Hinboun	17.72652	104.56755	26.5	7.56	3542.6	-	597	3	86	24	103	0.40	0	14	1355	1	0.710476	4
MEK17-169	2017-09-20	Nam Hinboun	17.72653	104.57569		7.21	3542.6	-	485	5	78	17	93	0.30	0	12	1073	3		
MEK16-051	2016-09-15	Nam Kading	18.32405	103.99742	26.4	7.85	3429.7	524	290	6	58	33	154	0.32	0	15	725	0	0.712900	16
MEK17-166	2017-09-20	Nam Kading	18.32444	103.99692	27.7	7.54	3429.7	524	263	8	55	28	143	0.30	0	12	608	4		
MEK16-012	2016-09-12	Nam Khan	19.7655	102.18206	23.7	7.97	2709.8	-	638	36	200	155	254	0.96	9	23	1802	1	0.711329	34
MEK17-141	2017-09-18	Nam Khan	19.76557	102.18179	7.8	26	2709.8	-	842	26	231	158	273	1.20	0	38	2271	0	0.710691	24
MEK16-041	2016-09-14	Nam Lik	18.63746	102.32649	26.9	7.56	3114.7	600	355	11	153	100	297	0.49	0	34	1068	0	0.708302	79
MEK17-146	2017-09-18	Nam Lik	19.21614	102.24476	27.6	7.96	3114.7	600	992	12	317	134	281	1.70	0	207	2214	3	0.708720	23
MEK17-160	2017-09-20	Nam Mang	18.37041	103.19867	26.6	6.5	3333	-	42	6	22	14	104	0.07	0	3	133	6		
MEK16-035	2016-09-14	Nam Ming	19.64294	102.19558	23.6	8.29	2662.3	-	1044	15	214	145	277	1.27	0	56	2598	0	0.709202	7
MEK17-143	2017-09-18	Nam Ming	19.64302	102.19557	24.1	8.41	2662.3	-	1222	10	211	120	248	1.49	0	54	2712	3	0.708657	45
MEK16-047	2016-09-15	Nam Ngiap	18.41749	103.60258	25.4	7.42	3376.5	544	191	13	75	68	225	0.27	0	7	609	0	0.713193	18
MEK17-164	2017-09-20	Nam Ngiap	18.41743	103.60261	26.7	7.14	3376.5	544	201	12	82	54	206	0.27	1	7	592	3		
MEK16-045	2016-09-15	Nam Ngjum	18.17997	103.05611	27.2	7.25	3290.5	950	252	10	88	102	177	0.29	50	17	724	0	0.709508	11
MEK17-158	2017-09-20	Nam Ngjum	18.17999	103.03612	28.2	7.04	3290.5	950	310	10	111	156	199	0.38	107	25	814	2	0.709400	0
MEK16-025	2016-09-13	Nam Ou	20.13944	102.31554	26.4	7.89	2684.2	1531	555	18	161	149	255	0.78	25	25	1543	0	0.710769	14
MEK17-127	2017-09-17	Nam Ou	20.11485	102.29245	26	8.2	2684.2	713	579	16	173	147	254	0.77	27	25	1519	3	0.711058	68
MEK16-050	2016-09-15	Nam Xan	18.39497	103.65372	25.9	7.15	3383.9	317	115	9	44	39	184	0.16	0	5	362	1	0.715325	
MEK17-165	2017-09-20	Nam Xan	18.395	103.6539	28.6	7.27	3383.9	317	126	8	45	40	187	0.17	0	4				
MEK16-015	2016-09-12	Nam Xeng	19.97917	102.24716	24.8	7.92	2696.4	-	515	21	157	128	274	0.78	0	33	1430	0	0.710439	
MEK17-137	2017-09-17	Nam Xeng	19.97778	102.24627	27.2	8.24	2696.4	-	710	17	214	145	285	1.07	0	49	1756	4	0.710751	

Table 4.3 *(continued)*: Dissolved major cations and anions and $^{87}Sr/^{86}Sr$ isotope data for Mekong tributary rivers, sampled repeatedly in 2014, 2016 and 2017. D/S = Downstream, U/S= Upstream, CB = Charge Balance, SE= Standard Error, Asterisk denotes rain corrected data.

Sample	Date	Location	Latitude	Longitude	T	pH	Distance from source	Discharge	Ca*	K*	Mg*	Na*	Si(OH)$_4$	Sr	Cl^{-*}	SO$_4^{2-*}$	HCO$_3^{-*}$	CB	$^{87}Sr/^{86}Sr$	SE
							km	m^{3}sec^{-1}	μmol/L									%		ppm
Tributaries																				
MEK16-009	2016-09-12	Nam Xong	19.07737	102.42953	23.9	7.97	3074.2	100	721	9	188	117	302	0.54	0	34	1891	0	0.707909	
MEK16-039	2016-09-14	Nam Xong	19.64294	102.19558	26.7	7.42	3074.2	100	244	9	115	101	320	0.27	0	15	800	0	0.708510	
MEK17-149	2017-09-18	Nam Xong	18.95512	102.43941	26.6	7.96	3074.2	100	792	5	239	127	318	0.64	0	44	2059	1	0.708017	
MEK17-242	2017-10-05	Pak Suai	17.97515	103.00139	29.5	6.53	3263.8	-	87	39	51	343	78	0.26	359	11				
MEK17-253	2017-10-06	Se Bok	15.31457	105.10700	17.4	6.36	3842.3	-	70	16	59	529	61	0.25	553	12	237	0		
MEK17-125	2017-09-15	Shunbi	25.49036	99.96952	21.9	8.17	1375	-	725	35	222	113	128	2.01	30	120	1603	5	0.710819	
MEK17-245	2017-10-05	Songkhram	17.61094	104.39594	31	6.29	3525.1	-	73	31	44	376	71	0.18	400	11	211	2		
CAMB140626-19	2014-06-26	Tonle Bassac	12.27914	104.95606	29.1	7.03	4563.3	-	407	24	165	187	165	1.07	118	101	857	8		
MEK17-001	2017-02-01	Tonle Bassac	11.54831	104.96406			4563.3	-	402	29	183	214	167	1.00	153	88			0.710434	
CAMB140620-07	2014-06-20	Tonle Kong	13.61091	106.09392	29	6.81	4152.1	2169	72	14	52	66	208	0.22	0	9	335	0	0.712558	
CAMB140723-122	2014-07-23	Tonle Kong	13.55882	106.03843	25.5	6.29	4152.1	6579	57	11	39	41	177	0.20	0	5	226	5		
MEK16-119	2016-09-20	Tonle Kong	13.55890	106.04160	28.2	7.08	4152.1	12276	67	16	47	55	195	0.23	0	6	291	2	0.711798	
MEK17-004	2017-02-04	Tonle Kong	13.56480	106.05981			4152.1	525	97	16	79	76	208	0.32	6	7			0.709172	
MEK17-207	2017-09-24	Tonle Kong	13.55923	106.03939	28.1	7.18	4152.1	2423	68	16	53	49	186	0.21	0	5	285	4		
MEK16-128	2016-09-21	Tonle San	13.61396	106.37408	29.4	7.02	4121.3	3497	55	26	37	52	184	0.28	0	5	258	2	0.710416	
MEK17-006	2017-02-05	Tonle San	13.60104	106.33011			4121.3	322	54	26	46	72	228	0.24	0	3			0.718576	
CAMB140623-16	2014-06-23	Tonle Sap	12.27914	104.67165	30.2	7.4	4512.3	-	548	28	219	293	185	1.54	136	192	1079	8		
CAMB140723-130	2014-07-23	Tonle Sekong	13.54443	106.00560	26.3	6.68	4152.3	-	70	15	50	63	199	0.29	0	6	245	13	0.710717	
CAMB140620-04	2014-06-20	Tonle Srepok D/S	13.56518	106.17322	29	7.11	4152.3	-	80	25	66	104	232	0.34	8	10	308	14	0.710837	
CAMB140723-117	2014-07-23	Tonle Srepok D/S	13.54641	106.03678			4152.3	-	85	13	65	73	201	0.34	0	7	259	19	0.710076	
MEK16-112	2016-09-20	Tonle Srepok D/S	13.54740	106.03508	27.8	7.02	4152.3	5585	59	20	47	60	151	0.25	0	6	295	1	0.710367	
MEK17-005	2017-02-05	Tonle Srepok D/S	13.50748	106.33884			4152.3	-	105	25	104	167	279	0.47	69	21			0.713258	
MEK17-201	2017-09-24	Tonle Srepok D/S	13.54567	106.03927	29.1	7.18	4152.3	2335	72	17	58	68	198	0.31	0	6	295	10		
MEK16-125	2016-09-21	Tonle Srepok U/S	13.44416	106.60375	29.3	7.13	4121.5	5229	92	16	72	90	175	0.37	0	10	423	2	0.709665	
MEK16-067	2016-09-16	Xe Bangfai	18.32405	103.99742	26.7	7.65	3627.2	698	689	6	121	12	105	0.44	0	10	1613	1	0.710377	
MEK16-070	2016-09-16	Xe Bangfai	17.13552	105.06117	26.6	7.55	3627.2	698	745	5	111	11	105	0.48	0	10	1727	0	0.709949	6
MEK17-173	2017-09-21	Xe Bangfai	17.07727	104.98485	27	7.45	3627.2	698	746	12	105	9	93	0.46	0	9	1540	6		
MEK16-077	2016-09-17	Xe Banghiang	16.09830	105.37571	28.4	7.13	3760.8	845	158	17	67	96	119	0.26	64	13	482	2	0.713622	6
MEK17-176	2017-09-21	Xe Banghiang	16.09806	105.37592	29.8	7.18	3760.8	845	150	17	66	84	134	0.23	50	10	448	4		
MEK16-080	2016-09-17	Xe Bangnouan	16.00270	105.47926	27.8	7.54	3783.8	-	126	6	34	26	121	0.29	0	1	318	8	0.714506	32
MEK17-179	2017-09-21	Xe Bangnouan	16.00273	105.47928	31.6	7.32	3783.8	-	146	3	36	31	138	0.29	0	1	400	3		
MEK16-087	2016-09-18	Xe Don	15.13292	105.80825	30	7.44	3944.4	666	134	13	94	81	241	0.42	0	4	592	-3	0.709859	
MEK17-183	2017-09-22	Xe Don	15.14851	105.78077	30.2	7.18	3944.4	119	197	13	129	102	285	0.57	0	7	706	4		
MEK17-120	2017-09-15	Yinjiang	25.40018	99.54830	20.5	8.09	1441.2	-	501	75	123	112	115	0.66	108	132	854	8	0.711392	

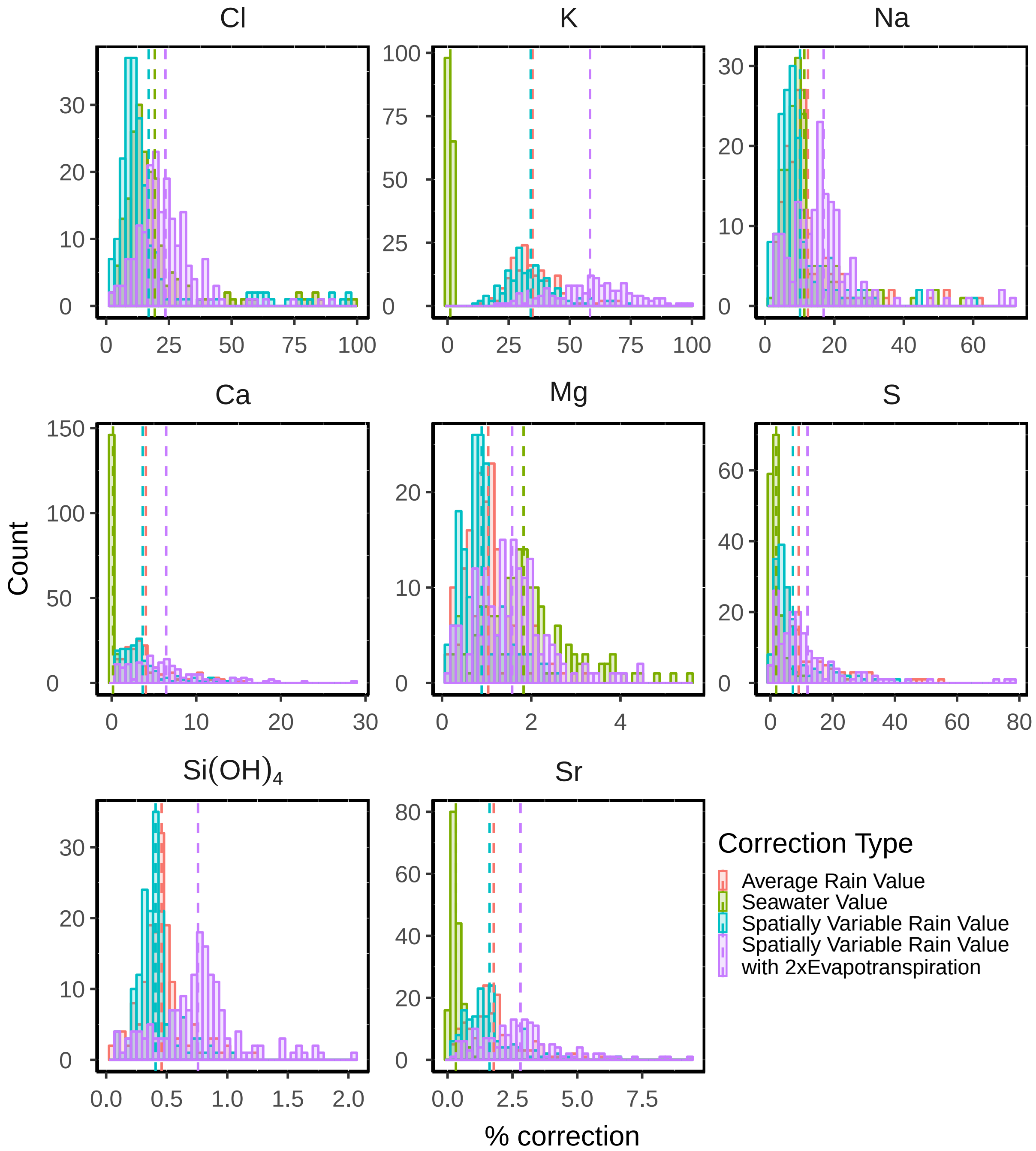

Figure 4.9: Evaluation of four different rain corrections on river water data. River water data was corrected for rain input with 4 different values for each element. The difference between the raw elemental concentration in the river and the rain corrected concentration is presented as a percentage correction in a histogram. Dashed lines are mean percent correction for each of the four corrections.

tributaries are dilute and Cl^- concentrations in the river are less than in the rain, Cl^*_{river} in Equation 4.2 which is set to 0μmol/L, assumes that all the Cl^- in the river is derived from rain. Cl^*_{river} is set to 0μmol/L for 26 samples which are mostly left bank Middle Mekong tributaries with Cl_{river} concentrations between 4.4 - 20.4μmol/L.

$$X^* = X_{river} - (Cl_{river} - Cl^*_{river}) \left(\frac{X}{Cl}\right)_{rain} \tag{4.1}$$

$$Cl^*_{river} = Cl_{river} - Cl_{rain} \tag{4.2}$$

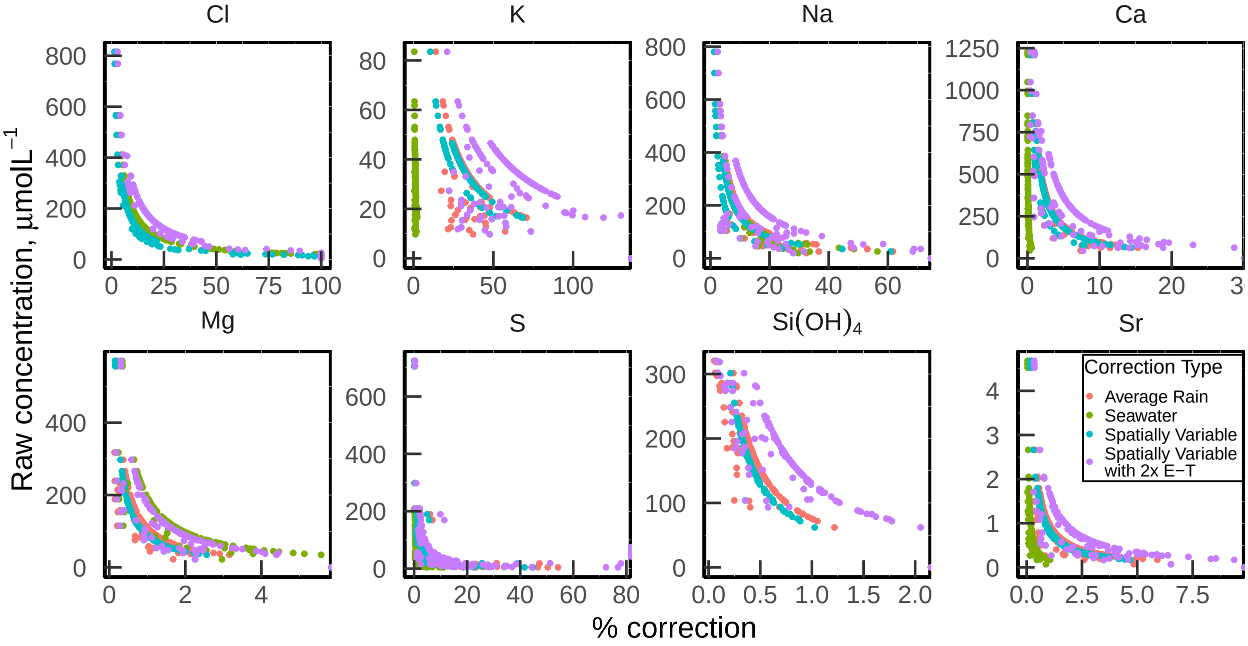

Figure 4.10: Magnitude of rain correction with varying river water concentration. For each element, the difference between the raw concentration in the river and the rain corrected concentration is presented as a percentage correction and plotted against the raw river water concentration. The colours are for each method of correction; one rain value applied across the whole basin (red), seawater value applied as a correction (green), variable rain samples applied to spatially close sub-basins (blue) and the effect of evapotranspiration (E-T), or river water concentrated by 2 times, applied to the variable rain sample correction (purple). The double curves that are seen best in Na and K for the spatially variable correction (with and without evapotranspiration taken into account) are caused by the different rain ratios applied to samples within basin. The magnitude of correction varies depending on the rain sample used. The magnitude of the rain water correction increases as river water concentration decreases.

Four different rain water corrections were evaluated to assess the sensitivity of a rain correction. First a 'cyclic salt' correction was applied using the Cl^- in rainwater and the cation/Cl^- ratio of the seawater. Secondly an average Cl^- and $\frac{X}{Cl}$ ratio of the four rainwater samples was applied to the whole basin. Finally river water corrections were made using variable Cl^- and $\frac{X}{Cl}$ ratios depending on the river water sample's proximity to the geographic location of the four rain samples. The potential effect of evapotranspiration on the river was taken into account by removing twice the concentration of the element from the river (this is done by doubling Cl_{rain} in Equation 4.2.

The magnitude of correction for each method is compared for an individual element in Figure 4.9. Mg, $Si(OH)_4$ and Sr receive less than a 10% rain correction and Ca and S are largely corrected by up to 20% irrespective of method. Cl are Na receive larger corrections, up to 100% where the samples with the largest corrections are the most dilute samples, less than 30% are samples with high Cl and Na concentrations. The correction for K varies the most of all elements between methods. Overall, samples are least corrected by the cyclic salt correction, which has been used commonly in the literature because of a lack of rain data (for example in a previous Mekong study by Li *et al.*, 2014a) The basin average and variable rainwater corrections are similar in magnitude and the largest correction is when two-times evapotranspiration is accounted for. The correction increases with decreasing concentration in the river water (Figure 4.10).

The cyclic salt correction is difficult to apply due to a combination of the prevailing wind and proximity to the Gulf of Thailand to the south and southwest and the South China sea to the east. Evapotranspiration is also difficult to quantify so the basin variable rainwater correction was chosen as most representative and applied to river water data. The spatial effects of the variable rainwater correction can be seen in the maps of each element displaying 2017 sample data (Figure 4.11). The left bank tributaries of the Mekong river receive a higher rainwater correction, particularly for Cl, K, Na. These tributaries receive the largest rainfall during the summer monsoon. The concentrated river waters in the headwaters of the Mekong receive insignificant rainwater corrections.

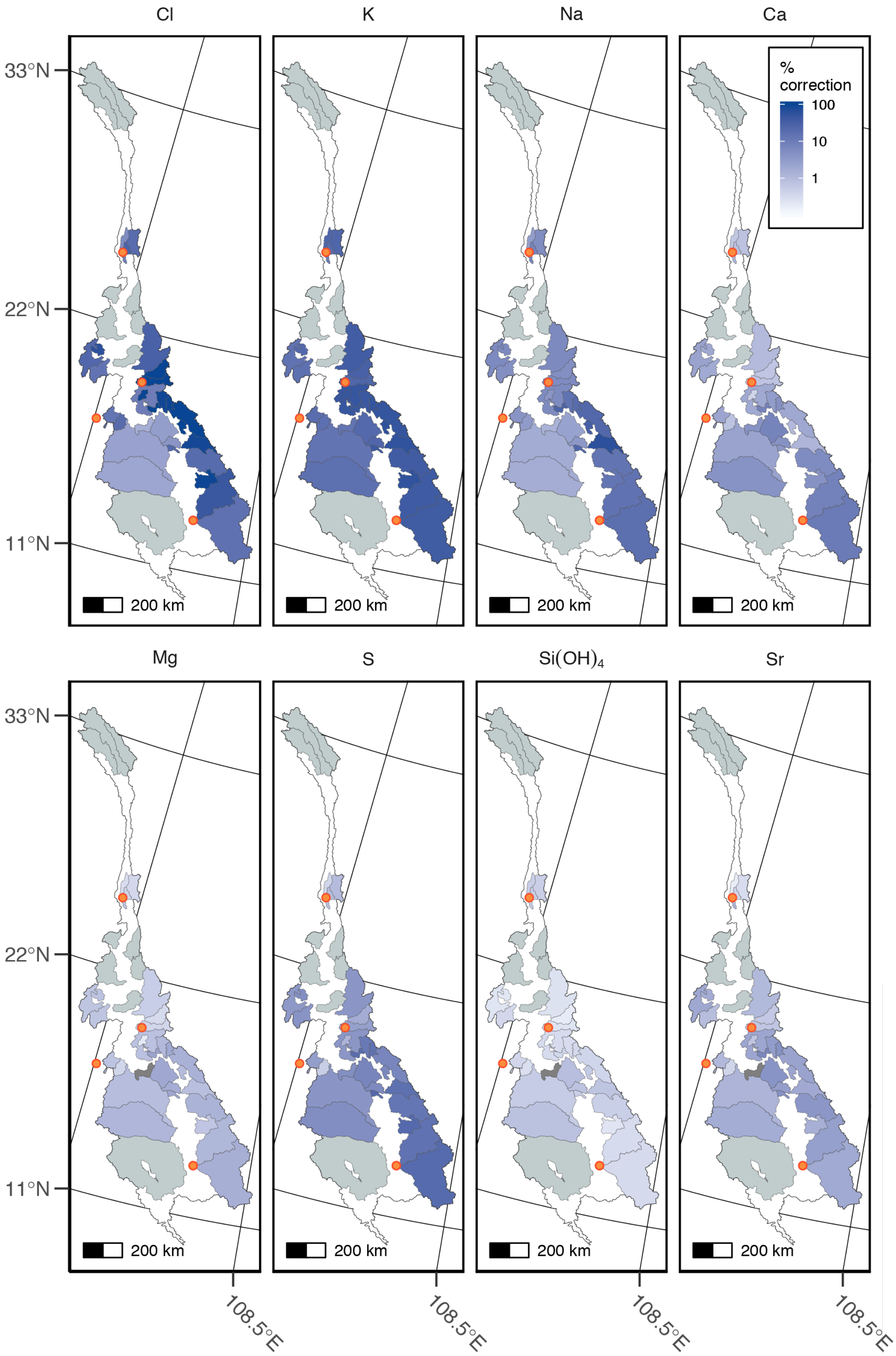

Figure 4.11: Spatial variability in magnitude of rain correction. Concentrations of each element are corrected for rain input using the composition of one of the four rain samples (orange circle) collected closest to the sub-basin. Larger basins with no chemical data are shown in grey and small basins with no data are white.

Table 4.4: Major element and Sr concentrations in rain water samples. Five rain samples were collected in 2017. Two samples were collected in Stung Treng to see if there was much difference in chemistry between the start and end of a long rain episode.

Sample	Date	Location	Rain Code	Latitude	Longitude	Ca	K	Mg	Na	$Si(OH)_4$	Cl^-	SO_4^{2-}	HCO_3^-	Sr
										μmol/L				10^3 μmol/L
MEK17-117	15/09/2017	Yongping Hotel, China	C	25.44903	99.52970						13.6	7.4		
MEK17-144	18/09/2017	Phoudam, Laos	LP	19.56533	102.23023	65.0	9.0	2.3	5.9	34.0	4.2	6.9	131.3	48.2
MEK17-197	23/09/2017	Stung Treng, Cambodia	ST	13.53110	105.97339	12.9	13.7	0.8	23.5	0.6	18.5	3.1	40.0	8.7
MEK17-198	23/09/2017	Stung Treng, Cambodia	ST	13.53110	105.97339	9.4	9.4	1.7	26.5	1.0	36.1	4.2	13.6	13.2
MEK17-235	03/10/2017	Ban Chattrakhan, N Thailand	NTH	17.27337	100.59893	6.0	8.8	0.9	9.5	0.6	11.8	2.3	15.8	8.0

4.3.2.2 Spatial Variations in Water Chemistry

Ternary diagrams are a useful tool to present dissolved major elements because river characteristics group (Edmond *et al.*, 1996) and highlight differences between tributaries of major rivers (Figure 4.12). The tributary cation data display an array between Ca^{2+} and Na^{+}+K^{+} apices (Figure 4.12a). The left bank tributaries cluster around the Ca^{2+} apex indicating carbonate weathering is the major contributor (42-85%) to cation concentrations. The tributaries on the right bank of the Mekong have a higher Na^{+}+K^{+} contribution to the cation budget than the majority of tributaries, these rivers (the Luang (MEK17-252), Mun (MEK17-254/257), Se Bok (MEK17-253), Songkhram (MEK17-245), Kam (MEK17-248) and Pak Suai (MEK17-242)) drain the Khorat Plateau in Thailand. Cambodian tributaries in the Lower Mekong have on average ~6% more Mg^{2+} and ~22% more Na^{+}+K^{+} than the Middle Mekong left bank tributaries, indicating a larger contribution from the weathering of silicate minerals.

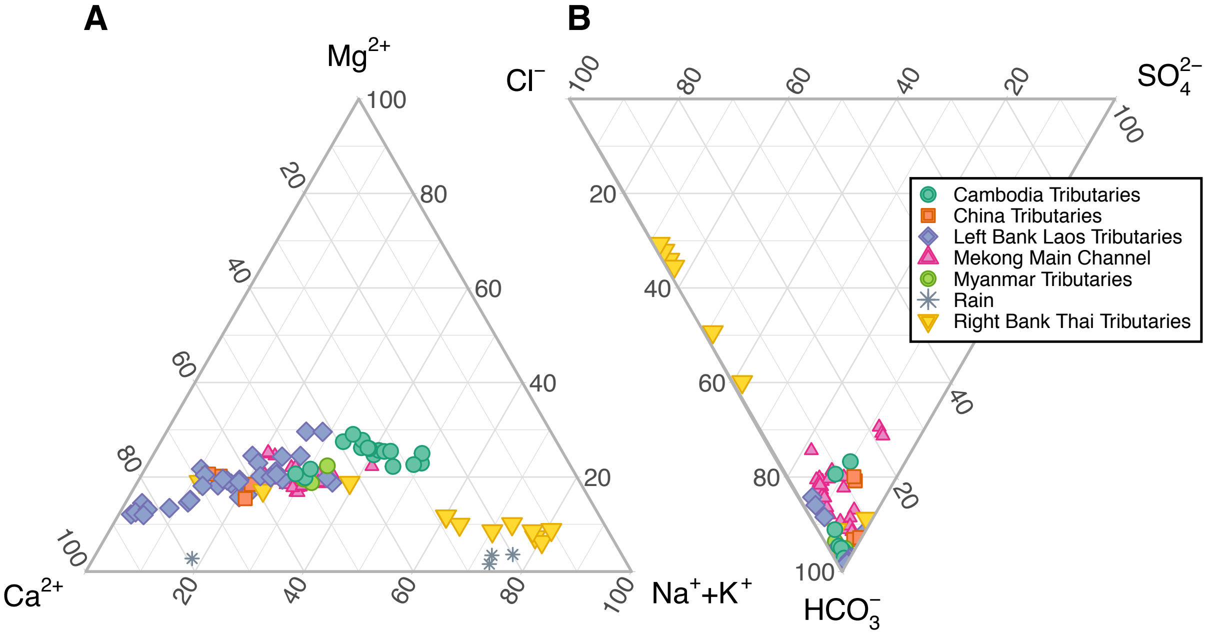

Figure 4.12: Ternary cation (A) and anion (B) diagrams for Mekong river waters. Concentrations are corrected for rain input.

From Luang Prabang downstream to Stung Treng, the tributaries draining the left bank have Cl^{-} concentrations less than 15μmol/L which is likely all from atmospheric input (Figure 4.8 and Table 4.4). Tributaries in the Upper Mekong and especially tributaries sampled on the right bank of the Middle Mekong have significantly greater concentrations of Cl^{-}, up to 815μmol/L (Figure 4.8).

The highest concentrations of HCO_3^- and SO_4^{2-} are found in the Upper Mekong. The main stem sample collected near Baoshan in Yunnan Province is up to ~6 times more concentrated than tributaries in that area, suggesting that the higher HCO_3^- and SO_4^{2-}concentrations are sourced further upstream. Two tributaries in the Middle Mekong, the Nam Lik (left bank tributary, MEK17-146) and the Loei (right bank tributary, MEK17-240) have a greater concentration of SO_4^{2-} and HCO_3^- than the main stem, ~205μmol/L.

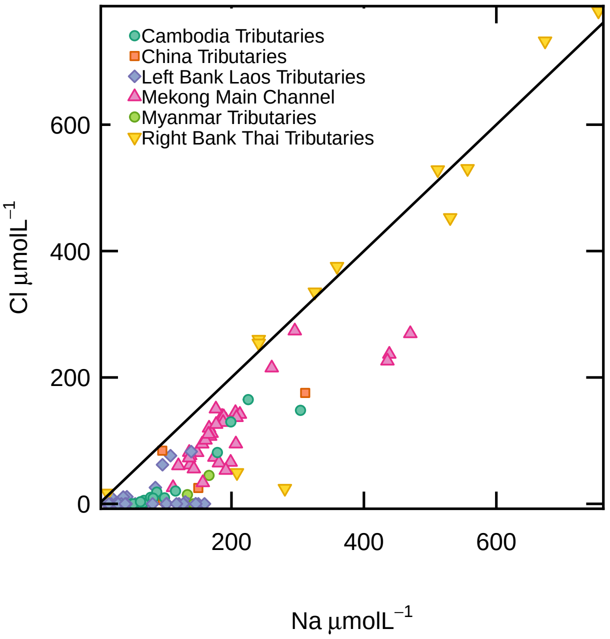

Figure 4.13: Na^+ and Cl^- concentrations in Mekong river water highlighting presence of evaporites. Samples taken on the right bank of the Mekong on the Khorat Plateau in Thailand (yellow inverted triangles) have Na^+:Cl^- ratios close to 1 (black line), indicating halite (NaCl) dissolution. The downstream main stem samples (pink triangles) lie close to the line due to the influence of the tributaries draining these evaporites upstream.

Most tributaries are dominated by HCO_3^- anions (76.7% to 99.8%). Four tributaries are significantly different with Cl^- dominating 50% to 69% of the total anions (30% to 48% HCO_3^-). These tributaries, the Luang (MEK17-252), Mun (MEK17-254/257), Se Bok (MEK17-253) and the Songkhram (MEK17-245) drain the Khorat Plateau in Thailand on the right bank of the Mekong. The Chi tributary, which is the second largest sub-basin by area on the Khorat plateau (49402km^2, only ~4% smaller than the Mun sub-basin), lies between the majority and the extreme tributaries with 58.6% HCO_3^- and 39.5% Cl^-. The mixing line drawn between the Cl^- and HCO_3^- end members indicate evaporite weathering in these basins. Specifically, one type of evaporite that these right bank tributaries weather is halite. Samples that have high Cl^- also have high concentrations of Na^+ and fall close to a Na^+ to Cl^- ratio of 1:1, found in halites (Figure 4.13). Moreover there is increased

Na^+ and K^+ in these tributaries, (Figure 4.7c,d and 4.12a). The increased Na^+ is likely due to halite or borax deposits (sodium borate evaporate minerals) and K^+ is likely due to the dissolution of potash deposits (potassium rich evaporites) found in the Khorat plateau (Hite & Japakasetr, 1979; Zhang *et al.*, 2013). The main stem samples cluster around HCO_3^- apex (Figure 4.12b), with an average of 83% HCO_3^- contributing to the total anions. The Upper Mekong samples in Yunnan province, China, are distinct from the Middle and Lower Mekong main stem samples due to their higher SO_4^{2-} concentrations, ~22% SO_4^{2-}.

4.3.2.3 Seasonal Variations in Water Chemistry

In the samples collected close to the Mouth of the Mekong river, at Chroy Changvar from 2014 to 2017, there are systematic trends in cation and anion concentrations (Figure 4.14). Elemental concentrations fluctuate by up to an order of magnitude in cations and up to 2 orders of magnitude in anions. Concentrations are diluted during the monsoon period, with Ca, Na and Mg decreasing by a factor of between 3.3-3.7 and $Si(OH)_4$ and K showing a smaller reduction of 1.7-1.9. SO_4^{2-} is reduced by a factor of 22 in the monsoon, Cl by a factor of 7 and HCO_3^- by a factor of 2.8. The trends seen in concentration are mirror the single peak monsoonal hydrograph (Figure 1.3).

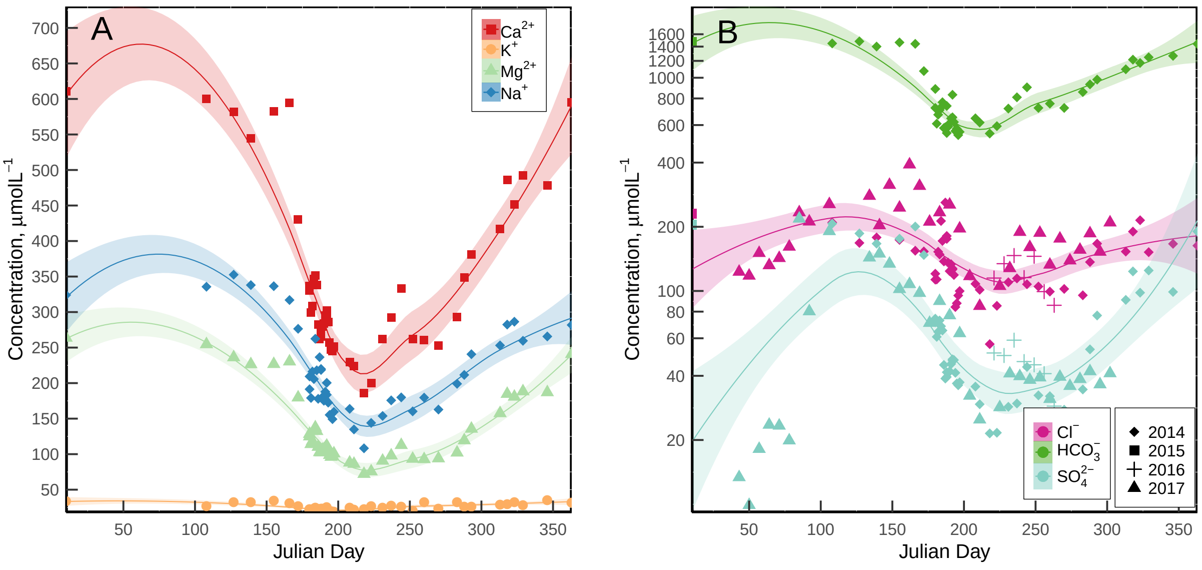

Figure 4.14: Temporal river water cation (A) and anion (B) concentrations at Chroy Changvar, Mekong mouth. A distinct effect of the single peak monsoonal hydrograph is seen in the annual elemental concentrations in the main stem. HCO_3^- is the most concentrated anion, an order of magnitude greater than SO_4^{2-}, shown by the logarithmic scale on the y-axis (b). Samples were collected by both the MRC and myself. Values are rain corrected.

There are also systematic trends in ^{87}Sr/^{86}Sr and $\delta^{18}O$ isotopes in the river water. ^{87}Sr/^{86}Sr ratios vary from 0.710412 to 0.710833 over the year and become more radiogenic during the summer monsoon period. This is the opposite to trends seen in temporal ^{87}Sr/^{86}Sr isotope records collected in other Himalayan draining rivers such as the Marsyandi by Tipper *et al.* (2006), the Brahmaputra by Rai & Singh (2007) and the Alaknanda and Ganga rivers by Tripathy *et al.* (2010). In these rivers, ^{87}Sr/^{86}Sr ratios are low in the summer months of the monsoon due to the significant increase in proportion of carbonate minerals to the dissolved load (Tipper *et al.*, 2006), which typically have a low ^{87}Sr/^{86}Sr signature. The annual trend in the Mekong does however match data from the Salween River in Myanmar (Chapman *et al.*, 2015), but the cause of high ^{87}Sr/^{86}Sr during the monsoon in the Salween is different to the cause of high ^{87}Sr/^{86}Sr in the Mekong. It was suggested that the Salween drains Himalayan carbonates which have extremely high ^{87}Sr/^{86}Sr ratios, up to 0.750 in massive dolomites and limestones of the Lesser Himalayas, due to Sr exchange between silicates and carbonates during metamorphism (Bickle *et al.*, 2001). Increased inputs from these lithologies during the monsoon causes the high ^{87}Sr/^{86}Sr ratios, rather than an increase in silicate weathering (Chapman *et al.*, 2015). The Mekong does not drain these radiogenic carbonate

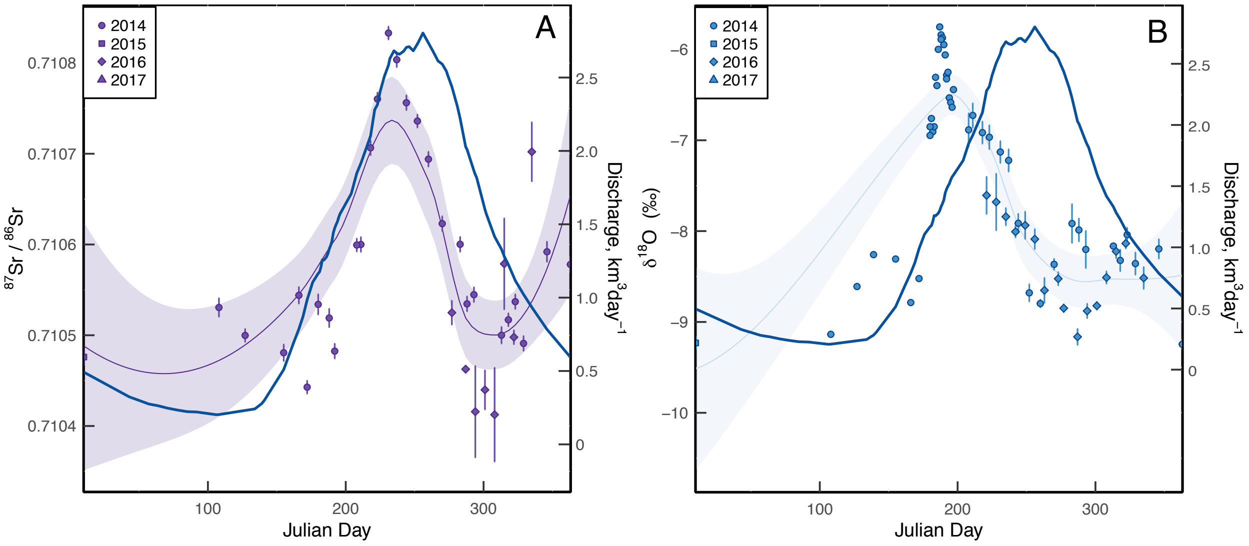

Figure 4.15: Temporal ^{87}Sr/^{86}Sr (A) and $\delta^{18}O$ (B) river water signal at Chroy Changvar, Mekong mouth. Discharge (continuous blue line) is an average of Mekong River Commission (2016) Historical discharge data collected between 1960-2002. ^{87}Sr/^{86}Sr samples (purple points) and $\delta^{18}O$ samples (blue points) are measured on samples collected by both the MRC and myself from 2014 - 2017. Errors on samples are 2σ. Loess regression smoothing fit is the coloured band through samples. $\delta^{18}O$ and ^{87}Sr/^{86}Sr values are uncorrected for rain input.

lithologies, based on leachate data (Figure 4.2), therefore a different source or process must be the cause of increasing ^{87}Sr/^{86}Sr isotope ratios during the monsoon. Strontium isotopes peak slightly before maximum discharge but this may be an artefact of the discharge data, which is an average of data from 1960-2002 where peak discharge varies between days 202 and 291 over the year. The changes in Sr could therefore be caused by spatially variable inputs from across the catchment, rather than a process control of carbonate to silicate weathering (e.g. Tipper *et al.*, 2006).

Oxygen isotopes vary by $\sim$4‰ over the year becoming heavier during the warmer monsoon summer months. Warmer mean seasonal air temperatures during the summer months increases the amount of moisture air can hold, specifically the heavier ^{18}O isotope (Kendall & Doctor, 2003). Precipitation therefore contains relatively more ^{18}O in the summer than in the winter where the moisture content of air decreases, precipitation forms faster and rains out with relatively more ^{16}O. The seasonal trend in $\delta^{18}O$ isotopes is mirrored by δD. The peak in heavier oxygen isotopes in river water arrives earlier than peak discharge, for which there may be a few reasons. First there is $\sim$45 day error in the exact day of peak discharge due to the averaging of historical data. Secondly, the cause of heavier $\delta^{18}O$ isotopes during the summer and the offset in peaks of $\delta^{18}O_{H_2O}$ and ^{87}Sr/^{86}Sr could be due to the impact of the monsoon arriving from the south (Section 1.2.3), first affecting the runoff and local area where the samples are collected, at Chroy Changvar, then the mixing of weathering signals from the tributaries which causes the increase in ^{87}Sr/^{86}Sr. It is clearly necessary, from the signals recorded at the mouth of the basin, to understand the chemistry of individual tributaries and their contribution to the solute flux.

Major cations, anions and Sr are normalised to Ca, at Chroy Changvar, close to the mouth of the Mekong, to illustrate any annual trends that are not caused by monsoonal dilution (Figure 4.16). The signals at the mouth of the river encompass all processes occurring throughout the basin. There are some similarities in trends of K/Ca, Si(OH)$_4$/Ca and HCO$_3^-$/Ca. These ratios peak at the same time as high discharge during the summer monsoon. Mg/Ca, Sr/Ca and SO$_4^{2-}$/Ca have an inverse trend to discharge with low ratios during the monsoon. There is a general increase in Na/Ca and Cl/Ca ratios during the middle of the year, around the pre-monsoon, but there is less annual variation compared to all other ratios. The trends indicate that there are other processes happening throughout the Mekong, varying on an annual time frame, other than purely monsoonal dilution.

To investigate where in the basin the processes creating the trends may be occurring, Ca-normalized ratios are illustrated with MRC historical data, collected at various downstream main stem sites, (Figure 4.18, no Sr concentrations are available for this dataset). The sites span

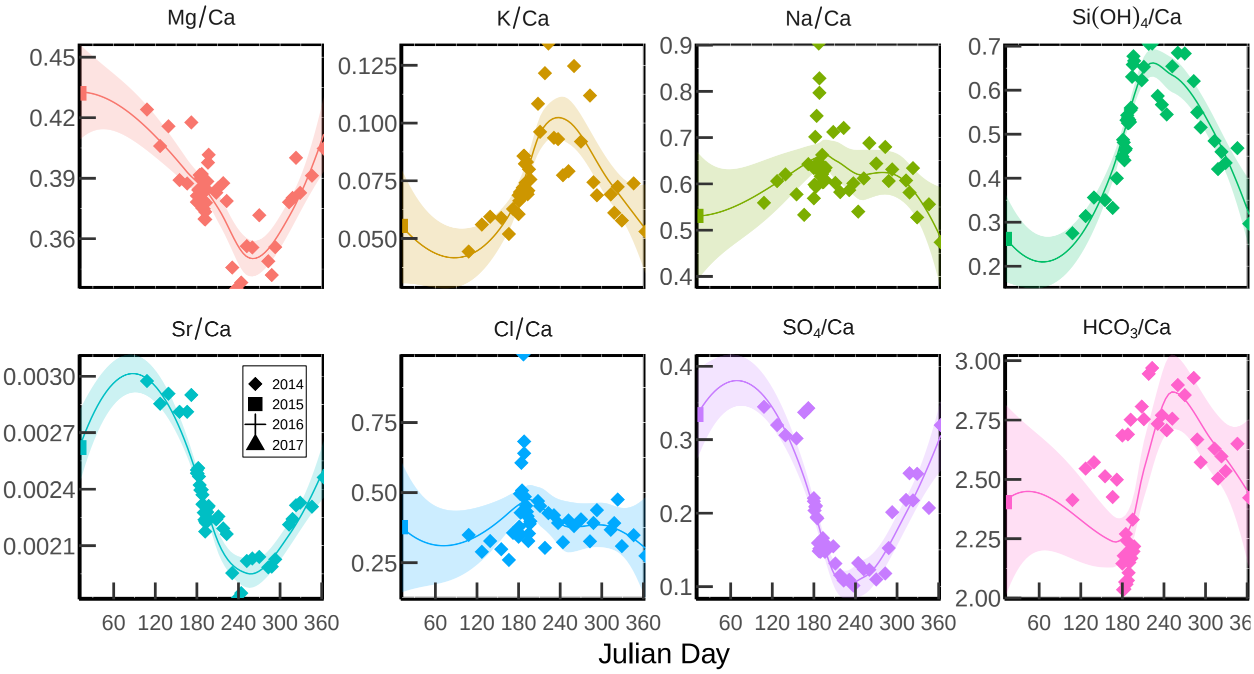

Figure 4.16: Time-series data from Mekong main stem close to the mouth at Chroy Changvar, presented as elemental ratios. Samples were collected by both the MRC and myself and data is rain corrected. Smoothed fit through samples is a Loess regression (coloured bands).

the Middle Mekong from the most northerly site, Chiang Saen, just south of the Chinese border downstream to Pakse, just north of the Khone Phapheng Falls where Laos meets Cambodia, further south is the Chroy Changvar site, location of data in Figure 4.16. There are two noticeable jumps in trends downstream, the first between Chiang Saen and Luang Prabang, and the second between Pakse and Chroy Changvar. At Chiang Saen there is a clear seasonal pattern in all ratios but at Luang Prabang the magnitude between the peaks and troughs of the seasonal trends is reduced for each ratio. Between Luang Prabang and Nakhon Phanom, the magnitude in seasonal difference is the same but the overall values of each of the ratios increase. Most trends remain reasonably similar between Nakhon Phanom and Pakse apart from HCO_3^-/Ca where the data is scattered and the seasonal fluctuation is muted. Between Pakse and Chroy Changvar the seasonal trends change, likely due to the influx of the three large tributaries in northern Cambodia. The peak in K/Ca is later, from day ~180 to day ~280 and becomes more pronounced. There is a smaller variability in annual Mg/Ca and Si/Ca values, the range is broadly similar in Na/Ca, SO_4^{2-}/Ca and HCO_3^-/Ca.

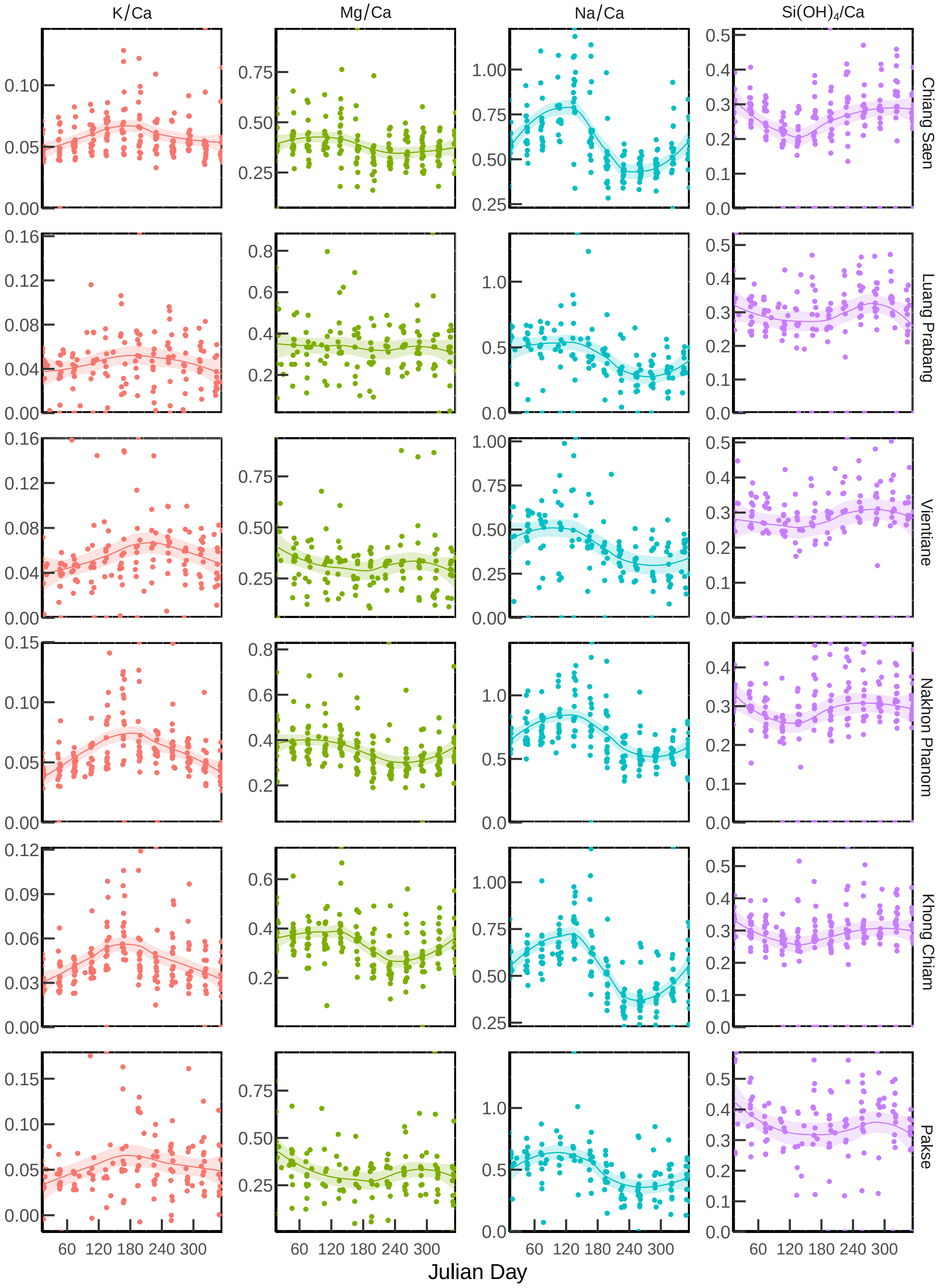

Figure 4.17 *(continues on next page)*

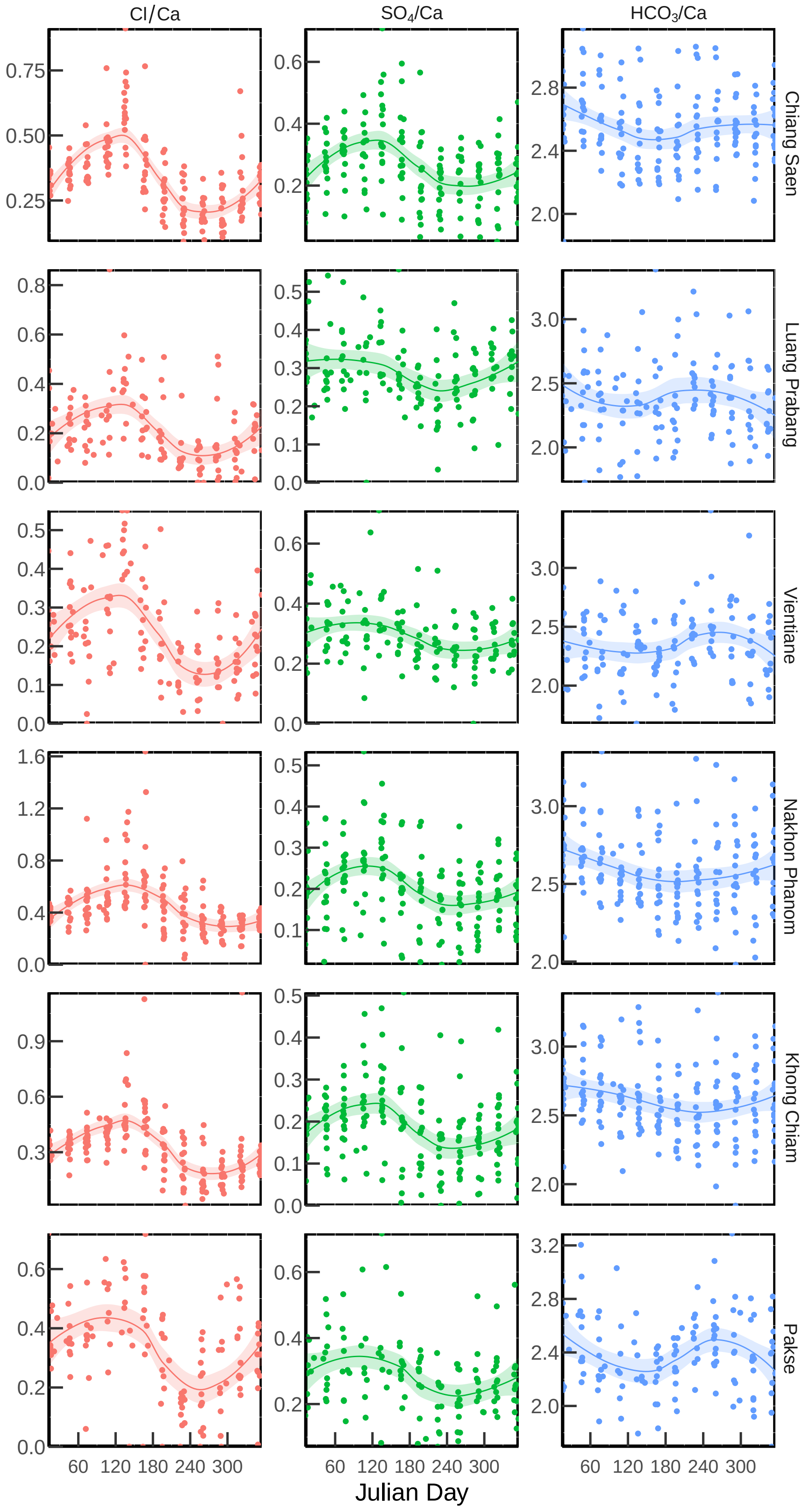

Figure 4.18 *(continued)*

4.4 Discussion

4.4.1 Lithological Controls on Water Chemistry

Five main sources contribute to river water composition, they are: cyclic salts, weathering of silicates, carbonates and evaporites and anthropogenic inputs (Galy & France-Lanord, 1999). A general overview of lithological contributions is given then sources contributing to the dissolved load are discussed and quantified.

The distribution of samples between the ternary apices in Figure 4.19 suggest that most of the tributaries lie in a mixing array between two main lithologies; carbonates (Ca^{2+}+Mg^{2+} apex) and silicates ($Si(OH)_4$ apex). There is a distinct group of tributaries on the right bank with a greater input from evaporite minerals (Na^{+}+K^{+} apex). Using elemental ratios, which remove the effect of discharge, Mekong samples can be compared to the world data set published by Gaillardet *et al.* (1999, and Figure 4.20a). Silicate end members are characterised by similarly low Ca/Na and Mg/Na ratios whilst carbonate end members have high Ca/Na and Mg/Na ratios. Most of the Mekong samples lie on a mixing line between these two end members. Cambodian tributaries that weather basalts, granites and Palaeozoic sediments lie close to the silicate end member whilst left bank Laos tributaries characterised by marine sediments plot close to the carbonate end member. The right bank tributaries draining the Khorat Plateau trend down towards the evaporite end member. The main stem samples cluster in the middle of the tributary data and have higher Mg/Na and Ca/Na ratios than a sample previously collected at the Mekong mouth by Gaillardet *et al.* (1999).

4.4.2 Evaporite Correction

Evaporites are present in the Mekong river basin indicated by the high concentrations of Cl and Na (Figure 4.7 and 4.8). Cl in the river is sourced only from rain inputs and evaporites (Equation 6.4). Halite, NaCl, is the third most common evaporite mineral, after gypsum and anhydrite, by

Figure 4.18 *(previous page)*: MRC Historical time-series concentration data from locations along the Mekong main stem, presented as elemental ratios. Data from 1985-2003 is compiled for each main stem site, data is rain corrected using this studies rain data and spatially variable rain correction method. Sample sites increase in distance downstream, from Chiang Saen (m), Luang Prabang (m), Vientiane (m), Nakhon Phanom (m), Khong Chiam (m) to Pakse (m). Smoothed fit through samples is a Loess regression (coloured bands).

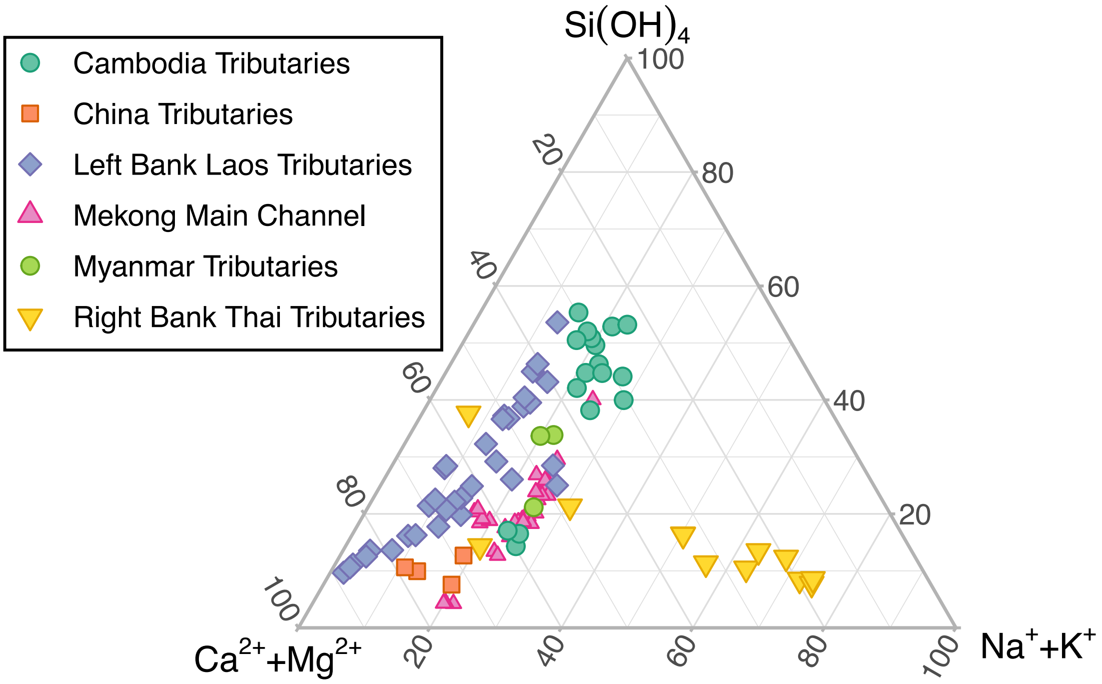

Figure 4.19: Ternary diagram with lithological apices. Main stem and tributary samples are plotted showing contributions from three end members: silicate end member ($Si(OH)_4$), carbonate end member (Ca^{2+} + Mg^{2+}) and biotite rich end member (Na^{+} + K^{+}).

volumetrically important deposits (Babel & Schreiber, 2014). Na and Cl are in a 1:1 ratio so Cl concentration in the river, once corrected for rain input (Equation 4.2), is equal to the concentration of Na cations delivered by halite dissolution (Equation 4.4). Elements corrected for rain input are identified with an asterisk, e.g. Cl^{*}_{riv} (Section 4.3.2.1).

$$Cl_{riv} = Cl_{rain} + Cl_{evp} \tag{4.3}$$

$$Na^{*}_{evp} = Cl^{*}_{riv} \tag{4.4}$$

Salt input to river water is calculated using Equation 4.4 for the Mekong basin (Figure 4.21). In the Mekong basin, some evaporites can be found in China but they are mostly concentrated in the Khorat Plateau, Thailand, on the right bank of the middle Mekong which is a distinct contrast to the left bank in Laos which has no evaporites. Dominated by a large evaporite basin, tributaries draining the Khorat Plateau have Cl^{*}_{riv} or Na^{*}_{evp}, concentrations up to 780μmol/L. It is useful to quantify evaporite input and to understand the lithological source of the river water ions, but more

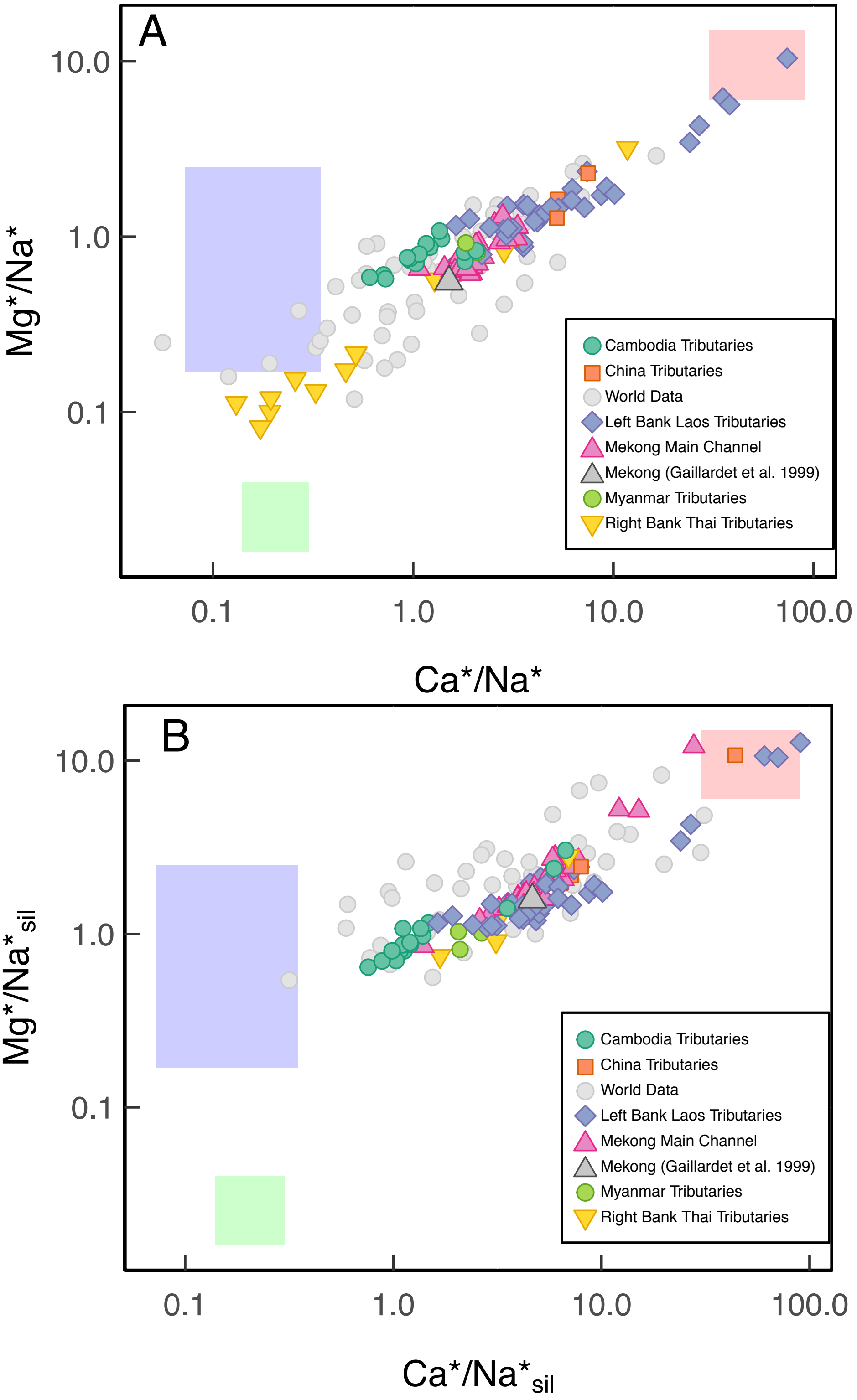

Figure 4.20: Mixing diagrams using Na-normalized molar ratios (uncorrected and evaporite corrected) in the dissolved load. River water concentrations are corrected for rain input, before normalising to Na, A, or normalising to Na corrected for halite, B. The silicate end member reservoir composition is Mekong residue data where Ca/Na = 0.21 ±0.14 and Mg/Na = 1.33 ±1.17 (blue box). Carbonates (red box) and evaporites (green box) end member compositions are based on values used in Gaillardet *et al.* (1999) where Ca/Na ratios are between 30-90 and 0.14-0.3, respectively and Mg/Na ratios are between 6-15 and 0.016-0.04, respectively.

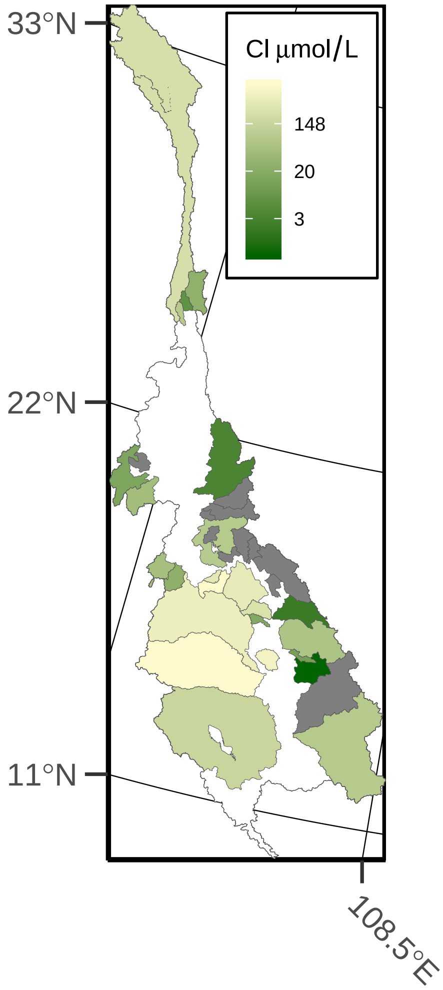

Figure 4.21: Spatial distribution of halite in the Mekong Basin. Dark grey tributaries have no evaporites, where Cl^*_{evp}, and Na^*_{evp} are 0. The highest Cl^*_{evp}, and Na^*_{evp} are in the Khorat Plateau, Thailand. No samples have been collected from the white areas.

importantly, evaporite concentrations are used for correcting other elements such as Na which are used to calculate silicate weathering fluxes.

All river water Na^+ remaining after correction for rain and halite is derived from weathering of silicate minerals, Equation 4.5, because negligible Na^+ is derived from carbonates (Berner, 2004). The importance of correcting for evaporites is illustrated in Figure 4.22 which shows the distribution of Na^+ concentrations in Mekong samples after correction for rain inputs then after correction for salt inputs. When there is a large contribution from evaporites and little to no Na-silicate in the catchment, salt can be over corrected resulting in negative Na_{sil}. Rain corrected data becomes negative for two samples when corrected for evaporites (Figure 4.22). This is clearly an artefact, therefore Na_{sil} is set to zero (Equation 6.12). The two tributaries, located on the Khorat Plateau, had a salt correction within 6% of total Na^*.

$$Na_{sil} = Na^* - Na^*_{evp} \tag{4.5}$$

$$if\ Na_{evp} > Na^*\ then\ Na_{sil} = 0 \tag{4.6}$$

Using the value for silicate derived Na, Na^*_{sil}, data in Figure 4.20a is replotted after correction for evaporite signal in Figure 4.20b. Samples are generally shifted to higher $\mathrm{Mg/Na}^*_{sil}$ and $\mathrm{Ca/Na}^*_{sil}$ values. These evaporite corrected values (Figure 4.20b) give a greater insight into the lithologies contributing to the river water chemistry. Cambodian tributaries and tributaries draining Myanmar have more or less remained stationary in the plot space suggesting a lack of evaporites in those tributaries. Three main stem samples have moved closer to the carbonate end member as has the Bijiang tributary, all in China indicating a presence of some evaporites in the Upper Mekong.

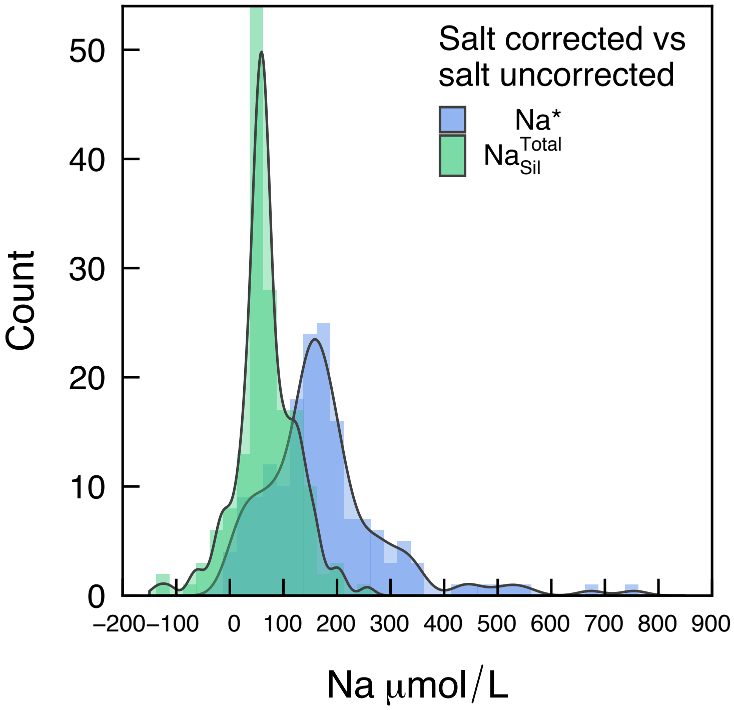

Figure 4.22: Histogram of Na concentration in Mekong tributaries, corrected for rain and salt inputs. Histogram is overlaid by density graph for data that has been corrected for cyclical salt (blue) and evaporite inputs (green).

Gypsum ($CaSO_4{\cdot}H_2O$) and anhydrite ($CaSO_4$) are the most common rock forming evaporite minerals (Babel & Schreiber, 2014) and may be present in the Mekong basin. Particularly in some of Middle Mekong tributaries which have higher Ca^{2+} and SO_4^{2-} concentrations than the main stem (Figure 4.7 and Figure 4.8). Calculating the quantity of sulfate evaporites is not as straight forward as halite, however, because both Ca^{2+} and SO_4^{2-} have multiple sources. Gypsum and oxidative weathering of pyrite both contribute sulfate ions to river water (Equation 4.7), but there is no simple stoichiometric ratio to calculate the sulfate derived from gypsum or anhydrite evaporites. Carbonates, silicates, evaporites and rain all contribute Ca to river water (Equation 4.8). If the amount of sulfate derived from evaporites is known then the amount of Ca derived from evaporites can be calculated due to the 1:1 ratio of Ca^{2+}:SO_4^{2-} in gypsum and anhydrite (Equation 4.9). Only using isotopic analysis can sulfate derived from evaporites be distinguished from pyrite-sulfate and used to calculate evaporite inputs to Ca^{2+} and SO_4^{2-} in river water. Isotopic analysis and modelling of sulfate sources is addressed in Chapter 5.

$$SO^*_{4\ riv} = SO_{4\ gyp} + SO_{4\ pyr} \tag{4.7}$$

$$Ca^*_{riv} = Ca_{gyp} + Ca_{sil} + Ca_{carb} \tag{4.8}$$

$$Ca_{gyp} = SO_{4\ gyp} \tag{4.9}$$

4.4.3 Anthropogenic Inputs

Natural river water signals can be polluted by anthropogenic sources such as sewage, agricultural fertilisers, factory effluents or city emissions. To avoid capturing anthropogenic signals, samples were collected upstream of any dwelling or city. Then, samples were analysed for pollution indicators such as high levels of Cl^- and NO_3^-, (Meybeck, 1998). Nitrate concentrations in the Mekong vary from 0 to 144 μmol/L which is five times less than the critical limit for drinking-water specified by the World Health Organisation ($\sim$800μmol/L, WHO, 2017). Cl^- levels are much greater but these are explained by the presence of evaporites, rather than anthropogenic pollution (see Section 4.4.2). Moreover, point source pollution is not seen in downstream trends of Cl^- or NO_3^-; concentration does not spike after the main stem passes a large city. Although the impact of dams on the sediment load of the Mekong has been recorded (Kondolf *et al.*, 2014; Kummu *et al.*, 2010; Xue *et al.*, 2011), the impact of the large population living in the Mekong basin and industrialisation of the countries that the river flows through is not observed in the major element and Sr isotope compositions of river water.

4.4.4 Silicate and Carbonate Inputs to the Dissolved Load

4.4.4.1 Quantifying Silicate Derived Cations in the Dissolved Load Using ^{87}Sr/^{86}Sr

To infer how much carbon dioxide the Mekong river basin may be sequestering through silicate weathering, it is useful to partition silicate from carbonate inputs. One way to quantify the fraction of silicate:carbonate derived cations in the dissolved load is by using a mass balance approach with ^{87}Sr/^{86}Sr isotopes. ^{87}Sr/^{86}Sr ratios are measured in the water, in the AcOH leachate removed from the bank sample and in the detrital residue of the bank sample. The leached bank sediment components lie on a mixing array in elemental and ^{87}Sr/^{86}Sr isotope ratio space and the water sample lies in the middle, confirming that the water chemistry is a mix of the weathered lithological components that comprise the bulk bank sediment (Figure 4.2). High Ca/Na and Ca/Mg ratios in the AcOH leachate is characteristic of a carbonate end member, whilst lower Ca/Na and Mg/Na ratios are characteristic of silicate minerals. Therefore ^{87}Sr/^{86}Sr values in the water, carbonate, and silicate end members are used to calculate f, or the fraction of Sr from carbonates and silicates where the fraction of silicate Sr and fraction of carbonate Sr sums to 1.

$$\left(\frac{^{87}Sr}{^{86}Sr}\right)_{water} = f\left(\frac{^{87}Sr}{^{86}Sr}\right)_{sil} + (1-f)\left(\frac{^{87}Sr}{^{86}Sr}\right)_{carb} \tag{4.10}$$

The fraction of silicate to carbonate in the Mekong dissolved load was calculated for four samples with sufficient isotope data (Figure 4.2). Fraction of silicate derived Sr for the Bijiang, Nam Lik, Tonle Srepok and Tonle Kong are; -0.03, -0.08, 0.28, -0.06. When the ^{87}Sr/^{86}Sr in the water is not between the residue and AcOH leach, fraction of silicate is negative. One reason for this could be the lack of rain correction on the water sample because of insufficient sample sizes to analyse ^{87}Sr/^{86}Sr in rain. Carbonate dust dissolved in the rain could be lowering the ^{87}Sr/^{86}Sr ratio of the water sample. Another reasonable suggestion is that the AcOH leach targeting the carbonate end member is too strong for this particular sample and the reagent has leached into high-Mg carbonates or the silicate fraction, tapping into a higher ^{87}Sr/^{86}Sr signal.

4.4.4.2 Partitioning Silicate Derived Elements Using a Forward Modelling Approach

The weathering of silicate minerals delivers four major cations to the dissolved load; Ca^{2+}, Mg^{2+}, Na^{+}, K^{+}. Ca and Mg in the river are also delivered by weathering of carbonate rocks. In order to partition Ca and Mg between silicate and carbonate sources, molar ratios Ca/Na and Mg/K in silicate minerals are used with a forward model, after Galy & France-Lanord (1999), to calculate silicate derived Ca and Mg (Ca^*_{sil} and Mg^*_{sil}, respectively) (Equation 4.11, 4.12). In the forward model equations below, Na in the river is corrected for rain and evaporite inputs (Na^*_{sil}) and all remaining K in the river after correction for rain inputs is assumed to be derived from silicate rocks (K^*).

$$Ca^*_{sil} = Na^*_{sil} \ * \ \left(\frac{Ca}{Na}\right)_{sil} \tag{4.11}$$

$$Mg^*_{sil} = K^* \ * \ \left(\frac{Mg}{K}\right)_{sil} \tag{4.12}$$

Previous studies have applied one ratio value to the whole river basin (e.g. Galy & France-Lanord, 1999; Mortatti & Probst, 2003; Moon *et al.*, 2007; Li *et al.*, 2014a), or even globally (Gaillardet *et al.*, 1999) when calculating silicate derived cations using a forward model, however stoichiometry in silicate minerals is highly variable (Deer *et al.*, 1992). Not only do molar ratios in silicate minerals vary between river catchments (Table 4.5), they vary within river catchments, as is the case in the Mekong river. Bank samples were collected at the mouth of all accessible tributaries in the Mekong river basin and were sequentially leached to target the detrital silicate fraction of the sediment (detailed in Section 4.3.1 and in the methodology, Chapter 3). The large spread in ε_{Nd} and $^{87}Sr/^{86}Sr$ in the silicate fraction illustrates the variation in silicate mineral chemistry in the Mekong (Figure 4.5). There is some grouping of silicate compositions, where the Myanmar tributaries have lower ε_{Nd} values and higher $^{87}Sr/^{86}Sr$ values and the China and right bank tributaries mostly have higher ε_{Nd} and lower $^{87}Sr/^{86}Sr$. There is a large spread in the left bank Laos and Cambodian tributaries. Clearly, using one average value of Ca/Na and Mg/K for the whole of the Mekong basin is not suitable given the large range in silicate characteristics. Using the individual basin silicate ratios provides a more representative estimation of Ca^*_{sil} and Mg^*_{sil}.

The range of Ca/Na and Mg/K values used to calculate Ca^*_{sil} and Mg^*_{sil} are displayed in Figure 4.3 and in Table 4.1. Weathering of silicate rocks contributes between 1% to 35% of the total Ca cations in the main stem dissolved load, where the largest contribution from silicate minerals is at Vientiane after the input from the karst tributaries in Northern Laos. There is a greater variability in Ca^*_{sil} values in the tributaries; 0% to 88%, mean of 7%. There is less variability in the proportion of Mg contributed by silicate rocks; 2% - 29% in the tributaries and 3% - 14% in the main stem of total Mg cations are derived from silicates.

Table 4.5: Silicate mineral molar cation ratios. References; 1 Gaillardet *et al.* (1999), 2 Chetelat *et al.* (2008), 3 Quade *et al.* (2003), 4 Moon *et al.* (2014), 5 Galy & France-Lanord (1999), 6 Wu *et al.* (2008), 7 Bickle *et al.* (2015), 8 Noh *et al.* (2009).

River	Mg/Na	Mg/K	Ca/Na	Sr/Na	Reference
World minimum	0.12		0.20	0.0030	1
World maximum	0.36		0.50	0.0070	1
Changjiang	0.20		0.35	0.0030	2
Seti-Arun River, Himalaya	0.24		0.41		3
Red	0.16		0.44		4
Ganges Brahmaputra minimum		0.25	0.15		5
Ganges Brahmaputra maximum		0.75	0.25		5
Lancang Jiang		0.50	0.17		6
Nu Jiang		0.42	0.29		6
Huang He		0.67	0.26		6
Marsyandi minimum	0.46	0.39	0.01	0.0004	7
Marsyandi maximum	0.72	0.54	0.33	0.0020	7
Alaknanda minimum	0.38	0.29	0.02	0.0010	7
Alaknanda maximum	2.60	2.70	0.55	0.0030	7
Upper Mekong	0.50		0.17		8
Mekong minimum	0.35	0.18	0.04	0.0023	
Mekong maximum	6.16	1.03	0.66	0.0166	
Mekong mean	1.33	0.53	0.21	0.0044	
Mekong 1σ	1.17	0.18	0.14	0.0028	

4.4.4.3 Quantifying Total Silicate Derived Cations in the Dissolved Load Using X$_{sil}$

X$_{sil}$ is a ratio of the total cations in the dissolved load derived from silicates to all cations derived from the weathering of silicate and carbonate lithologies (Equation 4.13) . X$_{sil}$ uses the partitioned cations, corrected for rain and evaporite input and is calculated in equivalent charge. The factors are the stoichiometric coefficients of the weathering reactions described in Chapter 2, more specifically, they are the ratio of cations released to alkalinity produced by weathering of carbonate and silicate lithologies.

$$X_{sil} = \frac{2 * Ca^*_{sil} + 2 * Mg^*_{sil} + K^* + Na^*_{sil}}{2 * Ca^* + 2 * Mg^* + K^* + Na^*_{sil}} \tag{4.13}$$

Previous studies choose between Mg/Na or Mg/K ratios of silicate end members to use in Equations 4.11 and 4.12. Mg$^*_{sil}$ calculated with each of the ratios was used in the calculation for

X_{sil}, resulting in only a minor difference. Average X_{sil} for tributaries and main stem sites in the Mekong basin is 0.15 or 0.17, using Mg/K or Mg/Na silicate ratios, respectively. There is a ~4% difference between X_{sil} calculated using Mg/K silicate ratios and X_{sil} calculated using Mg/Na silicate ratios. X_{sil} values calculated using Mg/Na are higher than X_{sil} values calculated using Mg/K possibly due to the difficulty in correcting for all evaporites. If Na concentrations in the river water are used to calculate Mg^*_{sil} then a correction is first made for rain contribution then evaporite derived Na in the river water. Less corrections are needed to calculate K^*_{sil}, where K in the river is only corrected for rain contribution (though K can be a difficult element to work with as it is impacted by the biosphere). Hence, Mg^*_{sil} calculations use the Mg/K ratio of silicate residues in this work.

Information on the silicate fraction of samples taken at Vientiane and Stung Treng is not available, therefore the Ca/Na and Mg/K ratios used in Mg^*_{sil} and Ca^*_{sil} calculations are from the bulk sediment. Additionally there is no specific bank sample data for the Kam, Shunbi and Nam Xan tributaries due to inaccessibility of the bank at time of sampling. The Ca/Na and Mg/K ratios used in Mg^*_{sil} and Ca^*_{sil} calculations for these tributaries are derived by an average of the bulk bank sediment of the surrounding tributaries. An average of bank sediment element concentrations were taken from the Bangsai and Songkhram tributaries and applied to the Kam, for the Shunbi tributary sediment samples from the Bijiang and Heihui tributaries were averaged and the Nam Ngiep and Nam Kading bank sediments were averaged for the Nam Xan.

The spatial variability of X_{sil} values downstream are illustrated in Figure 4.23. X_{sil} values increase downstream with maximum values in the main stem at Vientiane. The tributaries with the highest X_{sil} values (0.3-0.6) are recorded in the tributaries closest to the mouth in Cambodia; Tonle Kong, Tonle Srepok and Tonle San. Tributaries sampled in northeast Myanmar have X_{sil} values between 0.28-0.35, they drain Cretaceous to Late Paleozoic grantites and Pre-Cambrian metamorphic units. The remaining ~70% of cations are sourced from the Permian to Carboniferous marine units. Between Luang Prabang and Vientiane, contribution from silicates to the dissolved load increases by 20%. The Nam Xong (MEK16-039, Laos left bank) and Hueang (MEK17-236, Thai right bank) drain Cretaceous Intermediate to basic extrusive lithologies, likely containing with Ca-rich plagioclases, increasing X_{sil}. The average X_{sil} for this study is in good agreement with published X_{sil} values at the Mekong mouth have been calculated as 0.36 by Gaillardet *et al.* (1999) and in the Upper Mekong main channel as 0.12 by Wu *et al.* (2008) and between 0.12 and 0.29 by Zhang *et al.* (2016).

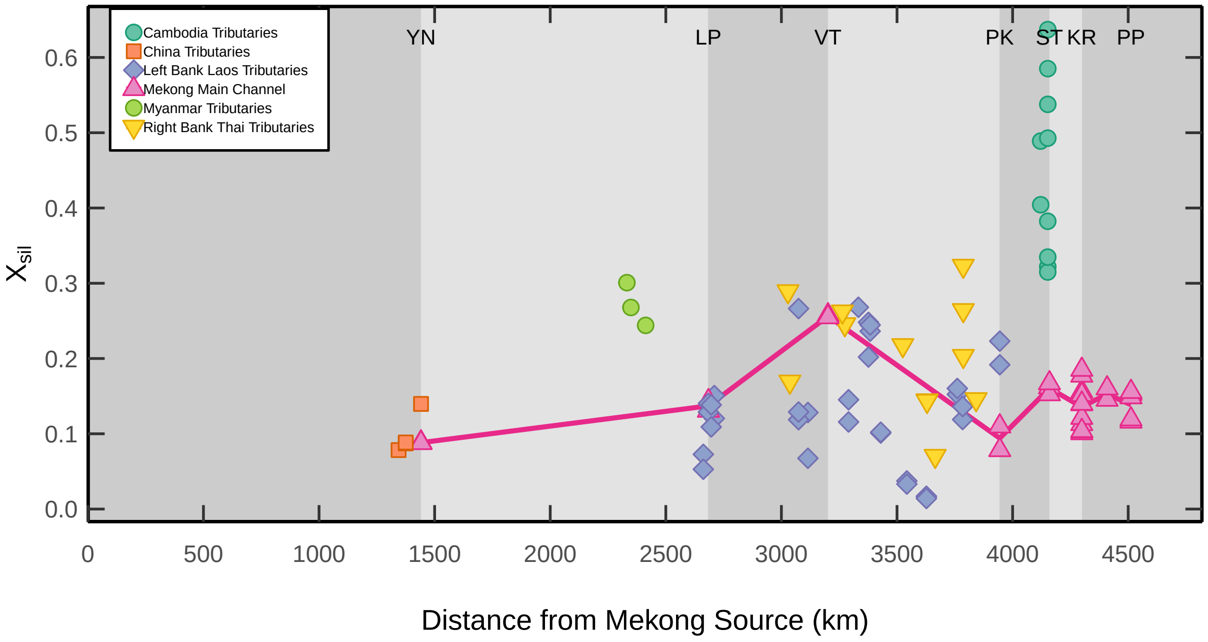

Figure 4.23: Fraction of silicate mineral weathering derived cations, X_{sil}, in Mekong river water. X_{sil} increases downstream from the Upper Mekong to Vientiane in the Middle Mekong, then X_{sil} decreases towards the mouth. Tributaries are divided into groups between Yunnan (YN), Luang Prabang (LP), Vientiane (V), Pakse (PK), Stung Treng (ST), Kratie (KR) and Phnom Penh (same location as Chroy Changvar) (PP), as detailed in section 4.2 and the main stem samples are joined by a pink line.

X_{sil} is reproducible over a number of years at main stem locations; between 2016 and 2017 sampling seasons there is a 4.7%, 0.5% and 16% difference in X_{sil} values at Luang Prabang, Vientiane and Pakse, respectively. Between 2014, 2016 and 2017 sampling seasons there is a 3.3% and 12% difference in X_{sil} values at Stung Treng and Kratie, respectively. At Kratie, the Mekong Mouth, X_{sil} has limited variation (~16%) through the year, but there is a seasonal trend illustrated in Figure 4.24. The lowest values of X_{sil} (0.03) are calculated in the Pre-Monsoon dry season which rise to the highest values (0.19) during the Monsoon. The 16% temporal variation at Kratie is also a good indication on the error for X_{sil} values throughout the basin.

There is a positive correlation (r^2=0.6) between the fraction of silicate calculated with X_{sil} or with $^{87}Sr/^{86}Sr$. Although these values should broadly agree with each other, they are not directly comparable. Firstly, elemental concentrations in the water are corrected for rain inputs. Samples collected for rain were not large enough to analyse strontium isotopes so $^{87}Sr/^{86}Sr$ in water is not rain corrected. Secondly, $^{87}Sr/^{86}Sr$ in the water is a mixture of carbonate and silicate inputs, but both end members exhibit significant variation and potential incongruent dissolution.

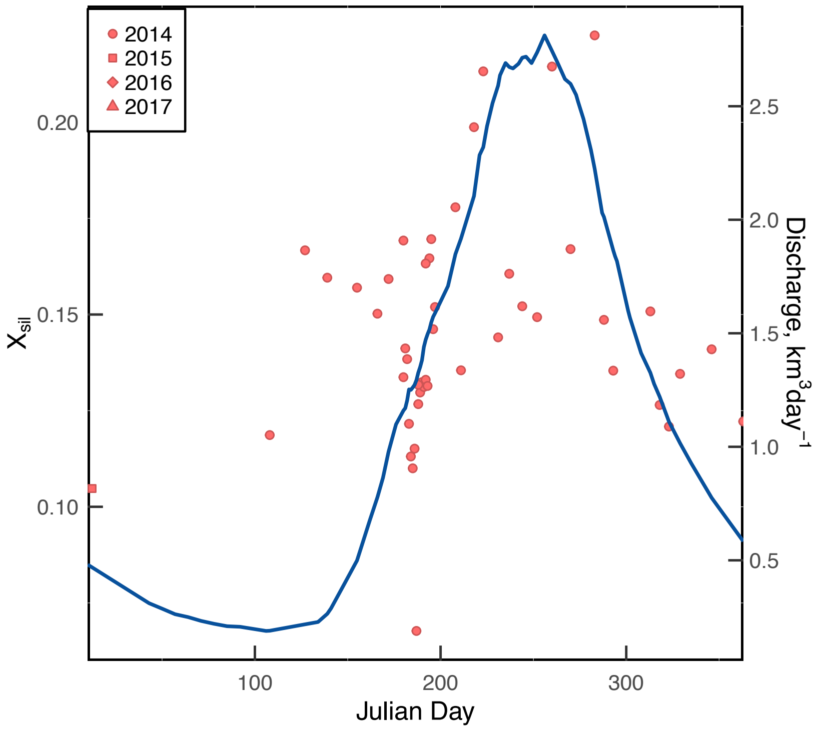

Figure 4.24: Temporal X_{sil} signal at Kratie, Mekong Mouth. Red points are X_{sil} values calculated for samples collected in 2014 and 2016 and from samples collected by the MRC (2015-2017) but analysed for this study at University of Cambridge. Discharge (continuous blue line) is an average of Mekong River Commission (2016) Historical discharge data collected between 1960-2002.

4.4.4.4 Mixing Trends in the Mekong River

Changes in the main stem may reflect both changes in the relative proportions of the major inputs and changes in weathering mechanisms. At Chroy Changvar, close to the mouth of the Mekong temperatures rise and there is a 20-fold increase in the discharge during the monsoon season, compared to the dry season (Mekong River Commission, 2016, and Figure 1.3). These variables are conducive to the preferential weathering of minerals with fast dissolution kinetics, namely carbonates and evaporites because the system becomes weathering-limited. Dissolution kinetics of carbonate minerals are much faster than dissolution kinetics of silicates (Plummer *et al.*, 1978; Brantley, 2003). It is expected that the ratio of silicate to carbonate derived cations would decrease in the monsoon period, illustrated, for example in the Marsyandi tributaries (Tipper *et al.*, 2006). This is not the case in the Mekong, where maximum X_{sil} is recorded during the monsoon period, therefore other processes must be occurring to create this signal. Moreover, the temporal variation in X_{sil}, combined with X_{sil} values of tributaries, can be used to explain the trend seen in temporal $^{87}Sr/^{86}Sr$ isotopes (Figure 4.15a). Temporal variation in $^{87}Sr/^{86}Sr$ and X_{sil} is likely caused by relative variations in inputs from different locations within the basin, from tributaries that drain different lithologies.

4.4.5 Weathering Implications of Mekong River Water Geochemistry

4.4.5.1 Mekong River Carbon Flux

The dissolved inorganic carbon (DIC) flux of the Mekong river can be calculated with the partitioned cations using the method set out in Chapter 2. The total DIC flux represents the dissolution of carbonate and silicate rocks with all acidity sources on the short–term and can be calculated with the following equation. Where all elements have been corrected for rain inputs (denoted by the asterisk) and Na is corrected for halite, Na^*_{sil}.

$$DIC_{total}\ flux = (2Ca^* + 2Mg^* + Na^*_{sil} + K^*) * Discharge \tag{4.14}$$

Ca derived from the weathering of carbonate minerals is calculated by removing the Ca derived from silicate mineral weathering, Ca^*_{sil}, from rain corrected total Ca in the river. The same method is applied for Mg delivered from the weathering of carbonate minerals. Equation 4.17 estimates the total short–term carbonate weathering budget.

$$Ca^*_{carb} = Ca^* - Ca^*_{sil} \tag{4.15}$$

$$Mg^*_{carb} = Mg^* - Mg^*_{sil} \tag{4.16}$$

$$DIC_{carb}\ flux = (2Ca^*_{carb} + 2Mg^*_{carb}) * Discharge \tag{4.17}$$

The cations delivered from silicate weathering provide a total short–term silicate weathering budget (Equation 4.18), where Ca^*_{sil} and Mg^*_{sil} have been calculated using element ratios in the silicate fraction of bank sediments (Section 4.4.4.2).

$$DIC_{sil}\ flux = (2Ca^*_{sil} + 2Mg^*_{sil} + Na^*_{sil} + K^*) * Discharge \tag{4.18}$$

DIC calculated over the year at Chroy Changvar varies, peaking in the monsoon, where 79% of the total carbon flux is delivered to the South China sea (Figure 4.25). The signal is so large during the monsoon that processes occurring during the dry season likely have little to no effect on the elemental budget delivered to the oceans. The temporal signal at the mouth is a homogenisation of signals throughout the basin. DIC flux was calculated for tributaries within the basin during monsoon season. The contribution of carbon from the Upper, Middle and Lower Mekong tributaries, to the total flux is spatially variable. 16% of the total carbon flux during the 2017 monsoon season was delivered from China (sampled at Yunnan, roughly two–thirds down the Upper Mekong). 62% of the total carbon flux is from the Middle Mekong (contributed from Yunnan to Stung Treng) and the remaining 22% of the total carbon flux is from the Lower Mekong during the monsoon.

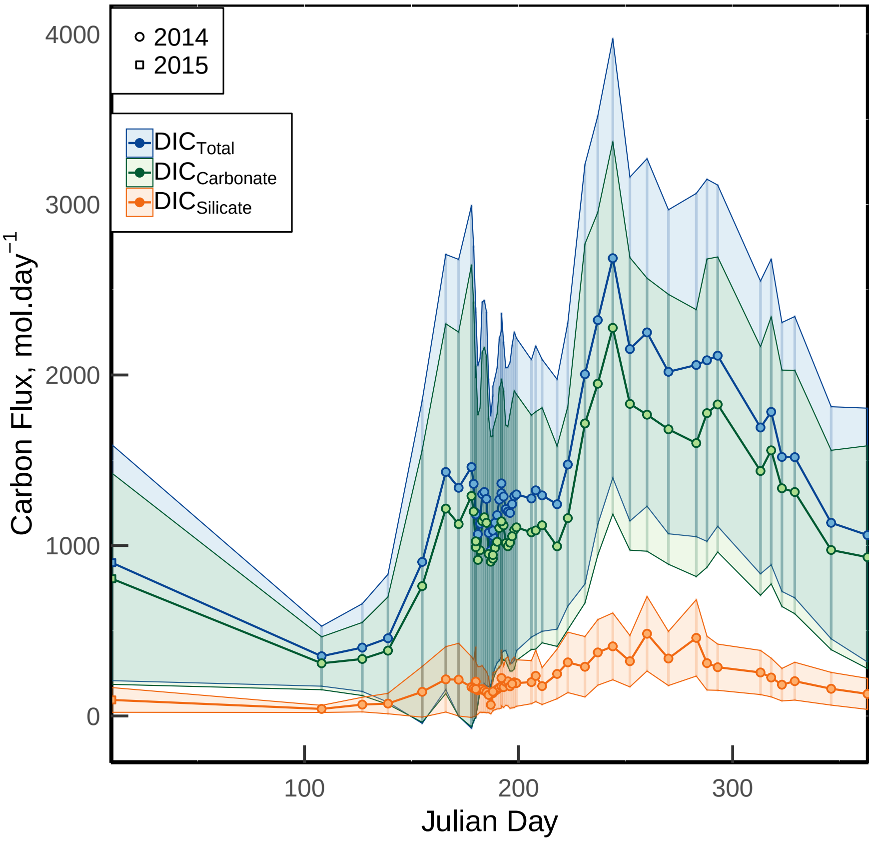

Figure 4.25: Specific annual carbon flux at Chroy Changvar, Mekong Mouth. Samples have been collected by the MRC and this study and all analysed at University of Cambridge. The total carbon budget over the year (blue) has been calculated with partitioned cations, corrected for rain input and halite salts using equations discussed in the text. The total carbon budget can be split into the carbon flux contributed from carbonate lithologies (green), which is significantly larger than the carbon flux associated with the weathering of silicate minerals (orange).

4.4.5.2 Acidity Sources

The hydrolysis of carbonate minerals provides a substantial proportion, over 70%, of the cations in the Mekong river dissolved load. It is important to note that this chapter has so far only considered the weathering of carbonates, and silicates, with acidity produced from the dissociation of atmospheric carbon dioxide dissolved in water. Although there is a large transfer of carbon through carbonic acid weathering of carbonates, the process is carbon neutral in the long term, with no net transfer of carbon in or out of the atmosphere. However sulfuric acid, if present in the basin can also weather minerals. The sulfuric acid weathering of carbonates is a net source of CO_2 both on instantaneous timescales and on timescales of carbonate precipitation in the ocean. SO_4^{2-} is present in the Mekong in concentrations up to 720μmol/L. If this sulfate is derived from the oxidation of sulfide minerals, rather than gypsum, the potential chemical weathering reactions between sulfuric acid and carbonates could significantly affect the carbon budget of the Mekong river (Chapter 5).

4.5 Conclusions

The Mekong river water chemistry is mostly dominated by Ca and HCO_3^- with the exception of a distinct group of tributaries draining the Khorat plateau that have water chemistry dominated by Na, K and Cl. Leaching bank sediment extracted individual lithological components and characterised the carbonate and silicate end members. Using $^{87}Sr/^{86}Sr$ in carbonate and silicate end members and in water, a silicate: carbonate budget was calculated. This method was compared against the values for X_{sil} which was calculated using Ca/Na and Mg/K ratios in the silicate fraction of bank samples. Although values calculated by these methods are comparative, values for X_{sil} are used because targeting the correct carbonate fraction using a leachate method is notoriously difficult. Analysis of the silicate residues, using $^{87}Sr/^{86}Sr$ and ε_{Nd}, highlighted the heterogeneous nature of silicate lithology in the Mekong basin. Hence, element ratios in silicate fractions of individual tributaries were used with the corresponding water sample for the most representative X_{sil} values. X_{sil} values suggest that over 70% of the cations in the dissolved load are derived from carbonate rocks. However, this may be an overestimation because Ca derived from the weathering of gypsum evaporites has not yet been accounted for. The Ca flux from the weathering of gypsum could be significant considering the high concentration of Cl in the Middle Mekong. It is important to note that this chapter has only considered carbonate and silicate weathering with carbonic acid which has vastly different consequences for the carbon cycle than chemical weathering with other acids. Specifically, if the high proportion of carbonate minerals that comprise the Mekong river basin are weathered by sulfuric acid then the Mekong river basin could be releasing CO_2. It is critical, therefore, to determine first, the source of the sulfate in the Mekong river. This is addressed in Chapter 5. Secondly using information on sulfuric acid weathering from Chapter 5, elements in the dissolved load can be more appropriately partitioned to the lithology and particular weathering reaction from which they were sourced. Then, in Chapter 6, the carbon budget for the Mekong river basic is calculated.

Chapter 5

Quantifying Sulfuric Acid Weathering

5.1 Introduction

The chemical weathering of carbonate rocks with sulfuric acid, derived from the oxidation of sedimentary sulfides, predominantly oxidation of pyrite, (Berner, 1984; Francois & Walker, 1992; Berner & Berner, 2012) releases geologically stored carbon into the atmosphere as carbon dioxide gas, CO_2 (Equation 5.1) (Torres *et al.*, 2014) or into the hydrosphere as dissolved inorganic carbon, HCO_3^- (Equation 5.2) (Spence & Telmer, 2005; Calmels *et al.*, 2007):

$$H_2SO_4 + CaCO_3 \Rightarrow CO_2(g) + H_2O + Ca^{2+} + SO_4^{2-} \tag{5.1}$$

$$H_2SO_4 + 2CaCO_3 \Rightarrow 2Ca^{2+} + SO_4^{2-} + 2HCO_3^- \tag{5.2}$$

Recent work has revealed that in several of the world's largest river basins, pyrite oxidation driven weathering of carbonates may release more CO_2 than is consumed via silicate and carbonate weathering with carbonic acid (Calmels *et al.*, 2007; Torres *et al.*, 2014; Liu *et al.*, 2017). Dissolved sulfate (SO_4^{2-}) present in river water could be an indication of pyrite oxidation and the assessment of Burke *et al.* (2018) on global sulfate fluxes ranks the Mekong river the 11th largest contributor.

Furthermore, the spatially detailed geochemical investigation of the Mekong presented in the previous Chapter measured SO_4^{2-} concentrations of up to 702μmol/L in catchments where greater than 80% of dissolved cations are derived from the weathering of carbonate rocks. Determination and quantification of the acidity agent responsible for mineral dissolution (carbonic or sulfuric) is hence imperative for a rigorous assessment of the local Mekong and global climate feedback resulting from chemical weathering.

In addition, the modern production of atmospheric sulfuric acid through the burning of fossil fuels is particularly relevant in the Mekong river, which flows through industrially developing countries. The effects of anthropogenic exacerbation of natural reactions like those shown in Equations 5.1 and 5.2 can been seen in other Asian rivers (e.g. Smith *et al.*, 2001; Xu & Liu, 2007; Li *et al.*, 2008; Yoon *et al.*, 2008; Li & Ji, 2016). Constraining sulfuric acid weathering is therefore timely in the context of global environmental change.

This chapter presents a new model, using improved methods, to partition the source and quantity of dissolved sulfate in rivers in a local and global context, thereby determining sulfate flux from oxidative weathering of pyrite. The isotopes of oxygen and sulfur in dissolved sulfate are used to discriminate the source of sulfate within individual catchments (tributaries and mainstream) and a two component mixing model is used to quantify the amount of sulfuric acid within each catchment. Uncertainties on these calculations are assessed using a Monte-Carlo approach.

5.2 Origin of Sulfate in River Water

Dissolved SO_4^{2-} in rivers is derived from multiple sources, not all of which are directly linked to the carbon cycle (Calmels *et al.*, 2007). The most significant sources to riverine SO_4^{2-} are the dissolution of sedimentary sulfates such as gypsum ($CaSO_4 \cdot H_2O$) and anhydrite ($CaSO_4$), oxidation of sedimentary sulfides such as pyrite (FeS_2) and to a lesser extent the weathering of magmatic sulfides (Berner & Berner, 2012). Additional inputs are from volcanic emissions, rain and anthropogenic pollution from fertilisers, industrial waste water and coal burning (Robinson & Bottrell, 1997; Canfield, 2004; Brenot *et al.*, 2007). Identifying the individual sources of sulfate is crucial due to their different implications on climate; the rapid oxidation of pyrite produces sulfuric acid which then reacts with carbonate minerals releasing sulfate and geologically stored carbon. On the other hand, sulfate that is the product of gypsum dissolution has no implication on the carbon cycle.

There are multiple ways to track the origin of the dissolved SO_4^{2-} ion, including the ratio of SO_4^{2-} to bicarbonate (HCO_3^-) coupled to stable carbon isotopes ($\delta^{13}C_{DIC}$) (Galy & France-Lanord, 1999; Li *et al.*, 2008). The difficulty in using carbon isotopes to track the oxidative weathering of pyrite coupled to carbonate dissolution is that the $\delta^{13}C_{DIC}$ tracks carbon, rather than the SO_4^{2-} ion, and there is a range in $\delta^{13}C$ of carbon sources (Telmer & Veizer, 1999). Whilst the $\delta^{13}C$ of carbonate rocks is close to 0‰ (Keith & Weber, 1964), multiple sources of CO_2 which are subsequently dissolved in water, result in a range of $\delta^{13}C$ values in carbonic acid (H_2CO_3). Atmospheric CO_2 dissolved in meteoric water has a slightly positive average $\delta^{13}C$ of +1.4‰ (due to fractionation during the dissolution of atmospheric CO_2 into H_2O to form H_2CO_3 of $\delta^{13}C$=-9 to -7‰ (Faure & Mensing, 2005). Additionally, tree roots or decomposing organic matter, with a range in carbon isotope signatures, respire CO_2 which is then dissolved in groundwater resulting in carbonic acid with $\delta^{13}C$ ranging from 0‰ to -22‰ (if both C3 and C4 plants are considered) (Telmer & Veizer, 1999; Faure & Mensing, 2005). The $\delta^{13}C$ signature of HCO_3^- in river waters is a mix of the aforementioned sources but further modifications to $\delta^{13}C$ could occur through secondary carbonate precipitation or degassing of dissolved inorganic carbon (DIC) from the river (Telmer & Veizer, 1999; Yang *et al.*, 1996). Moreover the impact of sulfuric acid weathering of carbonates could be over-estimated if $\delta^{13}C$ in DIC is compared to ratios of SO_4^{2-} to [SO_4^{2-} + HCO_3^-] because SO_4^{2-} cannot be easily corrected for gypsum contributions with element ratios, or for the SO_4^{2-} contribution from sulfuric acid weathering of silicate rocks which does not affect the carbon cycle and therefore has no $\delta^{13}C$ signature.

The acid mine drainage community pioneered a novel technique in the 1980's, combining the use of isotopic compositions of sulfur and oxygen atoms in sulfate ($\delta^{34}S_{SO_4}$ and $\delta^{18}O_{SO_4}$, respectively) (Taylor *et al.*, 1984a,b; van Everdingen & Krouse, 1985). They used $\delta^{34}S_{SO_4}$ and $\delta^{18}O_{SO_4}$ to track the oxidation pathway of sulfide ores and mine tailing piles to inform and monitor abatement procedures aimed at reducing the formation of environmentally damaging acid waters. $\delta^{34}S_{SO_4}$ and $\delta^{18}O_{SO_4}$ have been shown to be controlled predominantly by lithological source so have been used to track groundwater flow paths (Krouse & Mayer, 2000). Therefore this powerful technique could be applied to tracking sources of SO_4^{2-} in river water (Karim & Veizer, 2000; Pawellek *et al.*, 2002; Calmels *et al.*, 2007; Torres *et al.*, 2016).

5.2.1 Tracing Sulfate Sources with Sulfur Isotopes in Dissolved Sulfate

There are four stable isotopes of sulfur, of which ^{32}S is the most abundant, followed by ^{34}S. Stable isotopic compositions of sulfur are reported as ratios of ^{34}S/^{32}S measured in a sample, relative to the same ratio measured in a standard, expressed as per mil (‰) in delta notation (Equation 5.3) (Canfield, 2001). The standard used for sulfur isotopes is the Vienna Canyon Diablo Troilite (Coplen & Krouse, 1998). δ^{34}S isotopes are excellent tracers of processes due to the natural abundance of S valence states resulting in variable isotope compositions (Strauss, 1997; Krouse & Mayer, 2000). Moreover, the sulfur isotope signature in dissolved SO_4^{2-} ($\delta^{34}S_{SO_4}$) is a close reflection of the sulfur isotopic signature of the source material (Calmels *et al.*, 2007). The development of small sample sulfur isotope measurements by MC-ICP-MS heralds the promise that δ^{34}S might be used to track the origin of the sulfate ion in even small sample sizes (Paris *et al.*, 2013; Burke *et al.*, 2018).

$$\delta^{34}S = \left(\frac{\left(\frac{^{34}S}{^{32}S}\right)_{sample}}{\left(\frac{^{34}S}{^{32}S}\right)_{standard}} - 1 \right) * 1000‰ \tag{5.3}$$

There is a large range of around 40‰ in $\delta^{34}S_{SO_4}$ in the largest rivers in the world (e.g. Yang *et al.*, 1996; Karim & Veizer, 2000; Li *et al.*, 2006; Brenot *et al.*, 2007; Calmels *et al.*, 2007; Yoon *et al.*, 2008; Rock & Mayer, 2009; Yuan & Mayer, 2012; Turchyn *et al.*, 2013; Li *et al.*, 2014b, 2015; Hindshaw *et al.*, 2016; Torres *et al.*, 2016; Burke *et al.*, 2018; Zolkos *et al.*, 2018; Killingsworth *et al.*, 2018), suggesting that the sources must also have a large range in signatures (Figure 5.1). The range of sulfur isotope signatures in igneous sulfides, including granites and basic sills both centre over the primordial δ^{34}S value of 0‰ (Shima *et al.*, 1963). Modern seawater has a unique δ^{34}S value of 20.99‰ (Rees *et al.*, 1978; Kampschulte & Strauss, 2004) whilst the sulfur isotope signature of ancient oceans varied as shown by the 25‰ range in marine evaporites (Claypool *et al.*, 1980; Chakrapani & Veizer, 2006). Sedimentary sulfides have the largest δ^{34}S range, more varied than global rivers, ranging from -50‰ to +10‰ (Krouse *et al.*, 1991). However, there is significant overlap between end members which frustrates the use of δ^{34}S exclusively in partitioning SO_4^{2-} derived from different sources.

Moreover, there are additional processes modifying δ^{34}S other than source, including kinetic fractionation and microbial involvement. Taylor *et al.* (1984b) suggested that fractionation between solid sulfide and sulfate, $\varepsilon_{SO_4-FeS_2}$, is up to -1.7‰ with Thiobaccillus mediation however if the sulfide is aqueous and oxidation is bacterially mediated then there is a large fractionation where

$\varepsilon_{SO_4-FeS_2}$ = -6 to -18‰, but this fractionation is still within error of the large range in pyrite sulfur isotope signatures. Experiments have shown a small enrichment of ^{32}S in SO_4^{2-} relative to the oxidised sulfide when pyrite oxidation occurs anaerobically ($\varepsilon_{SO_4-FeS_2}$= -0.7‰ (Balci *et al.*, 2007), -0.9‰ (Mazumdar *et al.*, 2008), -0.8‰ (Heidel & Tichomirowa, 2011)). This is due to the incomplete oxidation of intermediaries created such as elemental S and polysulfides, between FeS_2 and SO_4^{2-} (Balci *et al.*, 2007) (Figure 5.2). There is no fractionation during the oxidation of pyrite to aqueous sulfate when molecular oxygen is present and no significant sulfur isotope fractionation

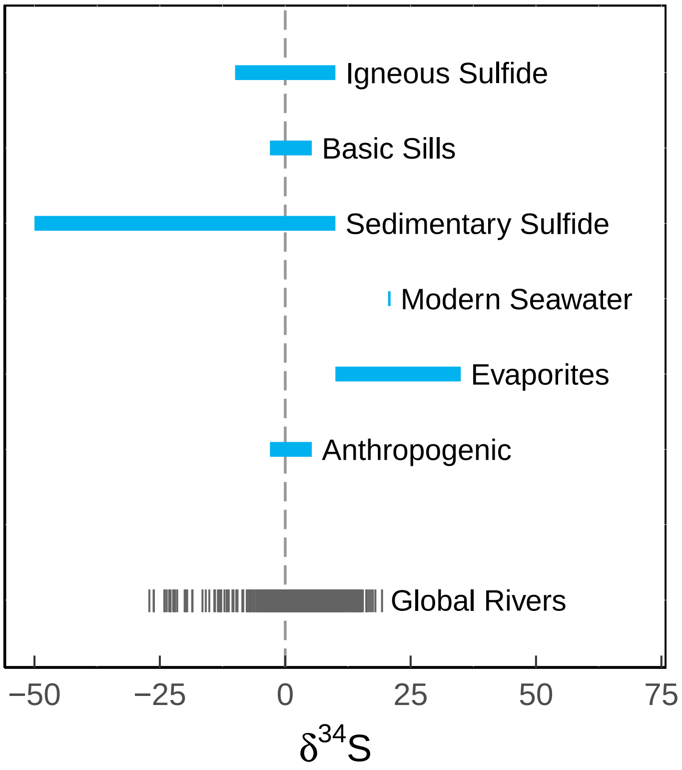

Figure 5.1: Range of δ^{34}S in dissolved sulfate of global rivers and δ^{34}S signature of sulfur sources. Global rivers span a large range of $\delta^{34}S_{SO_4}$ (Yang *et al.*, 1996; Karim & Veizer, 2000; Li *et al.*, 2006; Brenot *et al.*, 2007; Calmels *et al.*, 2007; Yoon *et al.*, 2008; Rock & Mayer, 2009; Yuan & Mayer, 2012; Turchyn *et al.*, 2013; Li *et al.*, 2014b, 2015; Hindshaw *et al.*, 2016; Torres *et al.*, 2016; Burke *et al.*, 2018; Zolkos *et al.*, 2018; Killingsworth *et al.*, 2018) however there is overlap between the many sources of sulfur. Igneous sulfides have δ^{34}S values in a narrow range from -10‰ to +10‰ (Chakrapani & Veizer, 2006), specifically basic sills range from -3.05‰ to 5.30‰ centered over 0‰, or the primordial δ^{34}S value highlighted by the dotted grey line (Shima *et al.*, 1963). Sedimentary sulfides have a large range of δ^{34}S values from -50‰ to +10‰ (Goldhaber, 2003; Kendall & Doctor, 2003; Strauss, 1997; Krouse *et al.*, 1991) which is an indication that the rock is not of primary origin or has been involved with biological cycles (Thode, 1991). Modern seawater has a distinct δ^{34}S value of 20.99‰ (Rees *et al.*, 1978; Kampschulte & Strauss, 2004) and marine evaporites range from +10 to +35‰ depending on age of evaporite (Claypool *et al.*, 1980; Chakrapani & Veizer, 2006). Anthropogenic sulfate in rainwater has a small range of -2.5‰ to 8‰ (Krouse & Mayer, 2000).

during the dissolution of gypsum (Kendall & Doctor, 2003).

Sulfur isotopes give an indication of source and process, however the overlap of end members and biological fractionation factors make δ^{34}S an imperfect tool for accurate source tracing. Importantly, it is difficult to distinguish with confidence between the heaviest sedimentary sulfide δ^{34}S and the lightest evaporite signatures, which has consequences for calculating pyrite weathering budgets (Burke *et al.*, 2018). To provide further constraints on the source of sulfate to rivers, oxygen isotopes in the SO_4^{2-} ion, $\delta^{18}O_{SO_4}$ are a complimentary combination to $\delta^{34}S_{SO_4}$ measurements. Whilst the $\delta^{34}S_{SO_4}$ in rivers should be controlled by the local δ^{34}S of the end-member lithology and any isotopic fractionations (Claypool *et al.*, 1980; Thode, 1991), $\delta^{18}O_{SO_4}$ should be controlled by the isotopic composition of the oxygen that is incorporated into the SO_4^{2-} ion at the time that the S-O bond is formed (Singer & Stumm, 1970; Claypool *et al.*, 1980). Once formed, the dissolved SO_4^{2-} can be transported far from it's source location and still retains it's original $\delta^{18}O_{SO_4}$ signature due to the strong S-O bond and very slow exchange between sulfate and water (Lloyd, 1968). Oxygen isotopes in sulfate therefore track the mechanism of sulfate formation (e.g. precipitation, or anaerobic or aerobic oxidation) and thereby provide an additional constraint on the origin of sulfate (Robinson & Bottrell, 1997; Karim & Veizer, 2000; Pawellek *et al.*, 2002; Calmels *et al.*, 2007; Turchyn *et al.*, 2013).

5.2.2 Tracing Sulfate Sources with Oxygen Isotopes in Dissolved Sulfate, $\delta^{18}O_{SO_4}$

In the case of sedimentary sulfates, such as gypsum ($CaSO_4{\cdot}H_2O$) or anhydrite ($CaSO_4$) evaporite minerals, the S-O bond is fixed at the time of precipitation, therefore $\delta^{18}O_{SO_4}$ will reflect the $\delta^{18}O$ of the water at the time of formation (in addition to any isotopic fractionation from the water) (Claypool *et al.*, 1980; Strauss, 1997). During weathering and dissolution of gypsum where sulfate is released into rivers, the S-O bond is not broken and the isotopic composition of the sulfate molecule still reflects that of the gypsum source (Equation 5.4)

$$CaSO_{4(s)} + H_2O \rightarrow Ca^{2+}_{(aq)} + SO^{2-}_{4\ (aq)} + H_2O \tag{5.4}$$

However, the oxidation of sulfide to sulfate is more complex, with multiple reaction pathways that produce SO_4^{2-} as a final product, and multiple sources of oxygen that can be incorporated into any of the four S-O bonds. The oxygen incorporated into sulfate can come from two distinct sources: H_2O which has a distinct light local signature (typically meteoric $\delta^{18}O_{H_2O}$ is between

-15‰ to 0‰ for mid-latitudes (Lee *et al.*, 2007)) or atmospheric O_2, either gaseous or dissolved, which has a heavy $\delta^{18}O$ signature of 23‰ (Kroopnick & Craig, 1972). The local water involved in oxidation reactions is predominantly rainwater, but could potentially include a mix of snowmelt (water sources derived from precipitation are collectively referred to as meteoric water, Coplen *et al.*, 2000), hot springs and older groundwater.

During the oxidation of sulfide to sulfate (S^{6+}) a total of seven or eight electrons are transferred per atom of S, depending on the mineral being a mono- (S^{-}) or di- (S^{2-}) sulfide (Taylor *et al.*, 1984b; Moses *et al.*, 1987; Heidel & Tichomirowa, 2011). Electrons are transferred step-wise, two at a time, through multiple reaction pathways forming many intermediate reaction species (Figure 5.2). The proportion of oxygen incorporated from available sources is influenced by the intermediate reactions and their products (Moses & Herman, 1991).

The source of oxygen available to participate in sulfide oxidation is determined by the environment in which the reaction takes place. Sulfide oxidation can occur in an anaerobic environment where sulfide is oxidised by the reduction of ferric iron or in an aerobic environment where molecular oxygen is available to be the oxidant. Anaerobic, or closed environments are typically aqueous (Bottrell & Tranter, 2002) where the reaction site is not open to the atmosphere (Figure 2.1, D). Aerobic environments, for example a rock fracture or rock surface exposed by land-sliding (Emberson *et al.*, 2018), are accessible to the atmosphere (Figure 2.1, C). Each reaction pathway results in variable amounts of O_2 incorporation from meteoric H_2O and atmospheric O_2.

5.2.2.1 Anaerobic Sulfide Oxidation

In anoxic environments pyrite, FeS_2, is rapidly oxidised via the reduction of ferric iron (Fe^{3+}) (Balci *et al.*, 2007). Reaction 5.5 describes this overall reaction (Moses *et al.*, 1987; Calmels *et al.*, 2007; Torres *et al.*, 2016) however this is a simplification of the progressive oxidation of intermediate sulfoxy species (Mazumdar *et al.*, 2008). In order to understand how and where oxygen is incorporated into SO_4^{2-} the sulfide oxidation mechanism will now be described in more detail.

$$FeS_2 + 14Fe^{3+} + 8H_2O \rightarrow 15Fe^{2+} + 2SO_4^{2-} + 16H^+ \tag{5.5}$$

The oxidation process has three initial steps for the transfer of electrons between sulfide and the oxidant (Luther, 1987; Moses & Herman, 1991), Fe^{3+} in this anaerobic scenario. The first step is the removal of a water ligand from an aqua-iron complex, hexaaquairon(III) or $Fe(H_2O)_6^{3+}$,

Figure 5.2a . This is a fast mechanism and produces a Lewis acid, $Fe(H_2O)_5^{3+}$, or a chemical species capable of accepting electrons (Luther, 1987). Next, the aqua-iron complex binds to the surface of FeS_2 where one S acts as a Lewis base, able to donate electrons (Luther, 1987). Finally electrons can transfer from S in FeS_2 to Fe^{3+} in the aqua-iron complex, Figure 5.2b (Luther, 1987; Rimstidt & Vaughan, 2003). For each pair of electrons that reduce two Fe^{3+} ions to Fe^{2+}, a O^{2-} ion is added to the terminal S of FeS_2 from H_2O, Figure 5.2c (Luther, 1987). The species produced, FeS_2O is unstable so steps 1 to 3 are repeated three times with continuous transfer of electrons from pyrite-S to additional $Fe(H_2O)_5^{3+}$ complexes until FeS_2O_3 is formed, which decomposes to Fe^{2+} and thiosulfate, $S_2O_3^{2-}$ (Luther, 1987). The overall reaction between sulfide and the first intermediate S species is described in Reaction 5.6 (Moses *et al.*, 1987; Luther, 1987).

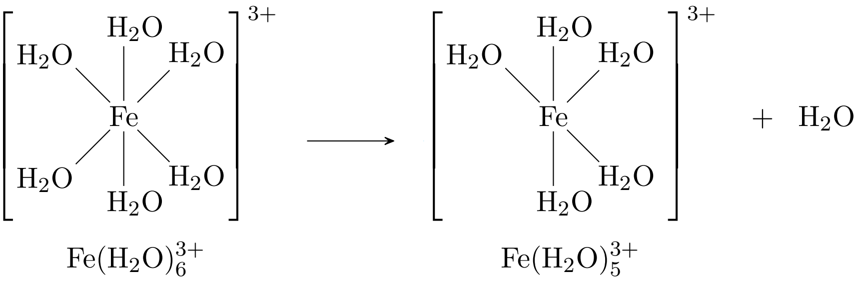

(a) Step 1: Removing water ligand from aqua-iron complex, producing a Lewis acid, $Fe(H_2O)_5^{3+}$

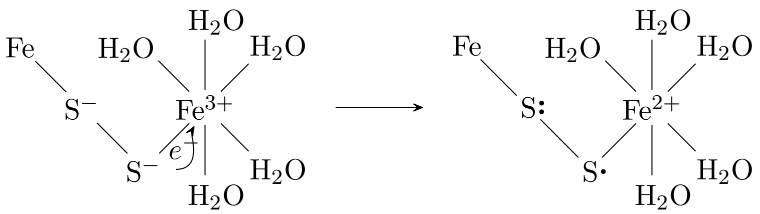

(b) Step 2: Aqua-iron complex $Fe(H_2O)_6^{3+}$ binds to pyrite. Terminal pyrite-S donates 1 electron to $Fe(H_2O)_6^{3+}$

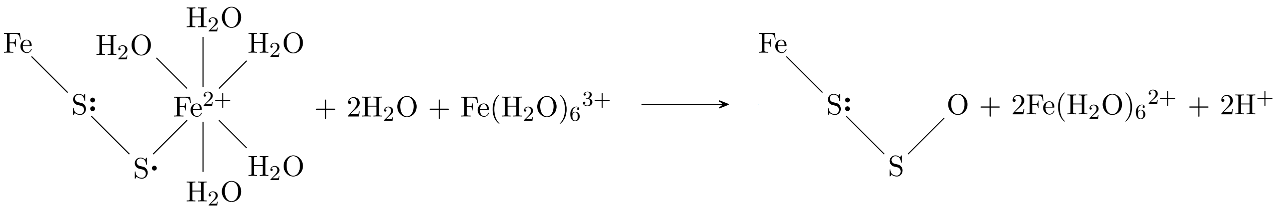

(c) Step 3: Pyrite further reacts with another aqua-iron complex, donating 1 more electron and adding one oxygen atom to the terminal pyrite-S to create FeS_2O

Figure 5.2: Reaction pathway of oxidation of pyrite to thiosulfate. Figure adapted from Moses *et al.* (1987, Figure 9) and Luther (1987).

$$FeS_2 + 6Fe(H_2O)_6^{3+} + 3H_2O \rightarrow Fe^{2+} + S_2O_3^{2-} + 6Fe(H_2O)_6^{2+} + 6H^+ \tag{5.6}$$

In an environment with excess Fe^{3+}, thiosulfate is oxidised to SO_4^{2-} via Reaction 5.7 (Luther, 1987). Reaction 5.6 and 5.7 sum to Reaction 5.5. In this scenario all oxygen in the final SO_4^{2-} molecule is derived from meteoric water which will have a distinctive local isotopic composition.

$$S_2O_3^{2-} + 8Fe^{3+} + 5H_2O \rightarrow 8Fe^{2+} + 2SO_4^{2-} + 10H^+ \tag{5.7}$$

Whilst Fe^{3+} is the direct oxidant of pyrite, in natural waters Fe^{2+} is adsorbed to pyrite surfaces which blocks the reaction site (Moses & Herman, 1991; Mazumdar *et al.*, 2008). In this case, to initiate the oxidation of sulfide, adsorbed aqua-iron complexes, $Fe(H_2O)_6^{2+}$, are oxidised via reduction of dissolved molecular O_2 to $Fe(H_2O)_6^{3+}$ (Moses & Herman, 1991; Heidel & Tichomirowa, 2011). The oxygen acts as an oxidizer and is not incorporated into the S-O bond. At low pH (pH <3) the oxidation of Fe^{2+} (Reaction 5.8) becomes rate limiting because abiotic oxidation of Fe^{2+} to Fe^{3+} is slow (Singer & Stumm, 1970). Microorganisms however, for example the acidophilic chemolithotroph Thiobacillus ferrooxidans, are able to accelerate Reaction 5.8 by up to a factor of 10^6 (Singer & Stumm, 1970).

$$Fe^{2+} + O_{2(aq)} \rightarrow Fe^{3+} \tag{5.8}$$

It is clear from the mechanism described in Figure 5.2 that all oxygen in SO_4^{2-} derived via the oxidation of sulfide through Fe^{3+} reduction, is incorporated from oxygen in meteoric water (H_2O) and therefore the oxygen in the sulfate molecule ($\delta^{18}O_{SO_4}$) has the same isotopic composition as the oxygen in meteoric water ($\delta^{18}O_{H_2O}$). To prove this, various experiments (eg. Taylor *et al.*, 1984b; van Everdingen & Krouse, 1985; Balci *et al.*, 2007) have measured $\delta^{18}O_{H_2O}$ and $\delta^{18}O_{SO_4}$ in sulfate derived from anaerobically oxidised sulfide. They found a strong positive correlation between $\delta^{18}O_{H_2O}$ and $\delta^{18}O_{SO_4}$ but with a small offset, indicating a small kinetic isotope fractionation during water-oxygen incorporation into SO_4^{2-}. The fractionation factor for oxygen between sulfate and water, $\varepsilon_{SO_4-H_2O}$, was quantified as 2.9‰ (Balci *et al.*, 2007) and 4.1‰ (Taylor *et al.*, 1984b) in anaerobic environments, which is significant but far smaller than that of the total range of meteoric water, ~50‰ (IAEA, 2019).

5.2.2.2 Aerobic Sulfide Oxidation

The oxidation of sulfide to sulfate can also involve atmospheric O_2 as an oxidant (Reaction 5.9).

$$FeS_2 + \frac{7}{2}O_2 + H_2O \rightarrow Fe^{2+} + 2SO_4^{2-} + 2H^+ \tag{5.9}$$

Early studies suggest that 87.5% atmospheric derived oxygen and 12.5% meteoric water derived oxygen is incorporated into SO_4^{2-} via the stoichiometry in Reaction 5.9 (Taylor *et al.*, 1984a). However, developments lead by scientists researching acid mine drainage have shown that in fact less than 15% of the oxygen incorporated into SO_4^{2-} in aerobic environments is derived from atmospheric O_2 (Balci *et al.*, 2007). The fraction of oxygen incorporated into sulfate both from water and atmospheric sources has since been calculated from sulfide oxidation experiments conducted in aerobic conditions with water and oxygen reactants with known $\delta^{18}O_{H_2O}$ and $\delta^{18}O_{atm}$ isotopic signatures. Mazumdar *et al.* (2008) calculate that 83 to 99.8% of sulfate oxygen is derived from water, in good agreement with the value calculated by Balci *et al.* (2007). The oxygen isotope signature of sulfate which formed in these aerobic experiments indicate that H_2O is the main contributor to sulfate-oxygen with only a minor contribution from molecular O_2 (Balci *et al.*, 2007; Mazumdar *et al.*, 2008), indicating that Reaction 5.9 is a simplification of multiple reactions occurring on the pyrite surface.

The oxygen-isotope fractionation factor between sulfate and water, $\varepsilon_{SO_4-H_2O}$, is similar for sulfide oxidation in aerobic (2.3‰ (Heidel & Tichomirowa, 2011), 2.6‰ (Mazumdar *et al.*, 2008), 2.8‰ (Balci *et al.*, 2007)) and anaerobic (2.9‰ (Balci *et al.*, 2007)) environments, indicating that the mechanism of oxygen incorporation into the sulfate molecule is the same, irrespective of environment. Moreover, it is unlikely that dissolved oxygen will directly oxidise FeS_2 because paramagnetic O_2 cannot form a strong bond with the terminal S of diamagmetic FeS_2 in the same way that Fe^{3+} in aquairon(III) $Fe(H_2O)_5^{3+}$ can (Luther, 1987; Balci *et al.*, 2007). Therefore, in the same way as described for anaerobic oxidation of sulfide, Figure 5.2, it is Fe^{3+} that acts as the direct oxidant of FeS_2 in aerobic environments with the same step-wise transfer of electrons between S and Fe^{3+}. The step-wise oxidation pathway creates intermediate sulfur species and it is the oxidation of these species to sulfate, where dissolved molecular O_2 is incorporated.

The oxidation reaction pathway of sulfide to sulfate is complex. The schematic Figure 5.3 indicates the cyclical nature of the oxidation pathways of sulfide to sulfate through a series of sulfur intermediate species. The key sulfur compounds and key reactants are shown in

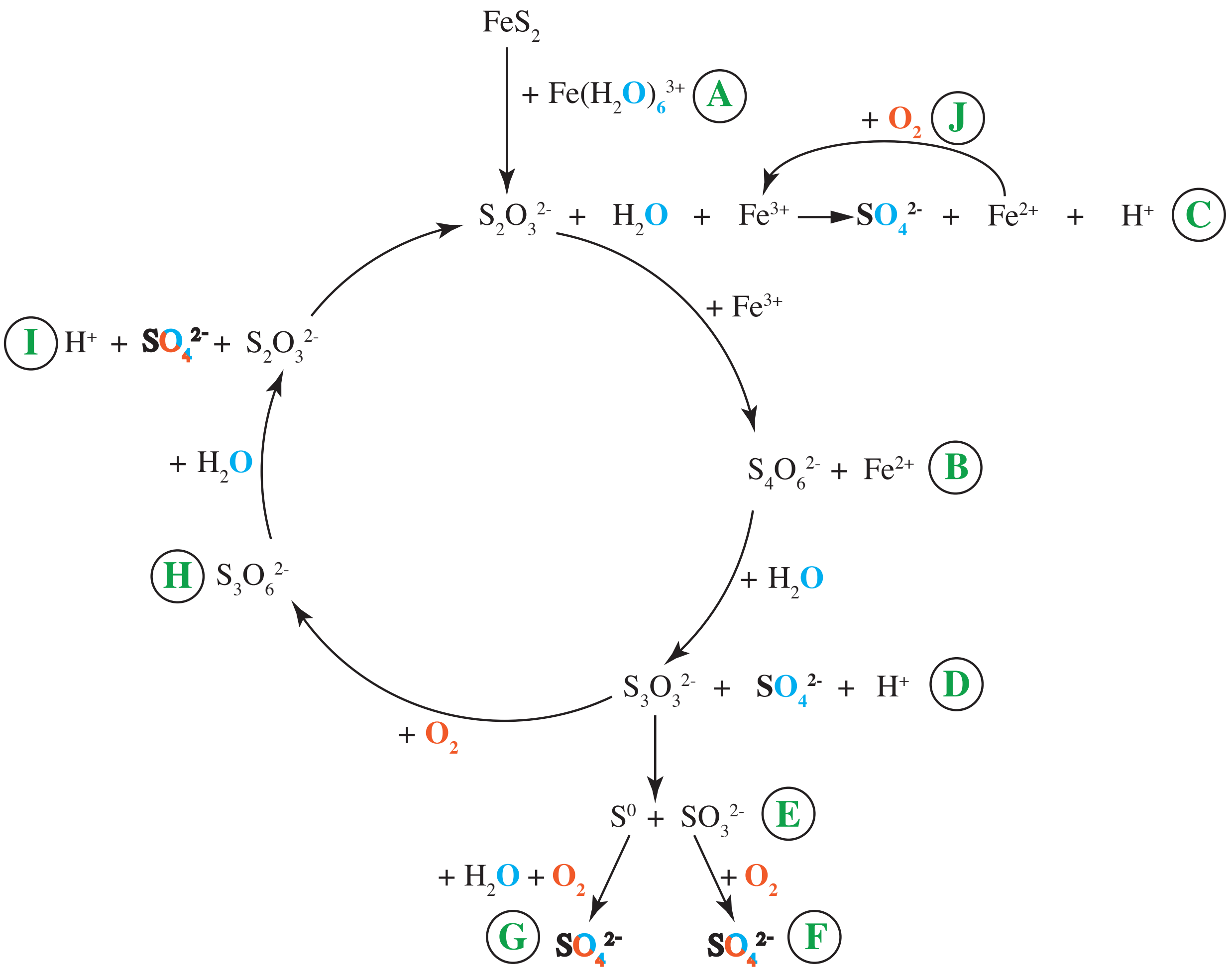

Figure 5.3: Schematic diagram of the complex reaction pathways of oxidation of sulfide to sulfate through intermediate sulfur species. Redrawn and adapted from Schippers *et al.* (1996, Figure 5). The key reactants and products are shown, and meteoric water (blue) and atmospheric oxygen (orange) sources are highlighted (note however, the reactions are not balanced). A: Initial sulfide oxidation to thiosulfate (Equation 5.6) (Moses *et al.*, 1987; Luther, 1987). B: Fast oxidation of thiosulfate to tetrathionate (Schippers *et al.*, 1996, Equation 5). C: Oxidation of thiosulfate to sulfate with excess Fe^{3+} (Equation 5.7) (Luther, 1987, Equation 6). D: Hydrolysis of tetrathionate produces disulfane-monosulfonic acid (DMA), sulfate and acidity (Schippers *et al.*, 1996, Equation 6). E: DMA decomposes to elemental sulfur and sulfite (Schippers *et al.*, 1996, Equation 10). F: Sulfite is chemically oxidised to sulfate incorporating atmospheric oxygen into the sulfate (Balci *et al.*, 2007, Equation 13). G: Elemental sulfur incorporates oxygen from both sources during its oxidation to sulfate (Schippers *et al.*, 1996, Equation 3). H: DMA can be oxidised to further intermediate sulfur species such as trithionate. DMA is oxidised by molecular oxygen so 50% of the oxygen in trithionate will be atmospheric in origin (Schippers *et al.*, 1996, Equation 9). I: Trithionate is hydolized to sulfate, containing atmospheric oxygen and meteoric water derived oxygen, and thiosulfate which can start the cycle again (Schippers *et al.*, 1996). J: Fe^{2+} produced by the reduction of Fe^{3+}in sulfur species oxidation is reoxidised to Fe^{3+} using molecular O_2. This Fe^{3+} can then participate in further oxidation reactions. This reaction which can happen at any point in the cycle with Fe^{2+} is the rate limiting step to sulfide oxidation (Singer & Stumm, 1970).

Figure 5.3, starting with the first intermediate sulfur species formed in Reaction 5.6, thiosulfate $S_2O_3^{2-}$ (Figure 5.3A). During sulfide oxidation experiments thiosulfate is rarely measured because it is quickly oxidised to tetrathionate, $S_4O_6^{2-}$ (Figure 5.3B) or to sulfate as in Reaction 5.7 (Figure 5.3C) (Rimstidt & Vaughan, 2003; Schippers *et al.*, 1996). Hydrolysis of tetrathionate produces disulfane-monosulfonic acid, sulfate and acidity in the form of H^+ ions (Schippers *et al.*, 1996) (Figure 5.3D). The sulfate product of this reaction contains oxygen solely from meteoric H_2O (Figure 5.3D). Disulfane-monosulfonic acid is highly reactive and degrades to elemental sulfur, S^0 or sulfite, SO_3^{2-} (Figure 5.3E). These sulfur species use molecular O_2 as the oxidant when they oxidise to SO_4^{2-} (Heidel & Tichomirowa, 2011) (Figure 5.3G,F). Disulfane-monosulfonic acid can react with molecular O_2 directly to form trithionate, $S_3O_6^{2-}$ (Figure 5.3H). The trithionate molecule may contain up to 50% oxygen from O_2. Trithionate can then be hydrolysed to SO_4^{2-} (Figure 5.3I) which can contain a fraction of molecular O_2. Fe^{2+} adsorbed to the pyrite surface or produced by the oxidation of pyrite can also be oxidised back to Fe^{3+} at any point during the cycle, which also provides an oxidant for pyrite oxidation (however, only represented once on the cycle in Figure 5.3). Importantly, the isotopes of oxygen from meteoric and atmospheric sources have very different compositions, therefore the source of oxygen in the reactions can be determined using a simple mass balance approach, discussed in Section 5.2.4.

5.2.3 Microbial Impact on Sulfide Oxidation

Many of the reaction pathways are biologically driven. An experiment by Balci *et al.* (2007) demonstrated that reactions in the presence of bacteria proceed at a faster rate than abiotic experiments, particularly in aerobic environments where bacteria increases sulfate production rates by up to two orders of magnitude. Whilst it is not possible to determine if the reaction was microbially mediated using $\delta^{18}O_{SO_4}$ (Toran & Harris, 1989), it is reasonable to assume that bacteria is present within the critical zone throughout the entirety of the Mekong Basin. It is important to stress, however, that multiple experiments have shown oxidation of pyrite via Fe^{3+} reduction is up to three orders of magnitude faster than aerobic oxidation (Moses & Herman, 1991; Balci *et al.*, 2007; Mazumdar *et al.*, 2008; Heidel & Tichomirowa, 2011) due to the ability for $Fe^{3+}$to directly react with the pyrite surface.

An additional process that sulfur and oxygen isotopes in SO_4^{2-} could record, is bacterial sulfate reduction (BSR) (Turchyn *et al.*, 2013). In anaerobic environments, bacteria respire utilising SO_4^{2-}, generating hydrogen sulfide (H_2S) and oxidising organic matter in the process (Aharon &

Fu, 2000; Mandernack *et al.*, 2003) (Equation 5.10). There are substantial fractionation factors associated with BSR (Kaplan & Rittenberg, 1964; Detmers *et al.*, 2001). The light sulfur isotope, ^{32}S, is preferentially incorporated into H_2S, fractionating the remaining SO_4^{2-} by up to 70‰ (Aharon & Fu, 2000; Turchyn *et al.*, 2013). There is a much smaller fractionation involved in the oxygen of the remaining SO_4^{2-} however this may still be up to -9.8‰ (Mandernack *et al.*, 2003).

$$SO_4^{2-} + 2CH_2O \rightarrow H_2S + 2HCO_3^- \tag{5.10}$$

Downstream trends in the Marsyandi river display progressively increasing $\delta^{34}S_{SO_4}$ and $\delta^{18}O_{SO_4}$. This trend cannot be explain with mixing between gypsum and oxidative pyrite weathering sources and therefore Turchyn *et al.* (2013) cite BSR in groundwaters, which are continually added to the Marsyandi, as the cause of the trend. It may be possible to track BSR where there is a high sampling frequency in a small catchment. However it is more difficult when samples have been collected at the mouth of tributaries and the sample is representative of all sources and processes within the sub-catchment. Unless there is good knowledge of the end members within the catchment and BSR is the only possible explanation for samples that do not fit within the end members, such as in the Marsyandi (Turchyn *et al.*, 2013), it is unlikely that BSR could be established from a spot sample. For example, there are at least four possible explanations for sulfate measured with positive $\delta^{34}S_{SO_4}$ and $\delta^{18}O_{SO_4}$. Firstly, the SO_4^{2-} could be sourced from gypsum weathering, secondly, the sulfate could have been sourced from a Permian gypsum with light $\delta^{18}O_{SO_4}$ and $\delta^{34}S_{SO_4}$ (Claypool *et al.*, 1980), but the measured isotopic signature is heavy due to subsequent BSR thus reflecting an evaporite of Silurian age. Thirdly the source of SO_4^{2-} could have been oxidation of pyrite with a negative $\delta^{34}S_{SO_4}$ and $\delta^{18}O_{SO_4}$ and subsequent BSR has left the remaining SO_4^{2-} with an isotope signature similar to SO_4^{2-} sourced from gypsum. The consequence of the latter explanation is that oxidative pyrite weathering is underestimated. Additionally, the H_2S generated by BSR could be reoxidised forming sulfate with $\delta^{34}S_{SO_4}$ similar to the sulfide but a negative $\delta^{18}O_{SO_4}$ reflective of the local water incorporated into the SO_4^{2-} molecule. It is clear that BSR dramatically effects SO_4^{2-} isotopic composition, but establishing if it is a process and moreover quantifying the extent to which it is occurring is difficult.

5.2.4 Quantifying Sulfide Oxidation Oxygen Source

Using a simple mass balance equation the range of possible values of oxygen isotopes in dissolved sulfate derived by oxidation of sulfide, $\delta^{18}O_{SO_4pyr}$, can be calculated using the following Equation:

$$\delta^{18}O_{SO_4\ pyr} = f_{O_2atm}\left(\delta^{18}O_{atm} + \epsilon_{O_2}\right) + f_{H_2O}\left(\delta^{18}O_{H_2O} + \epsilon_W\right) \tag{5.11}$$

$$f_{O_2atm} + f_{H_2O} = 1 \tag{5.12}$$

Where $\delta^{18}O_{atm}$ is the oxygen isotope value of atmospheric oxygen, 23‰ (Kroopnick & Craig, 1972) and $\delta^{18}O_{H_2O}$ is the oxygen isotope value of local water. The oxygen isotope signature of local water varies spatially, with greater than 40‰ range in global $\delta^{18}O_{H_2O}$ values (Bowen & Revenaugh, 2003). Local water is mostly meteoric which is derived from precipitation, therefore the four main factors controlling isotope values in precipitation are reflected in the local water signature of oxygen, $\delta^{18}O_{H_2O}$, and hydrogen, δD, isotopes. Increases in altitude, latitude and greater amounts of rainfall decrease $\delta^{18}O$ and δD values, as does increasing distance from the coast which decreases isotope values inland, this is known as the continental effect (Kendall & Doctor, 2003). These geographical and environmental factors define $\delta^{18}O_{H_2O}$ values unique to each river system.

$\varepsilon_{SO_4-O_2}$ and $\varepsilon_{SO_4-H_2O}$ are the fractionation factors between oxygen and sulfate and water and sulfate, respectively. Sulfide oxidation experiments have quantified $\varepsilon_{SO_4-O_2}$ between -8.4‰ to -11.4‰ (Taylor *et al.*, 1984b; Balci *et al.*, 2007; Heidel & Tichomirowa, 2011). An average value of -10.1‰ is used for $\varepsilon_{SO_4-O_2}$. The value for $\varepsilon_{SO_4-H_2O}$ is 2.9‰. f_{O_2atm} is the fraction of oxygen in sulfate derived from atmospheric O_2 and f_{H_2O} is the fraction of oxygen in sulfate derived from meteoric water. f_{O_2atm} and f_{H_2O} sum to 1. Using these parameters, a unique range of possible $\delta^{18}O_{SO_4pyr}$ end member values can be calculated for each sample. The lower bound for $\delta^{18}O_{SO_4pyr}$ is where all oxygen in sulfate is derived from meteoric water, or f_{H_2O}=1. The upper bound for the $\delta^{18}O_{SO_4pyr}$ value is where 17% of oxygen in sulfate is atmospheric due to aerobic sulfide oxidation, f_{O_2atm}=0.17. This maximum contribution from molecular oxygen has been constrained through sulfide oxidation experiments in controlled environments. Balci *et al.* (2007) calculates 85-92% of oxygen in SO_4^{2-} is derived from H_2O which is in good agreement with Mazumdar *et al.* (2008) who calculate molcular O_2 contributes 83-99.8% to sulfate-oxygen implying f_{O_2} is small and so taking a value of f_{O_2atm}=0.17 for the maximum amount of O_2 incorporation is a conservative amount.

5.2.5 Global Trends in Sulfate Source

The array defined by the global compilation of $\delta^{34}S_{SO_4}$ and $\delta^{18}O_{SO_4}$ in world rivers (Figure 5.4) highlights the range of sulfate sources. Rivers draining Arctic catchments, in Canada and Svalbard all have mostly negative $\delta^{18}O_{SO_4}$ and $\delta^{34}S_{SO_4}$ signature because they drain sedimentary sulfide lithologies (Calmels *et al.*, 2007) and the higher altitude and latitude of these catchments is reflected in the light local water which is incorporated into $\delta^{18}O_{SO_4}$. The few samples that have positive $\delta^{34}S_{SO_4}$ may drain magmatic sulfides. The range in δ^{34}S signature of sedimentary sulfides can be seen, the data with negative $\delta^{18}O_{SO_4}$ spans ~35‰ but samples with positive $\delta^{18}O_{SO_4}$ have positive $\delta^{34}S_{SO_4}$ in the range of 0‰ to ~15‰ which are characteristic of sedimentary sulfate sources. The overall array of world data suggests a mixing trend between sedimentary sulfates and sedimentary sulfides but individual catchments show tighter trends dominated by a particular lithology or they may have been influenced by secondary reduction, for example bacterial sulfate reduction (Turchyn *et al.*, 2013).

Another useful tool used to establish if rivers are draining sedimentary sulfides, is to compare the oxygen in the sulfate and oxygen in the water (Figure 5.5). If rivers are draining sedimentary sulfides there will be a strong positive relationship between oxygen in the water and oxygen in the dissolved sulfate. The reaction pathway of oxidative sulfide weathering, whether aerobic or anaerobic will determine the source of oxygen incorporated into SO_4^{2-} and therefore the exact relationship between $\delta^{18}O_{H_2O}$ and $\delta^{18}O_{SO_4}$ (contours on Figure 5.5 display the possibilities of this relationship depending on atmospheric O_2 incorporation), although it is likely that there is less than 17% oxygen incorporated from atmospheric O_2 (discussed in Section 5.2.2.1). Samples from Svalbard sit between the lowest contours of atmospheric O_2 incorporation indicate of oxidative weathering of pyrite. There is a larger spread in other samples because the sulfide end member signature is overprinted by mixing with sedimentary sulfates.

The difficulty in directly comparing the sulfate source of world rivers is the large variation in global $\delta^{18}O_{H_2O}$ which dominates 83 to 100% of the $\delta^{18}O_{SO_4}$ signal. In order to directly compare dissolved sulfate from rivers with different meteoric water signatures, the difference between $\delta^{18}O_{SO_4}$ and $\delta^{18}O_{H_2O}$ can be used ($\Delta^{18}\mathrm{O}_{SO_4-H_2O}$), taking into account a 2.9‰ $\varepsilon_{SO_4-H_2O}$ fractionation factor (Figure 5.6). In a similar way to Figure 5.5 which compares the relationship between oxygen of local meteoric water and oxygen in the sulfate, $\Delta^{18}\mathrm{O}_{SO_4-H_2O}$ corrects $\delta^{18}O_{SO_4}$ for the local meteoric water signature. The closer this variable is to zero, it suggests that more of the dissolved sulfate is delivered by the anaerobic oxidative weathering of sulfide where all of the oxygen in

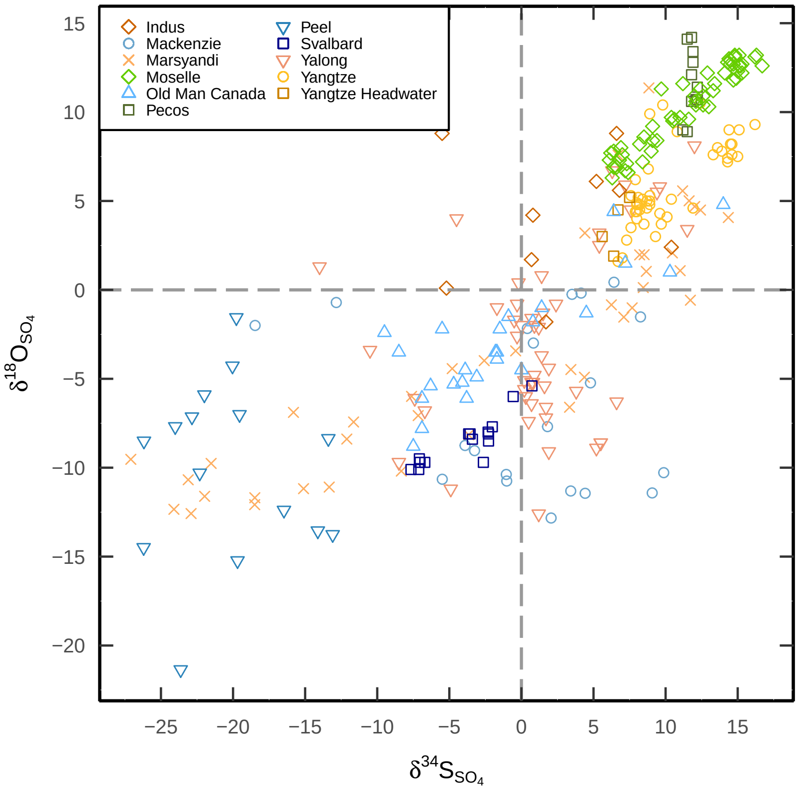

Figure 5.4: Sulfur and oxygen isotopes in dissolved sulfate of world rivers. The data presented is a literature compilation from the Yalong River and it's tributaries draining the eastern Tibetan Plateau, China (Li *et al.*, 2014b), which feeds into the Yangtze River (Li *et al.*, 2015), also Min Jiang, a headwater tributary of the Yangtze River (Yoon *et al.*, 2008), Svalbard, the glaciated Dryadbreen catchment and the unglaciated Fardalen catchment (Hindshaw *et al.*, 2016), Peel River (Zolkos *et al.*, 2018), Pecos River in New Mexico, USA (Yuan & Mayer, 2012), Moselle River in France (Brenot *et al.*, 2007), Oldman River Basin in Alberta (Canada) (Rock & Mayer, 2009), Marsyandi (Turchyn *et al.*, 2013), rivers draining the Sichuan basin (Li *et al.*, 2006), the Indus River (Karim & Veizer, 2000) and the Mackenzie River in Canada (Calmels *et al.*, 2007). The colours categorize samples into Arctic and Canadian rivers (blues), Asian rivers (oranges) and other rivers from N.America and Europe (greens).

the sulfate is derived from meteoric water. The further away $\Delta^{18}O_{SO_4-H_2O}$ is from zero there is influence from gypsum or incorporation of atmospheric oxygen into the sulfate.

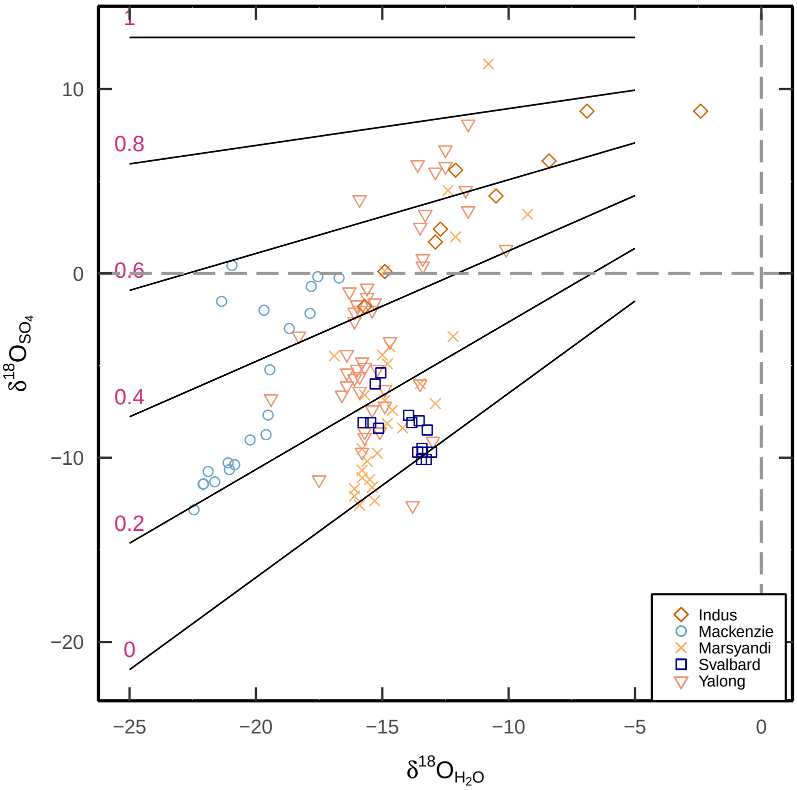

Figure 5.5: Oxygen isotopes in water and dissolved sulfate. Contours are drawn for sulfide derived SO_4^{2-} where the fraction (red values between 0 and 1) is the amount of atmospheric O_2 (f_{O_2atm}) incorporated into SO_4^{2-}during oxidative weathering of pyrite. If all oxygen in SO_4^{2-} is derived from meteoric H_2O, f_{O_2atm}=0, then $\delta^{18}O_{SO_4}$ is the same as $\delta^{18}O_{H_2O}$ taking into account fractionation. Increasing incorporation of atmospheric O_2 into SO_4^{2-} decreases the gradient of the relationship between $\delta^{18}O_{SO_4}$ and $\delta^{18}O_{H_2O}$. Interpretation of this diagram is complicated because sulfide oxidation signals are obscured by mixing of other sources such as sedimentary sulfates. Rivers draining sedimentary sulfide dominated lithologies have a strong positive correlation between oxygen in meteoric water, $\delta^{18}O_{H_2O}$ and oxygen in dissolve sulfate $\delta^{18}O_{SO_4}$. Within the global river water data, given that sedimentary sulfate signals have not been corrected for, the Mackenzie River basin (Calmels *et al.*, 2007) and the Indus river (Karim & Veizer, 2000) still show a positive correlation between $\delta^{18}O_{SO_4}$ and $\delta^{18}O_{H_2O}$ as both are dominated by shales containing pyrite. (Sources are given in caption for Figure 5.4.)

5.3 Methodology

5.3.1 Sample Collection in the Field

Samples for sulfur and oxygen isotope analysis on dissolved sulfate were collected from 18 tributaries and 6 main stem sites in 2016 and 2017 field seasons. River waters were collected from the surface of the water column from the centre of the main channel, using either a boat (main river), or a bucket suspended from a bridge (tributary) and filtered within 6 hours of collection through 142mm 0.2μm PES filters. 2.5 litres of filtered water were discarded before collection of samples. Because

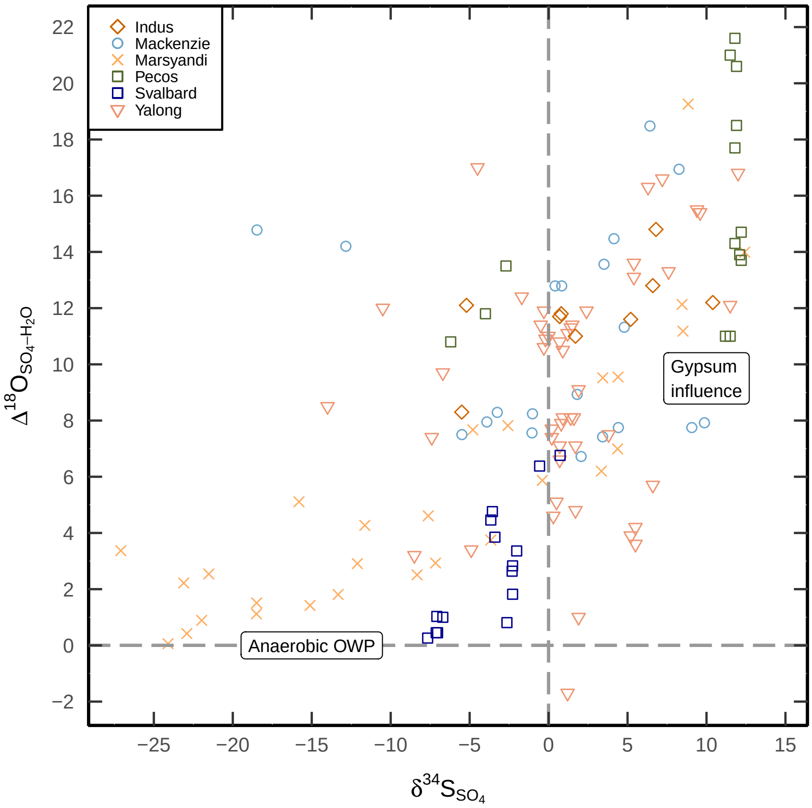

Figure 5.6: Comparison of world river data with local meteoric water signature removed. $\Delta^{18}O_{SO_4-H_2O}$ is $\delta^{18}O_{SO_4}$ corrected for local meteoric water signatures ($\delta^{18}O_{H_2O}$) and takes into account the 2.9‰ fractionation factor between SO_4^{2-} and H_2O. Removing $\delta^{18}O_{H_2O}$ from $\delta^{18}O_{SO_4}$ makes world data more comparable because the differences in local meteoric water signature are so large. This relationship is useful to compare rivers that may be draining sedimentary sulfides; SO_4^{2-} that is sourced from the anaerobic oxidative weathering of pyrite (Anaerobic OWP), will lie on a line of $\Delta^{18}O_{SO_4-H_2O}=0$. The samples are corrected for local meteoric water signatures ($\delta^{18}O_{H_2O}$) but not for other sources of oxygen in SO_4^{2-} such as atmospheric O_2 or sedimentary sulfate. The influence of these other sources are seen in samples with heavier oxygen isotopes (Gypsum influence).

of low SO_4^{2-} concentrations, a pre-concentration step was conducted in the field. Two litres of filtered river water were loaded onto columns filled with 5mL Dowex 1X8-200, 100-200 mesh, anion exchange resin (Hindshaw *et al.*, 2016). The resin was pre-conditioned with 60 mL of 3M distilled HCl, then 60 mL of 18.2MΩ H_2O. The SO_4^{2-} was stored on the resin and kept in a fridge until the time of sample preparation.

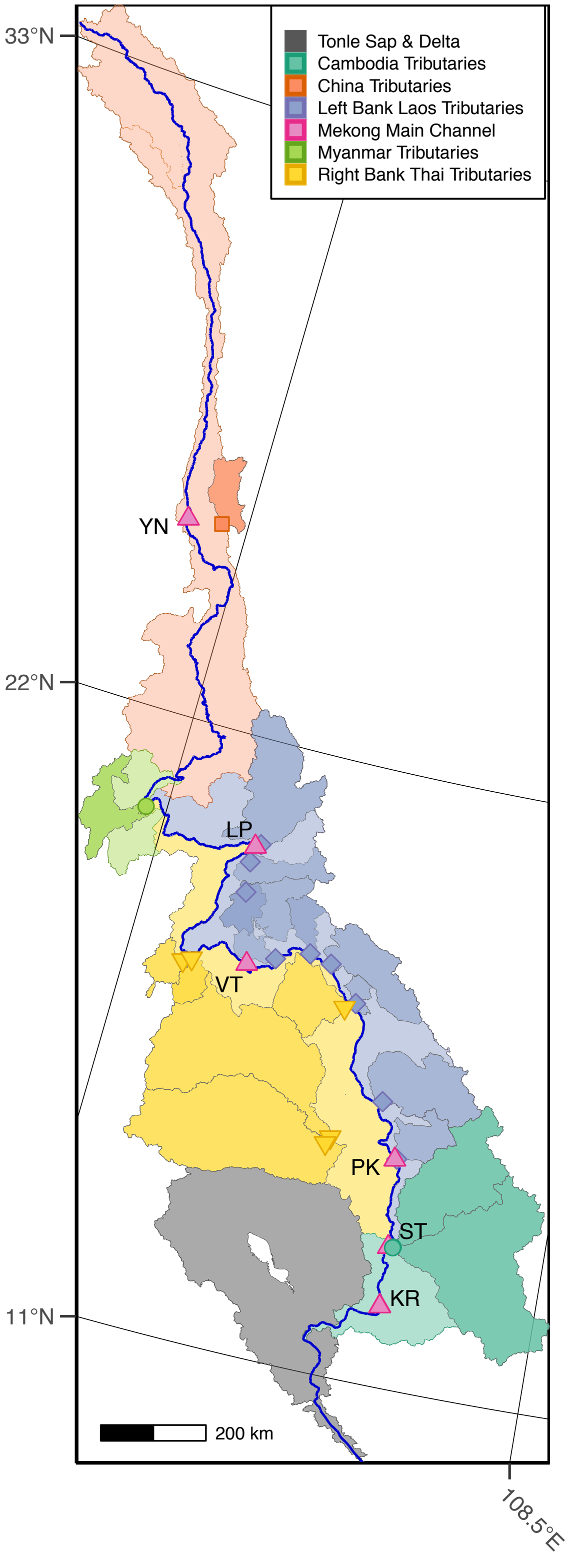

Figure 5.7: Samples collected for sulfur and oxygen isotope analysis in dissolved sulfate. Main stem sample sites (pink triangles) are Yunnan (YN), Luang Prabang (LP), Vientiane (VT), Pakse (PK), Stung Treng (ST) and Kratie (KR). Tributaries have been split into five main sections with locations of sampling denoted by a shape; China (orange squares), Myanmar and Northern Thailand (yellow green circles), Laos (purple diamonds), Thailand (yellow inverted triangle), Cambodia (blue green circles). Darker coloured areas within the sections outline the sampled catchment. Samples were collected in 2016 and 2017 field seasons for $\delta^{18}O_{SO_4}$ and $\delta^{34}S_{SO_4}$.

5.3.2 Sample Preparation in the Laboratory

Preparation took place in a class 1000 clean laboratory. Sulfate was eluted off the column with 20mLs 0.8M distilled HCl and mixed with $BaCl_2$ to precipitate barite ($BaSO_4$). Barite was cleaned with 6M HCl to remove precipitated $BaCO_3$ then rinsed three times with 18.2 MΩ H_2O. To improve purity, the barite was dissolved in 10mLs 0.05M diethylenetriaminepentaacetic acid (DTPA) then the pH of the solution was lowered to 3-4, allowing a slower reprecipitation of a purer barite which was then cleaned three times with 18.2 MΩ water (Bao, 2006). The pure barite was dried at 70°C for 12hours. Two full replicates of the method were made using OSIL IAPSO Atlantic Seawater resulting in values within error of standard seawater values (δ^{34}S=20.94‰ ±0.09 1σ, $\delta^{18}O_{SO_4}$=8.3‰ ±0.2 1σ) confirming there is no fractionation on the column.

The inevitable disturbance of the resin bed during transportation from the field to laboratories prevents elution of pure SO_4^{2-} off the columns. The single anion adsorption fronts are no longer separated within the column resin bed. Although calibration of a column in the lab (simulated to have been loaded in the field and transported back to the lab) provided a guide for anion elution profiles, SO_4^{2-} and NO_3^- were not able to be fully separated. The presence of NO_3^- in barite inclusions can significantly alter measured values of $\delta^{18}O_{SO_4}$. Oxygen in NO_3^-, if atmospheric in origin, can have $\delta^{18}O_{NO_3}$ values of up to 100‰ (Le Gendre *et al.*, 2017). Inclusions within the barite are determined by the speed of precipitation when $BaCl_2$ is added to the eluant. Dissolving the first precipitation of barite in DTPA then slowly lowering the pH of the solution allows a controlled re-precipitation of pure barite (Bao, 2006).

A test was conducted to understand how precipitated barite can be affected by other oxyanions present in the original eluant and whether DTPA was a suitable solution for removing these contaminants. Pure enriched water ($\delta^{18}O_{H_2O}$=162‰) was mixed in various ratios with Atlantic Seawater given in Table 5.1. $BaCl_2$ was mixed with the samples to precipitate $BaSO_4$ which was then cleaned with 6M HCL then three times with 18.2 MΩ H_2O. The barite was dried overnight at 70°C then an aliquot was taken for $\delta^{18}O_{SO_4}$ and $\delta^{34}S_{SO_4}$ analysis (Table 5.1, test 1). The remaining barite was dissolved in 0.05M DTPA and left overnight for full dissolution. Barite was reprecipitated slowly by adding concentrated distilled HCl to the solution, preventing the occurrence of inclusions in the barite. After removal of excess DTPA, the barite is cleaned three times with 18.2 MΩ H_2O, left to dry overnight and again sampled for analysis (Table 5.1, test 2). The barite was dissolved for a second time in DTPA and the same process repeated (Table 5.1, test 3). After each addition of DTPA, sample $\delta^{18}O_{SO_4}$ values converge on seawater values (Figure

5.8). In the most extreme mixed sample, with twice as much enriched water as seawater, DTPA removed the inclusions of enriched water in the precipitated barite, reducing the measured values from $\delta^{18}O_{SO_4}$=13.87‰ ±0.85 1σ in test 1, to $\delta^{18}O_{SO_4}$=8.97‰ ±0.53 1σ in test 2.

Table 5.1: Experiments devised to quantify improvement of barite purity

Ratio Seawater : Enriched water	**Test 1**	**Test 2**	**Test 3**
1:0	6M HCL then 18.2 MΩ H_2O x3 cleaning	DTPA treated	DTPA treated x2
1:0.067			
1:0.4			
1:2			

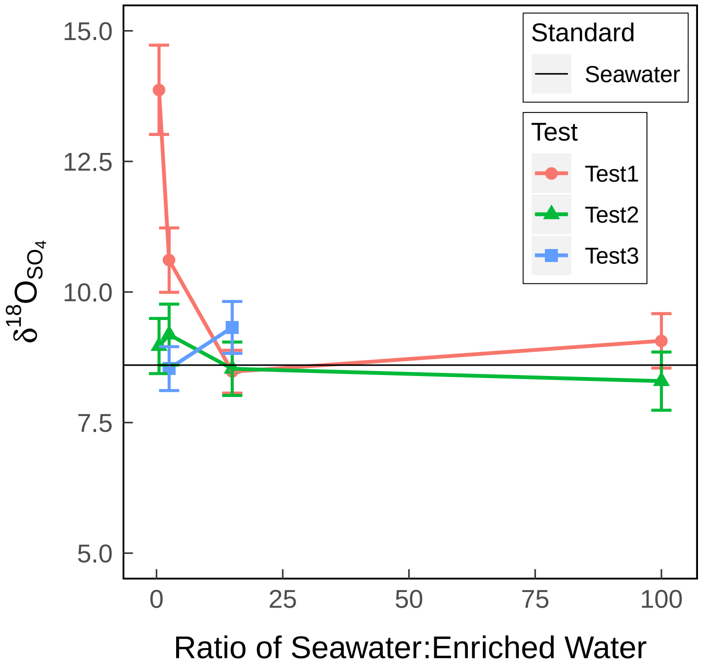

Figure 5.8: Effect of DTPA on enriched water inclusions in precipitated barite from seawater. Three tests detailed in Table 5.1 aim to improve the purity of barite precipitated from a range of solutions with variable ratios of seawater to enriched water. The effect of the enriched water in barite inclusions can be clearly seen when DTPA is not applied to barite, test 1 - red line. All samples converge on the seawater value, black line, after addition of DTPA for the first time, blue and green lines.

5.3.3 Sample Analysis

Major cation and anion analysis methodology is discussed in Chapter 3 and the results can be found in Table 4.2 and Table 4.3. Analysis of $\delta^{18}O_{SO_4}$ and $\delta^{34}S_{SO_4}$ were made by elemental analyser isotope ratio mass spectrometry (EA-IRMS) in the Godwin Laboratory, University of Cambridge. For $\delta^{18}O_{SO_4}$ analysis, 180μg barite samples and reference materials are placed in sealed silver capsules and loaded into an auto-sampler. Whilst being continuously purged with helium to prevent contamination with water, oxygen or nitrogen, they are dropped into a Thermo Finnigan High Temperature Elemental Conversion Analyser (TC/EA) consisting of a graphite crucible held at 1450°C. The gaseous products of pyrolysis (H_2, N_2, CO) are separated by a packed gas chromatographic molecular sieve column at 90°C and passed into a Thermo Delta V mass spectrometer via a ConFlo 3 for isotopic analysis. The $\delta^{18}O_{SO_4}$ isotope measurements are calibrated to V-SMOW. Samples were run in quadruple and data presented is an average of these replicates. 400μg samples for $\delta^{34}S_{SO_4}$ analysis were placed with 1200μg vanadium pentoxide in sealed tin capsules in an auto-sampler, combusted in excess oxygen in a Flash EA coupled to continuous flow and analysed by a Thermo Delta V Mass spectrometer. Both samples for sulfur and oxygen isotopes were normalised to NBS 127 ($\delta^{34}S_{SO_4}$= 21.1‰, $\delta^{18}O_{SO_4}$= 8.6‰). Drift in mass spectrometer measurements over the run was accounted for by correcting samples to NBS 127. The overall analytical precision is better than 0.3‰ 1σ for $\delta^{18}O_{SO_4}$ (n=22) and 0.09‰ 1σ for $\delta^{34}S_{SO_4}$(n=39). External standards IAEA SO-5 and IAEA SO-6 were precise to within 0.13‰ for $\delta^{18}O_{SO_4}$ (1σ, n=12) and 0.19‰ for $\delta^{34}S_{SO_4}$ (1σ, n=6) (these standards were not processed through columns). Two full procedural replicates of seawater reproduced ran through columns and precipitated as barite gave $1\sigma_{ext}$ =0.20 for $\delta^{18}O_{SO_4}$ and $1\sigma_{ext}$ = 0.09 for $\delta^{34}S_{SO_4}$. Error values on samples are 0.2‰ and 0.09‰, or individual sample standard deviation, which ever is larger, for $\delta^{18}O_{SO_4}$ and $\delta^{34}S_{SO_4}$, respectively.

5.4 Results

5.4.1 Sulfate Concentrations

SO_4^{2-} concentrations in the Mekong range between 702μmol/L to 4μmol/L with an average concentration of 194μmol/L (main stem monsoon samples average of 2016 and 2017, n=17) (Figure 5.9A). This is similar to previous data for the Mekong River (Manaka *et al.*, 2015; Burke *et al.*, 2018) but lower than the global average of sulfate concentration (332μmol/L, Burke *et al.*, 2018). Sulfate concentrations in the tributaries and main stem are most concentrated in the Upper Mekong. Concentrations decrease downstream with most tributaries diluting the main stem (Figure 5.9A). Although discharge increases downstream (Figure 5.9B) there is a variable contribution to total sulfate flux from each section of the river basin (Figure 5.9C). The Upper Mekong between the source and southern China contributes most of the sulfate flux (∼69%). 18% of the total sulfate flux is contributed from the Middle Mekong between Baoshan and Stung Treng and the Lower Mekong contributes the last ∼13% from the three large tributaries in Cambodia (contribution values are calculated from 2017 sulfate concentration and ADCP data). Samples from China, both in the main stem and the Bijiang tributary have high sulfate and high chlorine concentrations. Chlorine concentrations in the main stem increase between Vientiane to Pakse, from ∼77μmol/L to ∼138μmol/L due to the influx of concentrated Mun, Chi and Songkhram tributaries draining northeastern Thailand. These tributaries do not have the highest sulfate concentrations but their large discharge provides an overall high sulfate flux contribution to the Mekong river (Figure 5.9C).

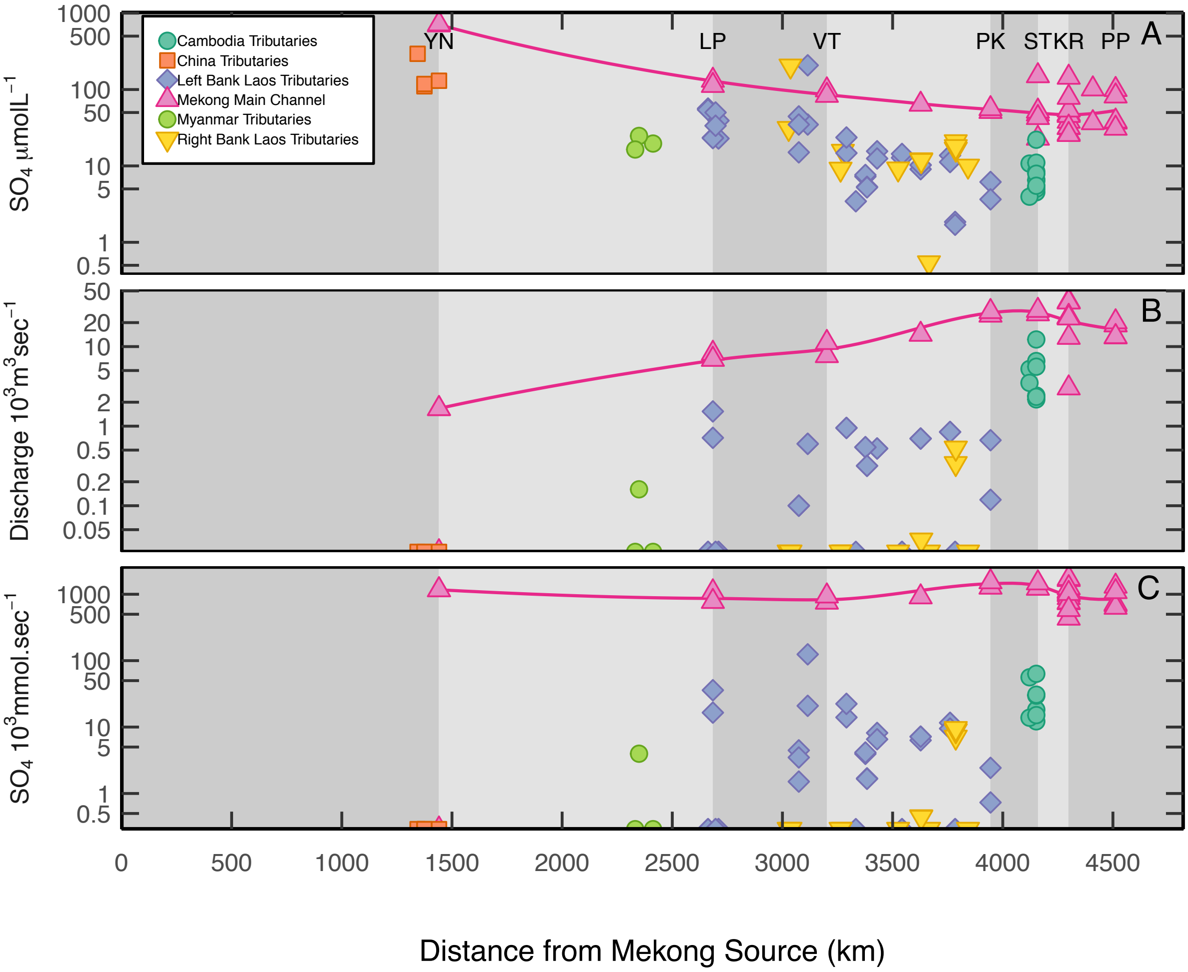

Figure 5.9 ***(continues on next page)***

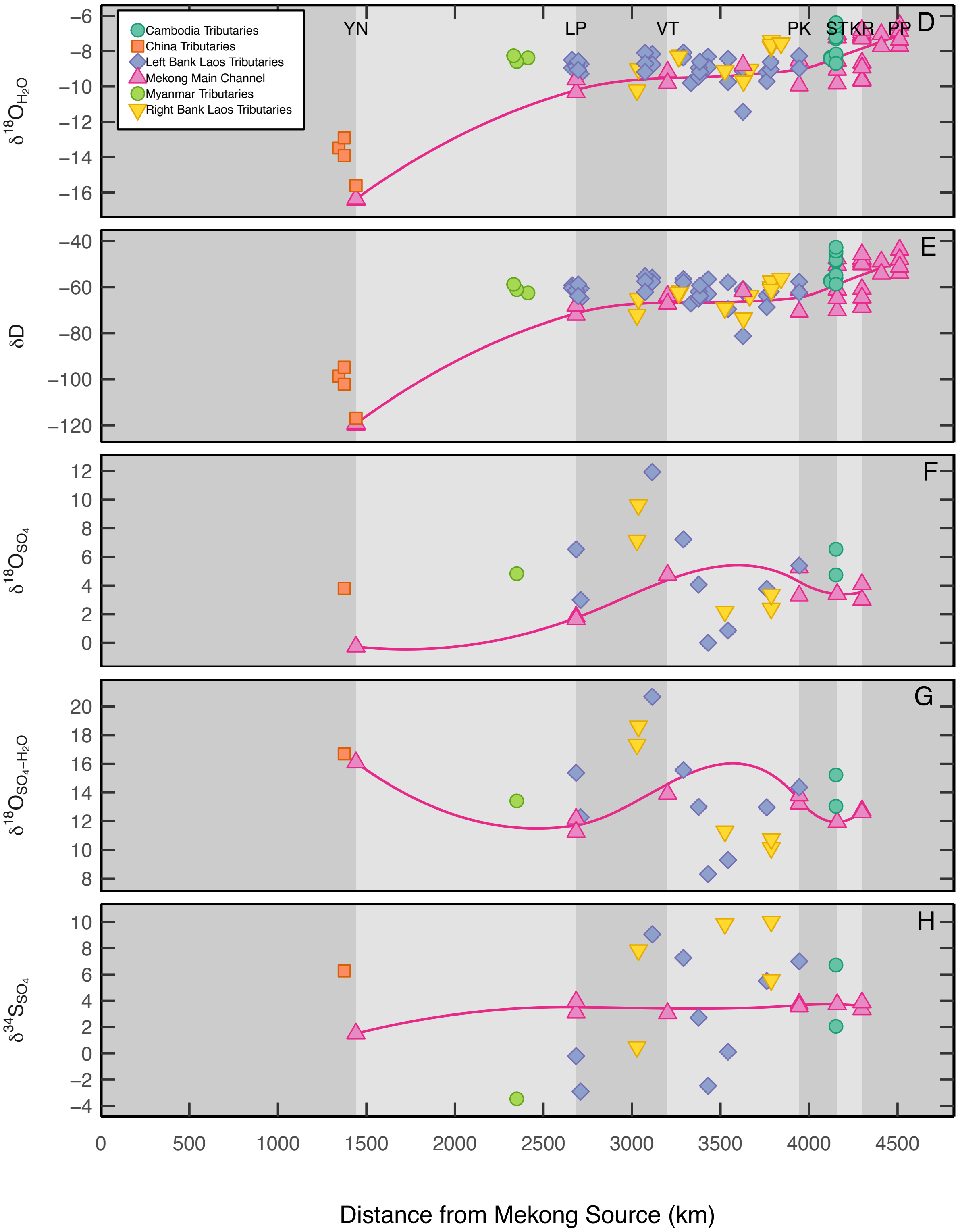

Figure 5.9 *(continued)*

5.4.2 Isotopes

There is a large range in $\delta^{18}O_{H_2O}$ (-18.02‰ to -5.75‰), increasing downstream which is expected with the range in latitude and altitude of the basin (Figure 5.9D). Most of this range occurs in the upper reaches of the basin, as this is where the Mekong leaves the 3-gorges region, with the $\delta^{18}O_{H_2O}$ of the main river tending to that of the tributaries by ~2600km downstream, indicating that the water is sourced locally. Most of the tributaries have higher $\delta^{18}O_{H_2O}$ than the mainstem, even in the lower reaches. The trend in δD is the same as $\delta^{18}O_{H_2O}$ which is a good indication that evaporation is not dominant (Figure 5.9E). The total range in $\delta^{18}O_{SO_4}$ downstream is 2.64‰, with the lowest values in the headwaters and the highest values close to the mouth (Figure 5.9F). The tributaries display a much larger range of $\sim$ 13‰ for $\delta^{18}O_{SO_4}$ (-0.35‰ to +11.94‰), with values both higher and lower than the main river. The larger variation in tributaries and the small decoupling of trend between $\delta^{18}O_{H_2O}$ and $\delta^{18}O_{SO_4}$ suggests there is another source contributing sulfate that does not contain local meteoric water. The difference between oxygen in sulfate and water, $\Delta^{18}\mathrm{O}_{SO_4-H_2O}$, is positive, between 8‰ and 20‰ and generally decreases downstream (Figure 5.9G), providing support for the hypothesis of a second source of sulfate with non-meteoric oxygen.

Figure 5.9 *(previous page)*: Mekong River downstream trends in discharge, concentration and isotopes. The length of the Mekong River is broken up into 7 sections at Baoshan (BS), Luang Prabang (LP), Vientiane (V), Pakse (P), Stung Treng (ST), Kratie (KR), using sampling sites on the main stem. Symbols separate the tributaries spatially, the Upper Mekong tributaries from the Source to Vientiane are in China (orange square) and Myanmar tributaries (light green circle), Middle Mekong tributaries between Vientiane and Pakse are Laotian rivers draining the left bank of the Mekong River (blue diamonds) and Laotian and Thai rivers draining the right bank of the Mekong River (yellow inverted triangles). The middle Mekong is split between left and right bank due to the distinct lithology on either side of the main river channel. The Lower Mekong from Pakse to the Mouth are in Cambodia (green circles). **A**: Sulfate concentrations decrease downstream in the main stem with most of the sulfate sourced in the Upper Mekong and subsequently diluted downstream. **B**: Discharge increases downstream with tributaries from the Middle Mekong left bank in Laos and Cambodian tributaries in the Lower Mekong contributing the most flux. Right bank Thai tributaries and tributaries in China contribute comparatively little. Discharge data is a combination of ADCP data collected in 2016 and 2017, MRC historical data set, Cambodian tributaries are from Someth *et al.* (2013) and some Laos tributaries from Nippon Koei (2001). **C**: Sulfate flux reflects a similar pattern as discharge. **D**: Oxygen isotopes in meteoric water increase downstream due to the decreasing altitude. **E**: Deuterium isotopes in meteoric water follow the same pattern as $\delta^{18}O_{H_2O}$ suggesting no appreciable evaporation. **F**: Oxygen isotopes in dissolved sulfate are lighter upstream with a large spread in tributary signatures. **G**: Difference in oxygen isotopes in dissolved sulfate and meteoric water to remove effect of local water signature in the sulfate. This does not include $\varepsilon_{SO_4-H_2O}$ fractionation factor. **H**: Sulfur isotopes in dissolved sulfate show little variation in the main stem but a large scatter of signatures in tributaries throughout the Mekong River basin.

Downstream $\delta^{34}S_{SO_4}$ shows a small variation of 2.64‰ (Figure 5.9H). The tributaries however show a ~13‰ range, similar to $\delta^{18}O_{SO_4}$ (-3.46‰ to +10.04‰) scattering to values above and below the main river. The lowest $\delta^{34}S_{SO_4}$ are from tributaries that drain northeast Myanmar and catchments in northern Laos whilst the heaviest sulfate is from catchments in northeastern Thailand. There is a large variation in Mekong samples, which are compared with global river data (Figure 5.4) in Figure 5.10. The tributaries that plot in the upper right hand quadrant of the graph, with positive oxygen and sulfur isotope signatures, coincide with some of the largest SO_4^{2-} fluxes of the Mekong tributaries, for example the Mun and Chi that both drain northeast Thailand, Nam Lik and Nam Ngjum both draining the left bank of the Middle Mekong in Laos and Tonle Kong, one of the three big rivers draining the southern Annamite mountains in northeastern Cambodia (Figure 5.7). Signals in the main stem have minimal variation between years, suggesting that mixing trends or processes are the same year on year and that the true signal has been captured. Samples collected in Luang Prabang, Pakse and Kratie in 2016 and 2017 reproduce to within 0.61‰ 1σ and 0.77‰ 1σ for $\delta^{34}S_{SO_4}$ and $\delta^{18}O_{SO_4}$, respectively.

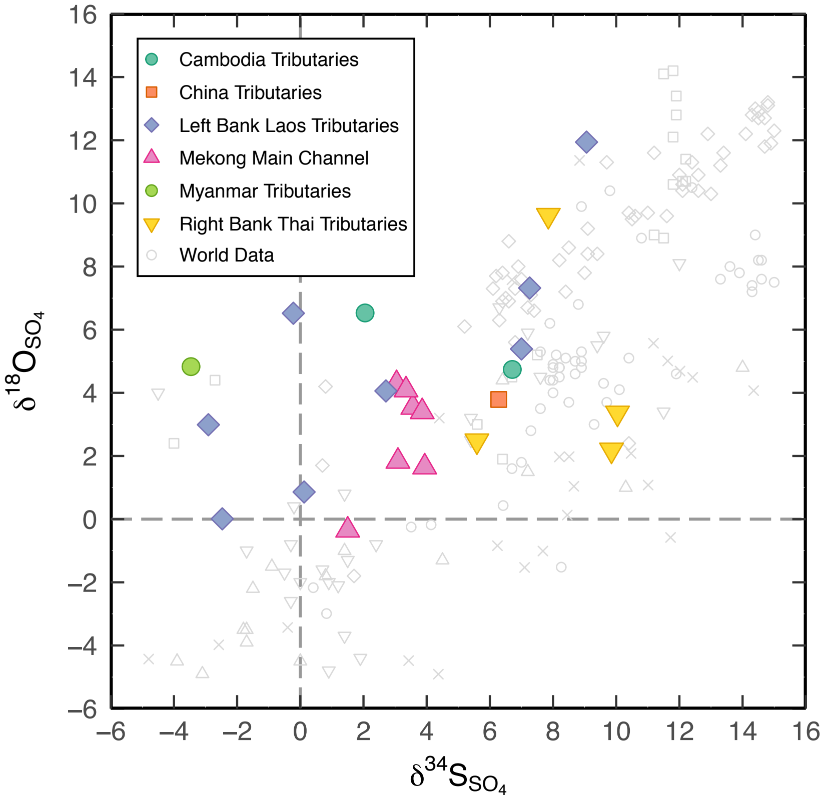

Figure 5.10: Sulfur and oxygen isotopes in Mekong river dissolved sulfate. Mekong data uses colours and symbols corresponding to basin sections in Figure 5.7. Error bars are smaller than symbols for Mekong data. Grey open symbols are global data, symbols correspond to the key in Figure 5.4.

5.5 Sedimentary Sulfate Sources in the Mekong Basin

The tributaries draining the right bank of the Middle Mekong in Thailand have high chlorine and sulfate fluxes and positive $\delta^{18}O_{SO_4}$ and $\delta^{34}S_{SO_4}$ isotopic signatures. These tributaries are among the rivers with the highest discharge within the Mekong River basin, therefore it is important to determine where the sulfate is sourced as the magnitude of flux could have a large impact on the carbon budget of the river basin.

The Khorat Plateau located in northeast Thailand to central Laos, is an epi-continental basin. The plateau is separated by the Phu Phan anticline into two depositional basins, the Khorat Basin in the south and the Sakhon Nakhon Basin in the north (Tabakh *et al.*, 1998; Carling, 2009; Hansen *et al.*, 2016). The lithology in the plateau consists of the Mesozoic Khorat Group made up of continental fluvial and lacustrine facies, including red beds, then sitting unconformably on top is the Maha Sarakham Formation, an extensive evaporite succession of Late Cretaceous to early Tertiary age. Fluvial facies in the Tertiary then alluvial facies in the Quaternary were subsequently deposited (Tabakh *et al.*, 1998, 1999).

The Maha Sarakham Formation is composed of three salt units, which consist of halite and anhydrite, separated by non-marine red-coloured siliclastics and is on average ~250m thick, increasing to a maximum of 1km in the centre of the basin (Tabakh *et al.*, 1998). Isotopic analysis of anhydrite beds and anhydrite nodules within halite beds gave sulfur isotope values, $\delta^{34}S_{SO_4}$, of +14.8 to +17.7‰ with a significantly lower δ^{34}S of +6.4 to +10.9‰ found in the thick clastic units (Tabakh *et al.*, 1999). Although there has been some debate on both the formation and age of the evaporites within the Khorat Plateau (e.g. Utha-Aroon, 1993; Hansen *et al.*, 2016; Kuroda *et al.*, 2017), the δ^{34}S of the Maha Sarakham fits with the contemporaneous δ^{34}S signature of global seawater which ranged from +14 to +18‰ from the Early to Late Cretaceous (Claypool *et al.*, 1980; Kampschulte & Strauss, 2004), suggesting that the evaporites precipitated from a marine derived aqueous sulfate. The Khorat Plateau is a continental basin that underwent three major marine influx events during the Cretaceous, due to relative sea level rise. The basin flooded from an inlet in the southwest, subsequent isolation due to sea level regression allowed for evaporite precipitation then deposition of terrogenous layers (Tabakh *et al.*, 1999, 2003; Hansen *et al.*, 2016). The lower member of the formation contains one of the world's largest salt deposits, from which potash, or potassium rich salt such as sylvite (KCl) is mined from the 50m thick unit (Hite & Japakasetr, 1979; Hansen *et al.*, 2016).

A basal anhydrite unit can be found between the top of the Khok Kruat Formation, the youngest unit within the Khorat Group, and the base of the Maha Sarakham formation throughout the Khorat Plateau. Tabakh *et al.* (1998) suggested that the basal anhydrite was formed by undersaturated water from an aquifer in the Khok Kruat Formation percolating upwards through Maha Sarakham beds. Salt leached from the Maha Sarakham beds then accumulated as a dissolution residue in an anhydrite unit with uniform thickness (~1m) throughout the basin. The similarity of sulfur isotope signatures of the basal anhydrite unit (δ^{34}S = +15 to +16‰ (Tabakh *et al.*, 1998)) and the Maha Sarakham formation supports this formation model.

The oxygen isotopic signature of the anhydrite beds in the three salt units in the Maha Sarakham formation has been measured by Pisutha-Arnond *et al.* (1986) at $\delta^{18}O_{SO_4}$ is +11 to +14.2‰, which corresponds to Claypool *et al.*'s (1980) Cretaceous marine oxygen isotope value of $\delta^{18}O_{SO_4}$= +13.5 to +15‰. The equilibrium of sulfate with surrounding water at low temperatures is slow enough to assume the measured signature has not been altered since deposition (Lloyd, 1968).

The evaporite outcrops are mostly contained within the Khorat Plateau and so the end member is well characterised for both $\delta^{34}S_{SO_4}$ and $\delta^{18}O_{SO_4}$ by literature values. There are two small outcrops by the northern Laos-southern Chinese border, which can be seen on the geological map Figure 1.2. There is no age or isotopic information in the literature specifically about these outcrops, however the geological map suggests they are the same age of the Maka Sarakham evaporites and therefore are assumed to have the same isotopic signature.

5.6 Mixing Model

With the exception of several tributaries with high atmospheric contributions, the SO_4^{2-} in the Mekong River basin is likely derived from the weathering of a mixture of sedimentary sulfates and sulfides which have different carbon cycle implications. To partition riverine SO_4^{2-} between its constituent sources, a two component mixing model is developed expressing the isotopic signatures of dissolved sulfate, in terms of the fractions of gypsum and pyrite end members. The results of this modelling will be used to quantify sulfuric acid that is available to participate in chemical weathering.

The isotopic values measured in the dissolved SO_4^{2-} samples (Figure 5.10) can be described by the following two equations. The oxygen, $\delta^{18}O_{SO_4}$, and sulfur $\delta^{34}S_{SO_4}$, isotopes of dissolved sulfate are a mix of the oxygen and sulfur isotopic signature from end members gypsum and pyrite, mixed in the proportions f_{gyp} and f_{pyr}, respectively.

$$\delta^{18}O_{SO_4} = f_{gyp}.\delta^{18}O_{SO_4gyp} + f_{pyr}.\delta^{18}O_{SO_4pyr} \tag{5.13}$$

$$\delta^{34}S_{SO_4} = f_{gyp}.\delta^{34}S_{SO_4gyp} + f_{pyr}.\delta^{34}S_{SO_4pyr} \tag{5.14}$$

Of the eight variables in Equations 5.13 and 5.14, $\delta^{18}O_{SO_4}$ and $\delta^{34}S_{SO_4}$ are measured in the dissolved SO_4^{2-} sample, f_{pyr} and f_{gyp} are values to be calculated, $\delta^{18}O_{SO_4gyp}$ can be constrained with literature values and $\delta^{18}O_{SO_4pyr}$ can be estimated by using the calculation in Equation 5.11. Previous studies have measured $\delta^{34}S_{SO_4gyp}$ (Section 5.5) but there is no literature on δ^{34}S signature of sulfides within the Mekong river basin, $\delta^{34}S_{SO_4pyr}$. As discussed in Section 5.2.1, $\delta^{34}S_{SO_4pyr}$ is difficult to constrain due to it's large natural variability, therefore this variable is unknown and is to be calculated by rearranging Equation 5.14. The mean values and 1σ variability in the end members and sample used in the model are shown in Figure 5.11.

The oxygen isotope signature of dissolved sulfate, $\delta^{18}O_{SO_4}$, described in Equation 5.13, can be expanded to Equation 5.15 to include more controls on $\delta^{18}O_{SO_4}$ from pyrite. Equation 5.15 describes the variables controlling sample $\delta^{18}O_{SO_4}$; the contribution of each lithology end member, for which the fraction of pyrite and fraction of gypsum must sum to 1 (Equation 5.16) and the proportion of molecular O_2 incorporated into pyrite oxidation derived SO_4^{2-}, $\delta^{18}O_{SO_4pyr}$, (Equation 5.11).

$$\delta^{18}O_{SO_4} = f_{gyp}.\delta^{18}O_{SO_4gyp} + (1 - f_{gyp})\left(f_{O_2atm}\left(\delta^{18}O_{atm} + \varepsilon_{O_2}\right) + f_{O_2Fe^{3+}}\left(\delta^{18}O_{H_2O} + \varepsilon_W\right)\right) \tag{5.15}$$

$$f_{pyr} = 1 - f_{gyp} \tag{5.16}$$

With greater confidence in oxygen isotopic constraints on end members and samples and all variables quantified in Equations 5.13 and 5.15, the mixing model initially uses oxygen isotopes in the sample and both end members to calculate f_{pyr} and f_{gyp}. To calculate f_{gyp}, Equation 5.15 is rearranged to Equation 5.17. Equation 5.17 assumes that fraction of oxygen incorporated into the SO_4^{2-} molecule during oxidation of sulfide, from either meteoric H_2O or molecular O_2, must sum to 1 (Equation 5.18).

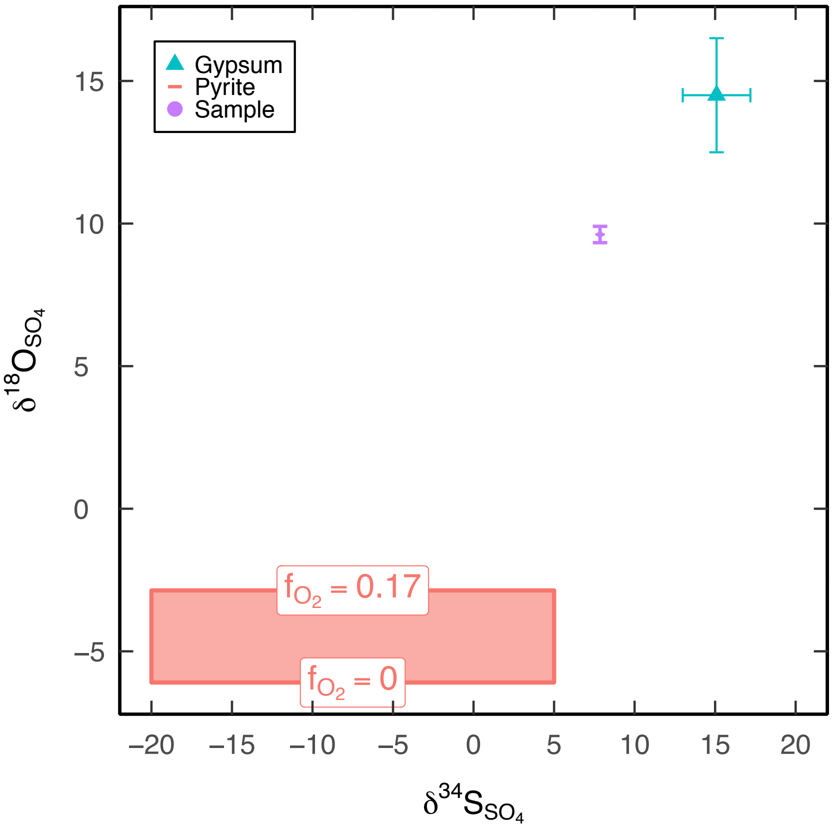

Figure 5.11: End member inputs for mixing model. Mean and 1σ of gypsum end members and sample used in the model parameters for an individual sample, MEK17-240. Values are displayed in table 5.2. Mean and 1σ values remain the same for gypsum for both $\delta^{34}S_{SO_4}$ and $\delta^{18}O_{SO_4}$ for every sample. $\delta^{34}S_{SO_4}$ and $\delta^{18}O_{SO_4}$ are unique for each sample, 1σ is analytical error. $\delta^{18}O_{SO_4pyr}$ is calculated for each sample using unique $\delta^{18}O_{H_2O}$ and Equation 5.11 between a range of f_{O_2atm} values (0 to 0.17). $\delta^{34}S_{SO_4pyr}$ of the sulfate delivered by oxidation of the pyrite end member is calculated by the mixing model, but $\delta^{34}S_{SO_4pyr}$ is expected to lie in the common range of sedimentary sulfides, -20‰ to +5‰ (Strauss, 1997; Goldhaber, 2003).

$$f_{gyp} = \frac{\delta^{18}O_{SO_4} - f_{O_2atm}\left(\delta^{18}O_{atm} + \varepsilon_{O_2}\right) - \left(1 - f_{O_2atm}\right)\left(\delta^{18}O_{H_2O} + \varepsilon_W\right)}{\delta^{18}O_{SO_4gyp} - f_{O_2atm}\left(\delta^{18}O_{atm} + \varepsilon_{O_2}\right) - \left(1 - f_{O_2atm}\right)\left(\delta^{18}O_{H_2O} + \varepsilon_W\right)} \tag{5.17}$$

$$f_{O_2Fe^{3+}} = 1 - f_{O_2atm} \tag{5.18}$$

For each individual sample, $\delta^{18}O_{SO_4pyr}$ is unique and is calculated using Equation 5.11. It is not possible to determine the exact reaction pathway of sulfide oxidation, thus there is a range of $\delta^{18}O_{SO_4}$ values in which SO_4^{2-} delivered from the sulfide end member may lie. This range is caused by the fraction of molecular O_2, f_{O_2atm}, incorporated into SO_4^{2-} which could vary from 0% to 17% depending on oxidation reaction pathway (Balci *et al.*, 2007; Mazumdar *et al.*, 2008). To

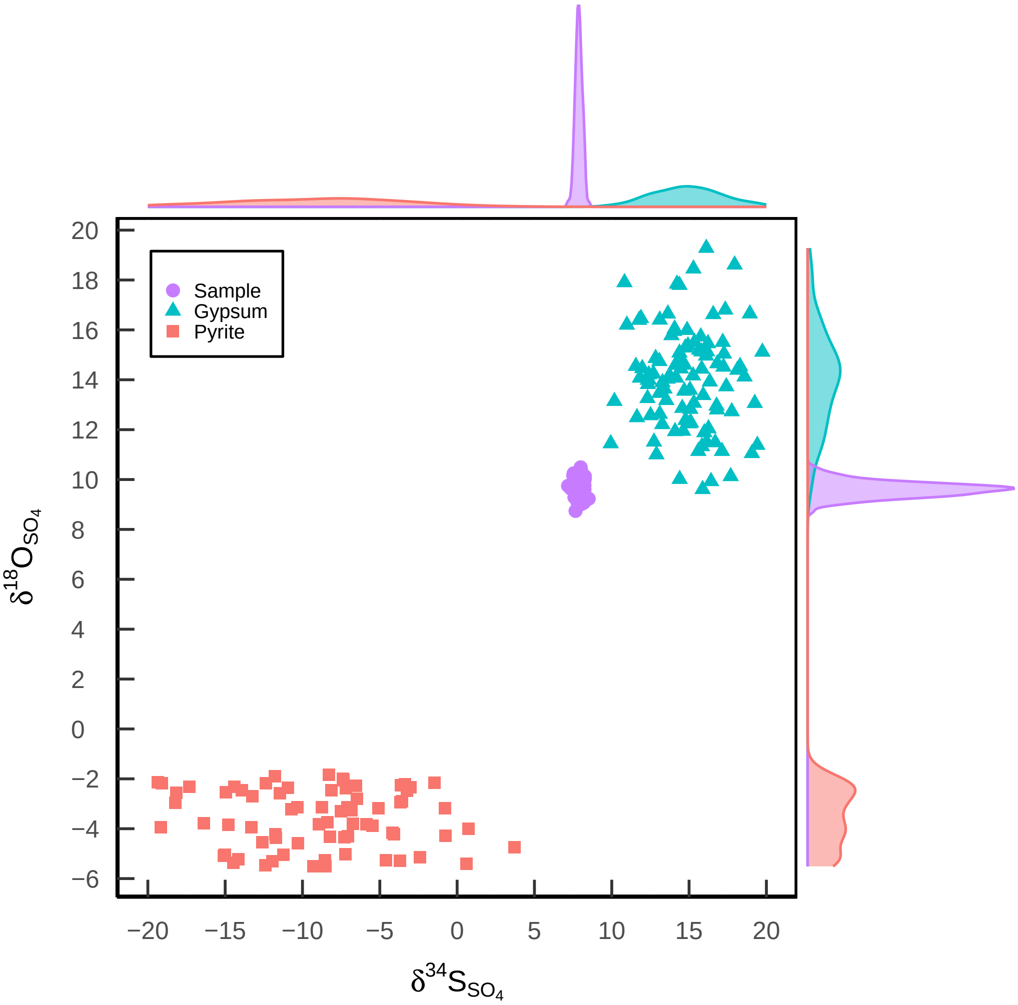

Figure 5.12: Monte-Carlo generated values for end member mixing. Domain of possible inputs for sample MEK17-240, defined by Monte Carlo method within parameters given in Table 5.2 and displayed in Figure 5.11. The Monte-Carlo method generates values with a normal probability distribution over the range given for the gypsum end member and sample and a random distribution for the pyrite end member, shown by the marginal density plots.

take into account the largest possible range of $\delta^{18}O$ values of the SO_4^{2-} delivered by sulfide end member, f_{O_2atm} is varied between between 0 and 0.17 for each sample, illustrated for one sample, MEK17-240 in Figure 5.11. The small range in oxygen isotopes of the gypsum end member, $\delta^{18}O_{SO_4gyp}$, is the same for each sample. A Monte-Carlo approach is used to generate 1000 values, within the ranges given for the gypsum and pyrite end members and within analytical uncertainty of the sample. The Monte-Carlo approach simulates values with a Gaussian distribution for the sample and gypsum end member, so most values centre around the mean. There is no indication of exactly how much atmospheric O_2 is incorporated into $\delta^{18}O_{SO_4pyr}$ therefore the Monte-Carlo simulates values with a random (uniform) distribution between the uncertainties given for the pyrite end member. The values generated by the Monte-Carlo approach are illustrated on Figure 5.12 for one sample, MEK17-240. The range of sulfide end members are between f_{O_2atm}= 0 and 0.17. f_{gyp} is calculated by mixing values in each of the end members through the sample using Equation 5.17. The mixing lines for each sample are shown in Figure 5.13.

f_{gyp} is calculated using oxygen isotopes in both end members and the sample, and is constrained using sulfur isotopes of the gypsum end member and the sample. First, sulfur isotope composition of the product sulfate from pyrite oxidation, $\delta^{34}S_{SO_4pyr}$, must be calculated. $\delta^{34}S_{SO_4pyr}$ can be calculated using Equation 5.19, which is Equation 5.14 (describing the sulfur isotopic composition of the water sample) rearranged. The Monte-Carlo approach generates n=1000 values for $\delta^{34}S_{SO_4pyr}$ (Figure 5.13). Some of these $\delta^{34}S_{SO_4pyr}$ values are extreme and are outside common sulfur isotope values of sedimentary sulfides (Figure 5.1). Only $\delta^{34}S_{SO_4pyr}$ values within the range -40‰ to +5‰ (determined using literature data, Figure 5.1), are used to calculate a mean f_{gyp} from the Monte Carlo iterations. A mean f_{gyp} and its 1σ error is calculated from the suitable Monte-Carlo generated values (values of n in Table 5.4 represent the discard iterations of $\delta^{34}S_{SO_4pyr}$ outside the determined range from 1000 Monte-Carlo iterations).

$$\delta^{34}S_{SO_4pyr} = \frac{\delta^{34}S_{SO_4} - f_{gyp}.\delta^{34}S_{SO_4gyp}}{(1 - f_{gyp})} \tag{5.19}$$

The parameters used for the variables described in Equations 5.13-5.19 are listed in Table 5.2. Measured $\delta^{18}O_{H_2O}$ and $\delta^{18}O_{SO_4}$ are specific to each sample. Fractionation factors $\varepsilon_{SO_4-H_2O}$ (ε_W) and $\varepsilon_{SO_4-O_2}$ (ε_{O_2}), calculated in sulfide oxidation experiments (Balci *et al.*, 2007), remain the same for each sample, as does the atmospheric O$_2$ value, $\delta^{18}O_{atm}$.

Table 5.2: Model parameters

Variable	Parameter
$\delta^{18}O_{H_2O}$	Oxygen isotope of meteoric H$_2$O in individual water sample
$\delta^{18}O_{SO_4}$	Oxygen isotope in dissolved SO$_4^{2-}$ in individual water sample
$\delta^{34}S_{SO_4}$	Sulfur isotope in dissolved SO$_4^{2-}$ in individual water sample
$\delta^{18}O_{SO_4gyp}$	Oxygen isotope of gypsum end member, 14.5‰ 1σ=2‰
$\delta^{34}S_{SO_4gyp}$	Sulfur isotope of gypsum end member, 15.09‰ 1σ=2.1‰
$\delta^{18}O_{SO_4pyr}$	Oxygen isotope of sulfide end member, calculated using Equation 5.11
$\delta^{34}S_{SO_4pyr}$	Sulfur isotope of sulfide end member, determined by model

Continued on the next page

Table 5.2: Model parameters (cont.).

Variable	Parameter
$\delta^{18}O_{atm}$	Atmospheric O_2, 23‰
ε_W	$\varepsilon_{SO_4-H_2O}$: Fractionation factor between H_2O and SO_4^{2-}, 2.9‰
ε_{O_2}	$\varepsilon_{SO_4-O_2}$: Fractionation factor between molecular O_2 and SO_4^{2-}, -10.1‰
f_{pyr}	Fraction of SO_4^{2-} delivered from pyrite, f_{pyr} + f_{gyp} = 1
f_{gyp}	Fraction of SO_4^{2-} delivered from gypsum, f_{pyr} + f_{gyp} = 1
f_{O_2atm}	Fraction of O_2 incorporated into dissolved $SO_4^{2-}$by molecular O_2, f_{O_2atm} is varied between 0% and 17%, f_{O_2atm} + f_{H_2O} = 1
f_{H_2O}	Fraction of O_2 incorporated into dissolved $SO_4^{2-}$by meteroric H_2O, 1 - f_{O_2atm} = f_{H_2O}

5.7 Model Results and Discussion

5.7.1 Fraction of Pyrite Derived Sulfate in the Mekong River Basin

The two end member mixing model partitions the source of SO_4^{2-} for each sample in the Mekong river between sulfate delivered by the dissolution of sedimentary sulfates, f_{gyp}, and sulfate sourced from the oxidative weathering of pyrite, f_{pyr}. f_{pyr} varies between 0.19 and 0.79 in the Mekong basin. The main stem has a mean f_{pyr} value of 0.57 with the highest values at Luang Prabang and lowest at Pakse. Using f_{gyp} and f_{pyr} values, the sulfate flux associated with dissolution of gypsum or oxidative weathering of pyrite can be calculated. By quantifying the flux of sulfate from each source, the carbon implications of sulfide oxidation can be inferred. The sulfur isotope value of dissolved sulfate delivered to the South China Sea at the mouth of the Mekong is +3.61‰ ±0.32, this is lower than estimates of mean global riverine $\delta^{34}S_{SO_4}$contribution (7‰, Kurtz *et al.* (2003) and 4.8‰, Burke *et al.* (2018)). Burke *et al.* (2018) calculate that 42% of global riverine sulfate is derived from oxidative pyrite weathering, this is lower than the 57% pyrite derived sulfate calculated for the Mekong by this study.

Tributaries in northern Thailand, Hueang and Loei have low f_{pyr} values (0.39 and 0.27, respectively), most of the SO_4^{2-} is delivered through the dissolution of sedimentary sulfates such as gypsum or anhydrite. These tributaries drain Triassic-Jurassic marine units. The Nam Lik

Table 5.3: Sulfate concentration and sulfur and oxygen isotope data in Mekong river dissolved load. Measured data with analytical errors and gypsum end member value from literature data (see text) are input values to the mixing model.

SampleID	Sample Date	River	Location	SO_4^{2-}	SO_4^{2-} 2σ	$\delta^{18}O_{H_2O}$	$\delta^{18}O_{H_2O}$ 2σ	$\delta^{34}S_{SO_4}$	$\delta^{34}S_{SO_4}$ 1σ	$\delta^{18}O_{SO_4}$	$\delta^{18}O_{SO_4}$ 1σ	$\delta^{34}S_{SO_4}$ gyp	$\delta^{34}S_{SO_4}$ gyp 1σ	$\delta^{18}O_{SO_4}$ gyp	$\delta^{18}O_{SO_4}$ gyp 1σ
				μmol/L		‰									
MEK17-107	9/12/17	Mekong	Baoshan Yongbao, China	700.9	35.0	-16.36	0.06	1.50	0.12	-0.27	0.77	15.09	2.1	14.5	2
MEK16-033	9/13/16	Mekong	Pak Ou, Luang Prabang, Laos	112.7	5.6	-9.61	0.07	3.94	0.09	1.65	0.29	15.09	2.1	14.5	2
MEK17-135	9/17/17	Mekong	Pak Ou, Luang Prabang, Laos	131.7	6.6	-10.33	0.12	3.09	0.30	1.83	0.20	15.09	2.1	14.5	2
MEK16-007	9/11/16	Mekong	Vientiane, Laos	98.6	4.9	-9.16	0.06	3.05	0.09	4.74	0.63	15.09	2.1	14.5	2
MEK16-096	9/18/16	Mekong	Pakse, Laos	55.9	2.8	-8.52	0.06	3.56	0.19	5.26	0.42	15.09	2.1	14.5	2
MEK17-189	9/22/17	Mekong	Pakse, Laos	51.5	2.6	-9.94	0.09	3.76	0.32	3.28	0.78	15.09	2.1	14.5	2
MEK16-106	9/19/16	Mekong	Stung Treng, Cambodia	47.6	2.4	-8.53	0.10	3.73	0.18	3.40	0.44	15.09	2.1	14.5	2
MEK16-137	9/22/16	Mekong	Kratie, Cambodia	26.5	1.3	-8.65	0.07	3.35	0.32	4.09	1.14	15.09	2.1	14.5	2
MEK17-213	9/25/17	Mekong	Kratie, Cambodia	45.8	2.3	-9.61	0.09	3.87	0.32	3.00	1.12	15.09	2.1	14.5	2
MEK16-077	9/17/16	Bang Hiang	Phosay, Laos	13.7	0.7	-9.20	0.08	5.51	0.32	3.77	0.43	15.09	2.1	14.5	2
MEK17-256	10/6/17	Chi	Ubon Ratchathani, Thailand	20.8	1.0	-7.74	0.06	5.59	0.09	2.40	0.20	15.09	2.1	14.5	2
MEK17-123	9/15/17	Heihui	Dali, China	110.2	5.5	-12.90	0.09	6.28	0.16	3.79	0.20	15.09	2.1	14.5	2
MEK17-236	10/4/17	Hueang	Nam Khaem, Thailand	31.1	1.6	-10.20	0.13	0.49	0.32	7.15	1.48	15.09	2.1	14.5	2
MEK17-240	10/4/17	Loei	Loei, Thailand	203.8	10.2	-8.99	0.14	7.85	0.22	9.62	0.29	15.09	2.1	14.5	2
MEK17-230	10/2/17	Mae Kok	Chiang Saen, Thailand	24.7	1.2	-8.58	0.10	-3.46	0.04	4.83	0.20	15.09	2.1	14.5	2
MEK17-257	10/6/17	Mun U/S	Si Sa Ket, Thailand	16.6	0.8	-7.40	0.08	10.04	0.26	3.36	0.63	15.09	2.1	14.5	2
MEK16-053	9/15/16	Nam Hinboun	Ban Nongboua, Laos	14.3	0.7	-8.43	0.04	0.12	0.15	0.86	0.43	15.09	2.1	14.5	2
MEK16-051	9/15/16	Nam Ka Ding	Pak Kading, Laos	15.6	0.8	-8.31	0.13	-2.47	0.10	0.01	0.57	15.09	2.1	14.5	2
MEK16-012	9/12/16	Nam Khan	Xiang Ngeun, Laos	22.9	1.1	-9.28	0.06	-2.91	0.10	2.99	0.26	15.09	2.1	14.5	2
MEK17-146	9/18/17	Nam Lik	Kasi, Laos	207.5	10.4	-8.76	0.12	9.06	0.18	11.92	0.25	15.09	2.1	14.5	2
MEK16-047	9/15/16	Nam Ngiap	Beung Kan, Laos	7.3	0.4	-8.93	0.05	2.71	0.10	4.06	0.42	15.09	2.1	14.5	2
MEK17-158	9/20/17	Nam Ngjum	Pak Ngum, Laos	23.6	1.2	-8.34	0.10	7.26	0.10	7.22	0.92	15.09	2.1	14.5	2
MEK17-127	9/17/17	Nam Ou	Phathung, Laos	23.1	1.2	-8.85	0.11	-0.22	0.09	6.52	0.40	15.09	2.1	14.5	2
MEK17-245	10/5/17	Songkhram	Si Songkhram, Thailand	9.2	0.5	-9.10	0.10	9.85	0.10	2.19	0.35	15.09	2.1	14.5	2
MEK16-119	9/20/16	Tonle Kong	Stung Treng, Cambodia	5.2	0.3	-8.30	0.09	6.71	0.10	4.74	0.38	15.09	2.1	14.5	2
MEK16-112	9/20/16	Tonle Srepok D/S	Stung Treng, Cambodia	5.5	0.3	-8.69	0.07	2.05	0.10	6.53	0.31	15.09	2.1	14.5	2
MEK16-087	9/18/16	Xe Don	Pakse, Laos	3.6	0.2	-8.97	0.04	7.00	0.10	5.39	0.48	15.09	2.1	14.5	2

Table 5.4: f_{pyr} and end member values from mixing model output. All variables have averages from n=1000 iterations and 1σ error. Only iterations where the $\delta^{34}S_{SO_4 pyr}$ end member value is between -40‰ and +10‰ are used in the average. The number of iterations discounted are published in the last column.

SampleID	Sample Date	River	$f_{O_2 atm}$	$f_{O_2 atm}$ 1σ	f_{pyr}	f_{pyr} 1σ	$\delta^{18}O_{SO_4}$ gyp	$\delta^{18}O_{SO_4}$ gyp 1σ	$\delta^{18}O_{SO_4}$ pyr	$\delta^{18}O_{SO_4}$ pyr 1σ	$\delta^{34}S_{SO_4}$ gyp	$\delta^{34}S_{SO_4}$ gyp 1σ	$\delta^{34}S_{SO_4}$ pyr	$\delta^{34}S_{SO_4}$ pyr 1σ	discarded
									‰						n
MEK17-107	9/12/17	Mekong	0.08	0.05	0.57	0.05	14.56	2.04	-11.29	1.28	15.06	2.06	-8.80	2.73	0
MEK16-033	9/13/16	Mekong	0.08	0.05	0.65	0.05	14.44	2.08	-5.06	0.97	15.07	2.10	-2.08	1.84	0
MEK17-135	9/17/17	Mekong	0.09	0.05	0.63	0.05	14.58	2.03	-5.67	1.00	15.17	2.01	-4.21	2.14	0
MEK16-007	9/11/16	Mekong	0.09	0.05	0.51	0.07	14.44	1.97	-4.61	0.93	15.12	2.07	-9.21	4.15	0
MEK16-096	9/18/16	Mekong	0.08	0.05	0.49	0.07	14.43	2.02	-4.06	0.91	14.98	2.19	-8.75	4.34	0
MEK17-189	9/22/17	Mekong	0.09	0.05	0.56	0.07	14.51	2.05	-5.35	1.01	15.08	2.12	-5.33	3.35	0
MEK16-106	9/19/16	Mekong	0.08	0.05	0.60	0.06	14.53	2.01	-4.07	0.91	15.04	2.18	-4.14	2.66	0
MEK16-137	9/22/16	Mekong	0.08	0.05	0.56	0.09	14.55	2.03	-4.18	0.92	15.03	2.17	-6.55	4.40	2
MEK17-213	9/25/17	Mekong	0.08	0.05	0.58	0.08	14.47	2.01	-5.05	0.96	15.07	2.08	-4.59	3.41	0
MEK16-077	9/17/16	Bang Hiang	0.08	0.05	0.56	0.06	14.59	1.99	-4.69	0.94	15.00	2.10	-2.31	2.81	0
MEK17-256	10/6/17	Chi	0.09	0.05	0.68	0.05	14.49	2.05	-3.30	0.89	15.00	2.18	1.00	1.60	0
MEK17-123	9/15/17	Heihui	0.09	0.05	0.47	0.05	14.42	1.90	-8.04	1.10	14.99	2.19	-3.77	3.41	0
MEK17-236	10/4/17	Hueang	0.08	0.05	0.39	0.07	14.97	1.83	-5.62	1.02	15.02	2.08	-22.99	7.47	186
MEK17-240	10/4/17	Loei	0.09	0.05	0.27	0.06	14.92	1.67	-4.44	0.95	15.03	2.08	-13.04	9.06	111
MEK17-230	10/2/17	Mae Kok	0.09	0.05	0.52	0.06	14.60	1.98	-4.09	0.93	15.07	2.15	-21.19	4.94	8
MEK17-257	10/6/17	Mun U/S	0.09	0.05	0.63	0.07	14.45	2.12	-3.01	0.89	15.19	2.04	6.93	1.67	15
MEK16-053	9/15/16	Nam Hinboun	0.08	0.05	0.74	0.05	14.46	2.04	-3.97	0.91	15.05	2.01	-5.31	1.75	0
MEK16-051	9/15/16	Nam Ka Ding	0.08	0.05	0.79	0.06	14.45	2.02	-3.86	0.91	15.13	2.08	-7.29	1.77	0
MEK16-012	9/12/16	Nam Khan	0.08	0.05	0.59	0.05	14.48	2.05	-4.75	0.94	15.14	2.14	-15.53	3.37	0
MEK17-146	9/18/17	Nam Lik	0.09	0.05	0.19	0.06	15.73	1.40	-4.24	0.91	14.68	1.99	-16.94	10.62	385
MEK16-047	9/15/16	Nam Ngiap	0.08	0.05	0.54	0.06	14.43	2.03	-4.47	0.93	15.13	2.08	-8.06	3.47	0
MEK17-158	9/20/17	Nam Ngjum	0.08	0.05	0.39	0.08	14.50	1.95	-3.95	0.91	15.15	2.12	-6.26	6.52	5
MEK17-127	9/17/17	Nam Ou	0.08	0.05	0.43	0.06	14.65	1.85	-4.36	0.92	15.02	2.04	-21.60	6.22	28
MEK17-245	10/5/17	Songkhram	0.08	0.05	0.64	0.05	14.56	2.00	-4.59	0.91	15.01	2.05	6.97	1.36	3
MEK16-119	9/20/16	Tonle Kong	0.09	0.05	0.53	0.06	14.52	1.98	-3.76	0.92	15.10	2.07	-1.00	3.13	0
MEK16-112	9/20/16	Tonle Srepok D/S	0.09	0.05	0.42	0.06	14.53	1.89	-4.19	0.90	15.07	2.02	-16.58	6.19	11
MEK16-087	9/18/16	Xe Don	0.09	0.05	0.48	0.07	14.46	1.98	-4.42	0.92	15.22	2.12	-2.42	3.70	0

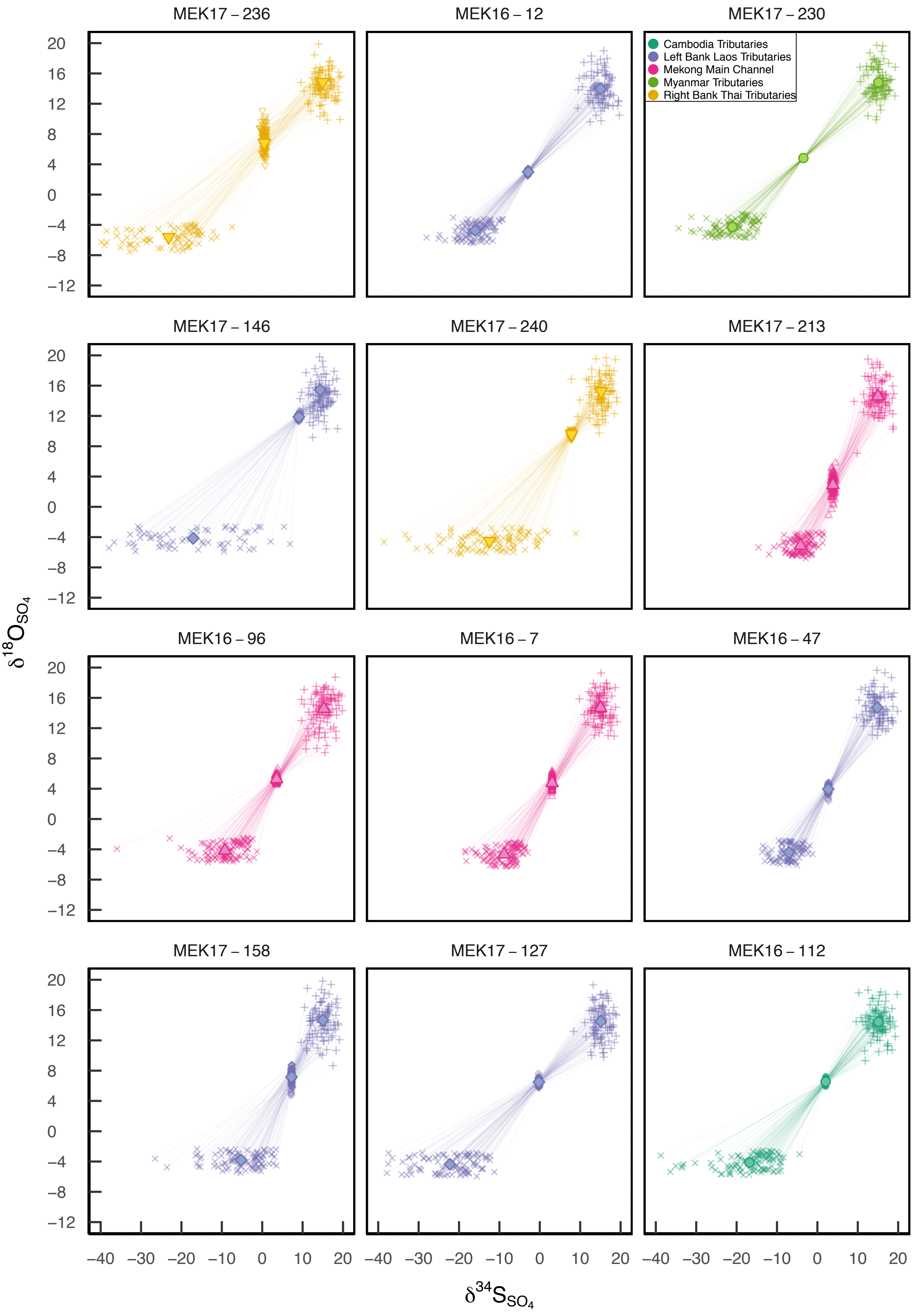

Figure 5.13 *(continues on next page)*

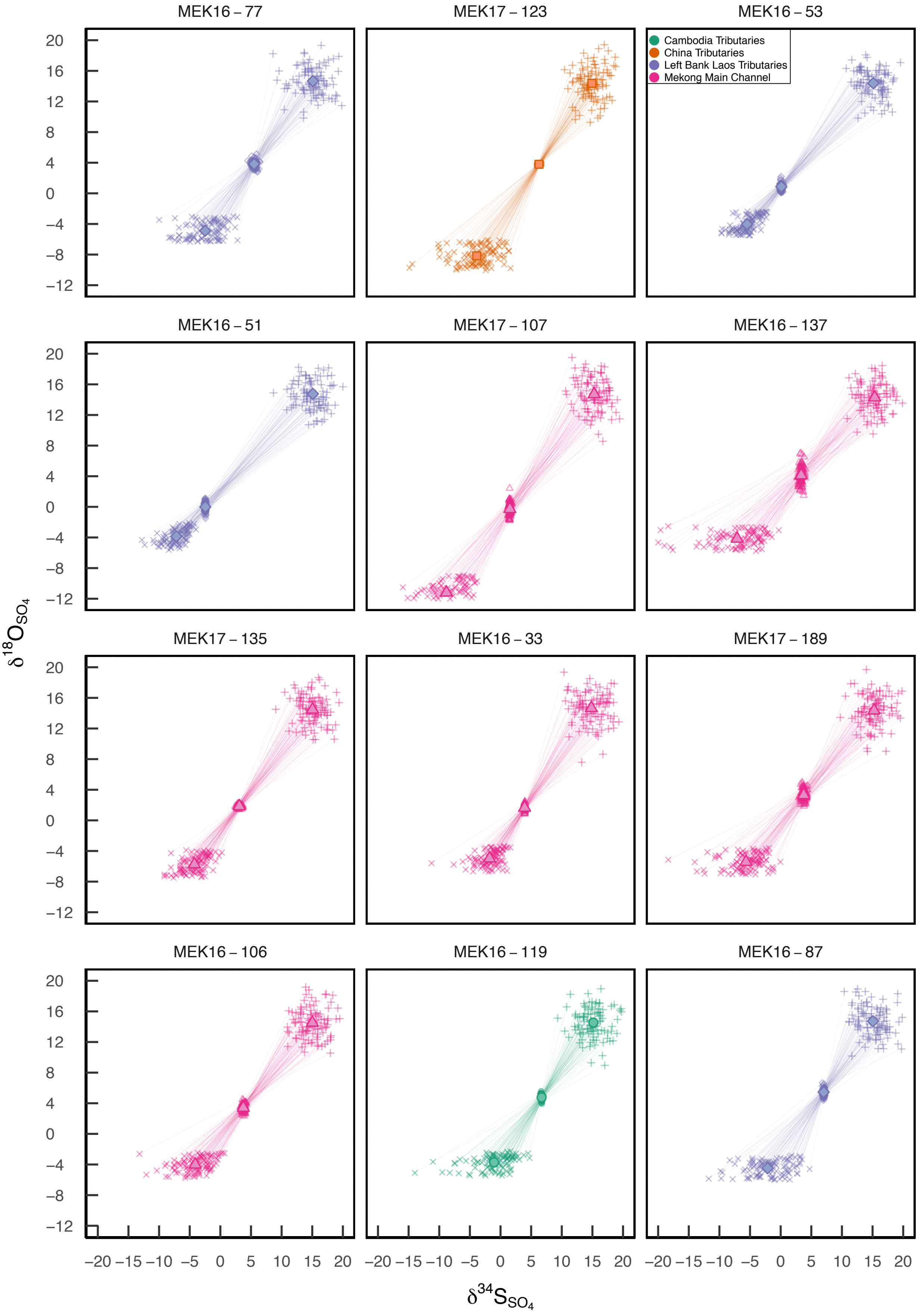

Figure 5.13 *(continued)*

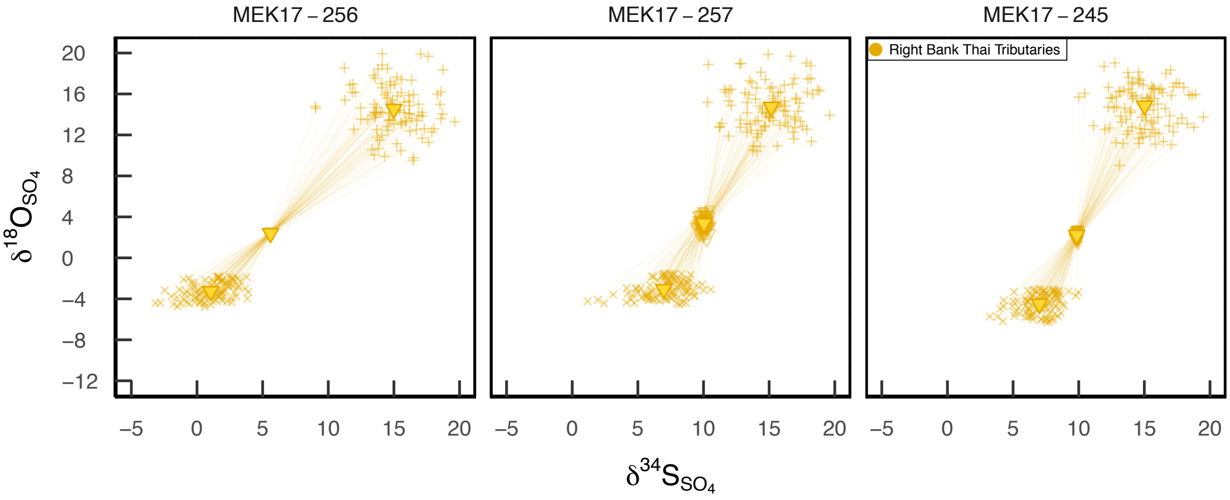

Figure 5.13 ***(continued)*****: Mixing lines between values generated by Monte Carlo method**. The gypsum end member values (+) are generated by Monte Carlo for the given mean and standard deviation. The pyrite end member (x) is calculated with Monte-Carlo generated values of $\delta^{18}O_{H_2O}$ and $\delta^{18}O_{SO_4}$ then $\delta^{34}S_{SO_4}$. The model uses n=1000, but the figures show n=100 for the Monte-Carlo results. The larger filled in symbols are the averages of the Monte Carlo generated values for the end members and sample. The symbols and colours match those in Figure 5.9, separating the samples into location; China Tributaries (orange), Myanmar Tributaries (green), Left Bank Laos Tributaries (lilac), Right Bank Thai Tributaries (yellow), Cambodia Tributaries (blue-green) and Mekong Main Stem (pink).

in northern Laos has the highest proportion of SO_4^{2-} derived from the dissolution of sedimentary sulfates (86%) and is the tributary with the largest sulfate flux.

Sulfate is delivered in almost equal quantities from oxidative weathering of sulfide and dissolution of sedimentary sulfates in nine tributaries. The Heihui tributary in China, is predominantly Jurassic marine units but there is a large area of Pre-Cambrian metamorphic rock from the Central Axis of the Himalayas (Figure 1.2). These metamorphic rocks are undifferentiated on the geological map, however pyrite is a common precipitate from circulating hydrothermal fluids in metamorphic rocks and pyrite is also common in some sedimentary rocks which survives as such in metamorphic rocks, a reasonable indication of why f_{pyr} is 0.47. The Nam Ou river drains northeastern Laos and is one of the largest tributaries in the Mekong basin by size and although it has a low concentration of SO_4^{2-}, 23.1μmol/L, it is the second largest in terms of sulfate flux because of the high discharge. The Nam Ou has a f_{pyr} value of 0.43, so about half of sulfate delivered from this catchment plays no role in the carbon cycle. The Nam Ou drains Devonian to Permian limestones and some Cretaceous to Jurassic gypsum and halite units (Kiernan, 2015) and has a landscape dominated by impressive karst. The Tonle Srepok drains Triassic to Jurassic marine units and Pliocene to Quaternary basalts in northeastern Cambodia and has a f_{pyr} value of 0.42. The Tonle Kong mostly drains Quaternary basalts which is reflected in the end member value of $\delta^{34}S_{SO_4pyr}$ = -1.00‰ and $\delta^{18}O_{SO_4pyr}$ = -3.76‰, calculated by the model. The Tonle Kong has a sulfate concentration of only 5.2μmol/L and f_{pyr} value of 0.53, but it is the tributary with the largest discharge in the Mekong therefore the second largest sulfate flux.

The tributaries with the highest f_{pyr} are found in the Upper Mekong close to the source and in the Middle Mekong on both banks of the main channel. The f_{pyr} value in the Mekong main channel at Baoshan, China is 0.57, indicating that there are more pyrite sources closer to the source of the Mekong, upstream of our most northerly sample. The surface lithology of the right bank of the Middle Mekong in Thailand is dominated by evaporite units. However the f_{pyr} values suggest that only 37% of the sulfate delivered by the Mun river, 32% of the sulfate delivered by the Chi river and 36% of the sulfate delivered by the Songkhram river is sourced from sedimentary sulfates. The vast majority of sulfate on the Khorat Plateau appears to come from pyrite. Sedimentary sulfates deliver high SO_4^{2-} concentrations but sulfate concentrations in the Mun, Chi and Songkram are less than 21μmol/L, in contrast Cl^- concentrations are between 400-804μmol/L indicating the dominant evaporite is halite. The Maha Sarakham evaporite formation is underlain by the Mesozoic Khorat Group which comprises sandstone, siltstone and shale units. These terrigenous Khorat Group units contain abundant disseminated pyrite and some galena and sphalerite (Tabakh *et al.*, 1998) which must contribute sulfate with important implications for the carbon budget of the Mekong river basin. The Nam Hinboun and Nam Kading have the highest f_{pyr} values, 0.74 and 0.79, respectively. They mainly drain Triassic to Jurassic and Carboniferous to Permian limestone units (Ponta & Aharon, 2014) where pyrite is common, they also drain Palaeozoic igneous units of the Annamite mountain range in the north (Ponta & Aharon, 2014). Although f_{pyr} is high, the sulfate flux contributed by these tributaries is less than 10% of the sulfate flux contributed by the Nam Lik.

5.7.2 Model End Members

In general the model works well to provide an estimate of mixing proportions between two end members. Samples are a mix of two end members that have a $\delta^{34}S_{SO_4}$ and $\delta^{18}O_{SO_4}$ of a reasonable value, dictated by literature values where few iterations of the Monte-Carlo mixing approach have been discarded. Some samples have less than 5% of the iterations removed before averaging f_{pyr} values because the slightly larger analytical errors in $\delta^{18}O_{SO_4}$ of the sample, allows for mixing between extremes of end members which is unlikely. There are three samples that have between

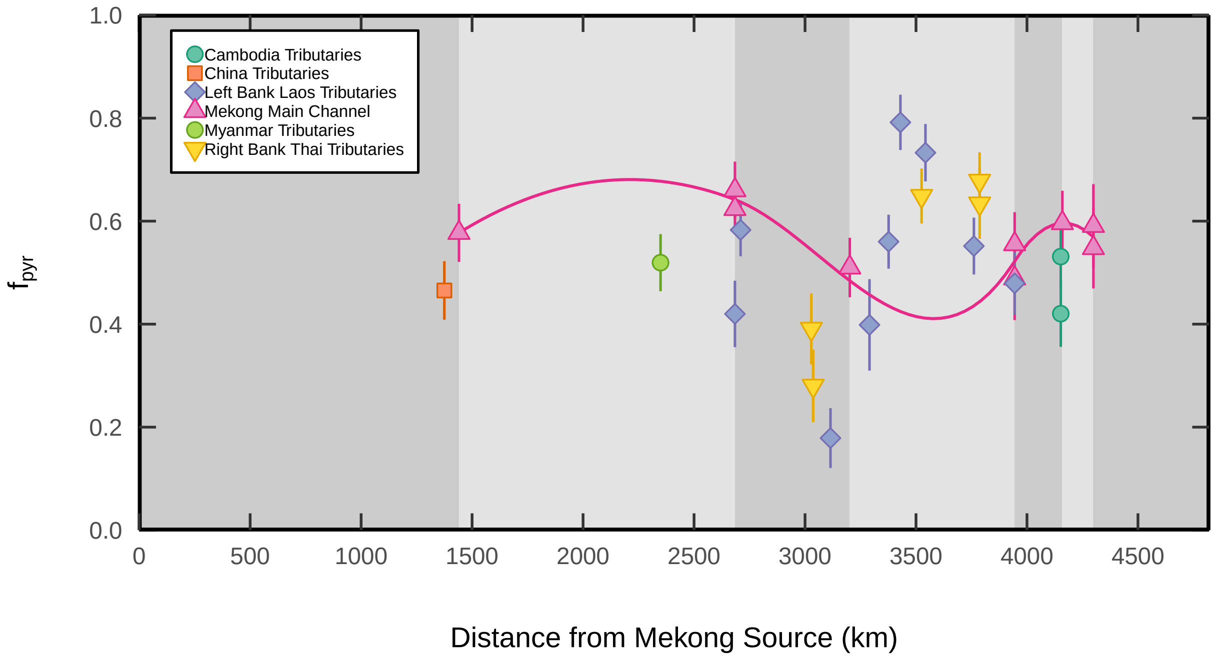

Figure 5.14: Model results of f_{pyr} downstream in Mekong main stem and tributaries. The main stem has an average f_{pyr} of 0.57± 0.06‰ 1σ with the highest values at Luang Prabang and lowest at Pakse. Symbols are explained in Figure 5.7.

11-38% of the Monte-Carlo iterations removed. The sample for Nam Lik (MEK17-146, Figure 5.13) lies very close to the gypsum end member, thus the model results in a f_{pyr} value of 0.19, but also a larger error in the pyrite end member, hence the model remove 385 iterations before averaging the model results. Similarly, the Loei tributary (MEK17-240, Figure 5.13) plots close to the gypsum end member (f_{pyr}=0.27) so 111 iteration of extreme mixing scenarios were removed before averaging final f_{pyr}. In the Hueang tributary 186 iterations were removed before f_{pyr} values were averaged (MEK17-236, Figure 5.13) because the sample has a larger analytical error of $\delta^{18}O_{SO_4}$ allowing for a larger mixing range passing through the sample and thus a large error in the pyrite end member.

As a check on the model, the $\delta^{34}S_{SO_4}$ values calculated for the sulfide end member can be compared to common lithological end member values, shown in Figure 5.1. $\delta^{34}S_{SO_4}$ values for sulfate delivered by sulfide end members in the Mekong are between -22.99‰ and +6.97‰, well within the range of sedimentary and igneous sulfides, therefore constraining the possible end members in the Mekong River basin. Because of the constraints on the inputs to the model, there are no samples that lie out with the common range.

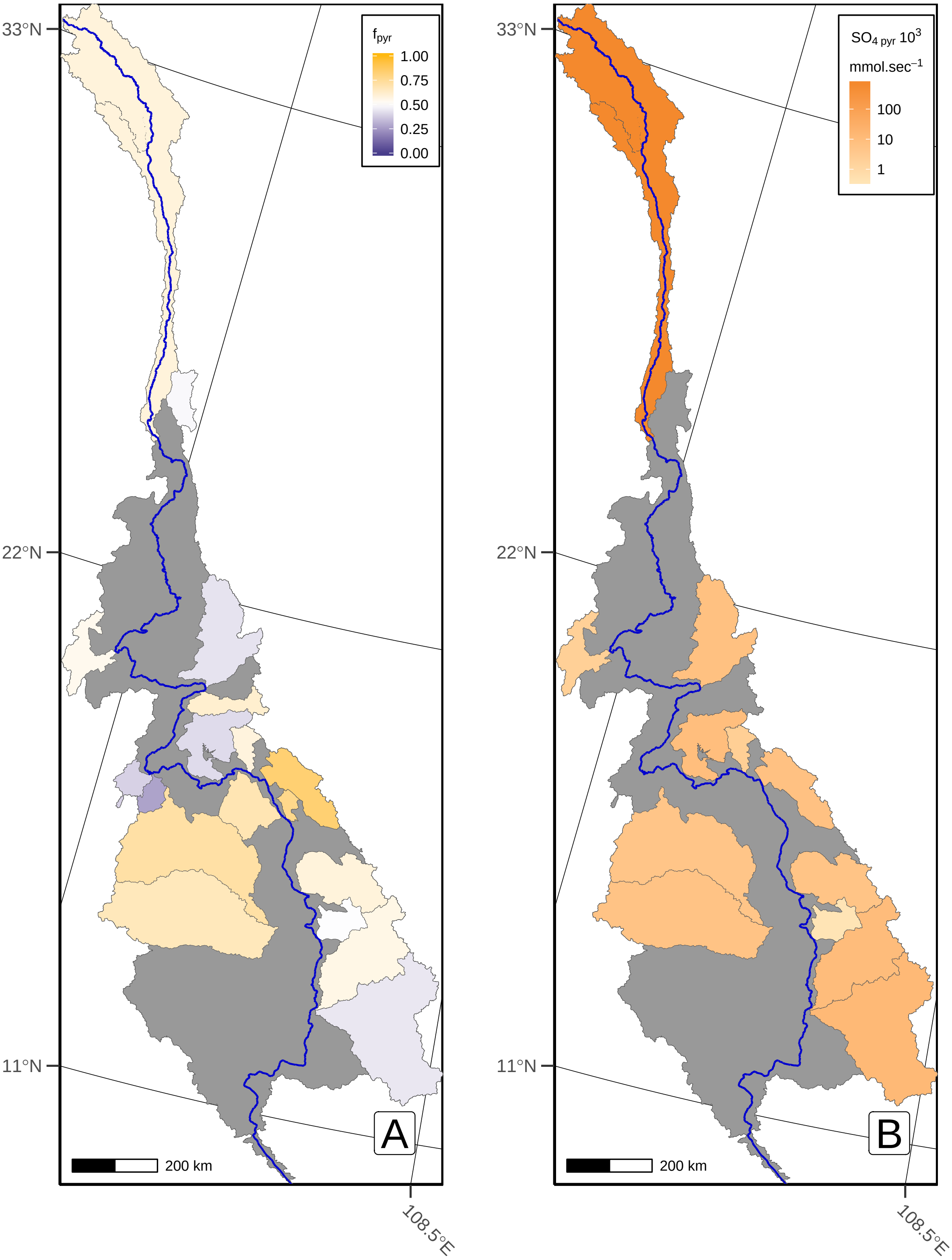

Figure 5.15: f_{pyr} **(A) and pyrite derived** SO_4^{2-} **flux (B) in Mekong tributaries.** Tributaries where f_{pyr} values >0.5 are yellow, <0.5 are blue (where there is more SO_4^{2-} derived from gypsum dissolution) and values close to 0.5 are white (A). Flux of sulfate derived from the oxidative weathering of pyrite (B) is calculated with f_{pyr} values calculated by the mixing model, measured SO_4^{2-} concentrations from this study and discharge from ADCP data, MRC historical data set and other literature sources cited in Figure 5.9 caption. No $\delta^{34}S_{SO_4}$ or $\delta^{18}O_{SO_4}$ data is grey. Tributaries plotted on A but not B are due lack of discharge data for these catchments.

5.7.3 Model Limitations

The biggest limitation of this model is not being able to give a precise value to $\delta^{18}O_{SO_4pyr}$. The exact fraction of atmospheric O_2 incorporated into sulfate cannot be constrained further than a range of 0% to 17%. Moreover no data for the sulfur isotopes of the sulfide end member has been input to this model, rather the $\delta^{34}S_{pyr}$ has been calculated by the model. A future improvement would be to analyse rock samples for $\delta^{34}S$. By determining $\delta^{34}S_{pyr}$ with measurements, it may be possible to reduce the range of $\delta^{18}O_{SO_4pyr}$. It must also be noted, that at main stem sample sites, calculations of $\delta^{18}O_{SO_4pyr}$ use the local water $\delta^{18}O_{H_2O}$ in the main stem although $\delta^{18}O_{SO_4}$ is derived from tributaries with water of different compositions, therefore f_{pyr} values calculated in tributaries are more reliable.

Additionally, this model only takes into account sulfate mixing between two end members, it does not take into account secondary processes such as BSR which can alter the isotopic composition of remaining SO_4^{2-} significantly (Kaplan & Rittenberg, 1964; Detmers *et al.*, 2001; Turchyn *et al.*, 2013). Large fractionations between sulfate and sulfide would alter remaining sulfate composition. Sulfate that is reduced to sulfide via BSR may also be re-oxidised to sulfate and this sulfate would have a different isotopic composition to the initial sulfate.

5.8 Conclusion

The Mekong river has one of the worlds largest sulfate fluxes and 57% of the sulfate flux that is delivered to the South China Sea is derived from the oxidative weathering of pyrite. This Chapter has presented a model to partition measured sulfate concentrations in river waters between two main lithological end members; sedimentary sulfates and sedimentary sulfides. A gypsum end member is constrained from literature data and $\delta^{18}O_{SO_4}$ of a sedimentary sulfide end member is calculated using individual sample $\delta^{18}O_{H_2O}$ values. $\delta^{34}S_{SO_4}$ of the sedimentary sulfide end member is subsequently determined by a new mixing model and confirmed acceptable by comparison against common literature values. The calculated values for f_{gyp} are used in the next Chapter to correct Ca^{2+} and SO_4^{2-} concentrations for evaporite input and f_{pyr} values are used in weathering calculations to determine the impact of pyrite derived sulfate on the carbon budget of the Mekong river basin (Chapter 6).

Chapter 6

Carbon Budget of the Mekong River Basin

6.1 Introduction

Large rivers play a vital role in transporting carbon from the continents to the oceans. Silicate weathering reactions on the continents consume atmospheric CO_2 and the subsequent precipitation of carbonate minerals in the oceans sequesters atmospheric CO_2 into the rock record, completing the negative feedback process that helps to regulate climate (Berner *et al.*, 1983; Walker *et al.*, 1981). Dissolved solids in river waters are used as a proxy for rock weathering and many studies have measured river waters in order to calculate the silicate weathering flux of global river basins (e.g. Gaillardet *et al.*, 1999). Studies quantifying chemical weathering rates have typically neglected the reaction of sulfuric acid with carbonates which can contribute to the solutes present in river water (Gaillardet *et al.*, 1999; Moon *et al.*, 2014; Mortatti & Probst, 2003; Singh *et al.*, 2005). Only recently has it been shown that the sulfuric acid weathering of carbonates could have serious significant global climatic consequences (Torres *et al.*, 2014, 2017).

Sulfuric acid weathering of carbonate minerals releases CO_2 to the atmosphere, but the timescale on which CO_2 is released depends on the environment where the reaction occurs. To reiterate, the weathering of carbonate minerals by sulfuric acid releases CO_2 instantaneously when the reaction site is connected to the atmosphere (Equation 6.1).

$$H_2SO_4 + CaCO_3 \Rightarrow CO_2(g) + H_2O + Ca^{2+} + SO_4^{2-} \tag{6.1}$$

Whereas, when the reaction site is confined and therefore not directly connected to the atmosphere, the released CO_2 is transferred as HCO_3^- to river water and eventually to the oceans (Equation 6.2). Over 10^5-10^6 year timescales the carbon released from carbonate minerals is degassed to the atmosphere as CO_2 when carbonate precipitates in the oceans. The release of CO_2 from carbonate minerals on any timescale could offset the CO_2 drawdown from silicate weathering and have significant climate implications.

$$H_2SO_4 + 2CaCO_3 \Rightarrow 2Ca^{2+} + SO_4^{2-} + 2HCO_3^- \tag{6.2}$$

Determining the flux of oxidative weathering of pyrite has been difficult due to multiple sources of SO_4^{2-} in river waters. As measuring techniques and precision have improved, $\delta^{18}O_{SO_4}$ and $\delta^{34}S_{SO_4}$ in SO_4^{2-} can be measured in increasingly small SO_4^{2-} sample sizes (Paris *et al.*, 2013). As such, SO_4^{2-} in river water can be successfully partitioned to it's sources to calculate the oxidative weathering of pyrite flux (Calmels *et al.*, 2007). In order to fully quantify a carbon budget, the amount of oxidative pyrite weathering of carbonates and thus the release of atmospheric CO_2 must too be calculated on instantaneous and 10^5-year timescales to access the offset from the atmospheric CO_2 removal by carbonic acid weathering of silicates.

Calculating the carbon budget cannot be achieved simply by measuring dissolved inorganic carbon (DIC), predominantly found as HCO_3^- species, in the river; not all chemical reactions supply DIC to the river, some carbon released from reactions is degassed, as in Equation 6.1. A modelling framework partitioning cations to their chemical weathering sources is set out in Chapter 4. Using this framework over 70% of the cations in the Mekong river are derived from chemical weathering of carbonate rocks. However, whether carbonic or sulfuric acid dissolves carbonate rocks has very different implications for global carbon budgets. Chapter 5 used $\delta^{18}O_{SO_4}$ and $\delta^{34}S_{SO_4}$ in a two end member mixing model, to partition SO_4^{2-} between gypsum and sedimentary pyrite sources. An average of 57% of sulfate in the Mekong is derived from pyrite and varies between 19% and 79% in the tributaries. The combination of a high proportion of carbonate rocks and 57% sulfate derived from oxidative weathering of pyrite could indicate carbon release in the Mekong River basin.

This Chapter justifies the forward modelling framework set out in Chapter 4 and develops the forward modelling framework (after Galy & France-Lanord, 1999) to partition solutes between mineral and acidity sources using the fraction of pyrite derived sulfate (calculated in Chapter 5). Torres *et al.* (2016) propose that chemical weathering reactions in confined and open environments release different products, which is included here and discussed in Section 6.2. It is useful to be able to summarise the results of the cation partitioning by plotting data on a summary figure comparing the relative contributions from carbonate and silicate lithologies and acidity sources (H_2CO_3 or H_2SO_4). It is particularly useful when discharge data is lacking and the forward model partitioned cations can not be calculated as fluxes. This second framework used to present partitioned cation data builds on work by Torres *et al.* (2016).

Finally, the net dissolved inorganic carbon budget for the Mekong River is calculated with the available discharge data. The climate implications with regards to CO_2 release or consumption will be discussed on the timescales of chemical dissolution within the catchment (instantaneous) and carbonate precipitation in the oceans ($>10^5$ years) (Section 6.5.3). The spatial and temporal controls of the CO_2 budget within the river basin will also be discussed.

6.2 Modelling Approaches to Elemental Partitioning

It is evident, from the matrices describing CO_2 consequences for each idealised weathering reaction in Chapter 2, that it is essential to partition the fraction of silicate and carbonate weathering and the fraction of H_2CO_3 and H_2SO_4 involved in weathering reactions due to the different implications on the carbon cycle. This section describes how dissolved constituents of river water are apportioned to their various sources - rain, evaporite, carbonates, silicates, sulfides, and anthropogenic - in order to quantify the impact of different weathering reactions on the carbon budget. Three main modelling approaches have previously been used to partition ions and isotopes. The advantages and drawbacks of each modelling approach is discussed below, and the appropriate model is selected for use on the collected Mekong basin data.

A direct method is to apportion the elements measured in the dissolved load to a suite of mineral phases with set element stoichiometries. The quantity of minerals being weathered is calculated using a matrix. In this modal decomposition method, used by Garrels & Mackenzie (1967) and later Bickle *et al.* (2015), the number of minerals specified is limited to the number of dissolved constituents measured, and therefore this may lead to an under-constrained problem in geologically complex basins. This method has not been widely utilised because of the simplified mineral compositions required in the model. Here, this issue of simplified mineral compositions is addressed by using Ca/Na and Mg/K ratios in silicate residues analysed for each individual catchment.

An inverse model has been used to partition solutes for many rivers including the Congo (Négrel *et al.*, 1993), on world rivers (Gaillardet *et al.*, 1999), the Mackenzie River system (Millot *et al.*, 2003), the Red River (Moon *et al.*, 2007), and the Yangtze (Chetelat *et al.*, 2008). The model is based on a mass budget equation describing the mixing of different end members in varying proportions for species such as Cl^-, Ca^{2+}, Mg^{2+}, HCO_3^-, and Sr isotopes. The model takes *a priori* parameters and iterates over the given range (the range is based on natural variability and knowledge of the reservoir) to calculate *a posteriori* values for end members and mixing proportions that best fit the measured data in a least squares sense. In the mixing calculations, concentrations of end members are normalised to Na to reduce effects of evaporation or dilution. Na is chosen for its lack of involvement in nutrient cycling (Millot *et al.*, 2003) and the sources of Na are more constrained than other elements.

Inverse models can be useful when end members are unknown, however, problems arise from this. There are multiple solutions for end members that mix in the same proportion to give the measured value (Sohn, 2013). It is also assumed that minerals dissolve congruently to give measured end member values. Moreover, only one solution for each end member is calculated and is applied to the whole river, or in the case of Gaillardet *et al.* (1999) to all world rivers, which clearly oversimplifies the lithological characteristics of a river basin (Figure 6.1A).

The forward model developed by Galy & France-Lanord (1999) and applied by numerous other studies (e.g. Moon *et al.*, 2007; Li *et al.*, 2014a) is also based upon mass budget equations for multiple elements, but elemental ratios of carbonate to silicate reservoirs are provided rather than calculated. The end member ratios are based on chemical analyses of whole-rock compositions, individual plagioclase grains (Galy & France-Lanord, 1999), or monolithological bedload analyses. As with the inverse model, it is assumed that minerals weather congruently to provide these end member ratios. The forward model is advantageous as it can incorporate individual end member ratios for each sample which allows spatial heterogeneity to be accounted for (Figure 6.1B). The forward model employed by Galy & France-Lanord (1999) corrects for rain inputs then the remaining solutes are accounted for by evaporites, sulfides, carbonates, and silicates. In Galy & France-Lanord (1999), or others that have used their model (e.g. Li *et al.*, 2014a), SO_4^{2-} in river water is attributed to sulfide oxidation, although no correction is made for other

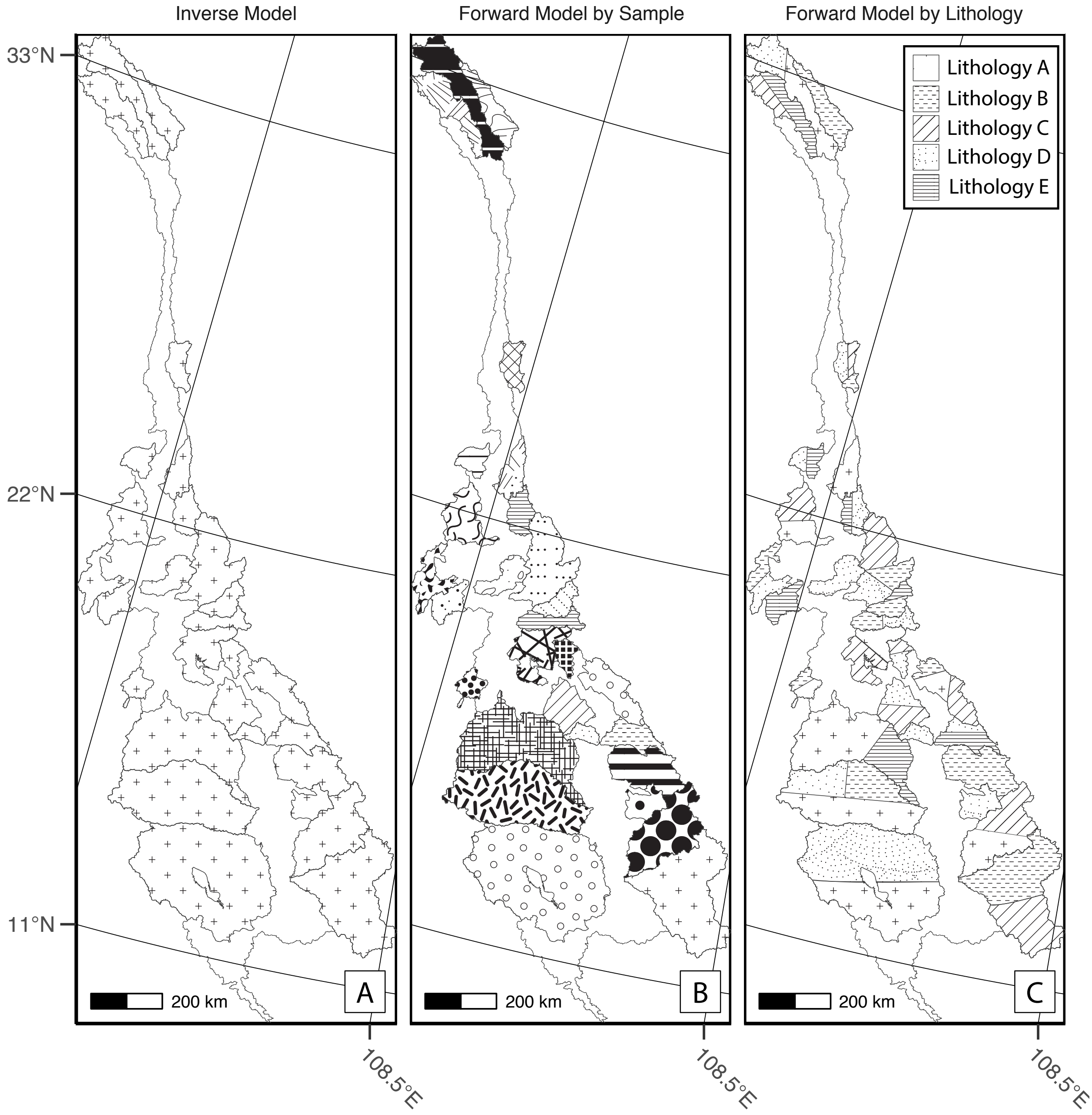

Figure 6.1: Example of the three methods previously used to model the partitioning of dissolved elements. A: The inverse model assigns one value to each of Ca/Na and Mg/K ratios in silicate end members over the whole catchment as is illustrated by continuous crossed–texture over all catchments in the Mekong (e.g. Gaillardet *et al.*, 1999). B: Analysed samples are used in the forward model to assign unique values to each catchment, illustrated by the exclusive pattern in each catchment in the Mekong. This is the method followed here, modified after Galy & France-Lanord (1999). C: Prescribed lithology compositions are used through the catchment, but in varying proportions (Torres *et al.*, 2016). This forms an adapted forwards model, as illustrated by the five lithologies applies in varying amounts to each catchment.

cations, for example Ca^{2+}, delivered by sulfuric acid reacting with other minerals. Furthermore, evaporite corrections are only made for halite, not gypsum, which also provides Ca^{2+} and SO_4^{2-} ions. Torres *et al.* (2016) partition solutes based largely on a forward model, but elemental ratios are fixed for multiple lithologies which are then mixed in different proportions to provide the river water composition (Figure 6.1C). Solutes are partitioned between sources of H_2CO_3 and H_2SO_4 weathering using SO_4^{2-}:total cation ratios and δ^{34}S isotopes (Torres *et al.*, 2016). Here, the forward model is modified to account for the complex and heterogeneous geology of the Mekong River basin. This is done by employing acidity partitioning using $\delta^{18}O_{SO_4}$ and $\delta^{34}S_{SO_4}$ isotopes (Chapter 5) and incorporating silicate end member ratios for each sample (Chapter 4).

6.3 A Revised Forward Model for Partitioning Elemental Contributions

In Chapter 4, river solute corrections for rain water and halite inputs were discussed, and cations were partitioned between silicate and carbonate weathering using Ca/Na and Mg/K ratios in bank residue ratios. For completeness the corrections and silicate mineral weathering partitioning method are repeated now as the forward model is developed and information from Chapter 5 is included to correct cations for gypsum evaporites and further partition cations between acidity source as well as lithology.

In order to calculate the amount of each weathering reaction occurring, the forward model is used to partition dissolved solutes between end members. Measured solutes in the river are a mixture of atmospheric and mineral weathering inputs, and can be expressed as a mass budget equation for each element, X (in molar concentrations):

$$[X]_{riv} = [X]_{atmos} + [X]_{evp} + [X]_{pyr} + [X]_{sil}^{Total} + [X]_{carb}^{Total} \tag{6.3}$$

Elements are shown with their $_{source}$ and ^{acidity} participating in the reaction, building upon the forward model established by Galy & France-Lanord (1999). X^{Total} indicates the weathering contribution from all acidity sources (though H_2CO_3 and H_2SO_4 are the main reagents involved in weathering reactions). The contribution to riverine solutes from cyclic or atmospheric deposition (*atmos*), evaporites (*evp*), sulfides (*pyr*), silicates (*sil*) and carbonates (*carb*) to the river (*riv*) are partitioned for elements K^+, Na^+, Ca^{2+}, Mg^{2+}, Cl^-, and the SO_4^{2-} ion using a forward model decomposition (Equations 6.4-6.9).

Rain Correction

Firstly, corrections are made for atmospheric inputs using the X/Cl ratio in rain. Due to the large size of the Mekong basin and the varying distance of sample sites to the coast, five rain samples were collected over the basin and applied to water samples within their geographic vicinity (further details on rain correction can be found in Section 4.3.2.1). Elements corrected for atmospheric inputs are indicated with an asterisk, X^*.

$$Cl^*_{riv} = Cl_{evp} \tag{6.4}$$

$$SO^*_{4\ riv} = SO_{4\ evp} + SO_{4\ pyr} \tag{6.5}$$

$$K^*_{riv} = K^{carb}_{sil} + K^{sulf}_{sil} \tag{6.6}$$

$$Na^*_{riv} = Na_{evp} + Na^{carb}_{sil} + Na^{sulf}_{sil} \tag{6.7}$$

$$Ca^*_{riv} = Ca_{evp} + Ca^{carb}_{sil} + Ca^{sulf}_{sil} + Ca^{carb}_{carb} + Ca^{sulf}_{carb} \tag{6.8}$$

$$Mg^*_{riv} = Mg^{carb}_{sil} + Mg^{sulf}_{sil} + Mg^{carb}_{carb} + Mg^{sulf}_{carb} \tag{6.9}$$

Evaporite Correction

Secondly, salt input is calculated. In the Mekong basin evaporites can be found in China, however, the majority of evaporites are concentrated in the Khorat Plateau, Thailand, on the right (west) bank of the Middle Mekong. This is in distinct contrast to the left bank in Laos which lacks evaporites (Figure 4.21). Dominated by a large evaporite basin, tributaries draining the Khorat Plateau have Na^*_{riv} concentrations up to 754μmol/L. Halite is a common salt that releases one mole of Na^+ for each mole of Cl^- when dissolved. Cl^- is sourced from atmospheric deposition or salts (Equation 6.4), so all rain corrected Cl^- (Cl^*) can be used to correct Na^*_{riv} for salt in the same ratio (Equation 6.10) (Galy & France-Lanord, 1999). Any remaining Na^+ after correction for rain and salt is derived from weathering of silicates with all acidity sources (Equation 6.11). Negligible Na^+ is derived from carbonates (Berner, 2004). If halite input is overcorrected $\mathrm{Na}^{Total}_{sil}$ becomes negative. This is where there is a large contribution from evaporites but little to no Na-silicate in the catchment. In the scenario presented here, $\mathrm{Na}^{Total}_{sil}$ is set to zero (Equation 6.12) (discussed in Chapter 4.4.2).

$$Na_{evp} = Cl^{*}_{riv} \tag{6.10}$$

$$Na^{Total}_{sil} = Na^{*}_{riv} - Na_{evp} \tag{6.11}$$

$$if\ Na_{evp} > Na^{*}_{riv}\ then\ Na^{Total}_{sil} = 0 \tag{6.12}$$

Evaporites such as anhydrite ($CaSO_4$) or gypsum ($CaSO_4{\cdot}H_2O$) provide Ca^{2+} and SO_4^{2-} in the same molar ratio (Equation 6.13). SO_4^{2-} in the river is supplied by a mixture of weathering of sedimentary sulfates and sulfides (Equation 6.5), and $\delta^{34}S_{SO_4}$ and $\delta^{18}O_{SO_4}$ are used to calculate the proportion of SO_4^{2-} derived from each source (discussed in detail in Chapter 5). The proportion of SO_4^{2-} derived from gypsum, f_{gyp}, is used to calculate $[SO_4^{2-}]_{gyp}$ (Equation 6.14) which can then be used to correct Ca^{*}_{riv} for gypsum contributions. This builds upon models by Galy & France-Lanord (1999) and Li *et al.* (2014a) in which the $[SO_4^{2-}]_{gyp}$ contributions are assumed to be equal to the minimum concentration of SO_4^{2-} in the Mekong catchment.

$$Ca_{gyp} = SO_{4\ gyp} \tag{6.13}$$

$$[SO_4^{2-}]_{gyp} = [SO_4^{2-}]^{*}_{riv} * f_{gyp} \tag{6.14}$$

Partitioning Solutes Between Silicate and Carbonate Sources

Weathering of silicates and carbonates supplies Ca^{2+} and Mg^{2+} to a river. The contribution of Ca^{2+} and Mg^{2+} from each lithological input is partitioned using elemental ratios in silicates. Most previous work has used one ratio for the entire basin whether elements have been partitioned using the forward or inverse model (e.g. Galy & France-Lanord, 1999; Gaillardet *et al.*, 1999; Millot *et al.*, 2003; Chetelat *et al.*, 2008; Li *et al.*, 2014a). In this study, bank samples collected from every tributary in the Mekong have been leached to analyse the silicate fraction and calculate unique Ca/Na and Mg/K ratios. The residue data presented in Chapter 4.3.1 highlights the range in geologically diverse basins such as the Mekong, this is an important improvement in the forward model.

Ca^{2+} contributed by both sulfuric and carbonic acid weathering of silicates (Ca^{Total}_{sil}) is calculated by Equation 6.15. Na^{*}_{riv} is used with the Ca/Na ratio in the silicate residue to calculate Ca^{Total}_{sil}. The Ca^{2+} supplied by total carbonate weathering (by both H_2CO_3 and H_2SO_4) (Equation 6.16) is the remaining Ca^{2+} after evaporite correction (Equation 6.13 - 6.14) and removal of silicates.

$$Ca_{sil}^{Total} = Na_{riv}^{*} * \left(\frac{Ca}{Na}\right)_{sil\ residue} \tag{6.15}$$

$$Ca_{carb}^{Total} = Ca_{riv}^{*} - Ca_{gyp} - Ca_{sil}^{Total} \tag{6.16}$$

Similarly, Mg-silicates are partitioned by Equation 6.17 using K_{riv}^{*} and Mg/K ratios in the silicate residue to calculate Mg_{sil}^{Total}. Mg/K ratios are used instead of Mg/Na due to the smaller range and a normal distribution in values (Figure 4.3), additionally less corrections are made on K than Na, making K more reliable. Remaining Mg^{2+} after atmospheric correction is from weathering of carbonates (by all acidity sources) (Equation 6.18).

$$Mg_{sil}^{Total} = K_{riv}^{*} * \left(\frac{Mg}{K}\right)_{sil\ residue} \tag{6.17}$$

$$Mg_{carb}^{Total} = Mg_{riv}^{*} - Mg_{sil}^{Total} \tag{6.18}$$

6.3.1 Developing the Forward Model with Acidity Source Partitioning

Partitioning Sulfuric Acid Between Silicate and Carbonate Minerals

Sulfuric acid (H_2SO_4) and carbonic acid (H_2CO_3) can weather carbonates and silicates with different carbon implications (Equations detailed in Chapter 2). Due to the current lack of experimental data, it is not possible to exactly determine in what proportion H_2SO_4 and H_2CO_3 weather silicates and carbonates, but a first order assumption is that both H_2CO_3 and H_2SO_4 weather carbonate and silicate minerals in the same proportion (Equation 6.19). For example the ratio of Ca_{carb}^{carb} to Ca_{sil}^{carb} is the same as the ratio of Ca_{carb}^{sulf} to Ca_{sil}^{sulf} (where n is the amount of the reaction).

$$\frac{n_{Carb}H_2CO_3}{n_{Sil}H_2CO_3} = \frac{n_{Carb}H_2CO_3 + n_{Carb}H_2SO_4^O}{n_{Sil}H_2CO_3 + n_{Sil}H_2SO_4} = \frac{n_{Carb}H_2SO_4^O}{n_{Sil}H_2SO_4} \tag{6.19}$$

The proportion of SO_4^{2-} derived from oxidative weathering of pyrite, f_{pyr}, is used to calculate $[SO_4^{2-}]_{pyr}$ (Equation 6.20). $[SO_4^{2-}]_{pyr}$ will be charge balanced by Ca^{2+} and Mg^{2+} from carbonates and K^+, Na^+, Ca^{2+}, Mg^{2+} from silicates. Therefore the amount of H_2SO_4 that is available to weather carbonates is the fraction of total carbonate ions over total ions derived from carbonates and silicates (Equation 6.21). Similarly for the H_2SO_4 available to weather total silicates (Equation 6.22).

$$[SO_4^{2-}]_{pyr} = [SO_4^{2-}]^*_{riv} * f_{pyr} \tag{6.20}$$

$$[SO_4^{2-}]_{Total\ carb} = [SO_4^{2-}]_{pyr} * \frac{Ca_{carb}^{Total} + Mg_{carb}^{Total}}{Ca_{sil}^{Total} + Ca_{carb}^{Total} + Mg_{sil}^{Total} + Mg_{carb}^{Total} + Na_{sil}^{Total} + K_{sil}^{Total}} \tag{6.21}$$

$$[SO_4^{2-}]_{Total\ sil} = [SO_4^{2-}]_{pyr} * \frac{Ca_{sil}^{Total} + Mg_{sil}^{Total} + Na_{sil} + K_{sil}}{Ca_{sil}^{Total} + Ca_{carb}^{Total} + Mg_{sil}^{Total} + Mg_{carb}^{Total} + Na_{sil}^{Total} + K_{sil}^{Total}} \tag{6.22}$$

The total amount of carbonate minerals weathered by sulfuric acid can be partitioned between Ca-carbonate and Mg-carbonate. The product of Equation 6.21 is the amount of H_2SO_4 available to weather total carbonates. $[SO_4^{2-}]_{Total\ carb}$ multiplied by the fraction of Ca or Mg derived from carbonate minerals, as a fraction of total Ca- and Mg-carbonate minerals, calculates the Ca or Mg derived from sulfuric acid weathering of carbonate minerals (Equations 6.23-6.24). Similarly for silicate minerals; the total amount of H_2SO_4 available to weather silicate minerals (Equation 6.22) is apportioned according to the proportion of each silicate mineral, Ca, Mg, K, and Na, as a ratio of total silicate minerals (Equations 6.25-6.28).

$$Ca_{carb}^{sulfO} = [SO_4^{2-}]_{Total\ carb} * \frac{Ca_{carb}^{Total}}{Ca_{carb}^{Total} + Mg_{carb}^{Total}} \tag{6.23}$$

$$Mg_{carb}^{sulfO} = [SO_4^{2-}]_{Total\ carb} * \frac{Mg_{carb}^{Total}}{Ca_{carb}^{Total} + Mg_{carb}^{Total}} \tag{6.24}$$

$$Ca_{sil}^{sulf} = [SO_4^{2-}]_{Total\ sil} * \frac{Ca_{sil}^{Total}}{Ca_{sil}^{Total} + Mg_{sil}^{Total} + Na_{sil}^{Total} + K_{sil}^{Total}} \tag{6.25}$$

$$Mg_{sil}^{sulf} = [SO_4^{2-}]_{Total\ sil} * \frac{Mg_{sil}^{Total}}{Ca_{sil}^{Total} + Mg_{sil}^{Total} + Na_{sil}^{Total} + K_{sil}^{Total}} \tag{6.26}$$

$$Na_{sil}^{sulf} = [SO_4^{2-}]_{Total\ sil} * \frac{Na_{sil}^{Total}}{Ca_{sil}^{Total} + Mg_{sil}^{Total} + Na_{sil}^{Total} + K_{sil}^{Total}} \tag{6.27}$$

$$K_{sil}^{sulf} = [SO_4^{2-}]_{Total\ sil} * \frac{K_{sil}^{Total}}{Ca_{sil}^{Total} + Mg_{sil}^{Total} + Na_{sil}^{Total} + K_{sil}^{Total}} \tag{6.28}$$

The partitioning of sulfuric acid between carbonate minerals (Equations 6.23-6.24) has so far only been calculated for the sulfuric acid weathering of carbonates in an open environment (Equation 2.3, Figure 2.1C), where one mole of SO_4^{2-} is released for one mole of Ca^{2+}. The second reaction pathway of sulfuric acid weathering of carbonates needs to be taken into account due the release of two moles of Ca^{2+} or Mg^{2+} for each mole of SO_4^{2-} in a confined environment (Equation 2.4, Figure 2.1D). Hence the coefficient 2 is applied to the total amount of sulfuric acid available to weather carbonate minerals ($[SO_4^{2-}]_{Total\ carb}$) when being partitioned between Ca and Mg carbonate minerals (Equations 6.29-6.30).

$$Ca_{carb}^{sulfC} = 2[SO_4^{2-}]_{Total\ carb} * \frac{Ca_{carb}^{Total}}{Ca_{carb}^{Total} + Mg_{carb}^{Total}} \tag{6.29}$$

$$Mg_{carb}^{sulfC} = 2[SO_4^{2-}]_{Total\ carb} * \frac{Mg_{carb}^{Total}}{Ca_{carb}^{Total} + Mg_{carb}^{Total}} \tag{6.30}$$

Calculating Carbonic Acid Mineral Weathering

Carbonates and silicates that are weathered by carbonic acid are calculated by removing the sulfuric acid weathered end member from total carbonate or total silicates, for all open (O) and confined (C) weathering environments (Equations 6.31-6.38).

$$Ca_{carb}^{carbO} = Ca_{carb}^{Total} - Ca_{carb}^{sulfO} \tag{6.31}$$

$$Ca_{carb}^{carbC} = Ca_{carb}^{Total} - Ca_{carb}^{sulfC} \tag{6.32}$$

$$Mg_{carb}^{carbO} = Mg_{carb}^{Total} - Mg_{carb}^{sulfO} \tag{6.33}$$

$$Mg_{carb}^{carbC} = Mg_{carb}^{Total} - Mg_{carb}^{sulfC} \tag{6.34}$$

$$Ca_{sil}^{carb} = Ca_{sil}^{Total} - Ca_{sil}^{sulf} \tag{6.35}$$

$$Mg_{sil}^{carb} = Mg_{sil}^{Total} - Mg_{sil}^{sulf} \tag{6.36}$$

$$Na_{sil}^{carb} = Na_{sil}^{Total} - Na_{sil}^{sulf} \tag{6.37}$$

$$K_{sil}^{carb} = K_{sil}^{Total} - K_{sil}^{sulf} \tag{6.38}$$

Solute Partitioning Verification

In order to verify that the assumptions used in the partitioning are reasonable, the results can be compared to the charge balance of the river. HCO_3^- delivered from weathering reactions is calculated using partitioned cations and compared against measured HCO_3^-, in equivalent units (Equations 6.39-6.40). Similarly the SO_4^{2-} delivered from sulfuric acid weathering of silicate and carbonate minerals and dissolution of gypsum is calculated using partitioned cations and can be compared against measured total SO_4^{2-}, in equivalent units (Equations 6.41-6.42).

$$[HCO_3^-]_{meas} = 2Ca_{carb}^{carbO} + 2Mg_{carb}^{carbO} + 2Ca_{sil}^{carb} + 2Mg_{sil}^{carb} + K_{sil}^{carb} + Na_{sil}^{carb} \tag{6.39}$$

$$[HCO_3^-]_{meas} = 2Ca_{carb}^{carbC} + 2Mg_{carb}^{carbC} + 2Ca_{sil}^{carb} + 2Mg_{sil}^{carb} + K_{sil}^{carb} + Na_{sil}^{carb} + 4Ca_{carb}^{sulfC} + 4Mg_{carb}^{sulfC} \tag{6.40}$$

$$2[SO_4^{2-}]_{meas} = 2Ca_{gyp} + 2Ca_{carb}^{sulfO} + 2Mg_{carb}^{sulfO} + 2Ca_{sil}^{sulf} + 2Mg_{sil}^{sulf} + K_{sil}^{sulf} + Na_{sil}^{sulf} \tag{6.41}$$

$$2[SO_4^{2-}]_{meas} = 2Ca_{gyp} + 4Ca_{carb}^{sulfC} + 4Mg_{carb}^{sulfC} + 2Ca_{sil}^{sulf} + 2Mg_{sil}^{sulf} + K_{sil}^{sulf} + Na_{sil}^{sulf} \tag{6.42}$$

Once each element has been partitioned into its end member sources, DIC contributions from weathering reactions and CO_2 consumption within the basin can be calculated (Table 6.1-6.3).

Table 6.1: Partitioned dissolved major cations and anions in the Mekong main channel, sampled repeatedly in 2014, 2016 and 2017

Sample	Location	Ca_{gyp}	$\text{SO}_{4\ pyr}$	$[\text{SO}_4^{2-}]^{Total}_{carb}$	$[\text{SO}_4^{2-}]^{Total}_{sil}$	$\text{Ca}^{sulf}_{carb}{}^{O}$	$\text{Ca}^{sulf}_{carb}{}^{C}$	$\text{Mg}^{sulf}_{carb}{}^{O}$	$\text{Mg}^{sulf}_{carb}{}^{C}$	Ca^{sulf}_{sil}	Mg^{sulf}_{sil}	Na^{sulf}_{sil}	K^{sulf}_{sil}	$\text{Ca}^{carb}_{carb}{}^{O}$	$\text{Ca}^{carb}_{carb}{}^{C}$	$\text{Mg}^{sulf}_{carb}{}^{O}$	$\text{Mg}^{carb}_{carb}{}^{C}$	Ca^{carb}_{sil}	Mg^{carb}_{sil}	Na^{carb}_{sil}	K^{carb}_{sil}
											μmol/L										
Main Channel																					
CAMB140620-01	Stung Treng	9	14	6	8	3	7	3	6	2.1	0.8	4.2	1.2	64	61	54	51	41	15	82	23
CAMB140621-10	Kratie	31	48	34	14	23	47	11	21	0.8	1.2	9.4	2.3	225	202	102	91	8	12	91	22
CAMB140622-13	Kampong Cham	40	61	45	16	31	62	14	28	1.0	1.5	11.1	2.7	279	248	127	113	9	13	101	25
CAMB140627-22	Chrouy Changvar	39	60	49	11	35	70	14	28	0.9	1.5	6.6	2.4	342	307	135	121	9	15	64	23
CAMB140718-66	Chrouy Changvar	15	23	18	5	13	26	5	10	0.4	0.7	3.3	1.0	224	211	86	81	8	11	57	18
CAMB140719-69	Kratie	10	16	11	5	8	15	3	7	0.3	0.4	3.2	0.7	173	165	79	75	6	9	73	16
CAMB140720-87	Chhlong, Kratie	21	32	27	6	19	39	7	15	0.3	0.7	3.4	1.3	271	252	105	97	4	9	47	18
CAMB140720-88	Chhlong, Kratie	15	23	18	5	13	25	5	10	0.3	0.5	3.5	1.0	210	197	86	80	5	8	58	16
CAMB140721-100	Chhlong, Kratie	13	19	14	5	10	21	4	8	0.3	0.4	3.2	0.8	190	180	76	72	5	8	58	15
CAMB140721-101	Chhlong, Kratie	19	29	24	5	17	35	7	13	0.3	0.6	3.0	1.1	251	233	98	91	4	9	43	16
CAMB140722-108	Kratie	13	19	15	4	11	21	4	9	0.3	0.4	2.9	0.8	188	178	76	71	4	8	52	14
CAMB140722-114	Kratie	18	28	22	6	16	32	6	12	0.3	0.6	3.6	1.0	239	223	93	87	5	8	55	15
CAMB140723-140	Stung Treng	16	27	20	6	15	30	5	11	1.6	0.7	3.1	1.0	247	232	91	86	26	11	52	16
CAMB140725-161	Chrouy Changvar	12	19	14	5	10	20	4	8	0.4	0.4	3.1	0.7	202	192	77	73	8	9	60	13
MEK16-007	Vientiane	47	51	34	18	24	48	10	20	6.7	1.1	8.2	1.7	379	355	157	147	106	17	130	27
MEK16-033	Luang Prabang	36	76	59	18	43	86	16	31	2.1	0.9	11.9	2.8	434	391	159	143	21	9	121	29
MEK16-096	Pakse	26	30	25	5	19	37	6	12	0.4	0.7	3.1	1.1	350	331	108	102	7	13	58	21
MEK16-106	Stung Treng	18	30	23	7	17	35	6	11	1.6	0.8	3.2	1.2	296	278	95	89	28	13	55	20
MEK16-137	Kratie	10	16	12	4	9	18	3	6	0.2	0.4	2.6	0.8	196	187	72	69	5	9	57	17
MEK17-002	Kratie	57	87	77	10	53	106	24	48	0.4	1.6	4.9	2.9	440	387	199	175	4	13	41	24
MEK17-003	Stung Treng	57	94	84	10	58	117	26	52	1.2	2.5	2.4	3.7	482	424	216	190	10	21	20	31
MEK17-107	China, Baoshan	291	410	341	69	213	427	128	256	5.7	5.8	48.4	8.6	671	458	402	274	18	18	152	27
MEK17-114	China, Baoshan	292	410	342	68	214	428	128	257	5.7	5.6	48.4	8.3	678	464	407	278	18	18	153	26
MEK17-135	Luang Prabang	46	86	67	18	48	97	19	37	2.1	1.1	11.7	3.6	435	386	168	150	18	10	105	32
MEK17-157	Vientiane	40	44	29	15	20	41	8	17	5.4	1.1	6.6	1.7	360	340	150	141	95	19	117	31
MEK17-189	Pakse	21	31	27	4	20	41	7	13	0.2	0.8	1.4	1.4	352	331	114	107	3	14	25	24
MEK17-195	Stung Treng	20	32	25	7	19	38	6	13	1.5	1.0	3.0	1.5	307	288	100	94	24	16	48	24
MEK17-213	Kratie	18	28	23	5	17	34	6	11	0.2	0.7	2.9	1.3	331	314	109	103	5	13	56	25
MEK17-225	Kratie	19	29	24	5	18	36	6	12	0.2	0.7	2.5	1.3	325	307	106	100	4	13	45	23

Table 6.2: Partitioned dissolved major cations and anions in Mekong tributary rivers, sampled repeatedly in 2014, 2016 and 2017

Sample	Location	Ca_{gyp}	$SO_{4\ pyr}$	$[SO_4^{2-}]^{Total}_{carb}$	$[SO_4^{2-}]^{Total}_{sil}$	$Ca^{sulf\ O}_{carb}$	$Ca^{sulf\ C}_{carb}$	$Mg^{sulf\ O}_{carb}$	$Mg^{sulf\ C}_{carb}$	Ca^{sulf}_{sil}	Mg^{sulf}_{sil}	Na^{sulf}_{sil}	K^{sulf}_{sil}	$Ca^{carb\ O}_{carb}$	$Ca^{carb\ C}_{carb}$	$Mg^{sulf\ O}_{carb}$	$Mg^{carb\ C}_{carb}$	Ca^{carb}_{sil}	Mg^{carb}_{sil}	Na^{carb}_{sil}	K^{carb}_{sil}
		μmol/L																			
Tributaries																					
MEK17-256	Chi	6	15	9	6.3	7	14	1.6	3.2	0.7	1.4	2.5	1.7	210	203	48	46	21	41	75	52
MEK17-123	Heihui	57	53	45	8.2	34	69	10.8	21.6	0.3	0.7	5.9	1.2	693	659	218	207	5	15	119	25
MEK17-236	Hueang	19	12	7	5.1	5	10	2.1	4.2	0.5	0.4	3.4	0.8	222	217	96	94	21	20	156	37
MEK17-240	Hueang	148	56	40	16.6	30	59	9.8	19.7	1.2	1.2	12.1	2.0	596	566	198	188	24	24	244	41
MEK17-230	Mae Kok	11	13	8	5.2	5	10	2.9	5.8	0.7	0.2	3.0	1.2	200	194	111	108	28	9	116	47
MEK17-254	Mun D/S	6	12	8	4.1	6	13	1.4	2.9	0.3	1.3	1.0	1.6	162	156	37	36	7	33	25	42
MEK17-257	Mun U/S	6	11	8	2.9	6	12	1.8	3.6	0.0	1.3	0.0	1.6	118	112	34	32	0	25	0	31
MEK17-169	Nam Hinboun	3	10	9	0.6	8	16	1.2	2.4	0.0	0.1	0.3	0.2	476	467	71	70	1	6	18	10
MEK16-053	Nam Hinboun	3	11	10	0.6	9	18	1.3	2.5	0.0	0.1	0.4	0.1	585	576	80	79	2	5	25	8
MEK17-166	Nam Kading	2	10	9	1.6	7	15	1.5	3.0	0.3	0.1	0.8	0.4	246	238	50	48	10	4	28	13
MEK16-051	Nam Kading	3	13	11	2.0	9	18	1.8	3.6	0.4	0.1	1.1	0.4	269	260	53	51	11	3	33	11
MEK17-141	Nam Khan	15	24	19	4.5	15	30	4.2	8.5	0.7	0.2	3.0	0.6	780	764	217	212	35	10	156	31
MEK16-012	Nam Khan	9	14	11	3.2	8	16	2.6	5.1	0.5	0.2	2.1	0.5	589	580	185	182	33	12	148	39
MEK17-146	Nam Lik	170	38	33	5.0	24	48	8.9	17.9	0.1	0.4	4.0	0.5	796	771	295	286	5	13	131	15
MEK16-041	Nam Lik	28	6	5	1.4	3	7	1.5	3.0	0.0	0.1	1.1	0.1	321	318	139	138	4	12	99	14
MEK17-164	Nam Ngiap	3	4	3	1.3	2	4	0.9	1.9	0.3	0.1	0.7	0.2	177	174	73	73	21	8	54	17
MEK16-047	Nam Ngiap	3	4	3	1.4	2	4	0.8	1.6	0.3	0.1	0.8	0.2	162	160	67	66	26	8	68	17
MEK17-158	Nam Ngjum	14	10	8	1.8	6	12	2.2	4.3	0.3	0.1	1.2	0.2	273	268	102	100	13	6	55	9
MEK16-045	Nam Ngjum	9	6	5	1.4	3	7	1.3	2.5	0.2	0.1	0.9	0.1	223	219	80	79	14	6	58	9
MEK17-127	Nam Ou	13	10	8	2.0	6	12	1.9	3.7	0.3	0.1	1.5	0.2	532	526	161	159	25	9	126	15
MEK16-025	Nam Ou	13	10	8	2.2	6	12	1.8	3.6	0.3	0.1	1.6	0.2	507	500	148	147	26	10	130	17
MEK17-245	Songkhram	3	6	4	1.9	3	6	1.4	2.7	0.0	0.6	0.0	1.4	64	61	29	28	0	12	0	29
MEK17-207	Tonle Kong	2	3	2	1.3	1	2	0.8	1.5	0.2	0.1	0.8	0.2	49	48	48	47	14	5	48	13
CAMB140620-07	Tonle Kong	4	5	2	2.4	1	2	1.2	2.3	0.5	0.1	1.6	0.3	46	45	47	46	19	4	64	11
CAMB140723-122	Tonle Kong	2	3	1	1.1	1	2	0.7	1.3	0.2	0.0	0.7	0.1	41	40	36	35	12	2	39	7
MEK16-119	Tonle Kong	2	3	2	1.3	1	2	0.7	1.4	0.1	0.1	0.9	0.2	55	54	41	40	7	5	53	13
MEK17-004	Tonle Kong	4	5	3	1.9	1	3	1.3	2.5	0.3	0.1	1.2	0.3	76	75	72	71	20	6	67	18
MEK17-201	Tonle Srepok D/S	4	3	1	1.8	0	1	0.7	1.3	0.6	0.1	0.9	0.3	28	27	50	49	43	8	67	19
MEK17-005	Tonle Srepok D/S	12	10	4	6.0	1	2	2.8	5.6	1.9	0.4	2.9	0.8	32	31	90	87	61	12	95	26
MEK16-112	Tonle Srepok D/S	3	2	1	1.7	0	0	0.5	1.1	0.5	0.1	0.8	0.2	17	17	39	39	38	8	59	17
CAMB140620-04	Tonle Srepok D/S	6	5	1	3.6	0	1	1.0	2.0	1.1	0.2	1.7	0.5	16	16	53	52	60	12	93	27
CAMB140723-117	Tonle Srepok D/S	4	3	1	2.1	1	1	0.9	1.7	0.7	0.1	1.1	0.2	36	35	58	57	46	6	72	14
MEK16-077	Xe Banghiang	6	8	6	1.9	4	9	1.7	3.4	0.1	0.3	0.9	0.6	148	144	56	55	4	9	31	19
MEK17-176	Xe Banghiang	5	7	5	1.6	4	7	1.4	2.8	0.1	0.2	0.8	0.5	142	139	56	55	4	9	33	19
MEK17-183	Xe Don	3	3	2	0.9	1	3	0.9	1.7	0.1	0.0	0.7	0.1	180	179	122	121	11	6	101	9
MEK16-087	Xe Don	2	2	1	0.6	1	1	0.5	1.0	0.1	0.0	0.5	0.1	121	120	87	86	9	6	80	10

Table 6.3: Partitioned dissolved major cations and anions in Mekong main channel timeseries at Chroy Changvar, Phnom Penh, Cambodia.

Sample	Date	Ca_{gyp}	$\mathrm{SO}_{4\ pyr}$	$[\mathrm{SO}_4^{2-}]^{Total}_{carb}$	$[\mathrm{SO}_4^{2-}]^{Total}_{sil}$	$\mathrm{Ca}^{sulf\ O}_{carb}$	$\mathrm{Ca}^{sulf\ C}_{carb}$	$\mathrm{Mg}^{sulf\ O}_{carb}$	$\mathrm{Mg}^{sulf\ C}_{carb}$	Ca^{sulf}_{sil}	Mg^{sulf}_{sil}	Na^{sulf}_{sil}	K^{sulf}_{sil}	$\mathrm{Ca}^{carb\ O}_{carb}$	$\mathrm{Ca}^{carb\ C}_{carb}$	$\mathrm{Mg}^{sulf\ O}_{carb}$	$\mathrm{Mg}^{carb\ C}_{carb}$	Ca^{carb}_{sil}	Mg^{carb}_{sil}	Na^{carb}_{sil}	K^{carb}_{sil}	
											μmol/L											
Timeseries at Chroy Changvar, Phnom Penh, Cambodia																						
CAMB140630-29	2014-06-30	24	37	29	8	21	41	8	16	0.7	1.0	5.1	1.5	246	225	94	86	8	12	61	18	24
CAMB140701-31	2014-07-01	25	39	30	9	22	44	8	17	0.7	1.1	5.1	1.7	252	230	96	88	8	13	58	20	25
CAMB140702-33	2014-07-02	29	44	35	9	26	51	10	20	0.6	1.2	4.7	1.9	284	259	109	99	7	14	53	22	29
CAMB140703-35	2014-07-03	27	41	34	7	24	49	9	19	0.5	1.2	3.8	1.9	293	269	113	103	6	14	46	23	27
CAMB140706-41	2014-07-06	15	23	21	2	16	31	6	11	0.0	0.9	0.0	1.4	231	215	83	77	0	13	0	21	15
CAMB140707-43	2014-07-07	16	24	19	5	14	28	5	10	0.3	0.8	2.2	1.3	230	216	83	78	5	14	37	21	16
CAMB140708-45	2014-07-08	16	25	20	5	15	29	5	10	0.3	0.8	2.5	1.3	243	228	86	81	6	14	42	22	16
CAMB140710-49	2014-07-10	18	27	22	6	16	32	6	11	0.4	0.8	3.2	1.2	253	237	90	85	7	12	51	19	18
CAMB140711-52	2014-07-11	19	29	23	6	17	33	6	12	0.5	0.8	3.4	1.3	253	236	91	85	7	12	53	19	19
CAMB140712-54	2014-07-12	19	29	23	6	17	33	6	12	0.5	0.8	3.4	1.3	243	227	89	83	7	12	50	19	19
CAMB140713-56	2014-07-13	16	25	19	6	13	27	5	10	0.6	0.7	4.1	1.1	217	204	82	77	9	11	67	17	16
CAMB140714-58	2014-07-14	15	22	16	6	12	24	4	9	0.5	0.7	3.6	1.1	212	200	79	75	9	12	64	19	15
CAMB140715-60	2014-07-15	14	22	17	5	12	24	5	9	0.4	0.6	2.9	1.0	211	199	81	76	7	11	51	18	14
CAMB140716-62	2014-07-16	15	23	17	5	12	25	5	10	0.4	0.7	3.2	1.0	216	204	84	79	8	11	56	18	15
MEK.US.PP 18.4.14	2014-04-18	82	125	100	25	68	135	32	64	2.3	2.3	17.0	3.6	434	366	206	174	15	15	109	23	82
MEK.US.PP 7.5.14	2014-05-07	74	113	82	31	57	113	25	50	3.0	2.4	21.6	3.8	427	370	190	165	22	18	163	29	74
MK.UP.PP 19.5.14	2014-05-19	66	101	74	26	51	103	23	46	2.5	2.3	17.9	3.6	406	354	183	160	19	18	142	29	66
MK.US.PP 4.6.14	2014-06-04	70	106	79	27	56	111	23	46	2.5	2.5	18.5	3.9	435	380	182	158	20	19	144	30	70
MK.US.PP 15.6.14	2014-06-15	79	121	91	30	64	127	27	54	2.9	2.5	21.0	4.0	429	366	184	156	19	17	141	27	79
MK.US.PP 21.6.14	2014-06-21	58	89	66	23	45	90	21	41	2.1	2.2	15.7	3.4	310	265	142	121	15	15	108	24	58
MK.US.PP 29.6.14	2014-06-29	28	43	32	12	23	46	9	17	1.0	1.1	7.6	1.8	266	243	102	93	12	13	89	21	28
MK.US.PP 7.7.14	2014-07-07	16	25	20	5	15	30	5	10	0.3	0.9	2.5	1.4	237	222	83	78	6	14	40	22	16
MK.US.PP 11.7.14	2014-07-11	19	29	22	7	16	32	6	11	0.6	0.9	4.3	1.5	257	241	90	85	10	15	70	24	19
MK.UP.PP 27.07.14	2014-07-27	14	22	16	6	12	23	4	8	0.4	0.9	3.1	1.4	197	185	68	64	7	15	53	24	14
MK.UP.PP 30.07.14	2014-07-30	12	18	14	4	10	21	4	7	0.2	0.7	1.7	1.1	197	187	69	65	4	13	32	20	12
MK.UP.PP 06.08.14	2014-08-06	8	13	9	4	7	14	2	5	0.3	0.6	2.1	0.9	164	157	55	53	7	14	50	22	8
MK.UP.PP 11.08.14	2014-08-11	9	13	9	4	7	14	2	4	0.3	0.6	2.2	1.0	176	170	56	54	8	16	57	26	9
MK.UP.PP 19.08.14	2014-08-19	11	17	14	4	10	21	3	6	0.3	0.7	1.9	1.0	235	224	72	69	6	15	42	24	11
MK.UP.PP 25.08.14	2014-08-25	12	18	14	4	10	21	3	6	0.3	0.7	2.3	1.0	262	251	78	75	8	17	59	26	12
MK.UP.PP 01.09.14	2014-09-01	17	27	20	6	15	31	5	10	0.5	0.8	3.7	1.3	290	275	91	87	9	16	69	24	17
MK.UP.PP 09.09.14	2014-09-09	13	20	15	5	11	23	4	8	0.4	0.6	2.6	1.0	230	219	76	73	7	13	53	20	13
MK.UP.PP 17.09.14	2014-09-17	13	19	13	6	10	20	3	6	0.5	0.9	3.4	1.4	227	217	69	66	10	20	77	31	13
MK.UP.PP 27.09.14	2014-09-27	11	17	12	4	9	19	3	6	0.3	0.6	2.4	0.9	224	215	76	73	8	14	58	22	11
MK.UP.PP 10.10.14	2014-10-10	14	21	14	7	11	21	3	7	0.6	0.8	4.2	1.3	254	244	78	75	14	20	99	31	14
MK.UP.PP 15.10.14	2014-10-15	21	32	25	7	19	37	6	12	0.6	1.0	4.4	1.5	299	280	97	91	10	15	71	24	21
MK.UP.PP 20.10.14	2014-10-20	30	46	36	10	27	54	9	19	0.8	1.3	5.8	2.1	314	287	110	100	9	15	68	24	30
MK.UP.PP 9.11.14	2014-11-09	36	55	42	13	30	60	11	23	1.1	1.5	8.2	2.4	337	307	128	116	13	17	92	26	36
MK.UP.PP 14.11.14	2014-11-14	49	75	59	15	43	85	17	33	1.3	1.9	9.3	3.0	382	339	149	133	11	17	83	27	49
MK.UP.PP 19.11.14	2014-11-19	39	59	48	11	34	69	14	27	0.8	1.8	6.1	2.8	369	335	146	133	9	19	66	30	39
MK.UP.PP 25.11.14	2014-11-25	49	75	59	17	42	84	17	33	1.4	1.8	10.6	2.8	386	344	154	137	13	16	97	26	49
MK.UP.PP 12.12.14	2014-12-12	39	60	46	13	33	67	13	26	1.1	1.8	7.8	2.8	392	358	152	139	12	21	91	33	39
MK.UP¿PP 29.12.14	2014-12-29	75	115	91	24	64	127	28	56	2.0	2.5	15.0	4.0	440	376	193	165	14	17	104	28	75
MK.UP¿PP 10.01.15	2015-01-10	81	123	102	22	69	138	32	65	1.7	2.9	12.6	4.5	448	379	210	177	11	19	82	29	81

6.4 Impact of Weathering Reactions on CO_2 Budget

The relative proportions of chemical weathering reactions occurring at any one time is controlled by the availability of lithology and acidity. Moreover, the relative ratio of CO_2 consuming reactions (carbonic acid weathering of silicates, Equation 2.1) to CO_2 releasing reactions (sulfuric acid weathering of carbonates, Equation 2.3-2.4) impacts the overall instantaneous and million–year carbon budget of the river catchment. It is useful to visualise how much the proportion of lithology and proportion of acidity can vary whilst still maintaining a CO_2–consuming, CO_2–releasing or CO_2–neutral weathering environment.

6.4.1 An Oceanographic Perspective on Atmospheric CO_2 Budgets

CO_2 consumption and release in the Andes–Amazon system has been studied in detail, and the parameter scenarios over which both processes occur can be presented diagrammatically showing the conditions under which CO_2 is released and consumed over short and long timescales (Torres *et al.*, 2016, and Figure 6.2). The impact of weathering on partial pressure of CO_2 in the atmosphere (pCO$_2$) is considered from an oceanographic perspective by investigating how river solutes may alter the ratio between alkalinity and dissolved inorganic carbon (DIC) in the oceans (Torres *et al.*, 2016). Alkalinity is the stoichiometric sum of bases in solution, i.e. the buffering capacity or ability of the solution to resist changes in pH, of which HCO_3^- is the major form in natural waters (Stumm & Morgan, 1996, as cited by Drever, 1997). The ratio of modern seawater alkalinity:DIC is 1:1; if alkalinity and DIC produced by continental weathering is delivered to the oceans in ratios other than 1:1, pCO$_2$ may be perturbed.

The various reactions between silicates and carbonates with H_2CO_3 and H_2SO_4 deliver alkalinity and DIC to the ocean in different ratios. Two reactions, Equations 6.43-6.44, describe carbonate and silicate mineral dissolution. The acid consumed by lithology in Equations 6.43-6.44 is generated by oxidation of pyrite or disassociation of carbonic acid, Equation 6.45 and Equation 6.46, respectively.

$$2H^+ + CaCO_3 \longleftrightarrow Ca^{2+} + H_2CO_3 \tag{6.43}$$

$$4H^+ + Ca_2SiO_4 \longleftrightarrow H_4SiO_4 + 2Ca^{2+} \tag{6.44}$$

Either acid consuming reaction (Equations 6.43-6.44) can combine with either acid generating

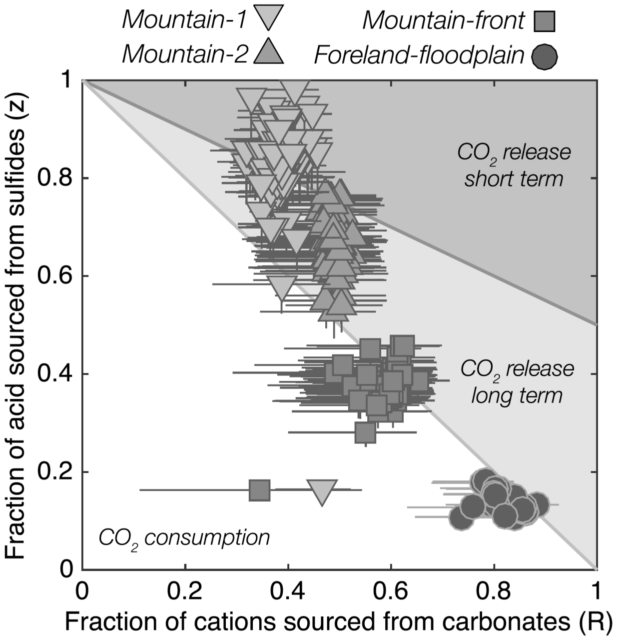

Figure 6.2: Carbon budget of a river catchment as a proportion of acidity and lithology. The fraction of acid sourced from sulfide weathering (z) is plotted against the fraction of cations sourced from carbonate mineral-weathering (R). Parameter space is sectioned by alkalinity:DIC ratio. An alkalinity:DIC ratio greater than 2 describes the conditions under which CO_2 is consumed on timescales longer than carbonate precipitation ($>10^5$–years, white). An alkalinity:DIC ratio less than 2 indicates that CO_2 will be released on long time scales (light grey), whereas a ratio less than 1 indicates that CO_2 is released on short timescales ($<10^5$–years, dark grey). The Andes–Amazon data presented here is from Torres *et al.* (2016, Figure 7).

half-reaction (Equations 6.45-6.46) to give the four full reactions for mineral weathering, i.e. sulfuric acid weathering of carbonate minerals (Equation 6.47) and sulfuric acid weathering of silicate minerals (Equation 6.48). The combination of half reactions are described in full in Torres *et al.* (2016, Supplementary Data).

$$4FeS_2 + 15O_2 + 14H_2O \longleftrightarrow 8SO_4^{2-} + 16H^+ + Fe(OH)_3 \tag{6.45}$$

$$H_2CO_3 \longleftrightarrow 2H^+ + CO_3^{2-} \tag{6.46}$$

$$0.5FeS_2 + \frac{15}{8}O_2 + \frac{7}{2}H_2O + CaCO_3 \longleftrightarrow Ca^{2+} + H_2CO_3 + SO_4^{2-} + 0.5Fe(OH)_3 \tag{6.47}$$

$$FeS_2 + \frac{15}{4}O_2 + \frac{7}{2}H_2O + CaSiO_4 \longleftrightarrow 2Ca^{2+} + H_4SiO_4 + 2SO_4^{2-} + Fe(OH)_3 \tag{6.48}$$

The ratio of alkalinity to DIC produced by these four reactions is then calculated. If H^+ ions are found on the left hand side (LHS) of the equation, it is assumed that this acidity is neutralised or buffered by alkalinity production, therefore H^+ on the LHS is used as a measure of alkalinity production (Torres *et al.*, 2016). DIC is written as H_2CO_3 species and if found on the right hand side (RHS) reflects DIC production. DIC and alkalinity ratios are calculated using three variables: the proportion of weathering driven by sulfuric acid (z); the cation contribution by carbonate weathering (x); and the cation contribution by silicate weathering (y). The fraction of cations derived from carbonate lithology to total cations from all lithology, R, is given by the following relationship:

$$R = \frac{Cation_{carb}}{Cation_{carb} + Cation_{sil}} = \frac{x}{x+y} \tag{6.49}$$

To discriminate between areas of short term CO_2 consumption and release on Figure 6.2, alkalinity:DIC is assumed to equal 1, where CO_2 consumption is neutral. The proportion of cations delivered by sulfuric acid driven weathering, z_{short}, is related to the amount of carbonate weathering, R, by:

$$z_{short} = 1 - (0.5R) \tag{6.50}$$

To determine CO_2 release on long timescales alkalinity:DIC is assumed to equal 2. CO_2 released on the long term by sulfuric acid–driven weathering, z_{long}, is determined by the CO_2 drawdown due to carbonic acid weathering of silicates (*1-R*):

$$z_{long} = 1 - R \tag{6.51}$$

If the ratio of alkalinity:DIC delivered to the oceans deviates from 1:1 then atmospheric CO_2 is consumed or released (Figure 6.2). Carbonate precipitation on million–year timescales removes alkalinity and DIC from the oceans in a 2:1 ratio. Carbonate precipitation therefore decreases oceanic DIC but increases $p\text{CO}_2$. Hence, to decrease $p\text{CO}_2$ on million-year times, an alkalinity:DIC ratio greater than 2 must be delivered to the oceans. H_2CO_3 weathering of carbonates (Equation 6.43) has an alkalinity:DIC ratio of 2:1 and therefore it is carbon neutral. H_2SO_4 weathering of carbonates (Equation 6.47) has an alkalinity:DIC ratio of 0:1 causing a short–term CO_2 release. Such samples with a ratio of less than 1 occupy the top area in Figure 6.2. H_2CO_3 weathering of silicates (Equation 6.44) has an alkalinity:DIC ratio of 4:0, therefore consuming CO_2 on the long term and occupying the bottom most area in Figure 6.2. H_2SO_4 weathering of silicates (Equation 6.48) plays no part in the carbon cycle and hence has an alkalinity:DIC ratio of 0:0.

Interpreting the CO_2 implications of the data plotted in Figure 6.2 is non–trivial; the conditions under which CO_2 is released on long term and short term timescales, overlap. Long–term CO_2 release occurs above the line of Equation 6.51. Short–term CO_2 release occurs above the line of Equation 6.50, however, this occupies the same parameter space as that of long–term CO_2 release (Figure 6.2). If data falls in the top area of Figure 6.2, it is unclear if the sample is releasing CO_2 on the short– or the long–term. Despite the ambiguity in timeframe of CO_2 release, the framework still provides a valuable overview of the carbon budget of a river catchment, particularly when no discharge data is available. However, a simplified framework could be used to summarise the carbon budget, without considering the alkalinity:DIC ratio of oceans, and that uses river solutes partitioned between acidity and lithology source.

6.4.2 A Catchment Perspective on Atmospheric CO_2 Budgets

A different approach to calculating the implications of combinations of weathering reactions on atmospheric CO_2 is to use ions delivered to the weathering zone. In the following explanation, it is shown that a graphical representation of CO_2 consumption or release can be achieved by tracking cations such as Ca^{2+}. The graphical areas for CO_2 consumption or release plot in the same location as Figure 6.2 (Torres *et al.*, 2016), but the realisation of these areas is achieved by a different calculation demonstrated in the following two sections.

6.4.2.1 Describing Acidity and Lithology Sources with River Solutes

The relationship between lithology type and acidity source can be described by the variables F_{carb} and F_{sulf}, where F_{carb} is the fraction of carbonate to silicate rocks contributing to the dissolved load, defined as:

$$F_{carb} = \frac{n_{Carb}H_2CO_3 + n_{Carb}H_2SO_4}{n_{Carb}H_2CO_3 + n_{Carb}H_2SO_4 + n_{Sil}H_2CO_3 + n_{Sil}H_2SO_4} \tag{6.52}$$

and F_{sulf} is the fraction of sulfuric acid to carbonic acid in the system, defined as:

$$F_{sulf} = \frac{n_{Carb}H_2SO_4 + n_{Sil}H_2SO_4}{n_{Carb}H_2CO_3 + n_{Carb}H_2SO_4 + n_{Sil}H_2CO_3 + n_{Sil}H_2SO_4} \tag{6.53}$$

To abbreviate, let

$$n1 = n_{Sil}H_2CO_3 \tag{6.54}$$

$$n2 = n_{Carb}H_2CO_3 \tag{6.55}$$

$$n3 = n_{Carb}H_2SO_4^O \tag{6.56}$$

$$n4 = n_{Carb}H_2SO_4^C \tag{6.57}$$

$$n5 = n_{Sil}H_2SO_4 \tag{6.58}$$

where n1 to n5 are the relative amounts of mineral weathering reactions occurring; n1 represents the amount of carbonic acid weathering of silicate minerals (Equation 2.1, Figure 2.1A), n2 is the carbonic acid weathering of carbonate minerals (Equation 2.2, Figure 2.1B), n3 is the sulfuric acid weathering of carbonate minerals in an open environment where released carbon is allowed to degas as CO_2 (Equation 2.3, Figure 2.1C), n4 is the sulfuric acid weathering of carbonate minerals in a confined environment where released carbon is transferred as DIC to the oceans (Equation 2.4, Figure 2.1D), and n5 is the sulfuric acid weathering of silicate minerals which is not involved in the carbon cycle but does deliver solutes to the weathering zone (Equation 2.5, Figure 2.1E). Equations 6.52 and 6.53 describing the cations delivered from the weathering of carbonates and from weathering by sulfuric acid in an open system respectively, are rewritten in 6.59 and 6.60:

$$F_{carb} = \frac{n2 + n3}{n1 + n2 + n3 + n5} \tag{6.59}$$

$$F_{sulf} = \frac{n3 + n5}{n1 + n2 + n3 + n5} \tag{6.60}$$

The amount of each reaction, n1 to n5, can be tracked by the charge equivalent amount of Ca^{2+}. For example, the reactions occurring in an open environment, where CO_2 can degas from the sulfuric acid weathering of carbonates (n3), can be written in equivalent units as such:

$$F_{carb} = \frac{Ca_{n2}^{2+} + Ca_{n3}^{2+}}{Ca_{n1}^{2+} + Ca_{n2}^{2+} + Ca_{n3}^{2+} + Ca_{n5}^{2+}} \tag{6.61}$$

$$F_{sulf} = \frac{Ca_{n3}^{2+} + Ca_{n5}^{2+}}{Ca_{n1}^{2+} + Ca_{n2}^{2+} + Ca_{n3}^{2+} + Ca_{n5}^{2+}} \tag{6.62}$$

This is equivalent to stating that n1 to n5 is the molar amount of Ca^{2+} released by each reaction. If the reaction of sulfuric acid and carbonate minerals is considered where CO_2 cannot degas (n4), there is one more mole of Ca^{2+} released. The sum of Ca^{2+} delivered from reactions of carbonic or sulfuric acid with carbonates in an open environment (n2 and n3) will remain the same as the sum of Ca^{2+} delivered from reactions of carbonic or sulfuric acid with carbonates in a confined environment (n2 and n4) because the total amount of carbonate available to weather does not change, only the reaction pathway. In a confined environment where carbon released is transferred as DIC to the oceans (n4), F_{carb} and F_{sulf} are defined in the following way:

$$F_{carb} = \frac{2Ca^{2+}_{n2} + Ca^{2+}_{n4}}{2Ca^{2+}_{n1} + Ca^{2+}_{n2} + Ca^{2+}_{n4} + Ca^{2+}_{n5}} \tag{6.63}$$

$$F_{sulf} = \frac{2Ca^{2+}_{n4} + Ca^{2+}_{n5}}{2Ca^{2+}_{n1} + Ca^{2+}_{n2} + Ca^{2+}_{n4} + Ca^{2+}_{n5}} \tag{6.64}$$

F_{carb} and F_{sulf} can also be described in charge equivalent terms for anions SO_4^{2-} and HCO_3^- produced by reactions with H_2SO_4 and H_2CO_3. Where the charge equivalent constants cancel to give F_{carb} and F_{sulf} in an open environment as:

$$F_{carb} = \frac{HCO^-_{3\ n2} + SO^{2-}_{4\ n3}}{HCO^-_{3\ n1} + HCO^-_{3\ n2} + SO^{2-}_{4\ n3} + SO^{2-}_{4\ n5}} \tag{6.65}$$

$$F_{sulf} = \frac{SO^{2-}_{4\ n3} + SO^{2-}_{4\ n5}}{HCO^-_{3\ n1} + HCO^-_{3\ n2} + SO^{2-}_{4\ n3} + SO^{2-}_{4\ n5}} \tag{6.66}$$

In a confined environment, the two moles of Ca^{2+} released by the sulfuric acid weathering of carbonates (n4) are charge balanced by one mole of SO_4^{2-} and two moles of HCO_3^-. Charge equivalent coefficients cancel to give F_{carb} and F_{sulf} as:

$$F_{carb} = \frac{SO^{2-}_{4\ n4} + HCO^-_{3\ n4} + HCO^-_{3\ n2}}{HCO^-_{3\ n1} + HCO^-_{3\ n2} + SO^{2-}_{4\ n4} + HCO^-_{3\ n4} + SO^{2-}_{4\ n5}} \tag{6.67}$$

$$F_{sulf} = \frac{SO^{2-}_{4\ n4} + HCO^-_{3\ n4} + SO^{2-}_{4\ n5}}{HCO^-_{3\ n1} + HCO^-_{3\ n2} + SO^{2-}_{4\ n4} + HCO^-_{3\ n4} + SO^{2-}_{4\ n5}} \tag{6.68}$$

A worked example comparing anion and cation calculations for F_{sulf} and F_{carb} can be seen in the box below.

Describing F_{carb} and F_{sulf} with cations or anions can be shown to be equivalent by the following example matrix (6.69).

$$\begin{array}{cc} & \begin{array}{ccccc} SilH_2CO_3 & CarbH_2CO_3 & CarbH_2SO_{4(g)} & CarbH_2SO_{4(aq)} & SilH_2SO_4 \end{array} \\ \begin{array}{c} Ca^{2+} \\ HCO_3^- \\ SO_4^{2-} \end{array} & \begin{pmatrix} 1 & 1 & 1 & 2 & 1 \\ 2 & 2 & 0 & 2 & 0 \\ 0 & 0 & 1 & 1 & 1 \end{pmatrix} \end{array} \cdot \begin{array}{c} \mu mol/l \\ \begin{pmatrix} 10\ n_{Sil}H_2CO_3 \\ 5\ n_{Carb}H_2CO_3 \\ 1\ n_{Carb}H_2SO_{4(g)} \\ 0\ n_{Carb}H_2SO_{4(aq)} \\ 2\ n_{Sil}H_2SO_4 \end{pmatrix} \end{array}$$

$$= \begin{array}{cc} & \begin{array}{ccccc} SilH_2CO_3 & CarbH_2CO_3 & CarbH_2SO_{4(g)} & CarbH_2SO_{4(aq)} & SilH_2SO_4 \end{array} \\ \begin{array}{c} Ca^{2+} \\ HCO_3^- \\ SO_4^{2-} \end{array} & \begin{pmatrix} 10 & 5 & 1 & 0 & 2 \\ 20 & 10 & 0 & 0 & 0 \\ 0 & 0 & 1 & 0 & 2 \end{pmatrix} \end{array} \tag{6.69}$$

F_{carb} is calculated with Ca^{2+} in the following equation:

$$F_{carb} = \frac{2*5Ca^{2+}_{n2} + 2*1Ca^{2+}_{n3}}{2*10Ca^{2+}_{n1} + 2*5Ca^{2+}_{n2} + 2*1Ca^{2+}_{n3} + 2*2Ca^{2+}_{n5}} = \frac{12}{36} \tag{6.70}$$

F_{carb} can also be calculated with anions, yielding the same value in the following equation:

$$F_{carb} = \frac{1*10HCO^{-}_{3\ n2} + 2*1SO^{2-}_{4\ n3}}{1*20HCO^{-}_{3\ n1} + 1*10HCO^{-}_{3\ n2} + 2*1SO^{2-}_{4\ n3} + 2*2SO^{2-}_{4\ n5}} = \frac{12}{36} \tag{6.71}$$

F_{sulf} is calculated with Ca^{2+} in the following equation:

$$F_{sulf} = \frac{2*1Ca^{2+}_{n3} + 2*2Ca^{2+}_{n5}}{2*10Ca^{2+}_{n1} + 2*5Ca^{2+}_{n2} + 2*1Ca^{2+}_{n3} + 2*2Ca^{2+}_{n5}} = \frac{6}{36} \tag{6.72}$$

F_{sulf} can also be calculated with anions yielding the same value in the following equation:

$$F_{sulf} = \frac{2*1SO^{2-}_{4\ n3} + 2*2SO^{2-}_{4\ n5}}{1*20HCO^{-}_{3\ n1} + 1*10HCO^{-}_{3\ n2} + 2*1SO^{2-}_{4\ n3} + 2*2SO^{2-}_{4\ n5}} = \frac{6}{36} \tag{6.73}$$

The same can be done when using n4 (sulfuric acid weathering of carbonates releasing DIC and two moles of Ca^{2+}) instead of n3 (sulfuric acid weathering of carbonates degassing CO_2).

F_{carb} and F_{sulf} can be treated as variables between 0 and 1. Therefore, Ca^{2+}, HCO_3^-, SO_4^{2-} and CO_2 consumption can be calculated over the entire parameter space of F_{carb} and F_{sulf}. To do this, n1, n2, n3, n4 and n5, need to be solved as a function of F_{carb} and F_{sulf}. This requires an additional assumption because there are 3 unknowns and 2 equations (6.59 and 6.60), making the problem under-constrained. It is assumed that the relative weathering of carbonate to silicate minerals occurs in equal proportions, irrespective of the acidity source. The relative weathering was expressed in Equation 6.19 (Section 6.3.1), and can be re–expressed as:

$$\frac{n2}{n1} = \frac{n2 + n3}{n1 + n5} = \frac{n3}{n5} \tag{6.74}$$

Thus Equations 6.59, 6.60 and 6.74 are rearranged as a function of F_{sulf} and F_{carb} relative to n3, to compute the contribution of each reaction n1, n2, and n5.

$$n1 = n2 \cdot \frac{1 - F_{carb}}{F_{carb}} \tag{6.75}$$

$$n2 = n3 \cdot \frac{1 - F_{sulf}}{F_{sulf}} \tag{6.76}$$

$$n5 = n3 \cdot \frac{1 - F_{carb}}{F_{carb}} \tag{6.77}$$

These equations are self consistent in that back calculations of F_{carb} and F_{sulf} from n1, n2, n3 and n5 recover the correct values of F_{carb} and F_{sulf}.

The sulfuric acid weathering of carbonates, n3, is held constant in order to mathematically solve the equations. n3 itself is chosen to physically represent a constant amount of sulfuric acid weathering of carbonates occurring across parameter space. The amount of reactions n1 (carbonic acid weathering of silicates), n2 (carbonic acid weathering of carbonate), and n5 (sulfuric acid weathering of silicates) occurring across parameter space are shown in Figure 6.3A-C. The amount of carbonic acid weathering of carbonates, n2, increases vertically downwards as H_2CO_3 (1-F_{sulf}) increases. This is because there is a constant amount of carbonate weathering across the parameter space but varying acidity between n2 and n3 involving sulfuric acid (Figure 6.3A). The carbonic acid weathering of silicates, n1, varies in both directions of parameter space due to the different acidity and lithology in n1 (carbonic acid and silicates) to n3 (sulfuric acid and carbonates). The maximum amount of n1 occurs at the highest proportion of silicate rocks (1-F_{carb}) and carbonic acid (1-F_{sulf}), i.e. where F_{carb} and F_{sulf} are close to zero (Figure 6.3B). The amount of n5 (sulfuric acid weathering of silicates) will increase vertically with increasing fraction of silicate to carbonate weathering, i.e. decreasing F_{carb}, because the acidity is the same for n5 as n3 that is being held constant (Figure 6.3C).

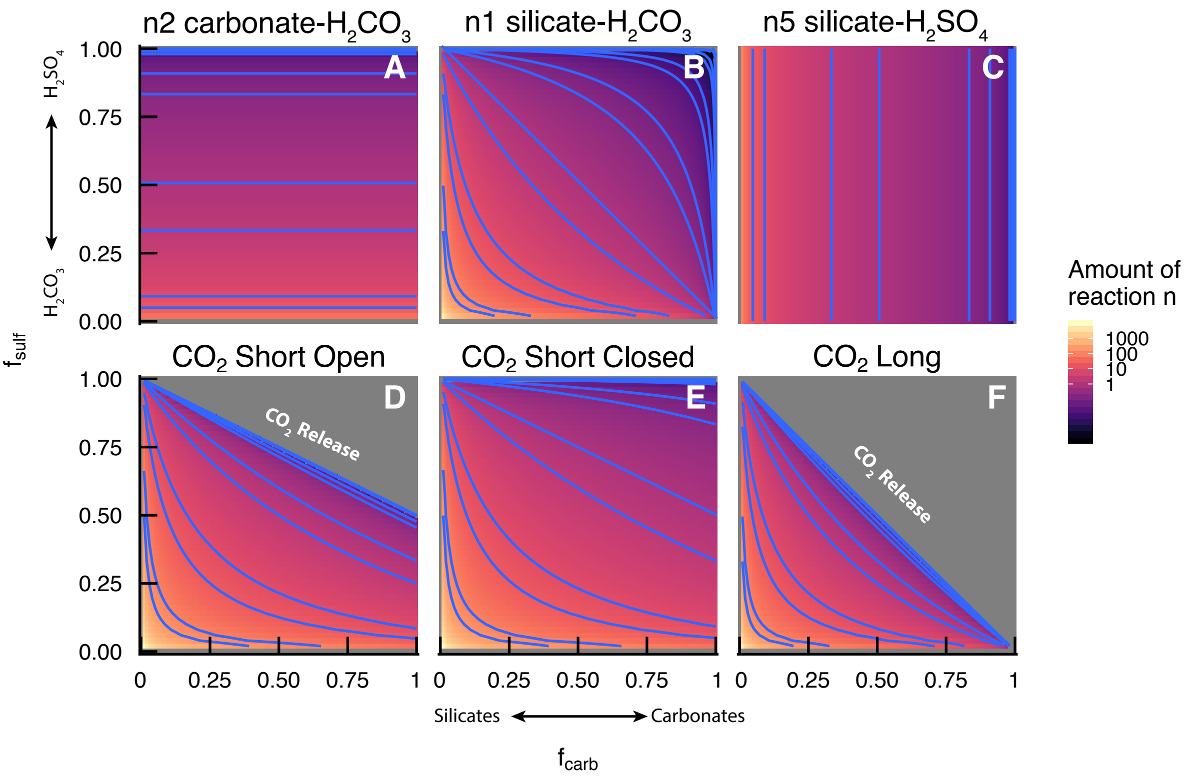

Figure 6.3: Amount of weathering reactions occurring relative to proportion of lithology and acidity source, and the CO_2 implications of the weathering reactions Panels A, B, and C show the amount of carbonic acid weathering of carbonates, n2, carbonic acid weathering of silicates, n1, and sulfuric acid weathering of silicates, n5, respectively, relative to a constant amount of sulfuric acid weathering of carbonates, n3, occurring over the parameter space. F_{carb} is the ratio of the total Ca^{2+} delivered from carbonate lithology to the total Ca^{2+} delivered by carbonate and silicate rocks. The proportion of silicate rocks is equivalent to 1-F_{carb}. F_{sulf} is the ratio of the total Ca^{2+} delivered from sulfuric acid driven weathering to the total Ca^{2+} delivered by sulfuric and carbonic acid weathering (the proportion of carbonic acid driven weathering is equivalent to 1-F_{sulf}). The amount of weathering reaction occurring relative to n3 is shown by the colour ramp; more of the reaction relative to n3 occurring is yellow, less reaction occurring relative n3 is purple. The blue contours indicate a certain amount of that reaction occurring which is constant along the contour. Panels D, E, and F show the carbon implications of combinations of weathering reactions. On timescales shorter than carbonate precipitation in the oceans ($<10^5$ years) atmospheric CO_2 is drawn down by carbonic acid weathering of silicates (n1) and carbonates (n2). In open environments any sulfuric acid weathering of carbonates occurring (n3) releases CO_2 and offsets the drawdown from carbonic acid weathering (Equation 6.78). The grey area in Panel D is parameter space where the combination of lithology and acidity releases more CO_2 than is consumed on the short term. CO_2 is consumed in the coloured area, with more consumption in yellow and less consumption in purple. Panel E is the relative CO_2 consumption for the combination of weathering reactions occurring in a confined environment. This panel considers the reactions of carbonic acid weathering of silicates (n1) and carbonates (n2), so no reactions release CO_2 (Equation 6.79). Panel F considers the long term carbon budget, where the CO_2 drawn-down by silicate weathering (n1) is offset by the release of CO_2 by sulfuric acid weathering of carbonates instantaneous degassing or by DIC delivered to the oceans and subsequently precipitated as carbonate, releasing CO_2 on million-year timescales (n3 or n4, and Equation 6.80). The CO_2 consumption is constant along the blue contour lines.

6.4.2.2 Impact of Acidity and Lithology Sources on CO_2 Budget

Where Torres *et al.* (2016) have derived the atmospheric CO_2 consequences of weathering reactions based on perturbations to the alkalinity:DIC ratio in the oceans. Here, CO_2 consumption or release is calculated by the stoichiometric balance of CO_2 being removed from the atmosphere by weathering of rocks with H_2CO_3 and CO_2 released back to the atmosphere via sulfuric acid weathering of carbonates. This CO_2 release may occur either instantaneously via sulfuric acid weathering of carbonates in an open environment, or on the long term after carbonate is precipitated in the oceans. The calculation of CO_2 consumption is straight forward after the amount of reactions n1-n5 have be computed across F_{carb}, F_{sulf} parameter space.

In open environments, the reactions occurring on the short–term are the carbonic acid weathering of silicates (n1) and carbonates (n2) and the sulfuric acid weathering of carbonates (n3). The sulfuric acid weathering of silicates (n5) also occurs but does not involve the C cycle. For each amount of carbonic acid weathering of silicates (n1) occurring, two moles of CO_2 are removed from the atmosphere. For each amount of carbonate weathered by carbonic acid (n2), an equal molar amount of CO_2 is removed from the atmosphere. For each given amount of sulfuric acid reacting with carbonates (n3) occurring, the same amount of CO_2 is released. The total CO_2 consumption on the short term in an open environment, $\Sigma CO_2^O{}_{short}$, is therefore described by the following equation:

$$\Sigma CO_2^O{}_{short} = 2n1 + n2 - n3 \tag{6.78}$$

CO_2 release is represented as the grey area on Figure 6.3D, where more CO_2 is released by the sulfuric acid weathering of carbonates (n3) than the atmospheric CO_2 removal by carbonic acid weathering of silicates (n1) and carbonates (n2).

When weathering occurs in a confined environment, the reactions are the same as in an open environment (n1, n2, n5), however the carbon delivered by sulfuric acid weathering of carbonates cannot degas as CO_2 and therefore is not taken into the CO_2 budget on the short term. No CO_2 is released in a confined environment, illustrated by Figure 6.3E where all parameter space is consuming CO_2. The total CO_2 consumption on the short term in a closed environment, $\Sigma CO_2^C{}_{short}$, is therefore described by the following equation:

$$\Sigma CO_2^C{}_{short} = 2n1 + n2 \tag{6.79}$$

When the solutes of weathering are delivered to the oceans and can precipitate as carbonate, there is a net drawdown of one mole of CO_2 per amount of silicates weathered by carbonic acid (n1). Carbonic acid weathering of carbonates (n2) is net CO_2 neutral so is not considered on the long term. All DIC delivered to the oceans from sulfuric acid weathering of carbonates from reactions in a confined environment (n4) is now released to the atmosphere. If the release of CO_2 is greater than the CO_2 sequestration by carbonic acid weathering of silicates (n1) and subsequent precipitation of carbonates then there is a net CO_2 release on $>10^5$–year timescales (grey area Figure 6.3F). This gives the following equation for total CO_2 consumption on the long term, $\Sigma CO_2\,_{long}$:

$$\Sigma CO_2\,_{long} = n1 - n4 \tag{6.80}$$

The lines dividing parameter space into areas of CO_2 consumption or release in Figures 6.3D–E represent scenarios of CO_2 neutral budget, i.e. where Equations 6.78 and 6.80 describing the CO_2 consumption or release on short and long timescales respectively, are equal to zero. Below these lines CO_2 is consumed and above the lines CO_2 is released. These lines are mathematically identical to the lines defined on Figure 6.2 (Torres *et al.*, 2016, Figure 7). This is demonstrated for the short term. The reactions describing amount of carbonic acid weathering of silicates (Equation 6.75) and carbonates (Equation 6.76) are rearranged to give:

$$n1 = \left(\frac{n_3}{F_{sulf}} - n_3\right)\left(\frac{1}{F_{carb}} - 1\right) \tag{6.81}$$

$$n2 = \frac{n_3}{F_{sulf}} - n_3 \tag{6.82}$$

which can be substituted into Equation 6.78, which describes the short term CO_2 budget, and set equal to zero:

$$0 = 2n1 + n2 - n3 \tag{6.83}$$

$$0 = 2\left(\frac{n_3}{F_{sulf}} - n_3\right)\left(\frac{1}{F_{carb}} - 1\right) + \left(\frac{n_3}{F_{sulf}} - n_3\right) - n3 \tag{6.84}$$

Equation 6.84 can be rearranged to give the same equation as that derived by Torres *et al.* (2016). The equation describes the amount of cations delivered by sulfuric acid–driven weathering is proportional to the amount of carbonate weathering (Equation 6.50) :

$$F_{sulf} = 1 - 0.5F_{carb} \tag{6.85}$$

CO_2 is released on the short term when the proportion of sulfuric acid weathering instantaneously degassing CO_2, n3, is greater than the combined CO_2 consumption from carbonic acid weathering of silicates, n1, and carbonates, n2, (Equation 6.78). This can be seen at high F_{carb} and F_{sulf} (Figure 6.3D). In confined environments, CO_2 is only consumed on the short term (Equation 6.79 and Figure 6.3E).

The lines dividing areas of long term CO_2 consumption or release on Figure 6.3F are shown to be the same as Figure 6.2 (Torres *et al.*, 2016, Figure 7) by rearranging Equation 6.75 to Equation 6.86 and inputting it into the long term CO_2 budget equation (Equation 6.80) set to zero. Further rearranging gives the same as Equation 6.51:

$$n1 = \frac{n_3\,(1 - F_{carb})}{F_{sulf}} \tag{6.86}$$

$$0 = \frac{n_3\,(1 - F_{carb})}{F_{sulf}} - n_3 \tag{6.87}$$

$$1 = \frac{1 - F_{carb}}{F_{sulf}} \tag{6.88}$$

$$F_{sulf} = 1 - F_{carb} \tag{6.89}$$

Whilst the areas on the graphs shown in Figure 6.3D–F look the same as Figure 6.2 (Torres *et al.*, 2016, Figure 7), it is possible, with this improved approach, to track different ions such as Ca^{2+}, Mg^{2+}, Na^{+}, K^{+}, SO_4^{2-}, and HCO_3^{-} over parameter space. Contouring of the space quantifies the reactions. With the graphs separated, reaction pathways of H_2SO_4 weathering of carbonates can be distinguished between open and confined, and short or long term CO_2 release can be explicitly seen.

6.4.2.3 Sulfuric Acid Weathering of Silicates: Implications for Atmospheric CO_2?

The equations calculating CO_2 consumption across parameter space (Equations 6.78–6.80) do not include the sulfuric acid weathering of silicates (n5) because neither reactants contains carbon. However this reaction consumes acidity and delivers SO_4^{2-} and Ca^{2+} to the river and ocean. To demonstrate the necessity of including n5 in calculations of F_{carb} and F_{sulf} to create Figure 6.3,

F_{carb} and F_{sulf} have been redefined without n5 in the following equations:

$$F_{carb} = \frac{n2 + n3}{n1 + n2 + n3} \tag{6.90}$$

$$F_{sulf} = \frac{n3}{n1 + n2 + n3} \tag{6.91}$$

The equations describing the amount of carbonic acid weathering of silicates (n1) and carbonates (n2) occurring (Equations 6.75–6.76) have also been redefined in terms of F_{carb} and F_{sulf} without n5. n3 is held constant so that there are two equations involving two unknowns:

$$n1 = n3 \cdot \frac{1 - F_{carb}}{F_{sulf}} \tag{6.92}$$

$$n2 = n3 \cdot \left(\frac{F_{carb}}{F_{sulf}} - 1 \right) \tag{6.93}$$

Without the reaction of sulfuric acid with silicate minerals occurring (n5), carbonic acid weathering of carbonates (n2) can only occur in half of the parameter space as indicated by the grey area in (Figure 6.4A). The only way to access the grey area in F_{carb}–F_{sulf} parameter space is to supply negative amounts of Ca^{2+} via the weathering of carbonate with carbonic acid (n2). This is equivalent to stating that the reaction n2 is occurring in reverse; that it is to say rather than dissolving carbonates, it is precipitating carbonate as described by the following reaction:

$$2HCO_3^- + Ca^{2+} \Rightarrow CaCO_3 + CO_2 + H_2O \tag{6.94}$$

This could occur in an open environment; if alkalinity reaches carbonate saturation point, the degassing of CO_2 raises the pH which can cause carbonate precipitation. This could occur as pedogenic carbonates on the continents or could be conceptualised as the precipitation of marine carbonates on longer time-scales.

The line dividing carbonate dissolution from carbonate precipitation (which occupies the grey area) in Figure 6.4A is $F_{carb} = F_{sulf}$, and where n2=0. This is shown in Equations 6.95–6.101:

$$\frac{n3 + n2}{n1 + n2 + n3} = \frac{n3}{n1 + n2 + n3} \tag{6.95}$$

$$\Longrightarrow \frac{n3}{n1 + n3} = \frac{n3}{n1 + n3} \tag{6.96}$$

$$\therefore Fcarb = Fsulf \tag{6.97}$$

$$or\ n2 = n3\left(\frac{F_{carb}}{F_{sulf}} - 1\right) \tag{6.98}$$

$$n2 = n3\left(\frac{F_{carb}}{F_{carb}} - 1\right) \tag{6.99}$$

$$n2 = n3\,(1 - 1) \tag{6.100}$$

$$\therefore n2 = 0 \tag{6.101}$$

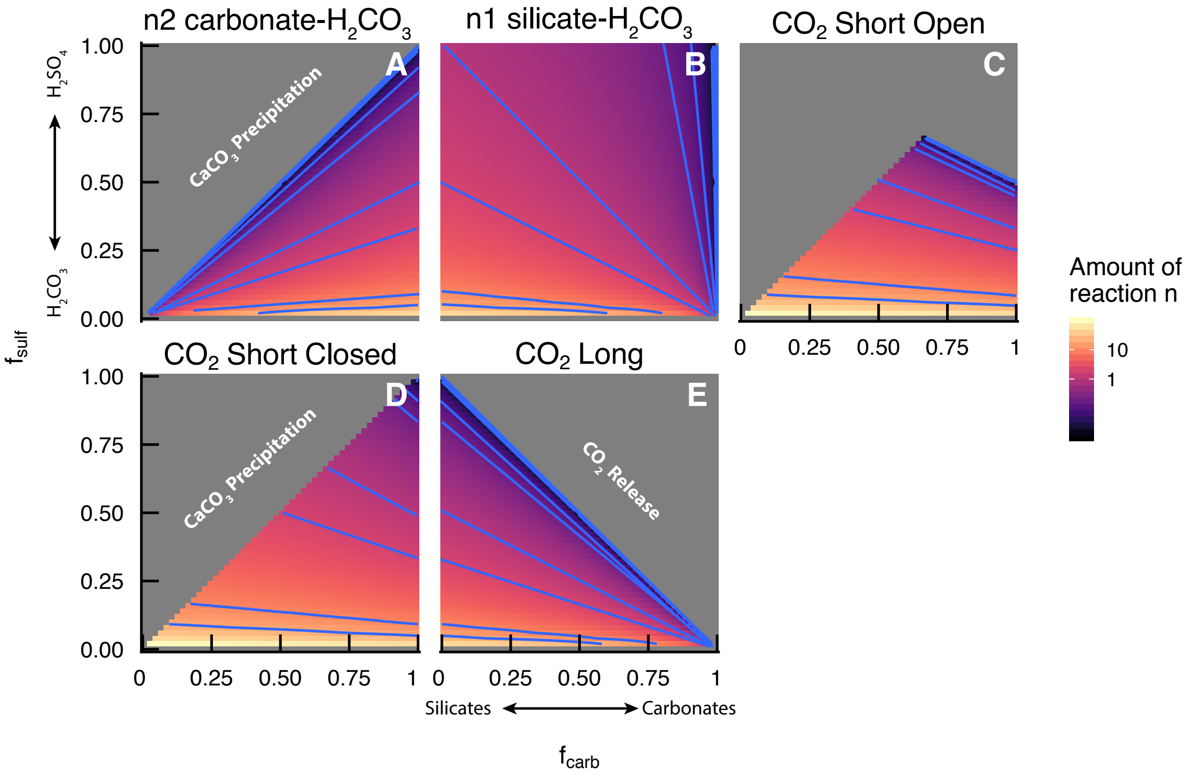

Figure 6.4: Amount of weathering reactions occurring relative to proportion of lithology and acidity source, and the CO_2 implications of the weathering reactions without considering sulfuric acid weathering of silicates. Calculations for Panels A–E are the same as in Figure 6.3. Panels A and B show the amount of carbonic acid weathering of carbonates (n2) and carbonic acid weathering of silicates (n1) respectively, relative to a constant amount of sulfuric acid weathering of carbonates (n3) occurring over parameter space. The amount of weathering reaction occurring relative to n3 is shown by the colour ramp: more of the reaction relative to n3 occurring is yellow, less reaction occurring relative n3 is purple. The blue contours indicate a certain amount of that reaction occurring which is constant along the contour. Panels C, D and E show the carbon implications of combinations of weathering reactions calculated with the same equations described in caption of Figure 6.3. The increased parameter space where CO_2 is released is due to conditions allowing carbonate precipitation releasing more CO_2. CO_2 is consumed in the coloured area, with more consumption in yellow and less consumption in purple. The CO_2 consumption is constant along blue contour lines.

The grey area above the line where F_{carb} equals F_{sulf}, is where carbonate precipitation is greater than carbonate dissolution (Figure 6.4A). Where F_{carb} is high and F_{sulf} is low, carbonate dissolution with H_2CO_3 (n2) is favourable, and values of carbonic acid weathering of carbonates decrease with increasing F_{sulf} and decreasing F_{carb}. Carbonate precipitation is not considered further.

If the sulfuric acid weathering of silicates is not considered, then there is more area within the parameter space of F_{sulf} and F_{carb} to precipitate carbonates and therefore release CO_2 (Figure 6.4). Figures 6.4C–E are calculated in the same way as Figures 6.3D–F, where the difference in the area of CO_2 release is due to the lack of n5 in Figure 6.4. When the environment is confined and sulfuric acid weathers carbonates (n4), no CO_2 should be released in the short term as all reactions draw down CO_2. However there is an area of CO_2 release on Figure 6.4D due to carbonate precipitation (negative n2). The area of CO_2 release in both Figure 6.3F and Figure 6.4E is due to carbonate precipitation in the oceans on the long–term timescale. However, the absolute values of CO_2 released could be inflated by not considering sulfuric acid weathering of silicates (n5, Figure 6.4D) and correcting for contributions to SO_4^{2-} and Ca^{2+}.

6.5 Weathering in the Mekong Basin

6.5.1 Reaction Pathway of Sulfuric Acid Weathering of Carbonates

Cations measured in the Mekong have been partitioned following Section 6.3 and DIC contributions from all combinations of lithology and acidity reactions have then been calculated. The measured HCO_3^-, an approximation of total DIC (ΣDIC) in the river is compared to the calculated ΣDIC, Figure 6.5A. In the same way, measured SO_4^{2-} is compared to SO_4^{2-} calculated from cations delivered from sulfuric acid and gypsum weathering, Figure 6.5B. The two reaction pathways of sulfuric acid weathering of carbonates deliver different products to the weathering zone, yielding different water chemistries. For example, in an open environment when CO_2 can instantaneously degas (n3), one mole each of SO_4^{2-} and Ca^{2+} is also released (Equation 2.3). In a confined environment if sulfuric acid reacts with carbonates, carbon is released as two moles of HCO_3^-, and one mole of SO_4^{2-} is also released. These anions are charge balanced by the release of two moles of Ca^{2+} (Equation 2.4).

HCO_3^- and SO_4^{2-} measured in river water are compared against the calculated HCO_3^- and SO_4^{2-} using Equations 6.39–6.41 to determine the reaction pathway of sulfuric acid weathering of carbonates. River water must be charge balanced (Drever, 1997), therefore HCO_3^- in the water must be equal to, in equivalent units, the summation of cations delivered by each weathering reaction that also delivers HCO_3^-. Similarly, measured SO_4^{2-} must also be equal to the total of all cations delivered by weathering reactions with sulphuric acid and gypsum dissolution. Cations are partitioned differently for each reaction pathway of sulfuric acid weathering of carbonates, therefore the closest relationship between measured values and cations partitioned for a particular reaction pathway indicate which reaction pathway must be occurring.

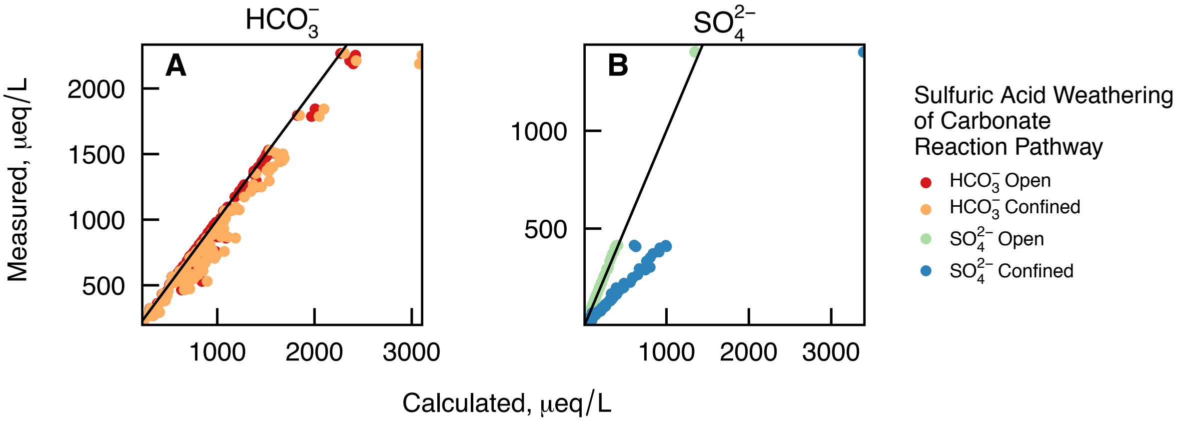

Figure 6.5: Reaction pathway of sulfuric acid weathering of carbonates. Measured HCO_3^- and SO_4^{2-} are compared against calculated HCO_3^- and SO_4^{2-} (in equivalent units, μeq/L), panel A and B respectively. Black line is 1:1. Cations are partitioned between chemical weathering reactions involving H_2SO_4, H_2CO_3, carbonates and silicates (Equations 2.1–2.5) and are partitioned differently depending on the reaction pathway for sulfuric acid weathering of carbonates (n3 or n4). The sum of charge equivalent partitioned cations delivered by weathering reactions that also deliver HCO_3^- should charge balance measured HCO_3^-. Summed cations partitioned for reaction pathway n3 (red) are closer to measured HCO_3^- than cations partitioned for reaction pathway n4 (orange). Similarly summed cations partitioned for reaction pathway n3 (green) are closer to measured SO_4^{2-} than cations partitioned for reaction pathway n4 (blue). Hence, sulfuric weathering of carbonates in the Mekong river most likely occurs in open environments where CO_2 can freely degas.

Calculated HCO_3^- is within 10% (average) of measured HCO_3^-, and calculated SO_4^{2-} is within 6% of measured $SO_4^{2-}$for reaction pathway n3. The relationship between measured HCO_3^- and SO_4^{2-} and HCO_3^- and SO_4^{2-} that have been calculated using partitioned cations is closest for sulfuric acid weathering of carbonates in an open environment where CO_2 can degas (n3). This is likely the reaction environment in which sulfuric acid weathering of carbonates takes place. Therefore sulfuric acid weathering of carbonates in the Mekong is most likely to occur in open environments where CO_2 can degas instantaneously.

Table 6.4: DIC and CO_2 calculated from partitioned dissolved major cations and anions in Mekong main channel, sampled repeatedly in 2014, 2016 and 2017

Sample	Location	F^{n3}_{carb}	F^{n4}_{carb}	F^{n3}_{sulf}	F^{n4}_{sulf}	DIC^{carb}_{sil}	$DIC^{carb\ O}_{carb}$	$DIC^{carb\ C}_{carb}$	$DIC^{sulf\ C}_{carb}$	$DIC^{Total\ O}_{Short}$	$DIC^{Total\ C}_{Short}$	CO_2^O Short	CO_2^C Short	CO_2 Int	CO_2^O Short	CO_2^C Short	CO_2 Int	CO_2^O Short	CO_2^C Short	CO_2 Int
								μmol/L				μmol/L CO_2			10^{18}mol CO_2.day^{-1}			mol CO_2.km^{-2}.day^{-1}		
Main Channel																				
CAMB140620-01	Stung Treng	0.61	0.63	0.05	0.13	218	237	225	12	455	455	330	330	51						
CAMB140621-10	Kratie	0.97	0.97	0.09	0.31	153	654	586	68	807	807	446	446	-14	5.01	5.01	-0.16	768	768	-24
CAMB140622-13	Kampong Cham	0.97	0.97	0.10	0.33	169	814	723	90	983	983	531	531	-23						
CAMB140627-22	Chrouy Changvar	0.97	0.98	0.09	0.31	135	955	858	98	1091	1091	564	564	-25	6.43	6.43	-0.29	960	960	-43
CAMB140718-66	Chrouy Changvar	0.97	0.97	0.05	0.19	113	619	583	36	732	732	404	404	1	6.53	6.53	0.02	976	976	3
CAMB140719-69	Kratie	0.97	0.97	0.04	0.15	119	502	480	22	621	621	359	359	4	7.07	7.07	0.08	1084	1084	12
CAMB140720-87	Chhlong, Kratie	0.99	0.99	0.07	0.23	92	751	697	54	843	843	440	440	-13	8.82	8.82	-0.27	1353	1353	-41
CAMB140720-88	Chhlong, Kratie	0.98	0.98	0.06	0.20	100	590	555	36	690	690	377	377	-4	7.56	7.56	-0.09	1160	1160	-14
CAMB140721-100	Chhlong, Kratie	0.97	0.98	0.05	0.18	100	533	504	29	633	633	352	352	-1	7.13	7.13	-0.03	1093	1093	-4
CAMB140721-101	Chhlong, Kratie	0.99	0.99	0.06	0.23	84	696	648	48	781	781	409	409	-12	8.28	8.28	-0.23	1270	1270	-36
CAMB140722-108	Kratie	0.98	0.98	0.05	0.19	90	528	499	30	618	618	339	339	-3	6.98	6.98	-0.06	1070	1070	-9
CAMB140722-114	Kratie	0.98	0.98	0.06	0.22	96	664	619	44	760	760	406	406	-9	8.35	8.35	-0.19	1281	1281	-29
CAMB140723-140	Stung Treng	0.90	0.91	0.06	0.19	142	677	637	41	820	820	460	460	17						
CAMB140725-161	Chrouy Changvar	0.96	0.96	0.05	0.17	107	558	530	28	665	665	372	372	3	6.56	6.56	0.05	980	980	7
MEK16-007	Vientiane	0.78	0.80	0.06	0.18	402	1071	1003	68	1473	1473	904	904	89	5.99	5.99	0.59	1962	1962	193
MEK16-033	Luang Prabang	0.95	0.96	0.09	0.30	210	1185	1068	117	1395	1395	744	744	-29	4.42	4.42	-0.17	1908	1908	-73
MEK16-096	Pakse	0.98	0.98	0.05	0.18	119	916	867	49	1035	1035	553	553	-5	13.10	13.10	-0.11	2414	2414	-20
MEK16-106	Stung Treng	0.91	0.92	0.06	0.19	157	781	735	46	938	938	525	525	18	11.65	11.65	0.41	2076	2076	72
MEK16-137	Kratie	0.98	0.98	0.04	0.16	103	536	512	24	639	639	359	359	2	11.49	11.49	0.07	1761	1761	11
MEK17-002	Kratie	0.99	0.99	0.11	0.35	98	1280	1125	155	1378	1378	661	661	-61	1.72	1.72	-0.16	263	263	-24
MEK17-003	Stung Treng	0.98	0.98	0.11	0.35	111	1396	1227	169	1507	1507	725	725	-54						
MEK17-107	China, Baoshan	0.97	0.98	0.24	0.64	252	2146	1464	682	2398	2398	984	984	-305	1.41	1.41	-0.44	1519	1519	-471
MEK17-114	China, Baoshan	0.97	0.98	0.24	0.64	251	2170	1485	685	2422	2422	994	994	-307	1.42	1.42	-0.44	1535	1535	-473
MEK17-135	Luang Prabang	0.96	0.97	0.10	0.33	194	1206	1072	134	1400	1400	730	730	-39	5.17	5.17	-0.27	2232	2232	-119
MEK17-157	Vientiane	0.79	0.81	0.05	0.17	375	1020	962	58	1395	1395	856	856	85	8.30	8.30	0.82	2719	2719	270
MEK17-189	Pakse	0.99	0.99	0.05	0.20	83	931	877	54	1013	1013	521	521	-10	11.13	11.13	-0.21	2050	2050	-39
MEK17-195	Stung Treng	0.93	0.93	0.06	0.20	153	814	764	51	968	968	535	535	15	13.13	13.13	0.37	2338	2338	66
MEK17-213	Kratie	0.99	0.99	0.05	0.18	117	881	836	45	997	997	534	534	-5	16.72	16.72	-0.14	2564	2564	-22
MEK17-225	Kratie	0.99	0.99	0.05	0.19	101	863	815	48	963	963	508	508	-8	15.90	15.90	-0.24	2438	2438	-37

Table 6.5: DIC and CO_2 calculated from partitioned dissolved major cations and anions in Mekong tributaries, sampled repeatedly in 2014, 2016 and 2017

Sample	Location	F_{carb}^{n3}	F_{carb}^{n4}	F_{sulf}^{n3}	F_{sulf}^{n4}	DIC_{sil}^{carb}	$DIC_{carb}^{carb\ O}$	$DIC_{carb}^{carb\ C}$	$DIC_{carb}^{sulf\ C}$	$DIC_{Short}^{Total\ O}$	$DIC_{Short}^{Total\ C}$	CO_2^O Short	CO_2^C Short	CO_2 Int	CO_2^O Short	CO_2^C Short	CO_2 Int	CO_2^O Short	CO_2^C Short	CO_2 Int
		μmol/L										μmol/L CO_2			10^{18}mol CO_2.day^{-1}			mol CO_2.km^{-2}.day^{-1}		
Tributaries																				
MEK17-256	Chi	0.91	0.91	0.03	0.11	251	515	498	17	766	766	500	500	53	0.15	0.15	0.02	298	298	32
MEK17-123	Heihui	0.99	0.99	0.05	0.17	184	1822	1731	91	2006	2006	1050	1050	-25	0.00	0.00	0.00	0	0	0
MEK17-236	Hueang	0.91	0.92	0.02	0.08	274	636	622	14	910	910	585	585	34	0.00	0.00	0.00	0	0	0
MEK17-240	Hueang	0.96	0.96	0.05	0.17	381	1588	1509	79	1969	1969	1135	1135	9	0.00	0.00	0.00	0	0	0
MEK17-230	Mae Kok	0.88	0.88	0.03	0.09	235	622	605	16	857	857	538	538	28	0.07	0.07	0.00	703	703	37
MEK17-254	Mun D/S	0.96	0.96	0.04	0.13	147	399	383	15	546	546	339	339	32	0.16	0.16	0.01	292	292	28
MEK17-257	Mun U/S	1.00	1.00	0.05	0.18	80	304	288	16	385	385	225	225	17	0.10	0.10	0.01	193	193	14
MEK17-169	Nam Hinboun	1.00	1.00	0.02	0.06	43	1093	1074	19	1135	1135	580	580	-2	0.00	0.00	0.00	0	0	0
MEK16-053	Nam Hinboun	1.00	1.00	0.02	0.06	46	1330	1309	21	1376	1376	701	701	-4	0.00	0.00	0.00	0	0	0
MEK17-166	Nam Kading	0.96	0.96	0.03	0.11	68	591	573	18	658	658	354	354	5	0.16	0.16	0.00	1083	1083	14
MEK16-051	Nam Kading	0.96	0.96	0.03	0.12	73	644	622	22	717	717	384	384	4	0.17	0.17	0.00	1174	1174	11
MEK17-141	Nam Khan	0.96	0.96	0.02	0.07	277	1992	1954	39	2269	2269	1254	1254	25	0.00	0.00	0.00	0	0	0
MEK16-012	Nam Khan	0.95	0.95	0.01	0.05	278	1546	1525	21	1824	1824	1040	1040	35	0.00	0.00	0.00	0	0	0
MEK17-146	Nam Lik	0.99	0.99	0.03	0.11	182	2180	2114	66	2362	2362	1239	1239	-15	0.64	0.64	-0.01	12208	12208	-149
MEK16-041	Nam Lik	0.99	0.99	0.01	0.04	144	921	911	10	1065	1065	599	599	10	0.31	0.31	0.01	5907	5907	103
MEK17-164	Nam Ngiap	0.89	0.90	0.01	0.04	128	500	494	6	629	629	375	375	25	0.18	0.18	0.01	3904	3904	265
MEK16-047	Nam Ngiap	0.86	0.86	0.01	0.04	153	457	451	6	610	610	378	378	31	0.18	0.18	0.01	3936	3936	325
MEK17-158	Nam Ngjum	0.95	0.96	0.02	0.08	102	751	735	16	852	852	469	469	11	0.38	0.38	0.01	2354	2354	54
MEK16-045	Nam Ngjum	0.94	0.94	0.02	0.06	106	605	596	9	711	711	404	404	15	0.33	0.33	0.01	2026	2026	73
MEK17-127	Nam Ou	0.96	0.96	0.01	0.04	209	1386	1370	16	1594	1594	894	894	26	0.55	0.55	0.02	2113	2113	61
MEK16-025	Nam Ou	0.95	0.95	0.01	0.05	218	1310	1294	16	1528	1528	865	865	28	1.14	1.14	0.04	4393	4393	141
MEK17-245	Songkhram	1.00	1.00	0.04	0.16	53	186	178	9	240	240	142	142	8	0.00	0.00	0.00	0	0	0
MEK17-207	Tonle Kong	0.77	0.78	0.02	0.05	99	193	190	3	292	292	194	194	17	0.41	0.41	0.04	1412	1412	125
CAMB140620-07	Tonle Kong	0.71	0.72	0.02	0.07	120	187	182	5	307	307	211	211	20	0.40	0.40	0.04	1375	1375	132
CAMB140723-122	Tonle Kong	0.78	0.79	0.02	0.06	75	154	151	3	229	229	151	151	13	0.86	0.86	0.07	2977	2977	251
MEK16-119	Tonle Kong	0.89	0.89	0.02	0.06	91	193	190	3	284	284	186	186	11	1.97	1.97	0.11	6836	6836	392
MEK17-004	Tonle Kong	0.79	0.80	0.02	0.06	137	297	292	5	434	434	283	283	23	0.13	0.13	0.01	445	445	37
MEK17-201	Tonle Srepok D/S	0.39	0.40	0.01	0.03	188	154	152	2	342	342	264	264	50	0.53	0.53	0.10	1061	1061	202
MEK17-005	Tonle Srepok D/S	0.35	0.36	0.03	0.06	266	245	237	8	511	511	385	385	69	0.00	0.00	0.00	0	0	0
MEK16-112	Tonle Srepok D/S	0.31	0.32	0.01	0.03	167	112	111	2	279	279	222	222	45	1.07	1.07	0.22	2135	2135	429
CAMB140620-04	Tonle Srepok D/S	0.21	0.22	0.02	0.03	265	139	136	3	404	404	333	333	71	0.00	0.00	0.00	0	0	0
CAMB140723-117	Tonle Srepok D/S	0.44	0.44	0.01	0.03	190	187	184	3	377	377	282	282	51	0.00	0.00	0.00	0	0	0
MEK16-077	Xe Banghiang	0.98	0.98	0.03	0.11	76	409	397	12	484	484	274	274	7	0.20	0.20	0.00	1001	1001	24
MEK17-176	Xe Banghiang	0.97	0.97	0.02	0.09	77	397	387	10	474	474	271	271	8	0.20	0.20	0.01	990	990	29
MEK17-183	Xe Don	0.94	0.94	0.01	0.03	145	604	600	4	749	749	445	445	15	0.05	0.05	0.00	621	621	21
MEK16-087	Xe Don	0.93	0.93	0.01	0.02	120	416	413	2	536	536	327	327	14	0.19	0.19	0.01	2559	2559	109

Table 6.6: DIC and CO_2 calculated from partitioned dissolved major cations and anions in Mekong main channel timeseries at Chroy Changvar, Phnom Penh, Cambodia, sampled repeatedly in 2014, 2016 and 2017

Sample	Date	F^{n3}_{carb}	F^{n4}_{carb}	F^{n3}_{sulf}	F^{n4}_{sulf}	DIC^{carb}_{sil}	$DIC^{carb\ O}_{carb}$	$DIC^{carb\ C}_{carb}$	$DIC^{sulf\ C}_{carb}$	$DIC^{Total\ O}_{Short}$	$DIC^{Total\ C}_{Short}$	CO_2^O Short	CO_2^C Short	CO_2 Int	CO_2^O Short	CO_2^C Short	CO_2 Int	CO_2^O Short	CO_2^C Short	CO_2 Int
							μmol/L					μmol/L CO_2			10^{18}mol CO_2.day^{-1}			mol CO_2.km^{-2}.day^{-1}		
Timeseries collected at Chroy Changvar, Phnom Penh, Cambodia																				
CAMB140630-29	2014-06-30	0.97	0.97	0.08	0.26	119	678	621	57	797	797	429	429	-9	5.02	5.02	-0.10	750	750	-15
CAMB140701-31	2014-07-01	0.97	0.97	0.08	0.27	119	697	636	61	816	816	438	438	-10	5.26	5.26	-0.12	786	786	-17
CAMB140702-33	2014-07-02	0.98	0.98	0.08	0.28	116	785	715	71	901	901	473	473	-14	5.92	5.92	-0.18	885	885	-27
CAMB140703-35	2014-07-03	0.98	0.98	0.08	0.26	110	811	743	68	921	921	482	482	-13	6.01	6.01	-0.16	899	899	-25
CAMB140706-41	2014-07-06	1.00	1.00	0.06	0.22	48	627	585	42	675	675	340	340	-8	4.40	4.40	-0.10	657	657	-15
CAMB140707-43	2014-07-07	0.98	0.98	0.06	0.20	95	627	588	38	722	722	389	389	-1	5.16	5.16	-0.01	771	771	-1
CAMB140708-45	2014-07-08	0.98	0.98	0.06	0.20	103	658	618	40	761	761	412	412	0	5.56	5.56	-0.01	831	831	-1
CAMB140710-49	2014-07-10	0.97	0.98	0.06	0.21	109	687	644	44	796	796	431	431	-3	6.19	6.19	-0.04	925	925	-5
CAMB140711-52	2014-07-11	0.97	0.98	0.06	0.22	111	688	643	45	799	799	432	432	-3	6.36	6.36	-0.05	950	950	-7
CAMB140712-54	2014-07-12	0.97	0.98	0.06	0.22	106	665	620	45	771	771	416	416	-4	6.21	6.21	-0.06	928	928	-9
CAMB140713-56	2014-07-13	0.96	0.96	0.06	0.20	124	599	562	37	723	723	405	405	1	6.14	6.14	0.02	917	917	3
CAMB140714-58	2014-07-14	0.96	0.96	0.05	0.19	124	581	549	33	706	706	399	399	4	6.17	6.17	0.07	921	921	10
CAMB140715-60	2014-07-15	0.97	0.97	0.05	0.19	105	585	551	34	690	690	380	380	1	5.98	5.98	0.02	893	893	3
CAMB140716-62	2014-07-16	0.97	0.97	0.05	0.19	113	600	566	34	713	713	395	395	2	6.28	6.28	0.03	938	938	4
MEK.US.PP 18.4.14	2014-04-18	0.97	0.97	0.14	0.42	191	1278	1079	200	1470	1470	731	731	-70	1.38	1.38	-0.13	205	205	-20
MEK.US.PP 7.5.14	2014-05-07	0.95	0.96	0.12	0.37	273	1234	1070	163	1507	1507	808	808	-41	1.75	1.75	-0.09	261	261	-13
MK.UP.PP 19.5.14	2014-05-19	0.95	0.96	0.11	0.36	246	1177	1028	149	1423	1423	760	760	-37	2.00	2.00	-0.10	298	298	-14
MK.US.PP 4.6.14	2014-06-04	0.96	0.96	0.11	0.36	253	1234	1076	158	1487	1487	791	791	-40	3.94	3.94	-0.20	588	588	-30
MK.US.PP 15.6.14	2014-06-15	0.96	0.97	0.13	0.40	241	1226	1044	182	1467	1467	763	763	-54	5.93	5.93	-0.42	885	885	-63
MK.US.PP 21.6.14	2014-06-21	0.95	0.96	0.13	0.40	190	903	772	131	1094	1094	576	576	-36	5.63	5.63	-0.35	841	841	-53
MK.US.PP 29.6.14	2014-06-29	0.96	0.96	0.08	0.27	160	735	672	63	895	895	496	496	-6	5.75	5.75	-0.07	859	859	-11
MK.US.PP 7.7.14	2014-07-07	0.98	0.98	0.06	0.21	102	640	600	40	741	741	402	402	0	5.32	5.32	-0.01	795	795	-1
MK.US.PP 11.7.14	2014-07-11	0.96	0.97	0.06	0.20	143	695	652	43	838	838	469	469	3	6.89	6.89	0.04	1030	1030	7
MK.UP.PP 27.07.14	2014-07-27	0.96	0.97	0.06	0.20	120	530	498	31	650	650	369	369	6	6.82	6.82	0.12	1019	1019	18
MK.UP.PP 30.07.14	2014-07-30	0.98	0.98	0.05	0.18	87	532	504	28	619	619	339	339	3	6.49	6.49	0.06	970	970	9
MK.UP.PP 06.08.14	2014-08-06	0.96	0.96	0.04	0.14	113	438	420	18	551	551	322	322	11	6.78	6.78	0.24	1013	1013	36
MK.UP.PP 11.08.14	2014-08-11	0.96	0.96	0.04	0.13	131	466	448	18	596	596	354	354	15	8.22	8.22	0.35	1227	1227	52
MK.UP.PP 19.08.14	2014-08-19	0.98	0.98	0.04	0.15	107	613	586	27	720	720	400	400	7	10.35	10.35	0.18	1546	1546	28
MK.UP.PP 25.08.14	2014-08-25	0.97	0.97	0.04	0.14	134	679	652	27	813	813	460	460	11	12.29	12.29	0.30	1836	1836	44
MK.UP.PP 01.09.14	2014-09-01	0.97	0.97	0.05	0.18	143	764	723	41	907	907	505	505	5	13.69	13.69	0.12	2044	2044	19
MK.UP.PP 09.09.14	2014-09-09	0.97	0.97	0.05	0.17	112	613	583	30	725	725	404	404	5	11.04	11.04	0.13	1650	1650	19
MK.UP.PP 17.09.14	2014-09-17	0.96	0.96	0.04	0.15	168	593	566	26	761	761	451	451	17	12.38	12.38	0.47	1850	1850	70
MK.UP.PP 27.09.14	2014-09-27	0.97	0.97	0.04	0.14	125	600	575	25	725	725	412	412	10	10.71	10.71	0.25	1600	1600	37
MK.UP.PP 10.10.14	2014-10-10	0.95	0.95	0.04	0.14	198	665	637	28	862	862	516	516	20	11.47	11.47	0.43	1714	1714	65
MK.UP.PP 15.10.14	2014-10-15	0.97	0.97	0.06	0.21	145	792	742	49	937	937	516	516	0	10.38	10.38	0.01	1551	1551	1
MK.UP.PP 20.10.14	2014-10-20	0.97	0.98	0.08	0.27	141	847	774	73	988	988	529	529	-12	9.85	9.85	-0.22	1472	1472	-33
MK.UP.PP 9.11.14	2014-11-09	0.96	0.97	0.08	0.28	177	929	846	83	1106	1106	600	600	-12	7.95	7.95	-0.16	1187	1187	-25
MK.UP.PP 14.11.14	2014-11-14	0.97	0.98	0.10	0.33	166	1062	943	119	1228	1228	638	638	-31	7.78	7.78	-0.38	1162	1162	-56
MK.UP.PP 19.11.14	2014-11-19	0.98	0.98	0.08	0.29	151	1031	935	96	1182	1182	619	619	-20	6.87	6.87	-0.22	1026	1026	-33
MK.UP.PP 25.11.14	2014-11-25	0.97	0.97	0.10	0.32	182	1079	961	118	1261	1261	662	662	-29	6.72	6.72	-0.30	1003	1003	-44
MK.UP.PP 12.12.14	2014-12-12	0.97	0.97	0.08	0.27	190	1087	994	93	1277	1277	687	687	-13	5.32	5.32	-0.10	794	794	-15
MK.UP¿PP 29.12.14	2014-12-29	0.97	0.97	0.13	0.40	195	1266	1083	183	1460	1460	736	736	-60	4.29	4.29	-0.35	640	640	-52
MK.UP¿PP 10.01.15	2015-01-10	0.98	0.98	0.13	0.42	170	1315	1112	203	1485	1485	726	726	-72	3.48	3.48	-0.34	520	520	-51

6.5.2 Source of DIC in the Mekong River Basin

6.5.2.1 Overview of Mekong Data as a Function of F_{sulf} and F_{carb}

The forward model developed here based on that by Galy & France-Lanord (1999) was used to partition Mekong river water solutes between lithology and acidity source. Using the framework developed from Torres *et al.* (2016), the Mekong can be plotted in varying acidity (F_{sulf}) and lithology (F_{carb}) parameter space (Figure 6.6). F_{sulf}, F_{carb}, and CO_2 values for Mekong data use only Ca^{2+} in the calculation so that the data is comparable to the contours and parameter space it is plotted on. Because Mg^{2+} is not included in the calculations, the CO_2 consumption from carbonic acid weathering of silicates (n1) will be underestimated, as will the CO_2 release from sulfuric acid weathering of carbonates (n3, n4). Furthermore, the data on Figure 6.6 is not scaled by discharge, therefore it does not represent the total carbon budget of the Mekong. However, Figure 6.6 does provide an initial estimate of the impact of weathering in the Mekong river basin on atmospheric CO_2 levels. All samples suggest that the Mekong is consuming atmospheric CO_2 on the short term. F_{carb} is high in most samples except samples from Cambodia, where X_{sil} is high (Figure 4.24). Over long timescales, samples from China, the Middle Mekong tributaries from the left bank in Laos, and the main stem are all releasing CO_2. The spread of data in F_{sulf} and F_{carb} parameter space suggests there is spatial variability in areas consuming or releasing CO_2 in the Mekong river basin. Timeseries samples collected at Chroy Changvar close to the mouth of the Mekong show temporal variability in F_{sulf} over the year (Figure 6.7). The samples show a hysteresis where the lowest F_{sulf} is the monsoonal months and the highest F_{sulf} values are calculated in the dry season.

6.5.2.2 Partitioned Source of Mekong DIC

The solutes measured in the Mekong are partitioned to their sources using the forward model set out in Section 6.3. DIC delivered from various acid-rock interactions is calculated for a time series collected at Chroy Changvar, close to the mouth of the Mekong river (using Equations described in 2.2.1). DIC delivered to the South China Sea is predominantly derived from H_2CO_3 weathering of carbonates (67% average), followed by carbonic acid weathering of silicates (32% average) (Figure 6.8B). If there was any DIC delivered by the H_2SO_4 weathering of carbonates reaction pathway n4, then there would only be an average contribution of 6% to the total DIC flux to the ocean. DIC flux delivered by H_2CO_3 weathering of silicates peaks before the flux of DIC delivered by carbonate weathering with H_2CO_3. This earlier peak in silicate weathering corresponds

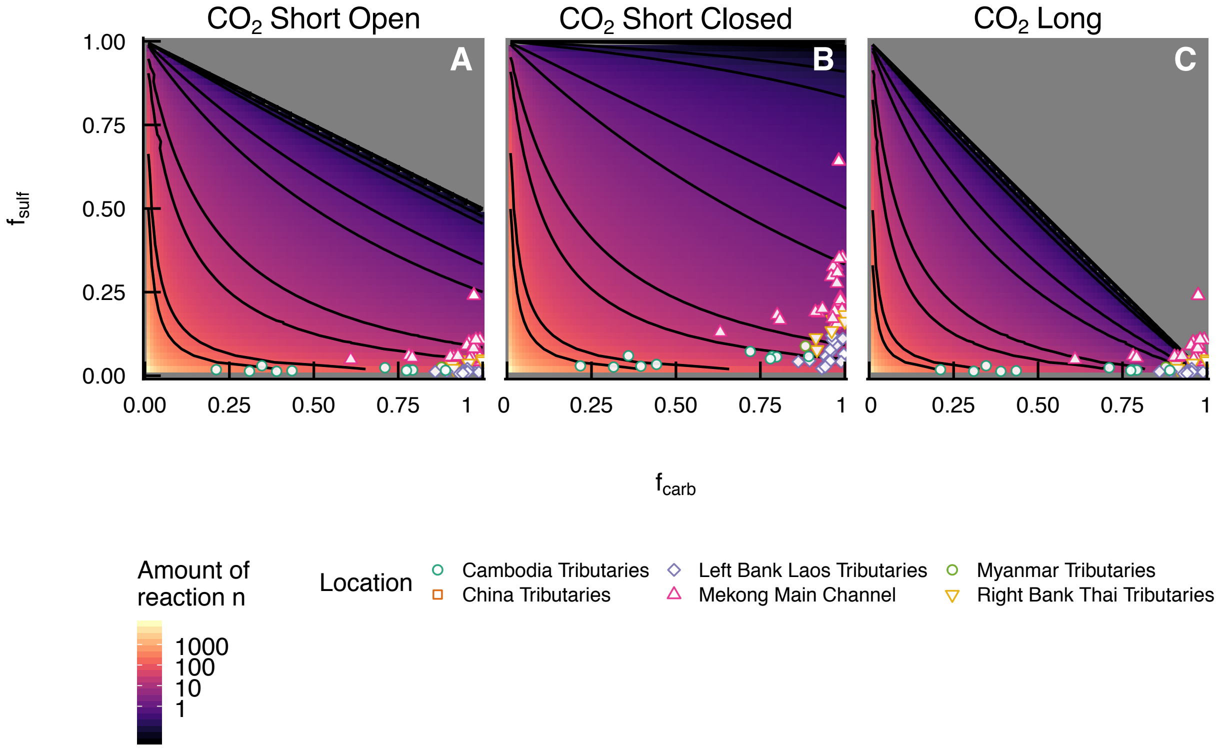

Figure 6.6: Mekong main stem and tributary data as a function of varying acidity (F_{sulf}) and lithology (F_{carb}). F_{sulf} is the fraction of acidity sourced from H_2SO_4 as a ratio of total H_2CO_3 and H_2SO_4. F_{carb} is the fraction of cations delivered from the weathering of carbonates as a ratio of the total rocks weathered, silicates and carbonates. The amount of CO_2 consumed (coloured area) or released (grey area) is relative to the amount of sulfuric acid weathering of carbonates instantaneously degassing CO_2 (n3). Amount of CO_2 consumption is constant along the contour lines. F_{sulf}, F_{carb} and CO_2 values for Mekong data use only Ca^{2+} in the calculation so the data is comparable to the contours and parameter space it is plotted on. A: Short term CO_2 impact from reactions occurring in an open environment takes into account the drawdown of atmospheric CO_2 by carbonic acid weathering of silicates (n1) and carbonates (n2) and the instantaneous release of CO_2 from sulfuric acid weathering of carbonates (n3). B: In a closed environment, short term CO_2 takes into account the same drawdown of atmospheric CO_2 by carbonic acid weathering of silicates (n1) and carbonates (n2) but sulfuric acid weathering of carbonates does not degas CO_2, DIC is transferred to the ocean (n4). C: Long term CO_2 is the offset of sulfuric acid weathering of carbonates (n3) against long term sequestration of CO_2 by carbonic acid weathering of silicates and subsequent carbonate precipitation (n1). Symbols are locations within the Mekong basin: the upper Mekong in China (orange squares), the left bank in the Middle Mekong draining Myanmar (green circles), and the left (Laos) bank of the Middle Mekong (lilac diamonds), and right (Thailand) bank of the middle Mekong (yellow inverted triangles), and the lower Mekong in Cambodia (blue-green circles).

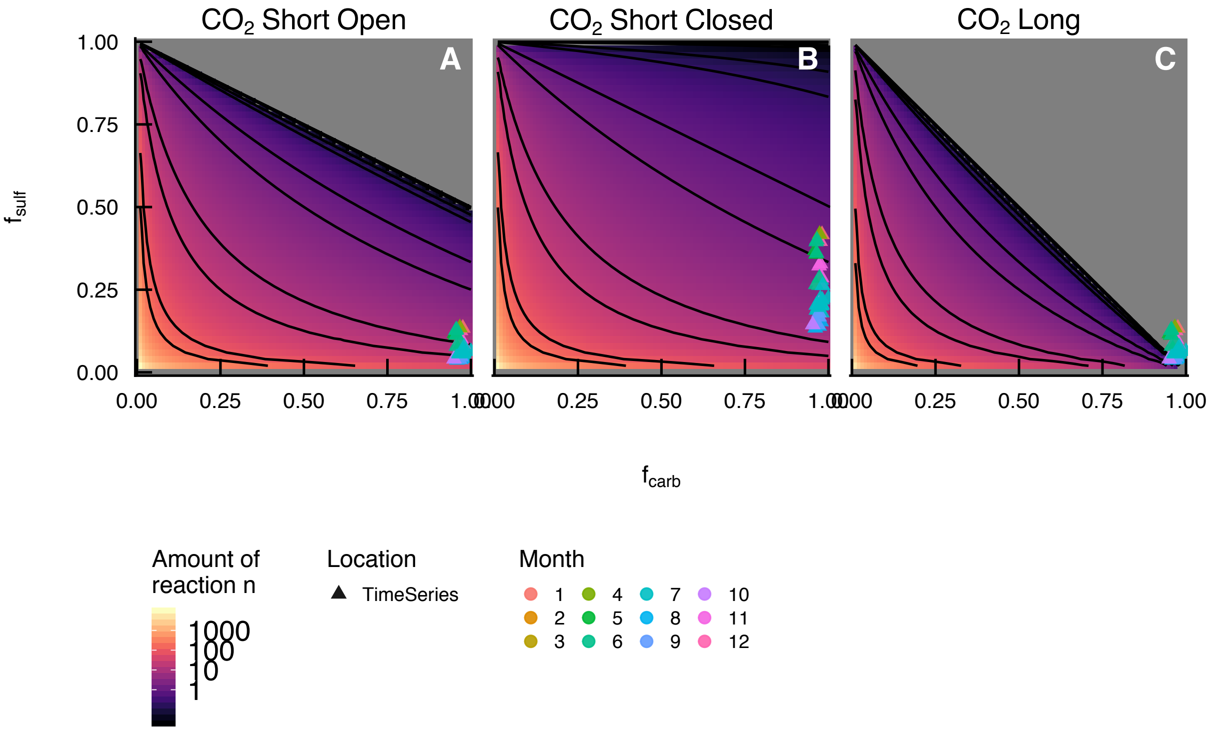

Figure 6.7: Timeseries at Chroy Changvar, Mekong main stem, as a function of varying acidity (F_{sulf}) and lithology (F_{carb}). F_{sulf}, F_{carb}, and n1, n2 are the same as in Figure 6.6, see caption. A: Short term CO$_2$ impact from reactions occurring in an open environment. B: Short term CO$_2$ impact from reactions occurring in a closed environment. C: Long term CO$_2$ impact.

to the Southeast Asian monsoon hitting the basin from the south east, first hitting the Tonle Kong, Tonle San and Tonle Srepok tributaries of Cambodia which are dominated by basalts and granites (Figure 1.2).

Variations in DIC delivered from the Mekong Basin depend on spatial and temporal variations in lithology (F_{carb}) and acidity source (F_{sulf}). There is more temporal variation in F_{sulf} than F_{carb} (Figure 6.8C), whereas there is more spatial variation in F_{carb} than F_{sulf} (i.e. Figure 4.23 and Figure 6.10A). F_{carb} remains constantly high during the year (Figure 6.8C). During the monsoon F_{sulf} decreases and in the early monsoon (June-November) there is a small peak in F_{carb}. The decrease in F_{sulf} during the monsoon is likely due to mixing rather than a process related decrease. An early increase in flux from southern tributaries in Cambodia would increase DIC flux from tributaries with relatively more carbonic acid weathering of silicates, therefore decreasing F_{sulf}. Post monsoon F_{sulf} increases, suggesting a relatively larger delivery of solutes from areas dominated by sulfuric acid weathering of carbonates.

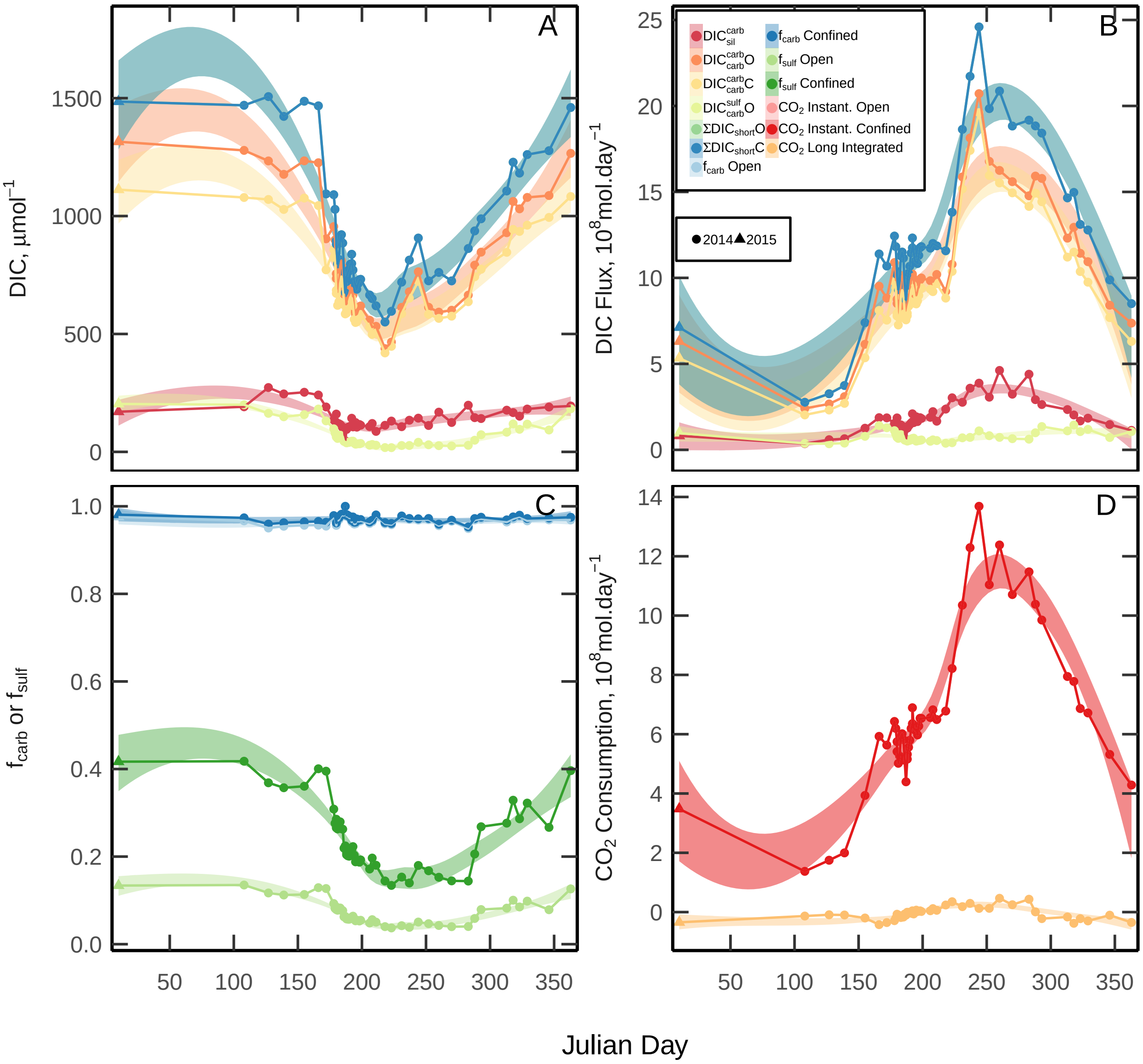

Figure 6.8: DIC and CO_2 fluxes close to the mouth at Chroy Changvar above Phnom Penh, Cambodia, on the Mekong main channel. A: DIC calculated with partitioned cations from river water measurements. DIC delivered by the acidity source H_2SO_4 $(^{sulf})$ or H_2CO_3 $(^{carb})$ and the lithology silicates $(_{sil})$ or carbonates $(_{carb})$ in an open (O) or confined (C) environment is the same in the legend for concentration (A) and flux (B). B: DIC flux calculated with discharge data collected by the MRC. C: F_{carb} and F_{sulf} parameters calculated from Equations 6.61–6.62. D: Variation in CO_2 consumption calculated across the year. The Mekong consumes CO_2 in the short term (red and pink), and is releasing CO_2, or may even be CO_2 neutral on long timescales (orange). Values are calculated using Equations 2.16, 2.17 and 2.29. Samples are plotted as points connected with line. A loess regression with 2σ error provides the smoothed error band through the samples.

6.5.3 CO_2 Budget of the Mekong River Basin

6.5.3.1 Spatial CO_2 Budget

The Mekong river is characterised by a high proportion of carbonate mineral weathering (average X_{sil} over all tributaries is 0.18 ranging between 0.05-0.64). Partitioning of sulfate sources indicates that 57% of sulfate in the Mekong is derived from oxidative weathering of pyrite. When CO_2 consumption is calculated using Equations 6.78-6.80 there are orders of magnitude difference between tributaries. CO_2 consumption has been calculated as a flux in units of mol.day^{-1} using discharge data from the MRC (Figure 6.9A-C), and as a specific flux where the CO_2 flux is divided by the basin area, units are mol.km^{-2}.day^{-1} (Figure 6.9D-F) . On the short term the Mekong is consuming CO_2 because of the large proportion of carbonic acid weathering of carbonates. CO_2 consumption is particularly high in China (X_{sil} = ~0.1) and on the left bank of the Mekong where the landscape is dominated by carbonate karst. The release of CO_2 from sulfuric acid weathering of carbonates is small (0.25 x 10^8mol.day^{-1}) compared to the CO_2 drawdown from carbonic acid weathering (3.62 x 10^8mol.day^{-1}) on the short term (7% average over all tributaries). However, the amount of sulfuric acid weathering releasing CO_2 on the short term is a larger flux, on average over all tributaries, than the long term sequestration of atmospheric CO_2 from the carbonic acid weathering of silicates and subsequent precipitation of carbonates in the ocean (0.23 x 10^8mol.day^{-1}). When long term CO_2 budget is mapped spatially the carbon budget for two catchments is a net source of atmospheric CO_2 (Figure 6.9C,F). This result remains the same whether the spatial CO_2 budget is calculated as a flux or as a specific flux.

F_{carb} is highest in China (0.99) and downstream decreases to the lowest value in the main stem at Vientiane (0.78). This decrease is due to the addition of tributaries draining Myanmar which have higher X_{sil} than China (Figure 6.10A). The effect of an increase in solutes being delivered by silicate weathering at Vientiane is a net CO_2 sink on the long term (Figure 6.10E). Karstic tributaries in Laos increase F_{carb} between Vientiane and Pakse. F_{carb} is lowest in tributaries in Cambodia, where X_{sil} is high and there are a high proportion of basalts. The tributaries in Cambodia contribute a large proportion of the total discharge of the Mekong river, the impact on short term CO_2 budget is a decrease in consumption due to the reduction of weatherability in silicates relative to carbonates (Figure 6.10C-D). However, on the long term CO_2 is only sequestered by silicate weathering which offsets the release from sulfuric acid weathering of carbonates, hence the signal at Kratie reflects CO_2 consumption on the long term (Figure 6.10E). F_{sulf} decreases

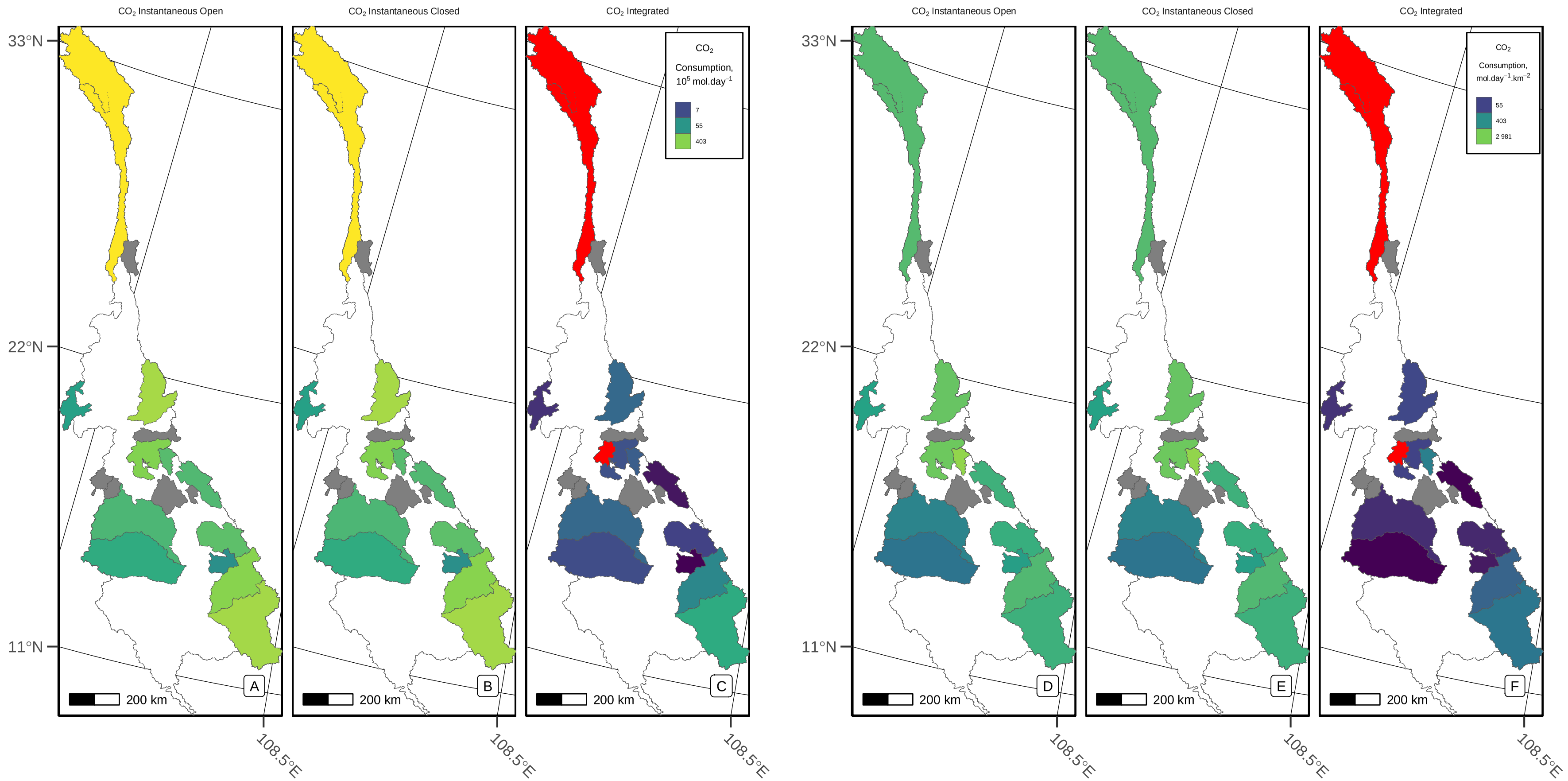

Figure 6.9: CO_2 flux and specific flux in Mekong tributaries. CO_2 fluxes in Mekong tributaries are calculated using partitioned cations and discharge data from a combination of ADCP data collected in 2016 and 2017, and MRC historical data set. Cambodian tributaries are from Someth *et al.* (2013) and some Laos tributaries from Nippon Koei (2001). Values are representative of monsoon CO_2 consumption or release. CO_2 Instantaneous calculations (A-B, D-E) consider the draw down of atmospheric CO_2 through carbonic acid weathering of carbonates and silicates and the instantaneous release of CO_2 from sulfuric acid weathering of carbonates (B, E). The CO_2 integrated calculations (C, F) look at the integrated short and long term effect of chemical weathering in each catchment, considering the long term sequestration of CO_2 from carbonic acid weathering of silicates and the CO_2 release by sulfuric acid weathering. Specific flux (D-F) takes tributary basin area into account so the CO_2 consumption or release is relative to size of the catchment. Red areas are releasing CO_2, grey areas have no discharge data and white areas are not sampled.

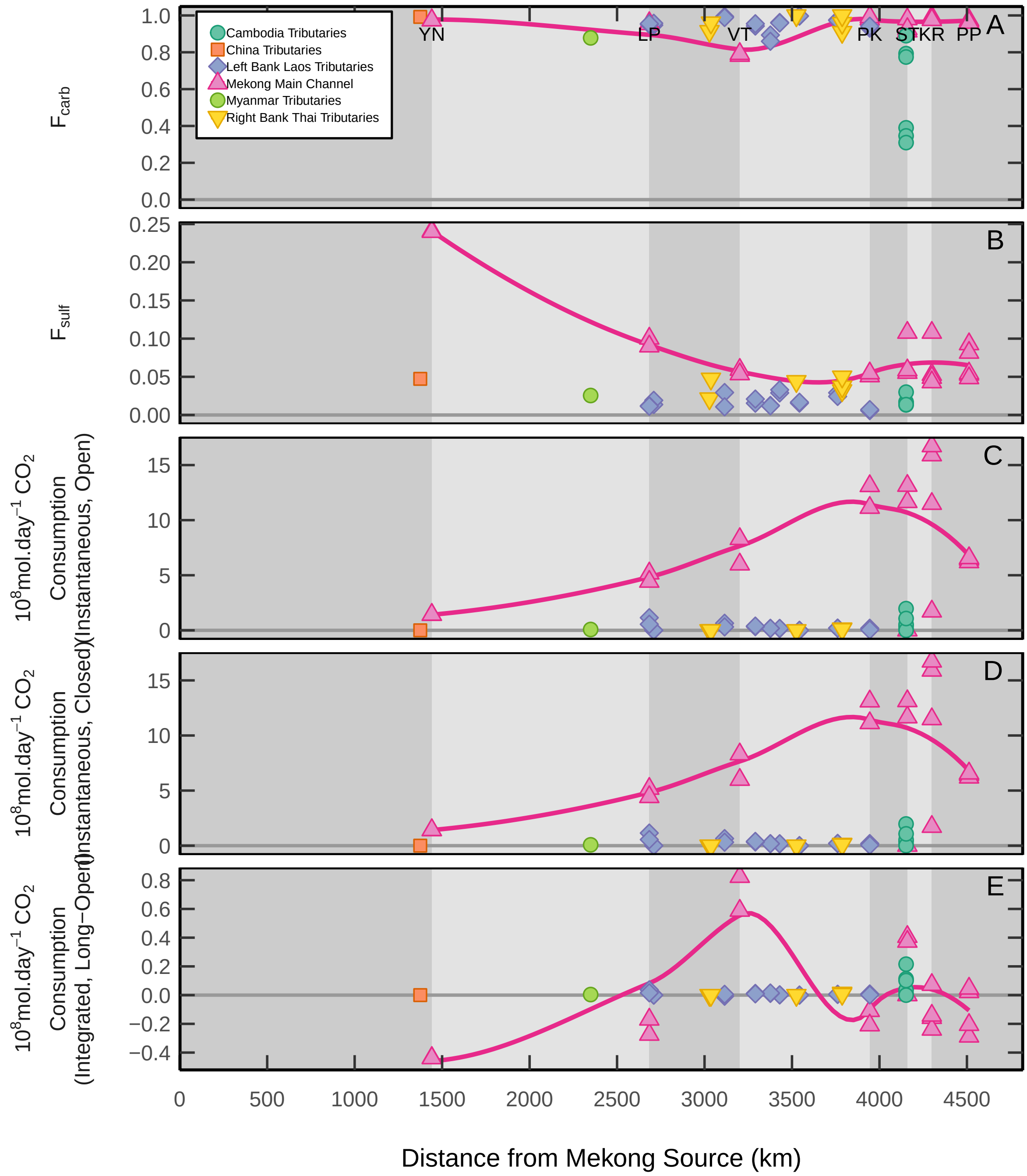

Figure 6.10: Downstream F_{carb}, F_{sulf} and CO_2 consumption. CO_2 fluxes in Mekong tributaries are calculated using partitioned cations and discharge data from sources mentioned in Figure 6.9. F_{carb} (A) and F_{sulf} (B) are calculated with Ca^{2+} only, wheras CO_2 budgets are calculated with all cations (C-E). Values are representative of monsoon CO_2 consumption or release. Instantaneous CO_2 consumption takes into account CO_2 consumption from carbonic acid weathering of carbonates and silicates and CO_2 instantaneous release from sulfuric acid weathering of carbonates in an open environment where carbon is degassed as CO_2 (C). The same carbonic acid weathering is considered for the instantaneous CO_2 budget in a closed environment but there is not instantaneous release of CO_2 from sulfuric acid weathering of carbonates because carbon is transferred as DIC to the oceans (D). Long term CO_2 is the CO_2 sequestration by carbonic acid weathering of silicates offset by CO_2 release by sulfuric acid weathering of carbonates (E). Horizontal line at zero indicates neutral CO_2 on Panel C-E; above this line the sample is consuming CO_2 and below the line, the sample releases CO_2.

downstream from 0.25 in China to 0.07 close to the mouth. 58% of the sulfate delivered from China is sourced from the oxidative weathering of pyrite resulting in the largest release of CO_2 on the long term from the mountainous Upper Mekong in China. Despite the fact that F_{sulf} decreases by $\sim$ 15% between China and Luang Prabang and continues to decrease due to dilution with H_2CO_3 dominated reactions further downstream, the flux of CO_2 release by sulfuric acid weathering of carbonates is comparative to the CO_2 drawdown on the long term from carbonic acid weathering of silicates. It is necessary to highlight that F_{carb} and F_{sulf} are calculated with Ca^{2+} only but CO_2 budgets are calculated with all cations.

Generally, the areas with higher topography are areas that release CO_2 on long timescales; specifically in China where there are high elevations and steep slopes, and in the Nam Lik, where there is dynamic karst topography. The values of consumption are also lower, relative to other areas of the basin, on the left bank of the Middle Mekong where the Annamite mountains are creating topography. Topography increases erosion rates, which can in turn increase weathering rates (Maher & Chamberlain, 2014). Whilst mountainous regions are typically weathering–limited (West *et al.*, 2005), sulfide minerals, for example pyrite, have faster oxidation rates than the dissolution of silicates and thus are proportionally important in mountainous areas. In the Mekong, mountainous areas correspond to geology with a high proportion of carbonate rocks indicating a release of CO_2. In order for weathering to consume CO_2 there must be enough time for silicates to weather congruently. In the Andes–Amazon system it has been suggested that for areas of rapid erosion, such as mountainous source regions of rivers, complete pyrite oxidation can occur whilst silicates weather incongruently as the system is kinetically–limited (Torres *et al.*, 2016). In lowland areas with less topography, the duration of weathering is longer, allowing for congruent silicate dissolution and resulting in these areas typically consuming CO_2. This is similar to the Mekong (Figure 6.9).

The greatest fraction of CO_2 drawdown on the short-term is from both from mountainous tributaries in the Upper Mekong in China and from the most southerly tributaries in Cambodia (Figure 6.9A,B). The Tonle Srepok tributary in Cambodia, Lower Mekong, has the highest specific flux for consuming on the integrated timescale CO_2 (Figure 6.9F). This tributary contains sandstones, gneiss, schist, granite, and basalt and has one of the highest discharges of the Mekong tributaries. Tributaries where the river cuts through deeply incised karst valleys (Northern Laos, left bank tributaries) also have some of the highest specific on the short- and integrated–term CO_2 flux. Some of largest tributaries by basin area, the Mun and the Chi on the right bank in Thailand, have a low specific– and total–flux due to the lithology is dominated by evaporites. On the long term, China becomes a CO_2 source whereas the majority of tributaries are close to CO_2 neutral on the long term (Figure 6.9).

6.5.3.2 Temporal CO_2 Budget

CO_2 consumption in the Mekong has been calculated for the long and short term reactions, described in Sections 2.2.2 and 2.3.1. The solutes measured at Chroy Changvar integrate the signals delivered from processes that occur within the basin. Therefore, the trends seen over the year indicate the impact that the Mekong as a whole has on atmospheric CO_2 (Figure 6.8). During the monsoon, CO_2 consumption (from timescales of dissolution in the catchment up to less than the million-year timescale of carbonate precipitation) is up to six times greater than CO_2 consumption in the dry season, due to the increased weatherability of carbonates (Figure 6.8D). Over the year, CO_2 is released on the long–term in the dry season when silicate weathering decreases ($\mathrm{DIC}_{sil}^{carb}$, Figure 6.8B) to fluxes smaller than sulfuric acid weathering of carbonates ($\mathrm{DIC}_{carb}^{sulf}$). Between July and September, during the monsoon, the Mekong consumes CO_2 when all weathering fluxes increase, the amount of carbonic weathering of silicates increases relative to sulfuric acid weathering of carbonates.

An annual total CO_2 budget is calculated for the Mekong by summing the average monthly CO_2 flux. The Mekong River is a transient sink of CO_2 but a small long term source of atmospheric CO_2. The annual specific fluxes ($\mathrm{tC.km^{-2}.yr^{-1}}$) for carbon transfer through chemical weathering reactions are illustrated in Figure 6.11. Carbonic acid weathering draws down 0.09 $\mathrm{tC.km^{-2}.yr^{-1}}$ through silicate dissolution (Equation 2.1, Figure 6.11A) and 0.24 $\mathrm{tC.km^{-2}.yr^{-1}}$ by carbonate dissolution (Equation 2.2, Figure 6.11B) on the short–term. CO_2 consumed on the short–term by silicate weathering includes the weathering of Na- and K-silicates. When the long–term CO_2 budget is calculated, only Ca- and Mg-silicates are taken into account because Na and K do not precipitate in carbonates (Berner, 1992) and CO_2 drawndown by Na- and K-silicates could be re-released through reverse weathering (Mackenzie & Garrels, 1966). Therefore the actual long term sink from carbonic acid weathering of silicates is 0.015 $\mathrm{tC.km^{-2}.yr^{-1}}$ (Figure 6.11F). The dissolution of carbonates with carbonic acid releases two moles of HCO_3^- where one mole of carbon is atmospheric derived and one mole is lithological carbon from the carbonate, when the HCO_3^- is precipitated as carbonate in the oceans, one mole of carbon is returned to carbonate lithology and one mole to the atmosphere making this a long–term carbon neutral process. The reaction of sulfuric acid and carbonates releases CO_2 to the atmosphere instantaneously if the reaction occurs

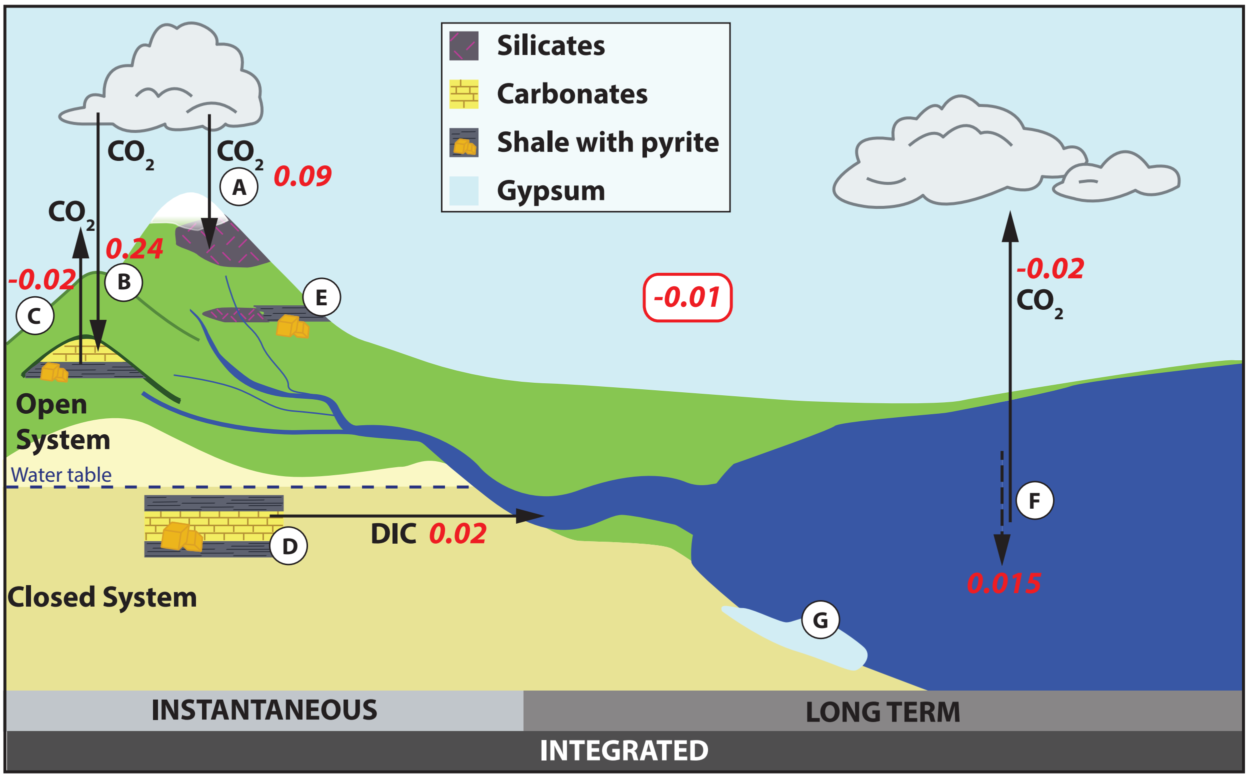

Figure 6.11: Specific CO_2 fluxes of chemical weathering reactions in the Mekong River basin. Specific fluxes of inorganic carbon from chemical weathering of rocks are in red ($tC.km^{-2}.yr^{-1}$). Reactions are categorised into two timescales. Letters indicate a reaction occurring and arrows represent the transfer of carbon. The weathering of silicate rocks draws down 0.09 $tC.km^{-2}.yr^{-1}$ of atmospheric carbon during dissolution with carbonic acid (A). Carbonic acid reacting with carbonate rocks draws down 0.24 $tC.km^{-2}.yr^{-1}$ of atmospheric carbon (B). Sulfuric acid weathering of carbonate rocks releases 0.02 $tC.km^{-2}.yr^{-1}$ of lithological carbon back to the atmosphere, instantaneously if the reaction occurs in an open environment, where carbon is degassed to the atmosphere as CO_2 (C) or in a confined environment where lithological carbon is released (D) and transferred to the oceans and precipitated as carbonate, releasing CO_2 on long–term (million-year) timescales (F). Sulfuric acid weathering of silicate minerals does not release carbon in any form (E). HCO_3^- that is sourced from carbonic acid weathering of silicates (A) is transported to the ocean and precipitates as $CaCO_3$ which is a sink of 0.02 $tC.km^{-2}.yr^{-1}$ atmospheric carbon (represented by the dashed downwards arrow in the ocean, F). The HCO_3^- delivered from carbonic acid weathering of carbonates (B) is returned to its source and is a carbon neutral process on long–term timescales (no number is written but 0.024$tC.km^{-2}.yr^{-1}$ is returned to the atmosphere at F). When carbonate precipitates it releases CO_2 back to the atmosphere (F). The precipitation of gypsum (G) from Ca^{2+} and SO_4^{2-} products of C, D and E is not involved in the carbon cycle. The Mekong is a net source of 0.01 $tC.km^{-2}.yr^{-1}$ to atmospheric carbon when all sources and sinks are accounted for on instantaneous and long timescales. Figure after (Gaillardet & Galy, 2008).

in an open environment (Equation 2.3, Figure 6.11C) or on the long term after carbon released from the reaction is transferred as HCO_3^- to the oceans and precipitated as carbonate releasing CO_2 (Equation 2.4, Figure 6.11D). Either reaction pathway releases 0.02 $tC.km^{-2}.yr^{-1}$ (Figure 6.11F). The overall carbon budget of the Mekong is calculated by the atmospheric CO_2 sequestration by carbonic acid weathering of silicates offset by the instantaneous CO_2 release from sulfuric acid weathering of carbonates (since this is the predominant reaction pathway in the Mekong (Section 6.5.1)). There is 15% difference in the long term CO_2 sequestration from carbonic acid weathering of silicates and the release of CO_2 by sulfuric acid weathering of carbonates resulting in the Mekong being a net source of CO_2 to the atmosphere by 0.01 ±0.001 $tC.km^{-2}.yr^{-1}$.

The range in spatial CO_2 consumption values presented in Figure 6.9 are calculated using individual discharge, silicate residue ratios and f_{pyr} values. Discharge values are a combination of ADCP data collected in 2016 and 2017, MRC historical data set, Cambodian tributaries are from Someth *et al.* (2013) and some Laos tributaries from Nippon Koei (2001). Ca/Na and Mg/K ratios are calculated from bedload samples collected from each tributary, similarly f_{pyr} values have been calculated from unique $\delta^{18}O_{SO_4}$ and $\delta^{34}S_{SO_4}$ measured in dissolved sulfate in each tributary. This comprehensive data set characterising each tributary provides a robust method to calculate the CO_2 budget in catchments spatially. The most representative annual total CO_2 budget would be calculated by summing the CO_2 flux of all tributaries for each month of the year. However monthly discharge data is not available for most tributaries in the Mekong basin, so this is not yet possible. Instead, the annual total CO_2 budget is calculated using the flux at Chroy Changvar, at the mouth of the Mekong.

Samples collected at Chroy Changvar use Ca/Na and Mg/K ratios calculated from bedload analysed from the sample site but an f_{pyr} value from Kratie because samples from $\delta^{34}S_{SO_4}$ and $\delta^{18}O_{SO_4}$ measurement were not collected in Chroy Changvar. One Ca/Na, Mg/K and f_{pyr} value is applied to samples collected across the year at Chroy Changvar which may be an under or over estimation of sulfuric acid weathering of carbonates if f_{pyr} were to vary annually, which cannot be determined from current data. Moreover one Ca/Na, Mg/K and f_{pyr} value is applied to partition the signal at the mouth of the river, effectively resorting back to a simpler forward partitioning of cations (Galy & France-Lanord, 1999), losing the detail from individual tributary partitioning. Finally, it is important to consider the $\delta^{34}S_{SO_4}$ and $\delta^{18}O_{SO_4}$ measured in SO_4^{2-} samples collected from main stem. The premise of using oxygen isotopes in sulfate relies upon the sedimentary sulfide being oxidised with local meteoric water and measured close to the location of oxidation so that

$\delta^{18}O$ and $\delta^{18}O_{SO_4}$ are relatable. However, it is unlikely that as much sedimentary sulfide is oxidised in the main stem as that which is oxidised in the tributaries. Therefor the measured SO_4^{2-} at Chroy Changvar is likely a mixture of sulfate oxidised in local tributaries and upstream and transported. The main stem f_{pyr} signature has only a small variation (~5%) so this may not be a substantial issue.

6.6 The Mekong in Global Perspective

The drawdown of atmospheric carbon by carbonic acid weathering of carbonates is 0.24 $tC.km^{-2}.yr^{-1}$ in the Mekong compared to 0.89 $tC.km^{-2}.yr^{-1}$ in the Mackenzie (Horan *et al.*, 2019). The long term carbon sequestration from carbonic acid weathering of silicates is 0.26-0.41 $tC.km^{-2}.yr^{-1}$ for the Mackenzie, 0.63 $tC.km^{-2}.yr^{-1}$ for the Amazon, 1.8 $tC.km^{-2}.yr^{-1}$ for the Brahmaputra and 0.71 $tC.km^{-2}.yr^{-1}$ for the Yangtze (Gaillardet *et al.*, 1999; Horan *et al.*, 2019) compared to 0.02 $tC.km^{-2}.yr^{-1}$ for the Mekong. Gaillardet *et al.* (1999) calculate that the Mekong consumes 2.93$tC.km^{-2}.yr^{-1}$ from one spot sample collected at the mouth of the Mekong using an inverse model. Li *et al.* (2014a) use MRC historical from Pakse to suggest the Mekong is a CO_2 sink, consuming 1.2$tC.km^{-2}.yr^{-1}$. In this calculation, Ca is corrected for evaporite input but not for sulfide input, therefore it is likely an over estimate of CO_2 consumption.

The most significant result of this study is that the Mekong River is a small net source of CO_2 over the year. It is crucial to re-consider the CO_2 budget in catchments where carbonate weathering is high, such as the Ganges-Brahmaputra, Yangtze, Mississippi, and Xijiang (Gaillardet *et al.*, 1999; Galy & France-Lanord, 1999) as the estimates could be overestimated due to sulfuric acid weathering of carbonates releasing CO_2 not being accounted for. A detailed carbon budget considering the sulfuric acid weathering of carbonates has so far only been demonstrated for the Mackenzie River (Calmels *et al.*, 2007; Horan *et al.*, 2019; Millot *et al.*, 2003), and now for the Mekong River. Further, it is vital to understand the impact of sulfuric acid weathering in catchments that are heavily populated and are within developing nations, as the rate of sulfuric acid weathering could increase with anthropogenic release of SO_2 though the burning of fossil fuels (e.g. Li *et al.*, 2008; Li & Ji, 2016; Smith *et al.*, 2001; Xu & Liu, 2007; Yoon *et al.*, 2008).

Chapter 7

Chemical Weathering in the Mekong River Basin: Summary and Conclusions

The aim of this thesis has been to calculate the inorganic carbon budget of one of the world's largest yet understudied river basins, the Mekong, and to assess the impact of sulfuric acid weathering of carbonate minerals on a continental scale river basin.

The Mekong water chemistry is dominated by high concentrations of Ca^{2+} and HCO_3^- with concentrations of most elements generally decreasing downstream from the headwaters in China. An exception to this trend are the peaks in concentration of Cl^-, Na^+ and K^+, from rivers draining the Khorat Plateau, on the right bank of the Middle Mekong, indicating halite and potash mineral dissolution.

Two approaches were discussed for partitioning solutes between carbonate and silicate lithologies. Firstly, bedload sediment is sequentially leached to extract lithological components from the bulk sediment. $^{87}Sr/^{86}Sr$ isotope measurements in the AcOH leach (thought to represent the carbonate end member), water, and residue (representing the silicate end member) are used to estimate fraction of silicate and carbonate weathering contributing to the water chemistry. Secondly, Ca/Na and Mg/K ratios were calculated from analysis of the silicate fraction remaining after sequential leaching of bedload sediment. A fused bead method of sediment digestion was adapted to ensure an efficient and versatile one-time digestion of small (50mg) sample sizes. With this micro-bead method it is possible to measure major element concentrations and multiple isotopes. Samples collected from most tributaries of the Mekong River were analysed in this way for major elements, ^{87}Sr/^{86}Sr, and ε_{Nd} isotopes. The isotopes highlight the heterogeneity of lithologies in the Mekong and the need for high–resolution spatial sampling of large rivers. Ca/Na and Mg/K ratios in the silicate fraction were combined with Na^+ and K^+ concentrations in river water, corrected for rain and halite inputs, to calculate the fraction of solutes derived from weathering of silicate minerals, X_{sil}. Although the results of these two approaches positively correlate, sequential leaching of sediment gave negative values of silicate fraction contribution potentially due to methodological issues with leaching, or, an unaccounted control of water chemistry, for example the exchangeable fraction. Therefore the method used to calculate silicate mineral weathering contribution is with Ca/Na and Mg/K ratios in silicate residues.

The weathering of carbonate minerals with sulfuric acid and dissolution of gypsum contribute solutes to water chemistry (particularly Ca^{2+} and SO_4^{2-}). Importantly the oxidative pyrite–driven weathering of carbonates also has carbon implications for the climate. A new two end member mixing model was used to partition the source of sulfate between gypsum, f_{gyp}, and pyrite, f_{pyr}. The model employs $\delta^{18}O_{SO_4}$ and $\delta^{34}S_{SO_4}$ isotopes of dissolved SO_4^{2-} to characterise end members. A gypsum end member is constrained from literature data and $\delta^{18}O_{SO_4}$ of a sedimentary sulfide end member is calculated using individual sample $\delta^{18}O_{H_2O}$ values and an assumption that pyrite is oxidised mostly by iron reduction, with only 17% incorporation of atmospheric O_2 into the product sulfate. $\delta^{34}S_{SO_4}$ of the sedimentary sulfide end member is subsequently determined by the mixing model and confirmed acceptable by comparison against common literature values. The oxidative weathering of pyrite accounts for on average 57% of the sulfate flux that is delivered to the South China Sea by the Mekong river, with tributary f_{pyr} values ranging between 0.18 and 0.83.

A concern highlighted by this study is the reliability of published geological maps and their agreement with geochemical data. For example, according to geological maps (Chinese Academy of Geological Sciences, 1975) the Khorat Plateau, in Thailand, is dominated by evaporites, whilst this thesis calculates up to 71% of the SO_4^{2-} measured in the Mun, Chi and Songkhram rivers draining the Khorat Plateau is derived from oxidation of sulfides, not sedimentary sulfates. The discrepancy between geochemical data and geological maps could be due to geological maps based on poor outcrop exposure or active weathering fronts may have reached bed rock of a different lithological unit. Budgets of CO_2 consumption from models that calculate chemical weathering rates based on global geology, should be corroborated with geochemical data to verify geological map accuracy (Suchet *et al.*, 2003; Dürr *et al.*, 2005; Hartmann & Moosdorf, 2012). Moreover, these maps highlight the lithological heterogeneity of the Earth's crust, and in order to understand the impact and the controls on chemical weathering reactions occurring with particular lithologies and at particular latitudes, high frequency sampling is preferable to one spot samples of large rivers (Burke *et al.*, 2018; Gaillardet *et al.*, 1999).

A forward model to partition sources of dissolved inorganic carbon (DIC) was developed from Galy & France-Lanord (1999) and incorporates the source of acidity in weathering reactions (carbonic or sulfuric) and the use of individual Ca/Na and Mg/K ratios in silicate end members of each tributary. Cations partitioned to their source lithology and acidity reaction can be used to calculate carbon budgets of a river basin, and the dominance of particular weathering reaction pathways may also be evaluated. The sulfuric acid weathering of carbonates instantaneously releases CO_2 as gas, or carbon released is transferred as HCO_3^- to the oceans, these two pathways result in different river water chemistry. Cations are partitioned assuming the products and stoichiometry of each reaction pathway. Charge balance calculations of the partitioned cations indicate that the most likely reaction pathway of CO_2 release from sulfuric acid weathering of carbonates is instantaneous degassing.

Using a framework to track partitioned Ca^{2+} ions, CO_2 consumption or release in the Mekong basin is shown graphically (Torres *et al.*, 2016). This framework demonstrates the necessity of considering sulfuric acid weathering of silicates, which consumes acidity and provides solutes to the river.

CO_2 drawdown or release was calculated for each chemical weathering reaction occurring in the Mekong River basin and the overall short–term and long–term carbon budgets were determined for each tributary. On timescales shorter than carbonate precipitation, all Mekong tributaries are a sink of atmospheric CO_2. On million–year timescales, the headwater regions in China and one karst dominated tributary in the Middle Mekong release CO_2. A bi-monthly time–series collected from Chroy Changvar close to the Mekong mouth, between 2014-2017, is used to investigate seasonality in carbon budgets. The carbon budget of the Mekong varies throughout the year. During the monsoonal months, the Mekong consumes atmospheric CO_2 but CO_2 is released during the dry season. The total annual carbon flux is calculated from this time–series. The drawdown of atmospheric carbon by carbonic acid weathering of silicates and carbonates is 0.33 $tC.km^{-2}.yr^{-1}$, 16 times larger than the instantaneous release of carbon to the atmosphere by sulfuric acid weathering of carbonates. However carbonic acid weathering of carbonates is carbon–neutral on million–year timescales. Thus the combination of a high proportion of carbonate rocks (low X_{sil}) and 57% of sulfate delivered by pyrite oxidation results in a greater release of CO_2 from sulfuric acid weathering of carbonates, marginally offsetting the long term sequestration of atmospheric CO_2 by carbonic acid weathering of silicates (0.02 $tC.km^{-2}.yr^{-1}$). Previous estimates of Mekong carbon budgets, using historical MRC data or spot sampling, suggest the basin is a net sink (Gaillardet *et al.*, 1999; Li *et al.*, 2014a), however this study determines that the Mekong river basin is an annual net source of 0.01 $tC.km^{-2}.yr^{-1}$ to the atmosphere.

7.1 The Importance of $\delta^{18}O_{SO_4}$ in Determining Sulfate Source

Determining oxygen-isotopes in river water sulfate and the source of that oxygen is vital for quantifying the proportion of pyrite derived sulfate. The pyrite end member in the two end member mixing model is characterised using $\delta^{18}O_{SO_4}$ which can change depending on the proportion of atmospheric O_2 incorporation. Increasing the proportion of atmospheric O_2 (with a heavy $\delta^{18}O$ signature) increases f_{pyr}. Although studies determining the source of O_2 incorporated into pyrite derived sulfate have constrained the range of the atmospherically sourced O_2 to between 0% and 17%, there is no way of interpreting where river samples lie in that range using $\delta^{18}O_{SO_4}$ and $\delta^{34}S_{SO_4}$. It may be possible, with the use of Δ^{17}O, to track atmospheric O_2 (Le Gendre *et al.*, 2017; Killingsworth *et al.*, 2018; Crockford *et al.*, 2019) which would constrain the pyrite end member further and therefore more accurately calculate the proportion of sulfate derived from pyrite oxidation.

The largest error in the two-end member mixing model and in the values of f_{pyr} calculated is due to the error in $\delta^{18}O_{SO_4}$ and $\delta^{34}S_{SO_4}$ of gypsum. The range in gypsum end member projects through the water sample generating a large spread in $\delta^{34}S_{SO_4}$. Minimising errors in gypsum minimises the spread in the pyrite end member, further constraining f_{pyr} values. Besides measuring Δ^{17}O on sulfate samples to calculate atmospheric O_2 incorporation during pyrite oxidation, end member compositions could be better characterised by collecting rock samples from catchments and measuring their isotopic compositions.

Additionally, secondary processes affecting the isotopic composition of SO_4^{2-}, such as bacterial sulfate reduction, are difficult to constrain from $\delta^{18}O_{SO_4}$ and $\delta^{34}S_{SO_4}$ analysis in one sample collected from each tributary. High-resolution spatial sampling downstream in tributary catchments could provide an insight into any secondary processes occurring. For example, decreases in SO_4^{2-} concentration or progressively heavier $\delta^{18}O_{SO_4}$ and $\delta^{34}S_{SO_4}$ could indicate bacterial sulfate reduction (e.g. Turchyn *et al.*, 2013).

7.2 Assumptions on Acidity Source

An assumption is made during the partitioning of cations, about the ratio by which sulfuric acid weathers carbonate and silicate minerals. It is assumed in the forward model that sulfuric acid and carbonate acid weather silicate and carbonate minerals in equal proportions (Chapter 6). The foundation of this assumption was based on the need to consider sulfuric acid weathering of silicates in order to partition cations in F_{sulf} (proportion of acidity derived from sulfuric acid) and F_{carb} (proportion of carbonate weathering) space (Section 6.4.2.3). However, carbonic acid is a weaker acid than sulfuric so any sulfuric acid present is likely to weather available minerals before carbonic acid (Amiotte Suchet *et al.*, 1995; Guo *et al.*, 2015). Moreover, silicates are less reactive than carbonate minerals (Plummer *et al.*, 1978; White *et al.*, 1999b). Hence in a hypothetical environment where both sulfuric and carbonic acid and both carbonate silicate minerals are present, the carbonate is likely to weather first with sulfuric acid, then carbonic acid would react more slowly with silicate minerals. If this is the case, the amount of sulfuric acid weathering of carbonates in the forward model has been underestimated, which would then suggest a greater release of lithologically sourced carbon. However, if carbonate dissolution exhausts the supply of sulfuric acid weathering then only carbonic acid will weather silicate minerals, all be it at a slower rate but the reaction results in a greater sequestration of atmospheric CO_2 on long time scales. A next step with this work would be to try and quantify when the supply of sulfuric acid weathering carbonates would be exhausted and if there is any sulfuric acid left to weather silicate minerals, or indeed if there are any carbonate minerals left that would then be weathered by carbonic acid.

7.3 Future Considerations

The proportion of sulfate delivered by pyrite oxidation and hence the proportion of sulfuric acid weathering carbonate minerals has been calculated at the mouth of the Mekong using one f_{pyr} value applied to the whole year. However, there are several reasons to suggest that the $\delta^{18}O_{SO_4}$

and $\delta^{34}S_{SO_4}$ signature may vary through the year. Firstly, the proportion of solutes delivered from different areas of the basin changes over the year with the affect of multiple monsoon systems affecting different parts of the basin at different times of the year. This will contribute different amounts of solutes derived from sulfuric acid weathering of carbonates and dissolution of gypsum throughout the year to the basin-integrated signal at the mouth. Hence the main stem value of f_{pyr} may change between monsoon and dry seasons. Secondly, the product sulfate from the oxidation of pyrite via iron reduction incorporates meteoric water, of which the $\delta^{18}O_{H_2O}$ signature changes through the year as a result of temperature fractionations. The $\delta^{18}O_{SO_4}$ ratio used to model the proportion of sulfate derived from pyrite, f_{pyr}, and the pyrite end member signature could therefore change depending on season of sample collection (Killingsworth *et al.*, 2018). Considerations for any future sample collection would be to measure $\delta^{18}O_{SO_4}$ and $\delta^{34}S_{SO_4}$ in a time-series to investigate magnitude in seasonal variation.

Generally the largest sources of error in calculating solutes or CO_2 fluxes in large rivers is the error associated with discharge measurements. Discharge data on the Mekong main channel has been collected by water level gauges and old ratings curves, rather than daily aDcp measurements. Ideally, to calculate the most representative carbon budget, monthly aDcp measurements made on every tributary in the Mekong basin would be combined with the individual Ca/Na and Mg/K ratios, f_{pyr} and water chemistry values and summed to calculate an annual carbon budget. The signals from each tributary are representative and no mixing would need to be accounted for. Although this would be a costly and labour intensive undertaking.

7.4 Concluding Remarks

It is important to carefully consider the timescale in which CO_2 is released. Although previous estimates suggest that the Mekong is consuming CO_2, these have been short–term drawdown estimates, including weathering of K- and Na-silicate minerals, and carbonate mineral weathering. Whereas the long term CO_2 budget only considers the weathering of Ca- and Mg-silicate minerals with carbonic acid and the reaction of sulfuric acid with Ca- and Mg-carbonate minerals. The short–term weathering reactions in the Mekong are an atmospheric CO_2 sink, not a transient source of CO_2, despite the reaction pathway of sulfuric acid weathering of carbonates instantaneously degassing CO_2 (Torres *et al.*, 2014).

The carbon budget of large river basins containing predominantly carbonate lithology should be reassessed. A large proportion of sulfuric acid weathering in these catchments could outweigh the smaller fluxes of atmospheric CO_2 drawdown from carbonic acid weathering of silicates. Further, it is vital to understand the impact of chemical weathering reactions in global river catchments in order to predict possible enhancement of sulfuric acid weathering of carbonates as a consequence of anthropogenic release of SO_2 though the burning of fossil fuels (e.g. Li *et al.*, 2008; Li & Ji, 2016; Smith *et al.*, 2001; Xu & Liu, 2007; Yoon *et al.*, 2008).

The considerations suggested here would make a small, but important, improvement to accuracy and precision of calculating f_{pyr}. For large river basins with carbon budgets close to carbon neutral, a small improvement may make a considerable difference to which side of carbon neutral their carbon budget balances. In light of the carbon budget calculated for the Mekong by this thesis, perhaps the role of silicate weathering in modulating climate should be re-evaluated; if large river basins are in a delicate balance between CO_2 release from sulfuric acid weathering of carbonates and CO_2 drawdown from carbonic acid weathering of silicates. If large rivers are not a CO_2 sink as was previously thought, then other sources of atmospheric CO_2 removal such as organic carbon burial or carbonate precipitation associated with marine sulfate reduction must be significant (Bradbury & Turchyn, 2018; Calmels *et al.*, 2007; France-Lanord & Derry, 1997; Hilton *et al.*, 2015; Horan *et al.*, 2019).

References

Adamson, P. T., Rutherfurd, I. D., Peel, M. C., & Conlan, I. A., 2009. The Hydrology of the Mekong River, in *The Mekong*, edited by I. C. Campbell, Aquatic Ecology, chap. 4, pp. 53 – 76, Academic Press, San Diego.

Aharon, P. & Fu, B., 2000. Microbial sulfate reduction rates and sulfur and oxygen isotope fractionations at oil and gas seeps in deepwater Gulf of Mexico, *Geochimica et Cosmochimica Acta*, **64**(2), 233 – 246.

Alin, S. R., de Fátima F. L. Rasera, M., Salimon, C. I., Richey, J. E., Holtgrieve, G. W., Krusche, A. V., & Snidvongs, A., 2011. Physical controls on carbon dioxide transfer velocity and flux in low-gradient river systems and implications for regional carbon budgets, *Journal of Geophysical Research: Biogeosciences*, **116**(G1).

Allègre, C. J., 2008. *Isotope geology*, Cambridge University Press.

Amiotte Suchet, P., Probst, A., & Probst, J. L., 1995. Influence of acid rain on CO_2 consumption by rock weathering: Local and global scales, *Water, Air, and Soil Pollution*, **85**(3), 1563–1568.

Anderson, S. P., 2005. Glaciers show direct linkage between erosion rate and chemical weathering fluxes, *Geomorphology*, **67**(1–2), 147 – 157, 35th Annual Binghamton Geomorphology Symposium on Weathering and Landscape Evolution.

Asahara, Y., Takeuchi, F., Nagashima, K., Harada, N., Yamamoto, K., Oguri, K., & Tadai, O., 2012. Provenance of terrigenous detritus of the surface sediments in the Bering and Chukchi Seas as derived from Sr and Nd isotopes: Implications for recent climate change in the Arctic regions, *Deep Sea Research Part II: Topical Studies in Oceanography*, **61-64**, 155 – 171, Climate Change Dynamics of Present and Past in the North Pacific and Its Northern Marginal Seas.

Babel, M. & Schreiber, B., 2014. Geochemistry of evaporites and evolution of seawater, *Treatise on Geochemistry*, **9**, 483–560.

Balci, N., Shanks, W. C., Mayer, B., & Mandernack, K. W., 2007. Oxygen and sulfur isotope systematics of sulfate produced by bacterial and abiotic oxidation of pyrite, *Geochimica et Cosmochimica Acta*, **71**(15), 3796 – 3811.

Bao, H., 2006. Purifying barite for oxygen isotope measurement by dissolution and reprecipitation in a chelating solution, *Analytical Chemistry*, **78**(1), 304–309.

Berner, E. K. & Berner, R. A., 2012. *Global environment : water, air, and geochemical cycles*, Princeton University Press, Princeton, N.J. ; London, 2nd edn.

Berner, R. A., 1984. Sedimentary pyrite formation: An update, *Geochimica et Cosmochimica Acta*, **48**(4), 605 – 615.

Berner, R. A., 1985. Sulphate reduction, organic matter decomposition and pyrite formation, *Philosophical Transactions of the Royal Society of London A: Mathematical, Physical and Engineering Sciences*, **315**(1531), 25–38.

Berner, R. A., 1992. Weathering, plants, and the long-term carbon cycle, *Geochimica et Cosmochimica Acta*, **56**(8), 3225 – 3231.

Berner, R. A., 1999. A new look at the long-term carbon cycle, *GSA Today*, **9**(11), 1–6.

Berner, R. A., 2004. A model for calcium, magnesium and sulfate in seawater over phanerozoic time, *American Journal of Science*, **304**(5), 438–453.

Berner, R. A. & Caldeira, K., 1997. The need for mass balance and feedback in the geochemical carbon cycle, *Geology*, **25**(10), 955–956.

Berner, R. A., Lasaga, A. C., & Garrels, R. M., 1983. The carbonate-silicate geochemical cycle and its effect on atmospheric carbon dioxide over the past 100 million years, *Am. J. Sci*, **283**(7), 641–683.

Bickle, M. J., Harris, N. B. W., Bunbury, J. M., Chapman, H. J., Fairchild, I. J., & Ahmad, T., 2001. Controls on the $^{87}Sr/^{86}Sr$ ratio of carbonates in the garhwal himalaya, headwaters of the ganges, *The Journal of Geology*, **109**(6), 737–753.

Bickle, M. J., Bunbury, J., Chapman, H. J., Harris, N. B., Fairchild, I. J., & Ahmad, T., 2003. Fluxes of Sr into the headwaters of the ganges, *Geochimica et Cosmochimica Acta*, **67**(14), 2567 – 2584.

Bickle, M. J., Tipper, E., Galy, A., Chapman, H., & Harris, N., 2015. On discrimination between carbonate and silicate inputs to himalayan rivers, *American Journal of Science*, **315**(2), 120–166.

Bickle, M. J., Chapman, H. J., Tipper, E., Galy, A., Rocha, C. L. D. L., & Ahmad, T., 2018. Chemical weathering outputs from the flood plain of the ganga, *Geochimica et Cosmochimica Acta*, **225**, 146 – 175.

Blaser, P., Lippold, J., Gutjahr, M., Frank, N., Link, J. M., & Frank, M., 2016. Extracting foraminiferal seawater Nd isotope signatures from bulk deep sea sediment by chemical leaching, *Chemical Geology*, **439**, 189 – 204.

Blum, J. & Erel, Y., 2003. Radiogenic Isotopes in Weathering and Hydrology, in *Treatise on Geochemistry*, edited by H. D. Holland & K. K. Turekian, vol. 5, chap. 12, pp. 365 – 392, Pergamon, Oxford.

Blum, J. D., Gazis, C. A., Jacobson, A. D., & Page Chamberlain, C., 1998. Carbonate versus silicate weathering in the raikhot watershed within the high himalayan crystalline series, *Geology*, **26**(5), 411–414.

Bluth, G. J. & Kump, L. R., 1994. Lithologic and climatologic controls of river chemistry, *Geochimica et Cosmochimica Acta*, **58**(10), 2341 – 2359.

Borges, J. B., Huh, Y., Moon, S., & Noh, H., 2008. Provenance and weathering control on river bed sediments of the eastern tibetan plateau and the russian far east, *Chemical Geology*, **254**(1–2), 52 – 72.

Bottrell, S. H. & Tranter, M., 2002. Sulphide oxidation under partially anoxic conditions at the bed of the haut glacier d'arolla, switzerland, *Hydrological Processes*, **16**(12), 2363–2368.

Bouchez, J., Gaillardet, J., France-Lanord, C., Maurice, L., & Dutra-Maia, P., 2011. Grain size control of river suspended sediment geochemistry: Clues from Amazon River depth profiles, *Geochemistry, Geophysics, Geosystems*, **12**(3).

Bouchez, J., Lupker, M., Gaillardet, J., France-Lanord, C., & Maurice, L., 2011. How important is it to integrate riverine suspended sediment chemical composition with depth? Clues from Amazon River depth-profiles, *Geochimica et Cosmochimica Acta*, **75**(22), 6955–6970.

Bowen, G. J. & Revenaugh, J., 2003. Interpolating the isotopic composition of modern meteoric precipitation, *Water Resources Research*, **39**(10).

Bradbury, H. J. & Turchyn, A. V., 2018. Calcium isotope fractionation in sedimentary pore fluids from ODP Leg 175: Resolving carbonate recrystallization, *Geochimica et Cosmochimica Acta*, **236**, 121 – 139, Chemistry of oceans past and present: A Special Issue in tribute to Harry Elderfield.

Brantley, S., 2003. Reaction Kinetics of Primary Rock-forming Minerals under Ambient Conditions, in *Treatise on Geochemistry*, edited by H. D. Holland & K. K. Turekian, vol. 5, chap. 3, pp. 73 – 117, Pergamon, Oxford.

Brantley, S. L., Goldhaber, M. B., & Ragnarsdottir, K. V., 2007. Crossing disciplines and scales to understand the critical zone, *Elements*, **3**(5), 307–314.

Brantley, S. L., Holleran, M. E., Jin, L., & Bazilevskaya, E., 2013. Probing deep weathering in the Shale Hills Critical Zone Observatory, Pennsylvania (USA): the hypothesis of nested chemical reaction fronts in the subsurface, *Earth Surface Processes and Landforms*, **38**(11), 1280–1298.

Bravard, J.-P., Goichot, M., & Tronchère, H., 2014. An assessment of sediment-transport processes in the Lower Mekong River based on deposit grain sizes, the {CM} technique and flow-energy data, *Geomorphology*, **207**, 174 – 189.

Brenot, A., Carignan, J., France-Lanord, C., & Benoît, M., 2007. Geological and land use control on δ^{34}S and δ^{18}O of river dissolved sulfate: The Moselle river basin, France, *Chemical Geology*, **244**(1-2), 25–41.

Broecker, W., 2003. The Oceanic $CaCO_3$ Cycle, in *Treatise on Geochemistry*, edited by H. D. Holland & K. K. Turekian, pp. 529 – 549, Pergamon, Oxford.

Brookfield, M., 1998. The evolution of the great river systems of southern asia during the cenozoic india-asia collision: rivers draining southwards, *Geomorphology*, **22**(3), 285 – 312.

Burke, A., Present, T. M., Paris, G., Rae, E. C., Sandilands, B. H., Gaillardet, J., Peucker-Ehrenbrink, B., Fischer, W. W., McClelland, J. W., Spencer, R. G., Voss, B. M., & Adkins, J. F., 2018. Sulfur isotopes in rivers: Insights into global weathering budgets, pyrite oxidation, and the modern sulfur cycle, *Earth and Planetary Science Letters*, **496**, 168 – 177.

Calmels, D., Gaillardet, J., Brenot, A., & France-Lanord, C., 2007. Sustained sulfide oxidation by physical erosion processes in the Mackenzie River basin: Climatic perspectives, *Geology*, **35**(11), 1003–1006.

Cameron, E. M. & Hattori, K., 1997. Strontium and neodynium isotope ratios in the Fraser River, British Columbia: a riverine transect across the Cordilleran orogen, *Chemical geology*, **137**(3-4), 243–253.

Canfield, D. E., 2001. Biogeochemistry of sulfur isotopes, *Reviews in Mineralogy and Geochemistry*, **43**(1), 607–636.

Canfield, D. E., 2004. The evolution of the earth surface sulfur reservoir, *American Journal of Science*, **304**(10), 839–861.

Carling, P. A., 2009. The Geology of the Lower Mekong River, in *The Mekong*, edited by I. C. Campbell, Aquatic Ecology, chap. 2, pp. 13 – 28, Academic Press, San Diego.

Chakrapani, G. & Veizer, J., 2006. Source of dissolved sulphate in the Alakananda-Bhagirathi rivers in the Himalayas, *Current Science*, **90**(4), 500–503.

Chaplot, V. A. M., Rumpel, C., & Valentin, C., 2005. Water erosion impact on soil and carbon redistributions within uplands of Mekong River, *Global Biogeochemical Cycles*, **19**(4).

Chapman, H., Bickle, M., Thaw, S. H., & Thiam, H. N., 2015. Chemical fluxes from time series sampling of the irrawaddy and salween rivers, myanmar, *Chemical Geology*, **401**, 15–27.

Cheong, C.-s., Ryu, J.-S., & Jeong, Y.-J., 2013. Simultaneous multiple collector-ICP-MS measurement of Nd isotopic composition and Sm/Nd ratio in geological reference materials by interference corrections and external calibration using matrix-matched standards, *Geosciences Journal*, **17**(4), 389–395.

Chetelat, B., Liu, C.-Q., Zhao, Z., Wang, Q., Li, S., Li, J., & Wang, B., 2008. Geochemistry of the dissolved load of the Changjiang Basin rivers: Anthropogenic impacts and chemical weathering, *Geochimica et Cosmochimica Acta*, **72**(17), 4254 – 4277.

Chinese Academy of Geological Sciences, C., 1975. *Geological Map of Asia, Scale: 1:5,000,000.*, Cartographic Publishing House, Beijing.

Clark, M., Schoenbohm, L., Royden, L., Whipple, K., Burchfiel, B., Zhang, X., Tang, W., Wang, E., & Chen, L., 2004. Surface uplift, tectonics, and erosion of eastern Tibet from large-scale drainage patterns, *Tectonics*, **23**(1), TC1006 1–20.

Claypool, G. E., Holser, W. T., Kaplan, I. R., Sakai, H., & Zak, I., 1980. The age curves of sulfur and oxygen isotopes in marine sulfate and their mutual interpretation, *Chemical Geology*, **28**, 199 – 260.

Coogan, L., Daëron, M., & Gillis, K., 2019. Seafloor weathering and the oxygen isotope ratio in seawater: Insight from whole-rock δ^{18}O and carbonate δ^{18}O and $\delta47$ from the Troodos ophiolite, *Earth and Planetary Science Letters*, **508**, 41 – 50.

Coogan, L. A. & Gillis, K. M., 2013. Evidence that low-temperature oceanic hydrothermal systems play an important role in the silicate-carbonate weathering cycle and long-term climate regulation, *Geochemistry, Geophysics, Geosystems*, **14**(6), 1771–1786.

Cook, B. I., Bell, A. R., Anchukaitis, K. J., & Buckley, B. M., 2012. Snow cover and precipitation impacts on dry season streamflow in the Lower Mekong Basin, *Journal of Geophysical Research: Atmospheres*, **117**(D16).

Coplen, T. B. & Krouse, H. R., 1998. Sulphur isotope data consistency improved, *Nature*, **392**(6671), 32–32.

Coplen, T. B., Herczeg, A. L., & Barnes, C., 2000. Isotope engineering—using stable isotopes of the water molecule to solve practical problems, in *Environmental tracers in subsurface hydrology*, pp. 79–110, Springer.

Crockford, P. W., Kunzmann, M., Bekker, A., Hayles, J., Bao, H., Halverson, G. P., Peng, Y., Bui, T. H., Cox, G. M., Gibson, T. M., Wörndle, S., Rainbird, R., Lepland, A., Swanson-Hysell, N. L., Master, S., Sreenivas, B., Kuznetsov, A., Krupenik, V., & Wing, B. A., 2019. Claypool continued: Extending the isotopic record of sedimentary sulfate, *Chemical Geology*, **513**, 200 – 225.

Dai, A. & Trenberth, K. E., 2002. Estimates of freshwater discharge from continents: Latitudinal and seasonal variations, *Journal of Hydrometeorology*, **3**(6), 660–687.

Darby, S. E., Leyland, J., Kummu, M., Räsänen, T. A., & Lauri, H., 2013. Decoding the drivers of bank erosion on the Mekong river: The roles of the Asian monsoon, tropical storms, and snowmelt, *Water Resources Research*, **49**(4), 2146–2163.

Darby, S. E., Hackney, C. R., Leyland, J., Kummu, M., Lauri, H., Parsons, D. R., Best, J. L., Nicholas, A. P., & Aalto, R., 2016. Fluvial sediment supply to a mega-delta reduced by shifting tropical-cyclone activity, *Nature*, **539**(7628), 276–279.

Deer, W. A., Howie, R. A., & Zussman, J., 1992. *An introduction to the rock-forming minerals*, Longman, Harlow, Essex, England, 2nd edn.

Delgado, J. M., Apel, H., & Merz, B., 2010. Flood trends and variability in the Mekong river, *Hydrology and Earth System Sciences*, **14**(3), 407–418.

Delgado, J. M., Merz, B., & Apel, H., 2012. A climate-flood link for the lower Mekong river, *Hydrology and Earth System Sciences*, **16**(5), 1533–1541.

Dessert, C., Dupré, B., Gaillardet, J., François, L., & J. Allègre, C., 2003. Basalt weathering laws and the impact of basalt weathering on the global carbon cycle, *Chemical Geology*, **202**, 257–273.

Detmers, J., Brüchert, V., Habicht, K. S., & Kuever, J., 2001. Diversity of sulfur isotope fractionations by sulfate-reducing prokaryotes, *Applied and Environmental Microbiology*, **67**(2), 888–894.

Drever, J., 1997. *The Geochemistry of Natural Waters: Surface and Groundwater Environments*, Prentice Hall, 3rd edn.

Drever, J. I. & Zobrist, J., 1992. Chemical weathering of silicate rocks as a function of elevation in the southern Swiss Alps, *Geochimica et Cosmochimica Acta*, **56**(8), 3209 – 3216.

Dupré, B., Gaillardet, J., Rousseau, D., & Allègre, C. J., 1996. Major and trace elements of river-borne material: The congo basin, *Geochimica et Cosmochimica Acta*, **60**(8), 1301 – 1321.

Dürr, H. H., Meybeck, M., & Dürr, S. H., 2005. Lithologic composition of the Earth's continental surfaces derived from a new digital map emphasizing riverine material transfer, *Global Biogeochemical Cycles*, **19**(4).

Eastham, J., Mpelaskova, F., Mainuddin, M., Ticehurst, C., Dyce, P., & Hodgson, G., 2008. *Mekong River Basin Water Resources Assessment: Impacts of Climate Change. CSIRO Water for a Healthy Country National Research Flagship report.*, CSIRO, Canberra.

Edmond, J., Palmer, M., Measures, C., Grant, B., & Stallard, R., 1995. The fluvial geochemistry and denudation rate of the Guayana Shield in Venezuela, Colombia, and Brazil, *Geochimica et Cosmochimica Acta*, **59**(16), 3301 – 3325.

Edmond, J., Palmer, M., Measures, C., Brown, E., & Huh, Y., 1996. Fluvial geochemistry of the eastern slope of the northeastern Andes and its foredeep in the drainage of the Orinoco in Colombia and Venezuela, *Geochimica et Cosmochimica Acta*, **60**(16), 2949 – 2974.

Ellis, E. E., Keil, R. G., Ingalls, A. E., Richey, J. E., & Alin, S. R., 2012. Seasonal variability in the sources of particulate organic matter of the Mekong River as discerned by elemental and lignin analyses, *Journal of Geophysical Research: Biogeosciences*, **117**(G1).

Emberson, R., Galy, A., & Hovius, N., 2018. Weathering of reactive mineral phases in landslides acts as a source of carbon dioxide in mountain belts, *Journal of Geophysical Research: Earth Surface*, **123**(10), 2695–2713.

Fasman, J., 2016. Requiem for a river, *The Economist*.

Faure, G., 1977. *Principles of isotope geology*, John Wiley and Sons, Inc., New York, NY.

Faure, G. & Mensing, T. M., 2005. *Isotopes: principles and applications*, Wiley, 3rd edn., Rev. ed. of: Principles of isotope geology. 2nd ed. c1986.

Fenton, C. H., Charusiri, P., & Wood, S. C., 2003. Recent paleoseismic investigations in northern and western thailand, *Annals of Geophysics*, **46**(5).

France-Lanord, C. & Derry, L. A., 1997. Organic carbon burial forcing of the carbon cycle from Himalayan erosion, *Nature*, **390**(6655), 65.

Francois, L. M. & Walker, J. C., 1992. Modelling the Phanerozoic carbon cycle and climate: constraints from the ^{87}Sr/^{86}Sr isotopic ratio of seawater, *Am. J. Sci*, **292**(2), 81–135.

Fromaget, J. & Saurin, E., 1952. Carte geologique de l'indochine, Map, online, Institut Geographique National Paris.

Fu, K., He, D., & Lu, X., 2008. Sedimentation in the Manwan reservoir in the Upper Mekong and its downstream impacts, *Quaternary International*, **186**(1), 91 – 99, Larger Asian rivers and their interactions with estuaries and coasts.

Gaillardet, J. & Galy, A., 2008. Himalaya–carbon sink or source?, *Science*, **320**(5884), 1727–1728.

Gaillardet, J., Dupré, B., & Allègre, C. J., 1995. A global geochemical mass budget applied to the Congo basin rivers: Erosion rates and continental crust composition, *Geochimica et Cosmochimica Acta*, **59**(17), 3469 – 3485.

Gaillardet, J., Dupre, B., Allegre, C. J., & Négrel, P., 1997. Chemical and physical denudation in the Amazon River Basin, *Chemical Geology*, **142**(3), 141 – 173.

Gaillardet, J., Dupré, B., Louvat, P., & C.J, A., 1999. Global silicate weathering and CO_2 consumption rates deduced from the chemistry of large rivers, *Chemical Geology*, **159**(1–4), 3 – 30.

Gaillardet, J., Viers, J., & Dupré, B., 2003. Trace Elements in River Waters, in *Treatise on Geochemistry*, edited by H. D. Holland & K. K. Turekian, vol. 5, chap. 9, pp. 225 – 272, Pergamon, Oxford.

Galy, A. & France-Lanord, C., 1999. Weathering processes in the Ganges–Brahmaputra basin and the riverine alkalinity budget, *Chemical Geology*, **159**(1), 31–60.

Galy, A. & France-Lanord, C., 2001. Higher erosion rates in the Himalaya: Geochemical constraints on riverine fluxes, *Geology*, **29**(1), 23–26.

Galy, A., France-Lanord, C., & Derry, L. A., 1999. The strontium isotopic budget of Himalayan rivers in Nepal and Bangladesh, *Geochimica et Cosmochimica Acta*, **63**(13–14), 1905 – 1925.

Garrels, R. M. & Mackenzie, F. T., 1967. *Origin of chemical compositions of some springs and lakes.*, vol. 67, chap. 10, pp. 222–242, American Chemical Society.

Gazulla, M. F., Barba, A., Orduña, M., & Rodrigo, M., 2008. Bead-releasing agents used in the preparation of solid samples as beads for WD-XRF measurement, *X-Ray Spectrometry*, **37**(6), 603–607.

Gislason, S., Arnorsson, S., & Ármannsson, H., 1996. Chemical weathering of basalt in southwest iceland: Effects of runoff, age of rocks and vegetative/glacial cover, *American Journal of Science*, **296**, 837–907.

Gislason, S. R., Oelkers, E. H., Eiriksdottir, E. S., Kardjilov, M. I., Gisladottir, G., Sigfusson, B., Snorrason, A., Elefsen, S., Hardardottir, J., Torssander, P., & Oskarsson, N., 2009. Direct evidence of the feedback between climate and weathering, *Earth and Planetary Science Letters*, **277**(1–2), 213 – 222.

Goddéris, Y. & François, L., 1995. The Cenozoic evolution of the strontium and carbon cycles: relative importance of continental erosion and mantle exchanges, *Chemical Geology*, **126**(2), 169 – 190, The Mantle-Ocean connection.

Goldhaber, M., 2003. Sulfur-rich sediments, *Treatise on Geochemistry*, **7**, 257–282.

Goldstein, S. J. & Jacobsen, S. B., 1987. The Nd and Sr isotopic systematics of river-water dissolved material: Implications for the sources of Nd and Sr in seawater, *Chemical Geology: Isotope Geoscience section*, **66**(3), 245 – 272.

Goldstein, S. J. & Jacobsen, S. B., 1988. Nd and Sr isotopic systematics of river water suspended material: implications for crustal evolution, *Earth and Planetary Science Letters*, **87**(3), 249 – 265.

Guo, J., Wang, F., Vogt, R. D., Zhang, Y., & Liu, C.-Q., 2015. Anthropogenically enhanced chemical weathering and carbon evasion in the yangtze basin, *Scientific Reports*, **5**.

Gupta, A., 2007. *The Mekong River: Morphology, Evolution, Management*, chap. 2, pp. 7–28, John Wiley & Sons, Chichester, UK.

Gupta, A., 2009. Geology and Landforms of the Mekong Basin, in *The Mekong*, edited by I. C. Campbell, Aquatic Ecology, chap. 3, pp. 29 – 51, Academic Press, San Diego.

Gupta, A. & Liew, S., 2007. The mekong from satellite imagery: A quick look at a large river, *Geomorphology*, **85**(3–4), 259 – 274, Monsoon Rivers of Asia.

Gupta, A., Hock, L., Xiaojing, H., & Ping, C., 2002. Evaluation of part of the Mekong River using satellite imagery, *Geomorphology*, **44**(3–4), 221 – 239, Geomorphology on Large Rivers.

Hallet, B. & Molnar, P., 2001. Distorted drainage basins as markers of crustal strain east of the Himalaya, *Journal of Geophysical Research: Solid Earth*, **106**(B7), 13697–13709.

Hansen, B. T., Wemmer, K., Eckhardt, M., Putthapiban, P., & Assavapatchara, S., 2016. Isotope Dating of the Potash and Rock Salt Deposit at Bamnet Narong, NE-Thailand, *Open Journal of Geology*, **6**(08), 875–894.

Harris, N., 2006. The elevation history of the Tibetan Plateau and its implications for the Asian monsoon, *Palaeogeography, Palaeoclimatology, Palaeoecology*, **241**(1), 4 – 15, Monsoon and Tectonics of AsiaIGCP 476, Monsoons and Tectonics.

Hartmann, J. & Moosdorf, N., 2012. The new global lithological map database GLiM: A representation of rock properties at the Earth surface, *Geochemistry, Geophysics, Geosystems*, **13**(12).

Heidel, C. & Tichomirowa, M., 2011. The isotopic composition of sulfate from anaerobic and low oxygen pyrite oxidation experiments with ferric iron — new insights into oxidation mechanisms, *Chemical Geology*, **281**(3), 305 – 316.

Henck, A. C., Huntington, K. W., Stone, J. O., Montgomery, D. R., & Hallet, B., 2011. Spatial controls on erosion in the Three Rivers Region, southeastern Tibet and southwestern China, *Earth and Planetary Science Letters*, **303**(1–2), 71 – 83.

Hess, J., Bender, M. L., & Schilling, J.-G., 1986. Evolution of the Ratio of Strontium-87 to Strontium-86 in Seawater from Cretaceous to Present, *Science*, **231**(4741), 979–984.

Hilton, R. G., Galy, V., Gaillardet, J., Dellinger, M., Bryant, C., O'Regan, M., Grocke, D. R., Coxall, H., Bouchez, J., & Calmels, D., 2015. Erosion of organic carbon in the arctic as a geological carbon dioxide sink, *Nature*, **524**(7563), 84–87.

Hindshaw, R., Tosca, N., Piotrowski, A., & Tipper, E., 2018. Clay mineralogy, strontium and neodymium isotope ratios in the sediments of two High Arctic catchments (Svalbard), *Earth Surface Dynamics Discussions*, **6**, 141–161.

Hindshaw, R. S., Heaton, T. H., Boyd, E. S., Lindsay, M. R., & Tipper, E. T., 2016. Influence of glaciation on mechanisms of mineral weathering in two high Arctic catchments, *Chemical Geology*, **420**, 37 – 50.

Hite, R. J. & Japakasetr, T., 1979. Potash deposits of the Khorat plateau, Thailand and Laos, *Economic Geology*, **74**(2), 448–458.

Horan, K., Hilton, R. G., Dellinger, M., Tipper, E., Galy, V., Calmels, D., Selby, D., Gaillardet, J., Ottley, C. J., Parsons, D. R., & Burton, K. W., 2019. Carbon dioxide emissions by rock organic carbon oxidation and the net geochemical carbon budget of the Mackenzie River Basin, *American Journal of Science*, **319**(6), 473–499.

Hren, M. T., Chamberlain, C. P., Hilley, G. E., Blisniuk, P. M., & Bookhagen, B., 2007. Major ion chemistry of the Yarlung Tsangpo–Brahmaputra river: Chemical weathering, erosion, and CO_2 consumption in the southern Tibetan plateau and eastern syntaxis of the Himalaya, *Geochimica et Cosmochimica Acta*, **71**(12), 2907 – 2935.

IAEA, 2019. Global Network of Isotopes in Precipitation. the GNIP Database., Tech. rep., World Meteorological Organization.

Jacobsen, S. B. & Wasserburg, G., 1980. Sm-Nd isotopic evolution of chondrites, *Earth and Planetary Science Letters*, **50**(1), 139 – 155.

Jiang, H., Li, W.-Q., Jiang, S.-Y., Wang, H., & Wei, X.-P., 2017. Geochronological, geochemical and Sr-Nd-Hf isotopic constraints on the petrogenesis of Late Cretaceous A-type granites from the Sibumasu Block, Southern Myanmar, SE Asia, *Lithos*, **268-271**, 32 – 47.

Jin, L., Ravella, R., Ketchum, B., Bierman, P. R., Heaney, P., White, T., & Brantley, S. L., 2010. Mineral weathering and elemental transport during hillslope evolution at the Susquehanna/Shale Hills Critical Zone Observatory, *Geochimica et Cosmochimica Acta*, **74**(13), 3669 – 3691.

Jochum, K. P., Nohl, U., Herwig, K., Lammel, E., Stoll, B., & Hofmann, A. W., 2005. GeoRem: A New Geochemical Database for Reference Materials and Isotopic Standards, *Geostandards and Geoanalytical Research*, **29**(3), 333–338.

Kabeya, N., Kubota, T., Shimizu, A., Nobuhiro, T., Tsuboyama, Y., Chann, S., & Tith, N., 2008. Isotopic investigation of river water mixing around the confluence of the tonle sap and mekong rivers, *Hydrological processes*, **22**(9), 1351–1358.

Kampschulte, A. & Strauss, H., 2004. The sulfur isotopic evolution of Phanerozoic seawater based on the analysis of structurally substituted sulfate in carbonates, *Chemical Geology*, **204**(3-4), 255–286.

Kaplan, I. R. & Rittenberg, S. C., 1964. Microbiological fractionation of sulphur isotopes, *Microbiology*, **34**(2), 195–212.

Karim, A. & Veizer, J., 2000. Weathering processes in the Indus River Basin: implications from riverine carbon, sulfur, oxygen, and strontium isotopes, *Chemical Geology*, **170**(1–4), 153 – 177.

Karl, T. R. & Trenberth, K. E., 2003. Modern Global Climate Change, *Science*, **302**(5651), 1719–1723.

Kasting, J. F., 1987. Theoretical constraints on oxygen and carbon dioxide concentrations in the Precambrian atmosphere, *Precambrian Research*, **34**(3), 205 – 229.

Keith, M. & Weber, J., 1964. Carbon and oxygen isotopic composition of selected limestones and fossils, *Geochimica et Cosmochimica Acta*, **28**(10), 1787 – 1816.

Kendall, C. & Doctor, D., 2003. Stable Isotope Applications in Hydrologic Studies, in *Treatise on Geochemistry*, edited by H. D. Holland & K. K. Turekian, pp. 319 – 364, Pergamon, Oxford.

Kiernan, K., 2015. Karst geomorphology along the Nam Ou, northern Lao PDR, *Cave and Karst Science*, **42**(2), 86–94.

Killingsworth, B. A., Bao, H., & Kohl, I. E., 2018. Assessing Pyrite-Derived Sulfate in the Mississippi River with Four Years of Sulfur and Triple-Oxygen Isotope Data, *Environmental Science & Technology*, **52**(11), 6126–6136, PMID: 29745225.

Kondolf, G. M., Rubin, Z. K., & Minear, J. T., 2014. Dams on the Mekong: Cumulative sediment starvation, *Water Resources Research*, **50**(6), 5158–5169.

Krishnaswami, S. & Singh, S. K., 1998. Silicate and carbonate weathering in the drainage basins of the Ganga-Ghaghara-Indus head waters: Contributions to major ion and Sr isotope geochemistry, *Proceedings of the Indian Academy of Sciences - Earth and Planetary Sciences*, **107**(4), 283–291.

Krishnaswami, S. & Singh, S. K., 2005. Chemical weathering in the river basins of the Himalaya, India, *Current science*, **89**(5), 841–849.

Kroopnick, P. & Craig, H., 1972. Atmospheric Oxygen: Isotopic Composition and Solubility Fractionation, *Science*, **175**(4017), 54–55.

Krouse, H., Gould, W., McCready, R., & Rajan, S., 1991. ^{18}O incorporation into sulphate during the bacterial oxidation of sulphide minerals and the potential for oxygen isotope exchange between O_2, H_2O and oxidized sulphur intermediates, *Earth and Planetary Science Letters*, **107**(1), 90 – 94.

Krouse, H. R. & Mayer, B., 2000. Sulphur and oxygen isotopes in sulphate, in *Environmental tracers in subsurface hydrology*, pp. 195–231, Springer.

Kummu, M. & Sarkkula, J., 2008. Impact of the Mekong River Flow Alteration on the Tonle Sap Flood Pulse, *AMBIO: A Journal of the Human Environment*, **37**(3), 185–192.

Kummu, M. & Varis, O., 2007. Sediment-related impacts due to upstream reservoir trapping, the Lower Mekong River, *Geomorphology*, **85**(3–4), 275 – 293, Monsoon Rivers of Asia.

Kummu, M., Lu, X., Wang, J., & Varis, O., 2010. Basin-wide sediment trapping efficiency of emerging reservoirs along the Mekong, *Geomorphology*, **119**(3–4), 181 – 197.

Kump, L. R., Brantley, S. L., & Arthur, M. A., 2000. Chemical Weathering, Atmospheric CO_2, and Climate, *Annual Review of Earth and Planetary Sciences*, **28**(1), 611–667.

Kuroda, J., Hara, H., Ueno, K., Charoentitirat, T., Maruoka, T., Miyazaki, T., Miyahigashi, A., & Lugli, S., 2017. Characterization of sulfate mineral deposits in central Thailand, *Island Arc*, **26**(2).

Kurtz, A. C., Kump, L. R., Arthur, M. A., Zachos, J. C., & Paytan, A., 2003. Early Cenozoic decoupling of the global carbon and sulfur cycles, *Paleoceanography*, **18**(4).

Lacan, F., Tachikawa, K., & Jeandel, C., 2012. Neodymium isotopic composition of the oceans: A compilation of seawater data, *Chemical Geology*, **300-301**, 177 – 184.

Lang, K. A., Huntington, K. W., Burmester, R., & Housen, B., 2016. Rapid exhumation of the eastern Himalayan syntaxis since the late Miocene, *Bulletin*, **128**(9-10), 1403–1422.

Le Gendre, E., Martin, E., Villemant, B., Cartigny, P., & Assayag, N., 2017. A simple and reliable anion-exchange resin method for sulfate extraction and purification suitable for multiple O- and S-isotope measurements, *Rapid Communications in Mass Spectrometry*, **31**(1), 137–144, RCM-16-0287.R1.

Lee, J.-E., Fung, I., DePaolo, D. J., & Henning, C. C., 2007. Analysis of the global distribution of water isotopes using the NCAR atmospheric general circulation model, *Journal of Geophysical Research: Atmospheres*, **112**(D16).

Leloup, P. H., Lacassin, R., Tapponnier, P., Schärer, U., Zhong, D., Liu, X., Zhang, L., Ji, S., & Trinh, P. T., 1995. The Ailao Shan-Red River shear zone (Yunnan, China), Tertiary transform boundary of Indochina, *Tectonophysics*, **251**(1), 3 – 84, Southeast Asia Structure and Tectonics.

Lenton, T. M. & Britton, C., 2006. Enhanced carbonate and silicate weathering accelerates recovery from fossil fuel CO_2 perturbations, *Global Biogeochemical Cycles*, **20**(3).

Li, C. & Ji, H., 2016. Chemical weathering and the role of sulfuric and nitric acids in carbonate weathering: Isotopes (^{13}C, ^{15}N, ^{34}S, and ^{18}O) and chemical constraints, *Journal of Geophysical Research: Biogeosciences*, **121**(5), 1288–1305.

Li, G., Hartmann, J., Derry, L. A., West, A. J., You, C.-F., Long, X., Zhan, T., Li, L., Li, G., Qiu, W., Li, T., Liu, L., Chen, Y., Ji, J., Zhao, L., & Chen, J., 2016. Temperature dependence of basalt weathering, *Earth and Planetary Science Letters*, **443**, 59 – 69.

Li, S., Lu, X., & Bush, R. T., 2013. CO_2 partial pressure and CO_2 emission in the Lower Mekong River, *Journal of Hydrology*, **504**, 40 – 56.

Li, S., Lu, X., & Bush, R. T., 2014. Chemical weathering and CO_2 consumption in the Lower Mekong River, *Science of The Total Environment*, **472**, 162 – 177.

Li, S.-L., Calmels, D., Han, G., Gaillardet, J., & Liu, C.-Q., 2008. Sulfuric acid as an agent of carbonate weathering constrained by δ^{13}CDIC: Examples from Southwest China, *Earth and Planetary Science Letters*, **270**(3–4), 189 – 199.

Li, S.-L., Chetelat, B., Yue, F., Zhao, Z., & Liu, C.-Q., 2014. Chemical weathering processes in the Yalong River draining the eastern Tibetan Plateau, China, *Journal of Asian Earth Sciences*, **88**, 74 – 84.

Li, X., Gan, Y., Zhou, A., & Liu, Y., 2015. Relationship between water discharge and sulfate sources of the Yangtze River inferred from seasonal variations of sulfur and oxygen isotopic compositions, *Journal of Geochemical Exploration*, **153**, 30 – 39.

Li, X.-D., Masuda, H., Kusakabe, M., Yanagisawa, F., & Zeng, H.-A., 2006. Degradation of groundwater quality due to anthropogenic sulfur and nitrogen contamination in the Sichuan Basin, China, *GEOCHEMICAL JOURNAL*, **40**(4), 309–332.

Liu, C.-Q., Zhao, Z.-Q., Wang, Q., & Gao, B., 2011. Isotope compositions of dissolved lithium in the rivers Jinshajiang, Lancangjiang, and Nujiang: Implications for weathering in Qinghai-Tibet Plateau, *Applied Geochemistry*, **26**, S357 – S359, Ninth International Symposium on the Geochemistry of the Earth's Surface (GES-9).

Liu, J., Li, S., Zhong, J., Zhu, X., Guo, Q., Lang, Y., & Han, X., 2017. Sulfate sources constrained by sulfur and oxygen isotopic compositions in the upper reaches of the Xijiang River, China, *Acta Geochimica*, **36**(4), 611–618.

Lloyd, R., 1968. Oxygen isotope behavior in the sulfate-water system, *Journal of Geophysical Research*, **73**(18), 6099–6110.

Louvat, P. & Allègre, C. J., 1997. Present denudation rates on the island of Réunion determined by river geochemistry: Basalt weathering and mass budget between chemical and mechanical erosions, *Geochimica et Cosmochimica Acta*, **61**(17), 3645 – 3669.

Louvat, P. & Allègre, C. J., 1998. Riverine erosion rates on Sao Miguel volcanic island, Azores archipelago, *Chemical Geology*, **148**(3), 177 – 200.

Lu, X. X. & Siew, R. Y., 2006. Water discharge and sediment flux changes over the past decades in the Lower Mekong River: possible impacts of the Chinese dams, *Hydrology and Earth System Sciences*, **10**(2), 181–195.

Lupker, M., France-Lanord, C., Lavé, J., Bouchez, J., Galy, V., Métivier, F., Gaillardet, J., Lartiges, B., & Mugnier, J.-L., 2011. A Rouse-based method to integrate the chemical composition of river sediments: Application to the Ganga basin, *Journal of Geophysical Research: Earth Surface*, **116**.

Lupker, M., France-Lanord, C., & Lartiges, B., 2016. Impact of sediment–seawater cation exchange on Himalayan chemical weathering fluxes, *Earth Surface Dynamics*, **4**(3), 675–684.

Luther, G. W., 1987. Pyrite oxidation and reduction: Molecular orbital theory considerations, *Geochimica et Cosmochimica Acta*, **51**(12), 3193 – 3199.

Mackenzie, F. T. & Garrels, R. M., 1966. Chemical mass balance between rivers and oceans, *American Journal of Science*, **264**(7), 507–525.

Mackenzie, F. T. & Kump, L. R., 1995. Reverse Weathering, Clay Mineral Formation, and Oceanic Element Cycles, *Science*, **270**(5236), 586–586.

Maher, K. & Chamberlain, C. P., 2014. Hydrologic regulation of chemical weathering and the geologic carbon cycle, *Science*, **343**(6178), 1502–1504.

Manaka, T., Otani, S., Inamura, A., Suzuki, A., Aung, T., Roachanakanan, R., Ishiwa, T., & Kawahata, H., 2015. Chemical weathering and long-termCO_2 consumption in the Ayeyarwady and Mekong river basins in the Himalayas, *Journal of Geophysical Research: Biogeosciences*, **120**(6), 1165–1175.

Mandernack, K. W., Krouse, H., & Skei, J. M., 2003. A stable sulfur and oxygen isotopic investigation of sulfur cycling in an anoxic marine basin, Framvaren Fjord, Norway, *Chemical Geology*, **195**(1), 181 – 200, Isotopic records of microbially mediated processes.

Mazumdar, A., Goldberg, T., & Strauss, H., 2008. Abiotic oxidation of pyrite by Fe(III) in acidic media and its implications for sulfur isotope measurements of lattice-bound sulfate in sediments, *Chemical Geology*, **253**(1), 30 – 37.

Mekong River Commission, M., 2005. *Overview of the Hydrology of the Mekong Basin*, Mekong River Commission, Vientiane.

Mekong River Commission, M., 2016. MRC Master Catalogue Search.

Meybeck, M., 1987. Global chemical weathering of surficial rocks estimated from river dissolved loads., *American Journal of Science*, **287**(5), 401–428, cited By 522.

Meybeck, M., 1998. Man and river interface: multiple impacts on water and particulates chemistry illustrated in the Seine river basin, *Hydrobiologia*, **373**(0), 1–20.

Michalopoulos, P. & Aller, R. C., 1995. Rapid Clay Mineral Formation in Amazon Delta Sediments: Reverse Weathering and Oceanic Elemental Cycles, *Science*, **270**(5236), 614–617.

Milliman, J. & Meade, R., 1983. World-wide delivery of sediment to the oceans., *Journal of Geology*, **91**(1), 1–21, cited By 1736.

Milliman, J. D. & Farnsworth, K. L., 2011. *River discharge to the coastal ocean: a global synthesis*, Cambridge University Press.

Millot, R., Gaillardet, J., Dupré, B., & Allègre, C. J., 2002. The global control of silicate weathering rates and the coupling with physical erosion: new insights from rivers of the Canadian Shield, *Earth and Planetary Science Letters*, **196**(1–2), 83 – 98.

Millot, R., Gaillardet, J., Dupré, B., & Allègre, C. J., 2003. Northern latitude chemical weathering rates: clues from the Mackenzie River Basin, Canada, *Geochimica et Cosmochimica Acta*, **67**(7), 1305 – 1329.

Moon, S., Huh, Y., Qin, J., & van Pho, N., 2007. Chemical weathering in the Hong (Red) River basin: Rates of silicate weathering and their controlling factors, *Geochimica et Cosmochimica Acta*, **71**(6), 1411 – 1430.

Moon, S., Chamberlain, C., & Hilley, G., 2014. New estimates of silicate weathering rates and their uncertainties in global rivers, *Geochimica et Cosmochimica Acta*, **134**, 257 – 274.

Mortatti, J. & Probst, J.-L., 2003. Silicate rock weathering and atmospheric/soil CO_2 uptake in the Amazon basin estimated from river water geochemistry: seasonal and spatial variations, *Chemical Geology*, **197**(1), 177 – 196.

Moses, C. O. & Herman, J. S., 1991. Pyrite oxidation at circumneutral pH, *Geochimica et Cosmochimica Acta*, **55**(2), 471 – 482.

Moses, C. O., Nordstrom, D. K., Herman, J. S., & Mills, A. L., 1987. Aqueous pyrite oxidation by dissolved oxygen and by ferric iron, *Geochimica et Cosmochimica Acta*, **51**(6), 1561 – 1571.

Négrel, P., Allègre, C. J., Dupré, B., & Lewin, E., 1993. Erosion sources determined by inversion of major and trace element ratios and strontium isotopic ratios in river water: The Congo Basin case, *Earth and Planetary Science Letters*, **120**(1), 59 – 76.

Négrel, P., Grosbois, C., & Kloppmann, W., 2000. The labile fraction of suspended matter in the Loire River (France): multi-element chemistry and isotopic (Rb–Sr and C–O) systematics, *Chemical Geology*, **166**(3), 271 – 285.

Nippon Koei, C. L., 2001. Master plan study on integrated agricultural development in Lao Peoples Democratic Republic, Tech. rep., Japan International Cooperation Agency.

Noh, H., Huh, Y., Qin, J., & Ellis, A., 2009. Chemical weathering in the Three Rivers region of Eastern Tibet, *Geochimica et Cosmochimica Acta*, **73**(7), 1857 – 1877.

Oliva, P., Viers, J., Dupré, B., Fortuné, J. P., Martin, F., Braun, J. J., Nahon, D., & Robain, H., 1999. The effect of organic matter on chemical weathering: study of a small tropical watershed: nsimi-zoétélé site, cameroon, *Geochimica et Cosmochimica Acta*, **63**(23), 4013 – 4035.

Oliva, P., Viers, J., & Dupré, B., 2003. Chemical weathering in granitic environments, *Chemical Geology*, **202**(3), 225 – 256, Controls on Chemical Weathering.

Ou, C. & Winemiller, K. O., 2016. Seasonal hydrology shifts production sources supporting fishes in rivers of the Lower Mekong Basin, *Canadian Journal of Fisheries and Aquatic Sciences*, **73**, 1–21.

Padoan, M., Garzanti, E., Harlavan, Y., & Villa, I. M., 2011. Tracing Nile sediment sources by Sr and Nd isotope signatures (Uganda, Ethiopia, Sudan), *Geochimica et Cosmochimica Acta*, **75**(12), 3627–3644.

Palmer, M. & Edmond, J., 1989. The strontium isotope budget of the modern ocean, *Earth and Planetary Science Letters*, **92**(1), 11 – 26.

Paris, G., Sessions, A. L., Subhas, A. V., & Adkins, J. F., 2013. MC-ICP-MS measurement of δ^{34}S and δ^{33}S in small amounts of dissolved sulfate, *Chemical Geology*, **345**, 50 – 61.

Parsons, D. R., Jackson, P. R., Czuba, J. A., Engel, F. L., Rhoads, B. L., Oberg, K. A., Best, J. L., Mueller, D. S., Johnson, K. K., & Riley, J. D., 2013. Velocity Mapping Toolbox (VMT): a processing and visualization suite for moving-vessel ADCP measurements, *Earth Surface Processes and Landforms*, **38**(11), 1244–1260.

Pawellek, F., Frauenstein, F., & Veizer, J., 2002. Hydrochemistry and isotope geochemistry of the upper Danube River, *Geochimica et Cosmochimica Acta*, **66**(21), 3839 – 3853.

Peel, M. C., Finlayson, B. L., & Mcmahon, T. A., 2007. Updated world map of the Köppen-Geiger climate classification, *Hydrology and Earth System Sciences Discussions*, **4**(2), 439–473.

Peucker-Ehrenbrink, B., Miller, M. W., Arsouze, T., & Jeandel, C., 2010. Continental bedrock and riverine fluxes of strontium and neodymium isotopes to the oceans, *Geochemistry, Geophysics, Geosystems*, **11**(3).

Picouet, C., Dupré, B., Orange, D., & Valladon, M., 2002. Major and trace element geochemistry in the upper Niger river (Mali): physical and chemical weathering rates and CO_2 consumption, *Chemical Geology*, **185**(1), 93 – 124.

Piotrowski, A. M., Banakar, V. K., Scrivner, A. E., Elderfield, H., Galy, A., & Dennis, A., 2009. Indian Ocean circulation and productivity during the last glacial cycle, *Earth and Planetary Science Letters*, **285**(1), 179 – 189.

Pisutha-Arnond, V., Chiba, H., & Yumuang, S., 1986. A preliminary sulphur and oxygen isotope study of the Maha Sarakham evaporitic anhydrite from the Bamnet narong area of northeastern Thailand, *Geological Society of Malaysia*, **1**(19), 209–222.

Plummer, L. N., Wigley, T. M. L., & Parkhurst, D. L., 1978. The kinetics of calcite dissolution in CO_2 -water systems at 5 degrees to 60 degreesC and 0.0 to 1.0 atm CO_2, *American Journal of Science*, **278**(2), 179–216.

Ponta, G. M. & Aharon, P., 2014. Karst geology and isotope hydrology of the upstream section of Nam Hinboun River, Khammouan Province (Central Laos), *Carbonates and Evaporites*, **29**(1), 127–139.

Price, J. R., Heitmann, N., Hull, J., & Szymanski, D., 2008. Long-term average mineral weathering rates from watershed geochemical mass balance methods: Using mineral modal abundances to solve more equations in more unknowns, *Chemical Geology*, **254**(1), 36 – 51.

Probst, A., Viville, D., Fritz, B., Ambroise, B., & Dambrine, E., 1992. Hydrochemical budgets of a small forested granitic catchment exposed to acid deposition: The strengbach catchment case study (Vosges massif, France), *Water, Air, & Soil Pollution*, **62**(3), 337–347.

Quade, J., English, N., & DeCelles, P. G., 2003. Silicate versus carbonate weathering in the Himalaya: a comparison of the Arun and Seti River watersheds, *Chemical Geology*, **202**(3), 275 – 296, Controls on Chemical Weathering.

Raczek, I., Jochum, K. P., & Hofmann, A. W., 2003. Neodymium and Strontium Isotope Data for USGS Reference Materials BCR-1, BCR-2, BHVO-1, BHVO-2, AGV-1, AGV-2, GSP-1, GSP-2 and Eight MPI-DING Reference Glasses, *Geostandards Newsletter*, **27**(2), 173–179.

Rai, S. K. & Singh, S. K., 2007. Temporal variation in Sr and $^{87}Sr/^{86}Sr$ of the Brahmaputra: Implications for annual fluxes and tracking flash floods through chemical and isotope composition, *Geochemistry, Geophysics, Geosystems*, **8**(8).

Raymo, M. E., 1991. Geochemical evidence supporting TC Chamberlin's theory of glaciation, *Geology*, **19**(4), 344–347.

Raymo, M. E. & Ruddiman, W. F., 1992. Tectonic forcing of late Cenozoic climate, *Nature*, **359**, 117 EP –.

Raymo, M. E., Ruddiman, W. F., & Froelich, P. N., 1988. Influence of late Cenozoic mountain building on ocean geochemical cycles, *Geology*, **16**(7), 649–653.

Rees, C., Jenkins, W., & Monster, J., 1978. The sulphur isotopic composition of ocean water sulphate, *Geochimica et Cosmochimica Acta*, **42**(4), 377 – 381.

Rimstidt, J. & Vaughan, D. J., 2003. Pyrite oxidation: a state-of-the-art assessment of the reaction mechanism, *Geochimica et Cosmochimica Acta*, **67**(5), 873 – 880, Advances in Oxide and Sulfide Mineral Surface Chemistry.

Robinson, B. W. & Bottrell, S. H., 1997. Discrimination of sulfur sources in pristine and polluted New Zealand river catchments using stable isotopes, *Applied Geochemistry*, **12**(3), 305 – 319.

Rock, L. & Mayer, B., 2009. Identifying the influence of geology, land use, and anthropogenic activities on riverine sulfate on a watershed scale by combining hydrometric, chemical and isotopic approaches, *Chemical Geology*, **262**(3), 121 – 130.

Rudnick, R. L. & Gao, S., 2003. Composition of the continental crust, *Treatise on geochemistry*, **3**, 659.

Saji, N. S., Wielandt, D., Paton, C., & Bizzarro, M., 2016. Ultra-high-precision Nd-isotope measurements of geological materials by MC-ICPMS., *J Anal At Spectrom*, **31**(7), 1490–1504.

Schippers, A., Jozsa, P., & Sand, W., 1996. Sulfur chemistry in bacterial leaching of pyrite., *Applied and Environmental Microbiology*, **62**(9), 3424–3431.

Shima, M., Gross, W., & Thode, H., 1963. Sulfur isotope abundances in basic sills, differentiated granites, and meteorites, *Journal of Geophysical Research*, **68**(9), 2835–2847.

Shrestha, B., Babel, M., Maskey, S., Van Griensven, A., Uhlenbrook, S., Green, A., & Akkharath, I., 2013. Impact of climate change on sediment yield in the Mekong River basin: a case study of the Nam Ou basin, Lao PDR, *Hydrology and Earth System Sciences*, **17**(1), 1.

Singer, P. C. & Stumm, W., 1970. Acidic Mine Drainage: The Rate-Determining Step, *Science*, **167**(3921), 1121–1123.

Singh, S. K. & France-Lanord, C., 2002. Tracing the distribution of erosion in the Brahmaputra watershed from isotopic compositions of stream sediments, *Earth and Planetary Science Letters*, **202**(3), 645 – 662.

Singh, S. K., Sarin, M., & France-Lanord, C., 2005. Chemical erosion in the eastern Himalaya: Major ion composition of the Brahmaputra and δ^{13}C of dissolved inorganic carbon, *Geochimica et Cosmochimica Acta*, **69**(14), 3573 – 3588.

Smith, S. J., Pitcher, H., & Wigley, T., 2001. Global and regional anthropogenic sulfur dioxide emissions, *Global and Planetary Change*, **29**(1), 99 – 119.

Sohn, R., 2013. A method for inverting ratio–ratio data to estimate end-member compositions in mixing problems, *Chemical Geology*, **352**, 63 – 69.

Someth, P., Chanthy, S., Pen, C., Sean, P., & Hang, L., 2013. Basin Profile of the Lower Sekong, Sesan and Spreok (3S) Rivers in Cambodia., in *Project report: Challenge Program on Water and Food Mekong project MK3 'Optimizing the management of a cascade of reservoirs at the catchment level'*, ICEM – International Centre for Environmental Management, Hanoi Vietnam, 2013.

Spence, J. & Telmer, K., 2005. The role of sulfur in chemical weathering and atmospheric CO_2 fluxes: Evidence from major ions, δ^{13}CDIC, and δ^{34}S in rivers of the Canadian Cordillera, *Geochimica et Cosmochimica Acta*, **69**(23), 5441 – 5458.

Stallard, R. F. & Edmond, J. M., 1983. Geochemistry of the Amazon: 2. the influence of geology and weathering environment on the dissolved load, *Journal of Geophysical Research: Oceans*, **88**, 9671–9688.

Stone, R., 2016. Dam-building threatens Mekong fisheries, *Science*, **354**(6316), 1084–1085.

Strauss, H., 1997. The isotopic composition of sedimentary sulfur through time, *Palaeogeography, Palaeoclimatology, Palaeoecology*, **132**(1), 97 – 118.

Stumm, W. & Morgan, J., 1996. *Aquatic chemistry: chemical equilibria and rates in natural waters*, Environmental science and technology, Wiley-Interscience, 3rd edn.

Suchet, P. A., Probst, J., & Ludwig, W., 2003. Worldwide distribution of continental rock lithology: Implications for the atmospheric/soil CO_2 uptake by continental weathering and alkalinity river transport to the oceans, *Global Biogeochemical Cycles*, **17**(2).

Sundquist, E. & Visser, K., 2003. The Geologic History of the Carbon Cycle, in *Treatise on Geochemistry*, edited by H. D. Holland & K. K. Turekian, vol. 8, chap. 9, pp. 425 – 472, Pergamon, Oxford.

Sundquist, E. T., 1991. Steady- and non-steady-state carbonate-silicate controls on atmospheric CO_2, *Quaternary Science Reviews*, **10**(2), 283 – 296.

Tabakh, M. E., Schreiber, B. C., Utha-Aroon, C., Coshell, L., & Warren, J. K., 1998. Diagenetic origin of basal anhydrite in the Cretaceous Maha Sarakham salt: Khorat Plateau, NE Thailand, *Sedimentology*, **45**(3), 579–594.

Tabakh, M. E., Utha-Aroon, C., & Schreiber, B., 1999. Sedimentology of the Cretaceous Maha Sarakham evaporites in the Khorat Plateau of northeastern Thailand, *Sedimentary Geology*, **123**(1), 31 – 62.

Tabakh, M. E., Utha-Aroon, C., Warren, J. K., & Schreiber, B., 2003. Origin of dolomites in the Cretaceous Maha Sarakham evaporites of the Khorat Plateau, northeast Thailand, *Sedimentary Geology*, **157**(3), 235 – 252.

Tanaka, T., Togashi, S., Kamioka, H., Amakawa, H., Kagami, H., Hamamoto, T., Yuhara, M., Orihashi, Y., Yoneda, S., Shimizu, H., Kunimaru, T., Takahashi, K., Yanagi, T., Nakano, T., Fujimaki, H., Shinjo, R., Asahara, Y., Tanimizu, M., & Dragusanu, C., 2000. JNdi-1: a neodymium isotopic reference in consistency with LaJolla neodymium, *Chemical Geology*, **168**(3), 279 – 281.

Tandon, S. K. & Sinha, R., 2007. *Geology of large river systems*, chap. 2, pp. 7–28, John Wiley & Sons, Chichester, UK.

Tang, J., Yin, X.-A., Yang, P., & Yang, Z., 2014. Assessment of Contributions of Climatic Variation and Human Activities to Streamflow Changes in the Lancang River, China, *Water Resources Management*, **28**(10), 2953–2966.

Taylor, B. E., Wheeler, M. C., & Nordstrom, D. K., 1984. Isotope composition of sulphate in acid mine drainage as measure of bacterial oxidation, *Nature*, **308**(5959), 538–541.

Taylor, B. E., Wheeler, M. C., & Nordstrom, D. K., 1984. Stable isotope geochemistry of acid mine drainage: Experimental oxidation of pyrite, *Geochimica et Cosmochimica Acta*, **48**(12), 2669 – 2678.

Telmer, K. & Veizer, J., 1999. Carbon fluxes, pCO_2 and substrate weathering in a large northern river basin, Canada: carbon isotope perspectives, *Chemical Geology*, **159**(1–4), 61 – 86.

Tessier, A., Campbell, P. G., & Bisson, M., 1979. Sequential extraction procedure for the speciation of particulate trace metals, *Analytical chemistry*, **51**(7), 844–851.

Thode, H., 1991. Sulphur isotopes in nature and the environment: an overview, *Stable isotopes: natural and anthropogenic sulphur in the environment*, **43**, 1–26.

Tipper, E. T., Bickle, M. J., Galy, A., West, A. J., Pomiès, C., & Chapman, H. J., 2006. The short term climatic sensitivity of carbonate and silicate weathering fluxes: Insight from seasonal variations in river chemistry, *Geochimica et Cosmochimica Acta*, **70**(11), 2737 – 2754.

Toran, L. & Harris, R. F., 1989. Interpretation of sulfur and oxygen isotopes in biological and abiological sulfide oxidation, *Geochimica et Cosmochimica Acta*, **53**(9), 2341 – 2348.

Torres, M. A., West, A. J., & Li, G., 2014. Sulphide oxidation and carbonate dissolution as a source of CO_2 over geological timescales, *Nature*, **507**(7492), 346–349.

Torres, M. A., West, A. J., Clark, K. E., Paris, G., Bouchez, J., Ponton, C., Feakins, S. J., Galy, V., & Adkins, J. F., 2016. The acid and alkalinity budgets of weathering in the Andes–Amazon system: Insights into the erosional control of global biogeochemical cycles, *Earth and Planetary Science Letters*, **450**, 381 – 391.

Torres, M. A., Moosdorf, N., Hartmann, J., Adkins, J. F., & West, A. J., 2017. Glacial weathering, sulfide oxidation, and global carbon cycle feedbacks, *Proceedings of the National Academy of Sciences*, **114**(33), 8716–8721.

Tripathy, G. R., Goswami, V., Singh, S. K., & Chakrapani, G. J., 2010. Temporal variations in Sr and ^{87}Sr/^{86}Sr of the Ganga headwaters: estimates of dissolved Sr flux to the mainstream, *Hydrological Processes*, **24**(9), 1159–1171.

Turchyn, A. V., Tipper, E. T., Galy, A., Lo, J.-K., & Bickle, M. J., 2013. Isotope evidence for secondary sulfide precipitation along the Marsyandi River, Nepal, Himalayas, *Earth and Planetary Science Letters*, **374**, 36 – 46.

Urey, H. C., 1952. On the Early Chemical History of the Earth and the Origin of Life, *Proceedings of the National Academy of Sciences of the United States of America*, **38**(4), 351–363.

Utha-Aroon, C., 1993. Continental origin of the maha sarakham evaporites, northeastern thailand, *Journal of Southeast Asian Earth Sciences*, **8**(1), 193 – 203, Seventh Regional Congress on Geology, Mineral and Energy Resources of Southeast Asia.

van Everdingen, R. O. & Krouse, H. R., 1985. Isotope composition of sulphates generated by bacterial and abiological oxidation, *Nature*, **315**(6018), 395–396.

Viers, J., Dupré, B., Braun, J.-J., Deberdt, S., Angeletti, B., Ndam Ngoupayou, J., & Michard, A., 2000. Major and trace element abundances, and strontium isotopes in the Nyong basin rivers (Cameroon): Constraints on chemical weathering processes and elements transport mechanisms in humid tropical environments, *Chemical Geology*, **169**, 211–241.

Walker, J. C. G., Hays, P. B., & Kasting, J. F., 1981. A negative feedback mechanism for the long-term stabilization of Earth's surface temperature, *Journal of Geophysical Research: Oceans*, **86**(C10), 9776–9782.

Weis, D., Kieffer, B., Maerschalk, C., Barling, J., De Jong, J., Williams, G. A., Hanano, D., Pretorius, W., Mattielli, N., Scoates, J. S.,*et al.*, 2006. High-precision isotopic characterization of USGS reference materials by TIMS and MC-ICP-MS, *Geochemistry, Geophysics, Geosystems*, **7**(8).

Weldeab, S., Emeis, K.-C., Hemleben, C., & Siebel, W., 2002. Provenance of lithogenic surface sediments and pathways of riverine suspended matter in the Eastern Mediterranean Sea: evidence from ^{143}Nd/^{144}Nd and ^{87}Sr/^{86}Sr ratios, *Chemical Geology*, **186**(1), 139 – 149.

West, A. J., Bickle, M. J., Collins, R., & Brasington, J., 2002. Small-catchment perspective on Himalayan weathering fluxes, *Geology*, **30**(4), 355–358.

West, A. J., Galy, A., & Bickle, M., 2005. Tectonic and climatic controls on silicate weathering, *Earth and Planetary Science Letters*, **235**(1–2), 211 – 228.

White, A. F. & Blum, A. E., 1995. Effects of climate on chemical weathering in watersheds, *Geochimica et Cosmochimica Acta*, **59**(9), 1729 – 1747.

White, A. F., Blum, A. E., Bullen, T. D., Vivit, D. V., Schulz, M., & Fitzpatrick, J., 1999. The effect of temperature on experimental and natural chemical weathering rates of granitoid rocks, *Geochimica et Cosmochimica Acta*, **63**(19), 3277 – 3291.

White, A. F., Bullen, T. D., Vivit, D. V., Schulz, M. S., & Clow, D. W., 1999. The role of disseminated calcite in the chemical weathering of granitoid rocks, *Geochimica et Cosmochimica Acta*, **63**(13-14), 1939–1953.

White, T., Brantley, S., Banwart, S., Chorover, J., Dietrich, W., Derry, L., Lohse, K., Anderson, S., Aufdendkampe, A., Bales, R.,*et al.*, 2015. The Role of Critical Zone Observatories in Critical Zone Science, in *Developments in Earth Surface Processes*, edited by J. R. Giardino & C. Houser, vol. 19, chap. 2, pp. 15 – 78, Elsevier.

WHO, W. H. O., 2017. *Guidelines for drinking-water quality: first addendum to the fourth edition*, Geneva: World Health Organization; 2017.

Wild, T. B. & Loucks, D. P., 2014. Managing flow, sediment, and hydropower regimes in the Sre Pok, Se San, and Se Kong Rivers of the Mekong basin, *Water Resources Research*, **50**(6), 5141–5157.

Willenbring, J. K. & von Blanckenburg, F., 2010. Long-term stability of global erosion rates and weathering during late-Cenozoic cooling, *Nature*, **465**(7295), 211–214.

World Waterfall Database, W., 2019. World's largest waterfalls.

Wu, W., Xu, S., Yang, J., & Yin, H., 2008. Silicate weathering and CO_2 consumption deduced from the seven Chinese rivers originating in the Qinghai-Tibet Plateau, *Chemical Geology*, **249**(3–4), 307 – 320.

Xu, Z. & Liu, C.-Q., 2007. Chemical weathering in the upper reaches of Xijiang River draining the Yunnan–Guizhou Plateau, Southwest China, *Chemical Geology*, **239**(1), 83 – 95.

Xue, Z., Liu, J. P., & Ge, Q., 2011. Changes in hydrology and sediment delivery of the Mekong River in the last 50 years: connection to damming, monsoon, and ENSO, *Earth Surface Processes and Landforms*, **36**(3), 296–308.

Yang, C., Telmer, K., & Veizer, J., 1996. Chemical dynamics of the "St. Lawrence" riverine system: δDH_2O, $\delta^{18}OH_2O$, $\delta^{13}CDIC$, $\delta^{34}SSO_4$, and dissolved $^{87}Sr/^{86}Sr$, *Geochimica et Cosmochimica Acta*, **60**(5), 851–865, cited By 140.

Yang, R., Fellin, M. G., Herman, F., Willett, S. D., Wang, W., & Maden, C., 2016. Spatial and temporal pattern of erosion in the Three Rivers Region, southeastern Tibet, *Earth and Planetary Science Letters*, **433**, 10 – 20.

Yoon, J., Huh, Y., Lee, I., Moon, S., Noh, H., & Qin, J., 2008. Weathering Processes in the Min Jiang: Major Elements, $^{87}Sr/^{86}Sr$, $\delta^{34}S_{SO4}$, and $\delta^{18}O_{SO4}$, *Aquatic Geochemistry*, **14**(2), 147–170.

Yuan, F. & Mayer, B., 2012. Chemical and isotopic evaluation of sulfur sources and cycling in the Pecos River, New Mexico, USA, *Chemical Geology*, **291**, 13 – 22.

Zachos, J., Pagani, M., Sloan, L., Thomas, E., & Billups, K., 2001. Trends, rhythms, and aberrations in global climate 65 Ma to present, *Science*, **292**(5517), 686–693.

Zachos, J. C., Dickens, G. R., & Zeebe, R. E., 2008. An early Cenozoic perspective on greenhouse warming and carbon-cycle dynamics, *Nature*, **451**(7176), 279–283.

Zhang, L.-L., Zhao, Z.-Q., Zhang, W., Tao, Z.-H., Huang, L., Yang, J.-X., Wu, Q.-X., & Liu, C.-Q., 2016. Characteristics of water chemistry and its indication of chemical weathering in jinshajiang, lancangjiang and nujiang drainage basins, *Environmental Earth Sciences*, **75**(6), 506.

Zhang, X., Ma, H., Ma, Y., Tang, Q., & Yuan, X., 2013. Origin of the late cretaceous potash-bearing evaporites in the vientiane basin of laos: 11b evidence from borates, *Journal of Asian Earth Sciences*, **62**, 812 – 818, Geology of Baikal Region.

Zhao, C., Liu, S., Dong, S., Isange, S., Liu, Q., An, N., & Li, X., 2015. Spatial and seasonal dynamics of organic carbon in physically fractioned sediments associated with dam construction in the middle Lancang-Mekong River, *Journal of Soils and Sediments*, **15**(11), 2323–2333.

Zhao, Q., Liu, S., Deng, L., Dong, S., Yang, J., & Wang, C., 2012. The effects of dam construction and precipitation variability on hydrologic alteration in the Lancang River Basin of southwest China, *International Journal of Applied Earth Observation and Geoinformation*, **26**.

Ziv, G., Baran, E., Nam, S., Rodríguez-Iturbe, I., & Levin, S. A., 2012. Trading-off fish biodiversity, food security, and hydropower in the Mekong River Basin, *Proceedings of the National Academy of Sciences*, **109**(15), 5609–5614.

Zolkos, S., Tank, S. E., & Kokelj, S. V., 2018. Mineral Weathering and the Permafrost Carbon-Climate Feedback, *Geophysical Research Letters*, **45**(18), 9623–9632.